Stony Brook University

Evolution of Ferric Sulfates with Relative Humidity and Temperature and Their Potential Usage as Environmental Indicators in Martian Research

A Dissertation Presented

by

Wenqian Xu

to

The Graduate School

in Partial Fulfillment of the Requirements

for the Degree of

Doctor of Philosophy

in

Geosciences

Stony Brook University

May 2011

Stony Brook University

The Graduate School

Wenqian Xu

We, the dissertation committee for the above candidate for the
Doctor of Philosophy degree,
Hereby recommend acceptance of this dissertation

Dr. John B. Parise, Dissertation Advisor
Professor, Department of Chemistry and Geosciences

Dr. Richard J. Reeder, Chairperson of Defense
Professor, Department of Geosciences

Dr. Scott M. McLennan, Committee Member
Professor, Department of Geosciences

Dr. A. Deanne Rogers, Committee Member
Research Assistant Professor, Department of Geosciences

Dr. Ronald C. Peterson, Outside Member
Professor, Department of Geological Sciences and Geological Engineering,
Queen's University

This dissertation is accepted by the Graduate School

Lawrence Martin
Dean of the Graduate School

Abstract of the Dissertation

Evolution of Ferric Sulfates with Relative Humidity and Temperature and their Potential Usage as Environmental Indicators in Martian Research

by

Wenqian Xu

Doctor of Philosophy

in

Geosciences

Stony Brook University

2011

Ferric sulfates have attracted attention of geochemists since the discovery of jarosite on surface of Mars in 2004. To date, several ferric sulfates have been identified or suggested on Mars, including ferricopiapite, paracoquimbite, etc. These ferric sulfates, formed in evaporation or diagenetic processes, serve as mineralogical evidence for past water activity on Mars. More than proving the presence of water, ferric sulfates are hygroscopic and display complex hydration and dehydration transitions with change of air humidity and temperature, which suggest they may have application in tracing paleo-environment on Mars.

On Earth, ferric sulfate minerals are environmentally important. Primarily distributed in acid mine drainage areas, ferric sulfates are hosts for various toxic metals and acidity. Their dissolution and precipitation greatly affect water quality and local environment.

In this dissertation research, phase stabilities and transformations of ferric sulfates as functions of temperature (T), relative humidity (RH) and atmospheric pressure (P) were studied in detail. Techniques were developed and applied in this research to follow phase transitions of ferric sulfates *in situ* with changing environmental parameters and simultaneously collecting X-ray diffraction (XRD) data. Combined with parallel *ex situ* studies employing humidity buffer technique, phase relationships among ferric sulfates and the RH-T phase diagrams were delineated. Humidity and temperature effects on the evaporation of concentrated ferric sulfate solution were also investigated. Phase evolution sequences from concentrated ferric sulfate solution, including phases occurring in both precipitation and post-precipitation alteration processes, were characterized as a function of relative humidity, temperature and time. A typical evolution sequence, $Fe_2(SO_4)_3$ solution → (ferricopiapite, rhomboclase) → kornelite → paracoquimbite, was identified at 40% to 60% RH at room temperature. An amorphous ferric sulfate formed from the $Fe_2(SO4)_3$ solution at RH < 30%.

$(H_3O)Fe(SO_4)_2$ was identified as a dehydration product of rhomboclase, $(H_5O_2)Fe(SO_4)_2 \cdot 2H_2O$, at low RH or high temperature. The phase boundary between these two compounds was resolved with *in situ* XRD studies at controlled RH and T and plotted in the RH-T phase diagram.

Temperature is shown to be an important factor dictating ferric sulfate transition rates. The low temperature as present on Mars (-150 °C to 20 °C) could kinetically inhibit intermediate hydration phases, such as ferricopiapite and the amorphous ferric sulfate, from

transforming to thermodynamically stable phases. This is why phase evolution maps resolved in this study are complementary to calculated phase diagrams. *In situ* T- and P-controlled XRD experiments showed ferric sulfates could be stabilized against variation of RH at T < 0 °C, indicating the diurnal RH variation (from almost 0 up to 100%) on the present day Martian surface can not affect hydration states of most ferric sulfates, except for a slight possibility to dehydrate ferricopiapite, which was found to be unstable at 6 °C and RH <1%.

Table of Contents

List of Figures

List of Tables

Acknowledgements

I greatly appreciate many collaborators who contributed their time and effort in my dissertation. I also greatly appreciate people who helped me and enlightened me in my five years' Ph.D. study. Above all, I thank my advisor, Professor John Parise, for his guidance, encouragement, corrections and support on my research. I thank Professor Scott McLennan and Nick Tosca for very helpful discussions on the ferric sulfate project. I thank former and present colleagues in John's group, especially the following: Aaron Celestian, who got me on board by letting me join his titanosilicate project and trained me to operate quite a few lab instruments; Paul Foster and Hyunsoo Park, who taught me techniques of single-crystal X-ray crystallography; Marc Michel, who introduced me pair distribution function analysis. Richard Harrington, Doug Hausner and I worked closely on a ferrihydrite project. Some of the results are reported in Chapter 6. Lauren Borkowski collected synchrotron micro-crystal diffraction data for an iron sulfate reported in Appendix.

Chapter 4, Chapter 6 and Appendix contain data collected at synchrotron X-ray facilities. Helps come from Jon Hanson at beamline X7B at National Scattering Light Source, and Peter Lee at beamline 1-IDC at Advanced Photon Source, and Yusheng Chen at beamline 15-IDB at Advanced Photon Source. I also thank Ken Baldwin, who keeps our delicate lab diffractometers running.

Financial support comes from National Aeronautics and Space Administration (NASA) Grant MFRP07-0022, National Science Foundation (NSF) grant CHE0714183 through Collaborative Research in Chemistry (CRC) and NSF grant DMR-0800415.

Special thanks to Marc Michel, Nick Tosca, Paul Forster, Richard Harrington, Lauren Borowski and John Parise for helping me on my English writing in my preliminary proposal, meeting abstracts, paper manuscripts and this dissertation.

Finally, I thank my committee, Richard Reeder, Deanne Rogers, Scott McLennan, Ronald Peterson and John Parise, for their inspection on the dissertation.

Chapter 1

Introduction to Ferric Sulfates

Abstract

Ferric sulfates are present on Mars. These minerals are hygroscopic and display complex phase transitions as a function of temperature and relative humidity, and so can potentially serve as environmental indicators to past sedimentary environments on Mars. This dissertation research aims at revealing the ferric sulfate phase evolutions in evaporative and diagenetic processes under different temperature and relative humidity conditions. This chapter briefly introduces ferric sulfates: their composition and crystal chemistry, speciation and distribution on Mars, association with acid mine drainage and environmental impacts.

1.1. Introduction

The recent discovery of ferric sulfate minerals on Mars (Klingelhofer et al., 2004; Squyres et al., 2004) and their occurrence as contamination in acid mine drainage (AMD) areas on Earth (Hammarstrom et al., 2005; Nordstrom and Alpers, 1999) make these compounds of broad geochemical interest. On Mars, ferric sulfates are an important component of chemical sediments that preserve evidence of past water activity, as these minerals are of aqueous origin (Burns and Fisher, 1990; Squyres et al., 2004). Further,

ferric sulfates display hysteretic or irreversible phase transitions related to change of temperature (T) and relative humidity (RH) and therefore may yield details on paleo-environmental conditions on Mars (Madden et al., 2004). Despite the significance of ferric sulfates, their stability and complex phase relationships as functions of T and RH are not well characterized.

In AMD regions, ferric sulfates are efflorescent minerals formed from oxidation of pyrite (FeS_2) and other iron sulfide minerals (Hammarstrom et al., 2005). Under conditions of high humidity or as a result of a rising groundwater table, ferric sulfates will dissolve and pollute the local aquatic system in two ways (Nordstrom and Alpers, 1999). First, Fe(III) hydrolysis will greatly increase the water acidity. Second, ferric sulfate minerals are hosts of various toxic metals, e.g. Cr, Pb, etc, and will release the sequestered toxic metals to the aquatic system upon dissolution. Remediation methods to treat both acid and toxic metal pollution associated with sulfate are in need.

In order to make substantial progress in both fields of research – Martian sulfate geochemistry and AMD remediation, a fundamental understanding of the structure, stability and the chemistry of ferric sulfates, including their behavior with respect to environmental changes, is necessary.

The main goal of this research is to establish phase relationships among ferric sulfates and to understand their formation and the diagenetic transitions under different RH and T conditions. This is accomplished by a combination of *in situ* and *ex situ* X-ray diffraction (XRD) methods. These methods are not only useful for identifying ferric sulfate phases, but also facilitate a quantitative evaluation of their crystal structures and an understanding of phase transitions at the atomic level. *In situ* XRD are carried out

using both commercial and custom-built environmental chambers designed to allow reproducible conditions of T and RH. The collected XRD data enable a more thorough understanding of the X-ray scattering behavior of ferric sulfate minerals in order to robustly interpret data from the CheMin instrument on the Mars Science Laboratory (Bish et al., 2007), which is scheduled to launch in November 2011. Also, this research provides important complementary experimental data for on-going geochemical modeling work, an endeavor hindered by the lack of fundamental laboratory studies of ferric sulfates.

1.2. Background

1.2.1. Crystal Chemistry of Ferric Sulfates

The term "ferric sulfates" used in this dissertation refers to natural minerals or synthetic inorganic compounds that mainly consist of ferric ion (Fe^{3+}) and sulfate group (SO_4^{2-}), with other possible components including structural water (H_2O), hydroxyl (OH), hydronium (H_3O^+) and other metal cations (e.g. K^+, Mg^{2+}). For example, the term ferric sulfate is applied to copiapite with a formula $Fe^{2+}Fe^{3+}_4(SO_4)_6(OH)_2 \cdot 20H_2O$ in this thesis. Table 1.1 lists common ferric sulfates.

The crystal structure of a ferric sulfate typically contains FeO_6 octahedra and SO_4 tetrahedra. A FeO_6 octahedron may link to a SO_4 tetrahedron or another FeO_6 octahedron through corner-sharing an oxygen atom. Generally, FeO_6 octahedra do not share edges in the crystal structure of ferric sulfates, and an SO_4 tetrahedron does not directly connect with another SO_4. The fact that SO_4 groups do not share oxygen can be explained from

the bond valance point of view: an S-O bond has a valance of 1.5, equal to the valence of S(VI) divided by four; an S-O-S connection will have the bond valence sum of the two S-O bonds equal to 3.0, much exceeding the charge of O^{2-}, which destabilizes such connection. Water molecules in ferric sulfates are either isolated --- connecting to other atoms through hydrogen bonding, or bond to Fe by occupying part or all of the six oxygen sites in FeO_6 octahedra. Water molecules in ferric sulfates are easily removed and reincorporated in response to changes of temperature or humidity. Removal or incorporation of H_2O usually necessitates a rearrangement of atoms in the structure, which induces a phase transition. Figure 1.1 illustrates the structure of ferricopiapite ($Fe^{3+}_{0.67}Fe^{3+}_4(SO_4)_6(OH)_2 \cdot 20H_2O$), as an example showing the connections of FeO_6 octahedra, SO_4 tetrahedra and H_2O in ferric sulfates.

1.2.2. Ferric Sulfates on Mars

Ferric-bearing minerals are thought to contribute to the surficial coloring of Mars. This belief was later confirmed by the Viking Lander X-ray fluorescence spectroscopic (XRFS) experiments in the late 1970s, which identified high concentrations of ferric iron amounting to 18 wt. % Fe_2O_3 in Martian fines and duricrust samples analyzed at both Chryse and Utopia (Clark et al., 1982; Toulmin et al., 1977). High concentrations of sulfur were also found as 8 wt.% SO_3 in the fines, and even higher in the duricrust (Clark et al., 1982). Sulfur, assumed to be in the oxidized state as sulfate anion, was suggested to mainly occur as calcium sulfate and magnesium sulfate (Clark and Vanhart, 1981; Gooding et al., 1988). Based on the Viking chemistry measurements, Burns (1987) first predicted the presence of ferric sulfates including jarosite ($(Na,K)^+Fe_3(SO_4)_2(OH)_6$) and

copiapite ($M^{2+}Fe_4(SO_4)_6(OH)_2 \cdot 20H_2O$)) and the stabilization of these phases at low temperatures and pH conditions in Martian permafrost. The presence of jarosite was confirmed 17 years later from the Mossbauer (MB) spectra measured by Mars Exploration Rovers (MER) Opportunity in the outcrops at Meridiani Planum (Klingelhofer et al., 2004; Morris et al., 2006b). Miniature thermal emission (Mini-TES) spectra quantified the jarosite to be about 5% by volume, with an additional 15 to 35% Mg- and Ca- sulfate in the outcrops (Christensen et al., 2004; Glotch et al., 2006). Jarosite typically forms as a product of acid weathering of iron-rich sediments and rocks at pH < 4 (Dutrizac and Jambor, 2000; Stoffregen et al., 2000). Its presence on Mars provides mineralogical evidence for past aqueous processes, probably under water-limited acid-sulfate condition (Klingelhofer et al., 2004; McLennan et al., 2005; Morris et al., 2006b; Squyres and Knoll, 2005).

Other than jarosite, an unidentified ferric-bearing phase termed "Fe3D3" is observed in the MB spectra from the Opportunity Rover (Clark et al., 2005; Morris et al., 2006b). This phase is closely associated with sulfur-rich outcrop rocks from the Burns formation. The mineralogy of the Fe3D3 phase is suspected to be $Fe(SO_4)(OH)$, schwertmannite ($Fe_{16}O_{16}(SO_4)_2(OH)_{12} \cdot 10H_2O$) or super-paramagnetic hematite (Clark et al., 2005; Farrand et al., 2007; Morris et al., 2006b). The XRD pattern of the "Fe3D3" phase to be collected in the Mars Science Laboratory program should easily confirm the phase identity.

Another ferric sulfate hydrate phase(s) distinct from jarosite and the Fe3D3 phase is detected in Paso Robles soils found on the northwest slope of Husband Hill in Gusev Crater (Gellert et al., 2006; Ming et al., 2006; Morris et al., 2006a). This ferric sulfate

phase(s) accounts for 65% of the total Fe in the Paso Robles soils with the remaining Fe distributed in hematite, olivine and pyroxene, based on analysis of Mossbauer spectroscopic data (Morris et al., 2006a). Mass balance calculations based on Alpha Particle X-ray Spectroscopic (APXS) measurement indicate this ferric sulfate(s) accounts for about 25 to 29 wt. % of the Paso Robles composition, with an additional 15 wt. % Mg-sulfate and Ca-sulfate content (Gellert et al., 2006; Ming et al., 2006). Similar ferric sulfate-rich soils, so named "Paso Robles class soils", are also observed at two other locations in Gusev Crater, including Arad in the Northern Inner Basin south of Husband Hill and Tyrone Southeast of Home Plate, with the ferric sulfate phase taking up to 86% and 29% of the total Fe content, respectively (Arvidson et al., 2008; Morris et al., 2008). The Paso Robles class soil may actually be more widespread in the subsurface in Gusev Crater (Yen et al., 2008).

The mineralogy of the ferric sulfate phase(s) in Paso Robles class soil is suspected to be one or more of various ferric sulfate hydrates, including rhomboclase ($(H_3O^+)Fe(SO_4)_2 \cdot 3H_2O$), ferricopiapite ($Fe_{4.67}(SO_4)_6(OH)_2 \cdot 20H_2O$), fibroferrite ($Fe(OH)(SO_4) \cdot 5H_2O$) and paracoquimbite ($Fe_2(SO_4)_3 \cdot 9H_2O$), based on the visible and near infrared (Vis-NIR) reflectance spectra from the Spirit Rover (Johnson et al., 2007). Among these, ferricopiapite is further recognized to be the most promising candidate for the ferric sulfate phase in Paso Robles class soil due to its close spectral resemblance to observed Vis-NIR spectra, thermal emission spectra and Mossbauer spectra (Lane et al., 2008). Mixing with other ferric sulfates such as butlerite ($Fe(OH)SO_4 \cdot 2H_2O$), parabutlerite ($Fe(OH)SO_4 \cdot 2H_2O$), fibroferrite or metahohmanite ($Fe_2O(SO_4)_2 \cdot 4H_2O$) is also possible (Lane et al., 2008).

Ferric sulfates are potentially widely distributed within and near the equatorial Valles Marineris canyon system. The Vis-NIR reflectance data acquired from Mars Reconnaissance Orbiter (MRO) Compact Reconnaissance Imaging Spectrometer for Mars (CRISM) revealed hydrated ferric sulfates, including hydronium jarosite and probably dehydrated ferricopiapite, associated with opaline silica and glass in finely stratified deposits in this area (Milliken et al., 2008). Also using CRISM data, Farrand et al (2009) discovered a K-bearing jarosite in the Mawrth Vallis region far from the Valles Marineris canyon system (Farrand et al., 2009). Bishop et al. (2009) closely examined the light-toned sulfate-bearing layered deposits in Juventae Chasma, and found the Vis-NIR spectral features of polyhydrated sulfate outcrops are most consistent with ferricopiapite, melanterite ($FeSO_4 \cdot 7H_2O$) or starkeyite ($MgSO_4 \cdot 4H_2O$), though a specific mineral can not be uniquely identified. The ferric-bearing polyhydrated sulfates are also observed in West Candor Chasma (Mangold et al., 2008).

Similar Vis-NIR spectra indicate that polyhydrated sulfates are also observed in the etched terrains in Meridiani Planum by Observatoire pour la Mine´ralogie, l'Eau, les Glaces et l'Activite´ (OMEGA) imaging spectrometer on board the Mars Express spacecraft (Arvidson et al., 2005; Bibring et al., 2005; Gendrin et al., 2005). Polyhydrated sulfates such as copiapite ($(Fe^{2+}Fe_4(SO_4)_6(OH)_2 \cdot 20H_2O)$), epsomite ($MgSO_4 \cdot 7H_2O$) or halotrichite ($FeAl_2(SO_4)_4 \cdot 22H_2O$) are suggested in the study of Gendrin et al (2005). Further analyses of the OMEGA data show amaranite ($Fe(OH)SO_4 \cdot 3H_2O$) or schwertmannite may be better candidate minerals for the polyhydrated sulfates (Poulet et al., 2008).

In short, there are three types of ferric sulfates discovered so far on Mars: (1) Jarosite, which is unambiguously identified from MB spectra in Meridiani Planum, is also found in Valles Marineris and Mawrth Vallis, but not in Gusev Crater. (2) Polyhydrated sulfates, a mixture of various ferric and non-ferric sulfates with ferricopiapite being probably the major component, are found in Paso Robles class soils in Gusev Crater, in Valles Marineris, and in the etched terranes in Meridiani Planum. They are mostly present in layered formations in the subsurface. (3) Candidate ferric sulfate for Fe3D3 found on Meridiani Planum, possibly schwertmannite or hydrates of $Fe(SO_4)(OH)$. The MB spectrum of the Fe3D3 mineral is different from jarosite or Paso Robles sulfates. The observed distribution of these three types of ferric sulfates is also summarized in Table 1.2.

Beside ferric sulfate, Mg- and Ca- sulfate are also identified, and they are usually associated with ferric sulfates inside or surrounding Valles Marineris canyon system, at Meridiani Planum and Gusev Crater (Bibring et al., 2006; Christensen et al., 2004; Clark et al., 2005; Gendrin et al., 2005; Klingelhofer et al., 2006; Squyres and Knoll, 2005). Mg- and Ca- sulfate are also found in north polar region, where ferric sulfate is absent (Kounaves et al., 2010; Langevin et al., 2005).

Ferric sulfate minerals typically form from acid and oxidative weathering of Fe-rich and S-rich minerals such as pyrite (FeS_2) and pyrrhotite (Fe_7S_8). The presence of ferric sulfate minerals on Mars implies an existence of a warm, wet and acidic environment in Mar's early evolution (Bibring et al., 2006; Hurowitz et al., 2005; King and McSween, 2005). The acidic environment and deposition of sulfates dominated the so-called "theiikian" era, the second era in the proposed three-era Martian geological

history, after the “phyllosian” era when phyllosilicates formed at a pH-neutral aqueous condition, and before the ‘‘siderikian’’ era dominated by anhydrous ferric oxide formation during a slow superficial weathering, where liquid water was not playing a major role (Bibring et al., 2006).

1.2.3. Ferric Sulfates associated with acid mine drainage (AMD)

Acid mine drainage (AMD) refers to acidic water outflow from metal mines and coal mines, where the oxidation and dissolution of sulfide minerals provides the source of acidity, and various metal cations (e.g, Fe^{2+}, Zn^{2+}, Pb^{2+}) and sulfate anions (SO_4^{2-}) in the water. The primary mineral contributing to AMD is pyrite (FeS_2) on a global scale, with other sulfides such as pyrrhotite (Fe_7S_8) and chalcopyrite ($CuFeS_2$) that can be important in some local environments (Hammarstrom et al., 2005; Jambor et al., 2000). Acid water occurs naturally as a result of weathering of sulfide-containing rocks, but mining activity that exposes large amounts of sulfide minerals to air, rainfall and groundwater, greatly exacerbates environmental problems. World-famous AMD sites include Iron Mountain mine in California and the Tinto River in Spain.

Ferric sulfates forming in AMD sites as evaporites from ferric and sulfate rich solutions include minerals coquimbite, copiapite, rhomboclase, roemerite, jarosite, etc. Ferric sulfate minerals represent a more advanced stage in the oxidation sequence and are located further downstream from iron sulfide ores, compared to ferrous sulfates such as melanterite ($FeSO_4 \cdot 7H_2O$) that are usually proximal to the ores (Jambor et al., 2000). The pH of solutions precipitating ferric sulfates are generally below 3, above this pH precipitation of ferric hydroxides and oxyhydroxides such as ferrihydrite and goethite (α-

FeOOH) will be favored. An exception is precipitation of schwertmannite under a pH range from 4.5 to 6.5, in the presence of abundant SO_4^{2-} in solution (Bigham et al., 1996). Based on field measurements, the pH of water in equilibrium with a few other ferric sulfate minerals is: pH = 1 to 2.35 for jarosite; pH = -1 for copiapite, pH = -2.5 to -3.6 for rhomboclase (Jambor et al., 2000; Nordstrom and Alpers, 1999; Nordstrom et al., 2000).

Most ferric sulfates are readily soluble, and exhibit a rapid response to local climate change. Formation and dissolution of ferric sulfates play an important role in the storage and transport of acidity. Due to the strong hydrolysis effect of the ferric ion, dissolution of iron sulfates caused by rainfalls or change in seasonal humidity can dramatically increase the water acidity (Nordstrom et al., 2000).

The formation of iron sulfate minerals often results in the sequestration of many toxic metals. For example, lead mainly coprecipitates with jarosite (Giere et al., 2003), and arsenic tends to go into coquimbite (Romero et al., 2006) and copiapite (Jamieson et al., 2005). Dissolution of the host minerals will release the toxic metals into the aquatic system (Alpers et al., 1994). rainstorm events with the onset of the wet season after a prolonged dry period can lead to fish kills downstream of some AMD sites (Jambor et al., 2000). Knowledge of the stability of these iron sulfate minerals under changing environment conditions is necessary to choose a safe, effective and economic way to remediate contamination.

1.2.4. Relative humidity effect on sulfate hydration

Relative humidity (RH) is the measure of the amount of water vapor in a gaseous mixture of air and water vapor. It equals the partial pressure of water vapor (e_w) divided

by the saturated water vapor pressure (e^*_w) at a temperature, with a value ranging from 0 to 1, usually expressed as a percentage, as shown by the equation below:

$$RH = \frac{e_w}{e^*_w} \times 100\% \qquad \text{(Eq. 1.1)}$$

The denominator in the above equation, the saturated water vapor pressure (e^*_w), is a function of temperature, so RH is also related to temperature (T). RH is generally not affected by air pressure or air composition. Figure 1.2 is a plot of the saturated water vapor pressure as a function of temperature, calculated from empirical equations provided by (Buck, 1981). Details of the Buck's equations will be described in Chapter 5 where the equations are needed to calculate low temperature RH.

Many sulfate minerals are hydrated, and have various hydration states stabilized at different conditions of RH and T. Changes of hydration states were studied on several metal sulfate species in laboratory under controlled RH and T, including Na-sulfate (Linnow et al., 2006), Mg-sulfate (Chou and Seal, 2003b; Vaniman et al., 2004), Fe(II)-sulfate (Chou et al., 2002; Peterson and Grant, 2005), Co-sulfate (Chou and Seal, 2005a), Ni-sulfate (Chou and Seal, 2003a), Cu-sulfate (Chou et al., 2002) and Zn-sulfate (Chou and Seal, 2005b). Experimental methods applied in these studies all involve a humidity control apparatus used to equilibrate the sample under constant RH and T and a device that can sense different hydration states. For example, the series of studies performed by Chou and Seal (2002; 2003a,b; 2005a,b) employed a weight balance to measure the weight gain or loss caused by hydration or dehydration thereby constraining the equilibrium T and RH boundaries. The studies from Peterson and Grant (2005) and Linnow et al (2006) utilized XRD to discern phases. A humidity control system installed on the diffractometer ensured the phase transitions under varied RH could be followed *in*

situ by XRD. Results from these studies are generally shown as a RH-T phase diagram, where stability fields of different hydration states are separated by phase boundaries. Figure 1.3 shows the RH-T phase diagram of ferrous sulfate hydrate from the paper by Peterson and Grant (2005). The phase boundary between rozenite ($FeSO_4 \cdot 4H_2O$) and melanterite ($FeSO_4 \cdot 7H_2O$) extends from the bottom left corner, representing low T and low RH, toward the upright corner, representing high T and high RH. This is a general shape for hydration-dehydration phase boundaries, as higher T and lower RH favor the less hydrated phase, and vice versa.

1.3. Outline of the Thesis and Significant Results

The main objective of this research is to resolve phase relationships among common ferric sulfate phases as functions of RH and T, and to characterize the evaporation of concentrated ferric sulfate solutions and post-evaporation transformations. The principal experimental methods are *ex situ* and *in situ* RH and T -controlled XRD methods. Technical details will be introduced in experimental method sections in following chapters.

Chapter 2 focuses on phase transitions of ferric sulfates at ambient temperatures (22 – 25 ˚C) and at different RH (0 – 75%). Hydration series of two polymorphs of $Fe_2(SO_4)_3$ and dehydration series from concentrated ferric sulfate solutions are resolved with *ex situ* humidity buffer methods and *in situ* XRD method with dynamic RH control. The important observations include: evaporation of concentrated $Fe_2(SO_4)_3$ solution at

40% to 60% RH initially crystallizes ferricopiapite and rhomboclase that further evolves to kornelite and paracoquimbite; an amorphous ferric sulfate forms at < 30% RH.

Chapter 3 extends the phase evolution study to non-ambient temperatures. The phase evolution maps as function of RH, T and time are presented. The *In situ* RH and T – controlled XRD method identified a transition from paracoquimbite to ferric sulfate pentahydrate at 80 °C. A previously proposed RH-T phase diagram is rectified with the new experiment results. Both Chapter 2 and Chapter 3 focus on the "2 Fe(III) – 3 SO_4 – *n* H_2O" system where the overall Fe/S atomic ratio is fixed to equal to 2/3 with variable amounts of water.

In Chapter 4, the RH-T phase diagram of a more acidic ferric sulfate hydrate system, Fe(III) – 2 SO_4 – *n* H_2O with the Fe/S ratio equal to 1/2, is explored using RH and T -controlled *in situ* XRD methods. Rhomboclase ($(H_5O_2)Fe(SO_4)_2 \cdot 2H_2O$) dehydrates to form $(H_3O)Fe(SO_4)_2$ at high T or low RH. The boundary is mapped in the RH-T phase diagram.

In Chapter 5, *in situ* XRD methods are developed to study the stability of several important ferric sulfates under simulated Martian surficial temperature and pressure conditions. Most of the studied ferric sulfates are stable from -30 °C to 20 °C, except for ferricopiapite which dehydrates at 6 °C and 0.6% RH.

Chapter 6 addresses the structure of ferrihydrite, a nanocrystalline ferric oxyhydroxide that is positively identified on Mar and that has a diagenetic relationship with ferric sulfate.

Chapter 7 is a summation of the state of ferric sulfate research to date with a perspective on future research directions and tasks.

The appendix characterizes the crystal structure and thermal properties of a new ferric sulfate phase found as an intermediate product in the hydration of trigonal $Fe_2(SO_4)_3$ and in the dehydration process from ferric sulfate solution.

References:

Ackermann, S., Lazic, B., Armbruster, T., Doyle, S., Grevel, K.D., and Majzlan, J. (2009) Thermodynamic and crystallographic properties of kornelite [$Fe_2(SO_4)_3 \cdot 7.75H_2O$] and paracoquimbite [$Fe_2(SO_4)_3 \cdot 9H_2O$]. American Mineralogist, 94(11-12), 1620-1628.

Alpers, C.N., Nordstrom, D.K., and Thompson, J.M. (1994) Seasonal-Variations of Zn/Cu Ratios in Acid-Mine Water from Iron-Mountain, California. Environmental Geochemistry of Sulfide Oxidation, 550, 324-344.

Arvidson, R.E., Poulet, F., Bibring, J.P., Wolff, M., Gendrin, A., Morris, R.V., Freeman, J.J., Langevin, Y., Mangold, N., and Bellucci, G. (2005) Spectral reflectance and morphologic correlations in eastern Terra Meridiani, Mars. Science, 307(5715), 1591-1594.

Arvidson, R.E., Ruff, S.W., Morris, R.V., Ming, D.W., Crumpler, L.S., Yen, A.S., Squyres, S.W., Sullivan, R.J., Bell, J.F., Cabrol, N.A., Clark, B.C., Farrand, W.H., Gellert, R., Greenberger, R., Grant, J.A., Guinness, E.A., Herkenhoff, K.E., Hurowitz, J.A., Johnson, J.R., Klingelhofer, G., Lewis, K.W., Li, R., McCoy, T.J., Moersch, J., McSween, H.Y., Murchie, S.L., Schmidt, M., Schroder, C., Wang, A., Wiseman, S., Madsen, M.B., Goetz, W., and McLennan, S.M. (2008) Spirit Mars Rover Mission to the Columbia Hills, Gusev Crater: Mission overview and selected results from the Cumberland Ridge to Home Plate. Journal of Geophysical Research-Planets, 113, E12S33, DOI: 10.1029/2008JE003183.

Bibring, J.P., Langevin, Y., Gendrin, A., Gondet, B., Poulet, F., Berthe, M., Soufflot, A., Arvidson, R., Mangold, N., Mustard, J., Drossart, P., and Team, O. (2005) Mars surface diversity as revealed by the OMEGA/Mars Express observations. Science, 307(5715), 1576-1581.

Bibring, J.P., Langevin, Y., Mustard, J.F., Poulet, F., Arvidson, R., Gendrin, A., Gondet, B., Mangold, N., Pinet, P., Forget, F., and Team, O. (2006) Global mineralogical and aqueous mars history derived from OMEGA/Mars express data. Science, 312(5772), 400-404.

Bigham, J.M., Schwertmann, U., Traina, S.J., Winland, R.L., and Wolf, M. (1996) Schwertmannite and the chemical modeling of iron in acid sulfate waters. Geochimica Et Cosmochimica Acta, 60(12), 2111-2121.

Bish, D.L., Blake, D., Sarrazin, P., Treiman, A.H., Hoehler, T., Hausrath, E.M., Midtkandal, I., and Steele, A. (2007) Field XRD/XRF mineral analysis by the MSAL CheMin instrument. Lunar and Planetary Science XXXVIII, Abstract no. 1163.

Bishop, J.L., Parente, M., Weitz, C.M., Dobrea, E.Z.N., Roach, L.H., Murchie, S.L., McGuire, P.C., McKeown, N.K., Rossi, C.M., Brown, A.J., Calvin, W.M., Milliken, R., and Mustard, J.F. (2009) Mineralogy of Juventae Chasma: Sulfates in the light-toned mounds, mafic minerals in the bedrock, and hydrated silica and hydroxylated ferric sulfate on the plateau. Journal of Geophysical Research-Planets, 114, E00D09, DOI: 10.1029/2009JE003352.

Buck, A.L. (1981) New Equations for Computing Vapor-Pressure and Enhancement Factor. Journal of Applied Meteorology, 20(12), 1527-1532.

Burns, R.G. (1987) Ferric Sulfates on Mars. Journal of Geophysical Research-Solid Earth and Planets, 92(B4), E570-E574.

Burns, R.G., and Fisher, D.S. (1990) Iron-Sulfur Mineralogy of Mars - Magmatic Evolution and Chemical-Weathering Products. Journal of Geophysical Research-Solid Earth and Planets, 95(B9), 14415-14421.

Chou, I.M., and Seal, R.R. (2003a) Acquisition and evaluation of thermodynamic data for morenosite-retgersite equilibria at 0.1 MPa. American Mineralogist, 88(11-12), 1943-1948.

-. (2003b) Determination of epsomite-hexahydrite equilibria by the humidity-buffer technique at 0.1 MPa with implications for phase equilibria in the system $MgSO_4$-H_2O. Astrobiology, 3(3), 619-630.

-. (2005a) Acquisition and evaluation of thermodynamic data for bieberite-moorhouseite equilibria at 0.1 MPa. American Mineralogist, 90(5-6), 912-917.

-. (2005b) Determination of goslarite-bianchite equilibria by the humidity-buffer technique at 0.1 MPa. Chemical Geology, 215(1-4), 517-523.

Chou, I.M., Seal, R.R., and Hemingway, B.S. (2002) Determination of melanterite-rozenite and chalcanthite-bonattite equilibria by humidity measurements at 0.1 MPa. American Mineralogist, 87(1), 108-114.

Christensen, P.R., Wyatt, M.B., Glotch, T.D., Rogers, A.D., Anwar, S., Arvidson, R.E., Bandfield, J.L., Blaney, D.L., Budney, C., Calvin, W.M., Faracaro, A., Fergason,

R.L., Gorelick, N., Graff, T.G., Hamilton, V.E., Hayes, A.G., Johnson, J.R., Knudson, A.T., McSween, H.Y., Mehall, G.L., Mehall, L.K., Moersch, J.E., Morris, R.V., Smith, M.D., Squyres, S.W., Ruff, S.W., and Wolff, M.J. (2004) Mineralogy at Meridiani Planum from the Mini-TES experiment on the Opportunity Rover. Science, 306(5702), 1733-1739.

Christidis, P.C., and Rentzeperis, P.J. (1975) Crystal-Structure of Monoclinic $Fe_2(SO_4)_3$. Zeitschrift Fur Kristallographie, 141(3-4), 233-245.

-. (1976) Crystal-Structure of Rhombohedral $Fe_2(SO_4)_3$. Zeitschrift Fur Kristallographie, 144(5-6), 341-352.

Clark, B.C., Baird, A.K., Weldon, R.J., Tsusaki, D.M., Schnabel, L., and Candelaria, M.P. (1982) Chemical-Composition of Martian Fines. Journal of Geophysical Research, 87(Nb12), 59-67.

Clark, B.C., Morris, R.V., McLennan, S.M., Gellert, R., Jolliff, B., Knoll, A.H., Squyres, S.W., Lowenstein, T.K., Ming, D.W., Tosca, N.J., Yen, A., Christensen, P.R., Gorevan, S., Bruckner, J., Calvin, W., Dreibus, G., Farrand, W., Klingelhoefer, G., Waenke, H., Zipfel, J., Bell, J.F., Grotzinger, J., McSween, H.Y., and Rieder, R. (2005) Chemistry and mineralogy of outcrops at Meridiani Planum. Earth and Planetary Science Letters, 240(1), 73-94.

Clark, B.C., and Vanhart, D.C. (1981) The Salts of Mars. Icarus, 45(2), 370-378.

Dutrizac, J.E., and Jambor, J.I. (2000) Jarosites and Their Application in Hydrometallurgy. In C.N. Alpers, J.I. Jambor, and D.K. Nordstrom, Eds. Sulfate Minerals: Crystallography, Geochemistry, and Environmental Significance, Reviews in Mineralogy and Geochemistry, vol. 40, p. 405-452. Mineralogical Society of America, Geochemical Society, Washington, D. C.

Fanfani, L., Nunzi, A., and Zanazzi, P.F. (1970) The crystal structure of roemerite. American Mineralogist, 55(1-2), 78-89.

-. (1971) Crystal Structure of Butlerite. American Mineralogist, 56(5-6), 751-757.

Fanfani, L., Nunzi, A., Zanazzi, P.F., and Zanzari, A.R. (1973) Copiapite Problem - Crystal-Structure of a Ferrian Copiapite. American Mineralogist, 58(3-4), 314-322.

Fang, J.H., and Robinson, P.D. (1970) Crystal Structures and Mineral Chemistry of Hydrated Ferric Sulfates .1. Crystal Structure of Coquimbite. American Mineralogist, 55(9-10), 1534-1540.

Farrand, W.H., Bell, J.F., Johnson, J.R., Jolliff, B.L., Knoll, A.H., McLennan, S.M., Squyres, S.W., Calvin, W.M., Grotzinger, J.P., Morris, R.V., Soderblom, J.,

Thompson, S.D., Watters, W.A., and Yen, A.S. (2007) Visible and near-infrared multispectral analysis of rocks at Meridiani Planum, Mars, by the Mars Exploration Rover Opportunity. Journal of Geophysical Research-Planets, 112, E05S02, DOI: 10.1029/2006JE002773.

Farrand, W.H., Glotch, T.D., Rice, J.W., Hurowitz, J.A., and Swayze, G.A. (2009) Discovery of jarosite within the Mawrth Vallis region of Mars: Implications for the geologic history of the region. Icarus, 204(2), 478-488.

Fernandez-Martinez, A., Timon, V., Roman-Ross, G., Cuello, G.J., Daniels, J.E., and Ayora, C. (2010) The structure of schwertmannite, a nanocrystalline iron oxyhydroxysulfate. American Mineralogist, 95(8-9), 1312-1322.

Gellert, R., Rieder, R., Bruckner, J., Clark, B.C., Dreibus, G., Klingelhofer, G., Lugmair, G., Ming, D.W., Wanke, H., Yen, A., Zipfel, J., and Squyres, S.W. (2006) Alpha particle X-ray spectrometer (APXS): Results from Gusev crater and calibration report. Journal of Geophysical Research-Planets, 111, E02S05, DOI: 10.1029/2005JE002555.

Gendrin, A., Mangold, N., Bibring, J.P., Langevin, Y., Gondet, B., Poulet, F., Bonello, G., Quantin, C., Mustard, J., Arvidson, R., and LeMouelic, S. (2005) Sulfates in martian layered terrains: the OMEGA/Mars Express view. Science, 307(5715), 1587-1591.

Giere, R., Sidenko, N.V., and Lazareva, E.V. (2003) The role of secondary minerals in controlling the migration of arsenic and metals from high-sulfide wastes (Berikul gold mine, Siberia). Applied Geochemistry, 18(9), 1347-1359.

Glotch, T. D., Bandfield, J. L., Christensen, P. R., Calvin, W. M., McLennan, S. M., Clark, B. C., Rogers, A. D. & Squyres, S. W. (2006). Journal of Geophysical Research-Planets 111, E12S03, DOI: 10.1029/2005JE002672.

Gooding, J.L., Wentworth, S.J., and Zolensky, M.E. (1988) Calcium-Carbonate and Sulfate of Possible Extraterrestrial Origin in the Eeta-79001 Meteorite. Geochimica Et Cosmochimica Acta, 52(4), 909-915.

Hammarstrom, J.M., Seal, R.R., Meier, A.L., and Kornfeld, J.M. (2005) Secondary sulfate minerals associated with acid drainage in the eastern US: recycling of metals and acidity in surficial environments. Chemical Geology, 215(1-4), 407-431.

Hawthorne, F.C., Krivovichev, S.V., and Burns, P.C. (2000) The Crystal Chemistry of Sulfate Minerals. In C.N. Alpers, J.I. Jambor, and D.K. Nordstrom, Eds. Sulfate Minerals: Crystallography, Geochemistry, and Environmental Significance, Reviews in Mineralogy and Geochemistry, vol. 40, p. 1-112. Mineralogical Society of America, Geochemical Society, Washington, D. C.

Hurowitz, J.A., McLennan, S.M., Lindsley, D.H., and Schoonen, M.A.A. (2005) Experimental epithermal alteration of synthetic Los Angeles meteorite: Implications for the origin of Martian soils and identification of hydrothermal sites on Mars. Journal of Geophysical Research-Planets, 110, E07002, DOI: 10.1029/2004JE002391.

Inami, T., Nishiyama, M., Maegawa, S., and Oka, Y. (2000) Magnetic structure of the kagome lattice antiferromagnet potassium jarosite $KFe_3(OH)_6(SO_4)_2$. Physical Review B, 61(18), 12181-12186.

Jambor, J.I., Nordstrom, D.K., and Alpers, C.N. (2000) Metal-sulfate Salts from Sulfide Mineral Oxidation. In C.N. Alpers, J.I. Jambor, and D.K. Nordstrom, Eds. Sulfate Minerals: Crystallography, Geochemistry, and Environmental Significance, Reviews in Mineralogy and Geochemistry, vol. 40, p. 305-350. Mineralogical Society of America, Geochemical Society, Washington, D. C.

Jamieson, H.E., Robinson, C., Alpers, C.N., McCleskey, R.B., Nordstrom, D.K., and Peterson, R.C. (2005) Major and trace element composition of copiapite-group minerals and coexisting water from the Richmond mine, Iron Mountain, California. Chemical Geology, 215(1-4), 387-405.

Johnson, J.R., Bell, J.F., Cloutis, E., Staid, M., Farrand, W.H., Mccoy, T., Rice, M., Wang, A., and Yen, A. (2007) Mineralogic constraints on sulfur-rich soils from Pancam spectra at Gusev crater, Mars. Geophysical Research Letters, 34, L13202, DOI: 10.1029/2007GL029894.

King, P.L., and McSween, H.Y. (2005) Effects of H_2O, pH, and oxidation state on the stability of Fe minerals on Mars. Journal of Geophysical Research-Planets, 110, E12S10, DOI: 10.1029/2005JE002482.

Klingelhofer, G., Morris, R.V., Bernhardt, B., Schroder, C., Rodionov, D.S., de Souza, P.A., Yen, A., Gellert, R., Evlanov, E.N., Zubkov, B., Foh, J., Bonnes, U., Kankeleit, E., Gutlich, P., Ming, D.W., Renz, F., Wdowiak, T., Squyres, S.W., and Arvidson, R.E. (2004) Jarosite and hematite at Meridiani Planum from Opportunity's Mossbauer spectrometer. Science, 306(5702), 1740-1745.

Klingelhofer, G., Morris, R.V., De Souza, P.A., Rodionov, D., and Schroder, C. (2006) Two earth years of Mossbauer studies of the surface of Mars with MIMOS II. Hyperfine Interactions, 170(1-3), 169-177.

Kounaves, S.P., Hecht, M.H., Kapit, J., Gospodinova, K., DeFlores, L., Quinn, R.C., Boynton, W.V., Clark, B.C., Catling, D.C., Hredzak, P., Ming, D.W., Moore, Q., Shusterman, J., Stroble, S., West, S.J., and Young, S.M.M. (2010) Wet Chemistry experiments on the 2007 Phoenix Mars Scout Lander mission: Data analysis and

results. Journal of Geophysical Research-Planets, 115, E00E10, DOI: 10.1029/2009JE003424.

Lane, M.D., Bishop, J.L., Dyar, M.D., King, P.L., Parente, M., and Hyde, B.C. (2008) Mineralogy of the Paso Robles soils on Mars. American Mineralogist, 93(5-6), 728-739.

Langevin, Y., Poulet, F., Bibring, J.P., and Gondet, B. (2005) Sulfates in the north polar region of Mars detected by OMEGA/Mars express. Science, 307(5715), 1584-1586.

Linnow, K., Zeunert, A., and Steiger, M. (2006) Investigation of sodium sulfate phase transitions in a porous material using humidity- and temperature-controlled X-ray diffraction. Analytical Chemistry, 78(13), 4683-4689.

Madden, M.E.E., Bodnar, R.J., and Rimstidt, J.D. (2004) Jarosite as an indicator of water-limited chemical weathering on Mars. Nature, 431(7010), 821-823.

Majzlan, J., Botez, C., and Stephens, P.W. (2005) The crystal structures of synthetics $Fe_2(SO_4)_3(H_2O)_5$ and the type specimen of lausenite. American Mineralogist, 90(2-3), 411-416.

Majzlan, J., and Kiefer, B. (2006) An X-ray- and neutron-diffraction study of synthetic ferricopiapite, $Fe_{14/3}(SO_4)_6(OD,OH)_2(D_2O,H_2O)_{20}$, and ab initio calculations on the structure of magnesiocopiapite, $MgFe_4(SO_4)_6(OH)_2(H_2O)_{20}$. Canadian Mineralogist, 44, 1227-1237.

Majzlan, J., and Michallik, R. (2007) The crystal structures, solid solutions and infrared spectra of copiapite-group minerals. Mineralogical Magazine, 71(5), 553-569.

Mangold, N., Gendrin, A., Gondet, B., LeMouelic, S., Quantin, C., Ansan, V., Bibring, J.P., Langevin, Y., Masson, P., and Neukum, G. (2008) Spectral and geological study of the sulfate-rich region of West Candor Chasma, Mars. Icarus, 194(2), 519-543.

McLennan, S.M., Bell, J.F., Calvin, W.M., Christensen, P.R., Clark, B.C., de Souza, P.A., Farmer, J., Farrand, W.H., Fike, D.A., Gellert, R., Ghosh, A., Glotch, T.D., Grotzinger, J.P., Hahn, B., Herkenhoff, K.E., Hurowitz, J.A., Johnson, J.R., Johnson, S.S., Jolliff, B., Klingelhofer, G., Knoll, A.H., Learner, Z., Malin, M.C., McSween, H.Y., Pocock, J., Ruff, S.W., Soderblom, L.A., Squyres, S.W., Tosca, N.J., Watters, W.A., Wyatt, M.B., and Yen, A. (2005) Provenance and diagenesis of the evaporite-bearing Burns formation, Meridiani Planum, Mars. Earth and Planetary Science Letters, 240(1), 95-121.

Mereiter, K. (1974) Die Kristallstruktur von Rhomboklas $H_5O_2Fe(SO_4)_2 \cdot 2H2O$. Tschermaks Mineralogische Und Petrographische Mitteilungen, 21, 216-232.

Milliken, R.E., Swayze, G.A., Arvidson, R.E., Bishop, J.L., Clark, R.N., Ehlmann, B.L., Green, R.O., Grotzinger, J.P., Morris, R.V., Murchie, S.L., Mustard, J.F., and Weitz, C. (2008) Opaline silica in young deposits on Mars. Geology, 36(11), 847-850.

Ming, D.W., Mittlefehldt, D.W., Morris, R.V., Golden, D.C., Gellert, R., Yen, A., Clark, B.C., Squyres, S.W., Farrand, W.H., Ruff, S.W., Arvidson, R.E., Klingelhofer, G., McSween, H.Y., Rodionov, D.S., Schroder, C., de Souza, P.A., and Wang, A. (2006) Geochemical and mineralogical indicators for aqueous processes in the Columbia Hills of Gusev crater, Mars. Journal of Geophysical Research-Planets, 111, E02S12, DOI: 10.1029/2005JE002560.

Miura, H., Niida, K., and Hirama, T. (1994) Mikasaite, $(Fe^{3+}, Al)_2(SO_4)_3$, a New Ferric Sulfate Mineral from Mikasa City, Hokkaido, Japan. Mineralogical Magazine, 58(393), 649-653.

Morris, R.V., Klingelhofer, G., Schroder, C., Fleischer, I., Ming, D.W., Yen, A.S., Gellert, R., Arvidson, R.E., Rodionov, D.S., Crumpler, L.S., Clark, B.C., Cohen, B.A., Mccoy, T.J., Mittlefehldt, D.W., Schmidt, M.E., de Souza, P.A., and Squyres, S.W. (2008) Iron mineralogy and aqueous alteration from Husband Hill through Home Plate at Gusev Crater, Mars: Results from the Mossbauer instrument on the Spirit Mars Exploration Rover. Journal of Geophysical Research-Planets, 113, E12S42, DOI: 10.1029/2008JE003201.

Morris, R.V., Klingelhofer, G., Schroder, C., Rodionov, D.S., Yen, A., Ming, D.W., de Souza, P.A., Fleischer, I., Wdowiak, T., Gellert, R., Bernhardt, B., Evlanov, E.N., Zubkov, B., Foh, J., Bonnes, U., Kankeleit, E., Gutlich, P., Renz, F., Squyres, S.W., and Arvidson, R.E. (2006a) Mossbauer mineralogy of rock, soil, and dust at Gusev crater, Mars: Spirit's journey through weakly altered olivine basalt on the plains and pervasively altered basalt in the Columbia Hills. Journal of Geophysical Research-Planets, 111, E02S13, DOI: 10.1029/2005JE002584.

Morris, R.V., Klingelhofer, G., Schroder, C., Rodionov, D.S., Yen, A., Ming, D.W., de Souza, P.A., Wdowiak, T., Fleischer, I., Gellert, R., Bernhardt, B., Bonnes, U., Cohen, B.A., Evlanov, E.N., Foh, J., Gutlich, P., Kankeleit, E., McCoy, T., Mittlefehldt, D.W., Renz, F., Schmidt, M.E., Zubkov, B., Squyres, S.W., and Arvidson, R.E. (2006b) Mossbauer mineralogy of rock, soil, and dust at Meridiani Planum, Mars: Opportunity's journey across sulfate-rich outcrop, basaltic sand and dust, and hematite lag deposits. Journal of Geophysical Research-Planets, 111, E12S15, DOI: 10.1029/2006JE002791.

Nordstrom, D.K., and Alpers, C.N. (1999) Negative pH, efflorescent mineralogy, and consequences for environmental restoration at the Iron Mountain Superfund site, California. Proceedings of the National Academy of Sciences of the United States of America, 96(7), 3455-3462.

Nordstrom, D.K., Alpers, C.N., Ptacek, C.J., and Blowes, D.W. (2000) Negative pH and extremely acidic mine waters from Iron Mountain, California. Environmental Science & Technology, 34(2), 254-258.

Peterson, R.C., and Grant, A.H. (2005) Dehydration and crystallization reactions of secondary sulfate minerals found in mine waste: In situ powder-diffraction experiments. Canadian Mineralogist, 43, 1171-1181.

Peterson, R.C., Valyashko, E., and Wang, R.Y. (2009) The atomic structure of $(H_3O)Fe^{3+}(SO_4)_2$ and rhomboclase, $(H_5O_2)Fe^{3+}(SO_4)_2 \cdot 2H_2O$. Canadian Mineralogist, 47(3), 625-634.

Poulet, F., Arvidson, R.E., Gomez, C., Morris, R.V., Bibring, J.P., Langevin, Y., Gondet, B., and Griffes, J. (2008) Mineralogy of Terra Meridiani and western Arabia Terra from OMEGA/MEx and implications for their formation. Icarus, 195(1), 106-130.

Robinson, P.D., and Fang, J.H. (1971) Crystal Structures and Mineral Chemistry of Hydrated Ferric Sulphates .2. Crystal Structure of Paracoquimbite. American Mineralogist, 56(9-10), 1567-1572.

-. (1973) Crystal-Structures and Mineral Chemistry of Hydrated Ferric Sulfates .3. Crystal-Structure of Kornelite. American Mineralogist, 58(5-6), 535-539.

Romero, A., Gonzalez, I., and Galan, E. (2006) The role of efflorescent sulfates in the storage of trace elements in stream waters polluted by acid mine-drainage: The case of Pena del Hierro, southwestern Spain. Canadian Mineralogist, 44, 1431-1446.

Scordari, F. (1981) Fibroferrite - a Mineral with a $Fe(OH)(H_2O)_2SO_4$ Spiral Chain and Its Relationship to $Fe(OH)SO_4$, Butlerite and Parabutlerite. Tschermaks Mineralogische Und Petrographische Mitteilungen, 28(1), 17-29.

Scordari, F., Ventruti, G., and Gualtieri, A.F. (2004) The structure of metahohmannite, $Fe^{3+}{}_2[O(SO_4)_2] \cdot 4H_2O$, by in situ synchrotron powder diffraction. American Mineralogist, 89(2-3), 365-370.

Squyres, S.W., Grotzinger, J.P., Arvidson, R.E., Bell, J.F., Calvin, W., Christensen, P.R., Clark, B.C., Crisp, J.A., Farrand, W.H., Herkenhoff, K.E., Johnson, J.R., Klingelhofer, G., Knoll, A.H., McLennan, S.M., McSween, H.Y., Morris, R.V., Rice, J.W., Rieder, R., and Soderblom, L.A. (2004) In situ evidence for an ancient aqueous environment at Meridiani Planum, Mars. Science, 306(5702), 1709-1714.

Squyres, S.W., and Knoll, A.H. (2005) Sedimentary rocks at Meridiani Planum: Origin, diagetiesis, and implications for life on Mars. Earth and Planetary Science Letters, 240(1), 1-10.

Stoffregen, R.E., Alpers, C.N., and Jambor, J.I. (2000) Alunite-Jarosite Crystallography, Thermodynamics, and Geochronology. In C.N. Alpers, J.I. Jambor, and D.K. Nordstrom, Eds. Sulfate Minerals: Crystallography, Geochemistry, and Environmental Significance, Reviews in Mineralogy and Geochemistry, vol. 40, p. 453-480. Mineralogical Society of America, Geochemical Society, Washington, D. C.

Susse, P. (1972) Crystal-Structure and Hydrogen-Bonding of Copiapite. Zeitschrift Fur Kristallographie Kristallgeometrie Kristallphysik Kristallchemie, 135(1-2), 34-55.

Thomas, J.N., Robinson, P.D., and Fang, J.H. (1974) Crystal-Structures and Mineral Chemistry of Hydrated Ferric Sulfates .4. Crystal-Structure of Quenstedtite. American Mineralogist, 59(5-6), 582-586.

Toulmin, P., Baird, A.K., Clark, B.C., Keil, K., Rose, H.J., Christian, R.P., Evans, P.H., and Kelliher, W.C. (1977) Geochemical and Mineralogical Interpretation of Viking Inorganic Chemical Results. Journal of Geophysical Research, 82(28), 4625-4634.

Vaniman, D.T., Bish, D.L., Chipera, S.J., Fialips, C.I., Carey, J.W., and Feldman, W.C. (2004) Magnesium sulphate salts and the history of water on Mars. Nature, 431(7009), 663-665.

Yen, A.S., Morris, R.V., Clark, B.C., Gellert, R., Knudson, A.T., Squyres, S., Mittlefehldt, D.W., Ming, D.W., Arvidson, R., Mccoy, T., Schmidt, M., Hurowitz, J., Li, R., and Johnson, J.R. (2008) Hydrothermal processes at Gusev Crater: An evaluation of Paso Robles class soils. Journal of Geophysical Research-Planets, 113, E06S10, DOI: 10.1029/2007JE002978.

Table 1.1 List of common ferric sulfates

Mineral name	Formula	Reference
1. $Fe_2(SO_4)_3 \cdot n\ H_2O$		
Mikasaite	$Fe_2(SO_4)_3$ (rhombohedral)	(Christidis and Rentzeperis, 1976; Miura et al., 1994)
(synthetic)	$Fe_2(SO_4)_3$ (monoclinic)	(Christidis and Rentzeperis, 1975)
(synthetic)	$Fe_2(SO_4)_3 \cdot 5H_2O$	(Majzlan et al., 2005)
Lausenite*	$Fe_2(SO_4)_3 \cdot 6H_2O$	(Majzlan et al., 2005)
Kornelite	$Fe_2(SO_4)_3 \cdot 7.25 – 7.75\ H_2O$	(Ackermann et al., 2009; Robinson and Fang, 1973)
Coquimbite	$Fe_2(SO_4)_3 \cdot 9H_2O$	(Fang and Robinson, 1970)
Paracoquimbite	$Fe_2(SO_4)_3 \cdot 9H_2O$	(Ackermann et al., 2009; Robinson and Fang, 1971)
Quenstedtite	$Fe_2(SO_4)_3 \cdot 11H_2O$	(Thomas et al., 1974)
2. with hydronium or hydroxyls		
Rhomboclase	$(H_5O_2)Fe(SO_4)_2 \cdot 2H_2O$	(Majzlan and Kiefer, 2006; Mereiter, 1974; Peterson et al., 2009)
Ferricopiapite	$Fe_{4.67}(SO_4)_6(OH)_2 \cdot 20H_2O$	(Fanfani et al., 1973; Majzlan and Kiefer, 2006)
Butlerite	$Fe(OH)(SO_4) \cdot 2H_2O$	(Fanfani et al., 1971)
Fibroferrite	$Fe(OH)(SO_4) \cdot 5H_2O$	(Scordari, 1981)
Metahohmannite	$Fe_2O(SO_4)_2 \cdot 4H_2O$	(Scordari et al., 2004)
Schwertmannite[$]	$Fe_{16}O_{16}(SO_4)_2(OH)_{12} \cdot 10H_2O$	(Bigham et al., 1996; Fernandez-Martinez et al., 2010)
3. mixed with other metal cations		
Copiapite group	$M^{2+}Fe_4(SO_4)_6(OH)_2 \cdot 20H_2O$ ($M = Fe^{2+}, Mg^{2+}, Ca^{2+}$)	(Majzlan and Michallik, 2007; Susse, 1972)
Jarosite group	$M^{+}Fe_3(SO_4)_2(OH)_6$ ($M = K^{+}, Na^{+}, H_3O^{+}$)	(Inami et al., 2000)
Roemerite	$Fe^{2+}Fe_2(SO_4)_4 \cdot 14H_2O$	(Fanfani et al., 1970)
Bilinite	$Fe^{2+}Fe_2(SO_4)_4 \cdot 22H_2O$	(Hawthorne et al., 2000)

* Lausenite, with an empirical formula $Fe_2(SO4)_3 \cdot 6H_2O$, is suspected to be same with the ferric sulfate pentahydrate $Fe_2(SO_4)_3 \cdot 5H_2O$ by Majzlan et al (2005).

[$] Schwertmennite is nanocrystalline and the structure is not well established. For details of the latest structural models, refer to Fernandez-Martinez et al (2010).

Table 1.2 Ferric sulfates identified and suspected on Mars

Ferric sulfate	Sites of occurrence	Reference
Jarosite	Meridiani Planum	Klingelhofer et al. (2004) Morris et al. (2006b)
	Valles Marineris	Milliken et al. (2008)
	Mawrth Vallis	Farrand et al. (2009)
Polyhydrated sulfates, most probably ferricopiapite	Gusev Crater: Paso Robles, Arad and Tyronne Possibly widespread in subsurface	Morris et al. (2006a) Johnson et al. (2007) Lane et al (2008)
	Valles Marineris	Milliken et al. (2008)
	Juventae Chasma	Bishop et al. (2009)
	West Candor Chasma	Mangold et al. (2008)
	Meridiani Planum Etched terranes	Gendrin et al. (2005)
Fe3D3, possibly schwertmannite or $Fe(SO_4)(OH)$	Meridiani Planum	Morris et al. (2006) Clark et al. (2005) Farrand et al. (2007)

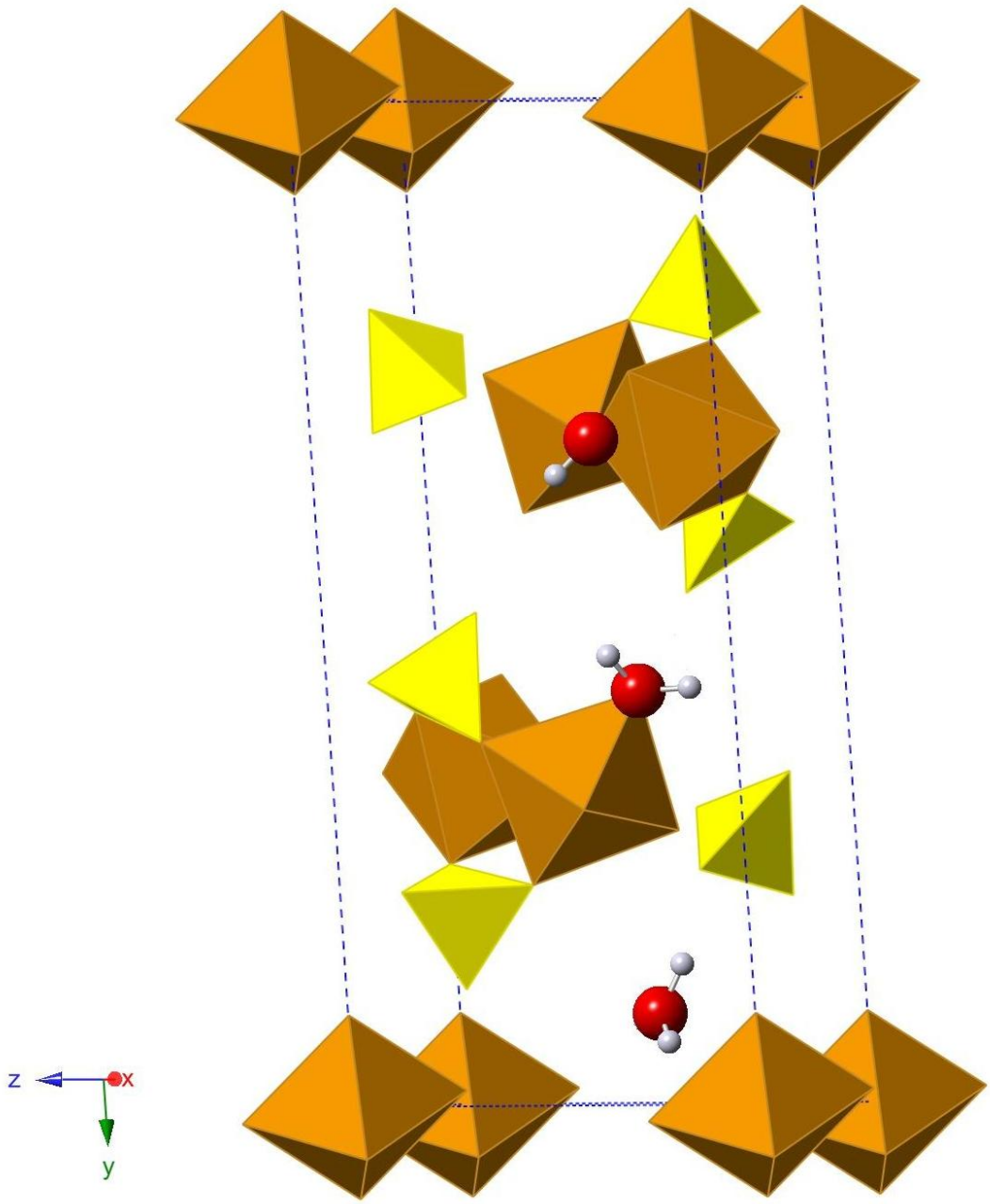

Figure 1.1. Crystal structure plot of ferricopiapite based on the structure reported in Fanfani et al (1973). Brown octahedra represent FeO_6 groups; yellow tetrahedra represent SO_4 groups; red spheres represent oxygen atoms; smaller grey spheres represent hydrogen atoms. An isolated H_2O and an H_2O bonded to Fe are shown in the picture (Not all H_2O in the structure are plotted for clarity). The OH group in ferricopiapite is located at the bridging oxygen site of two corner-shared FeO_6 octahedra. Dashed lines represent the lattice of the unit cell.

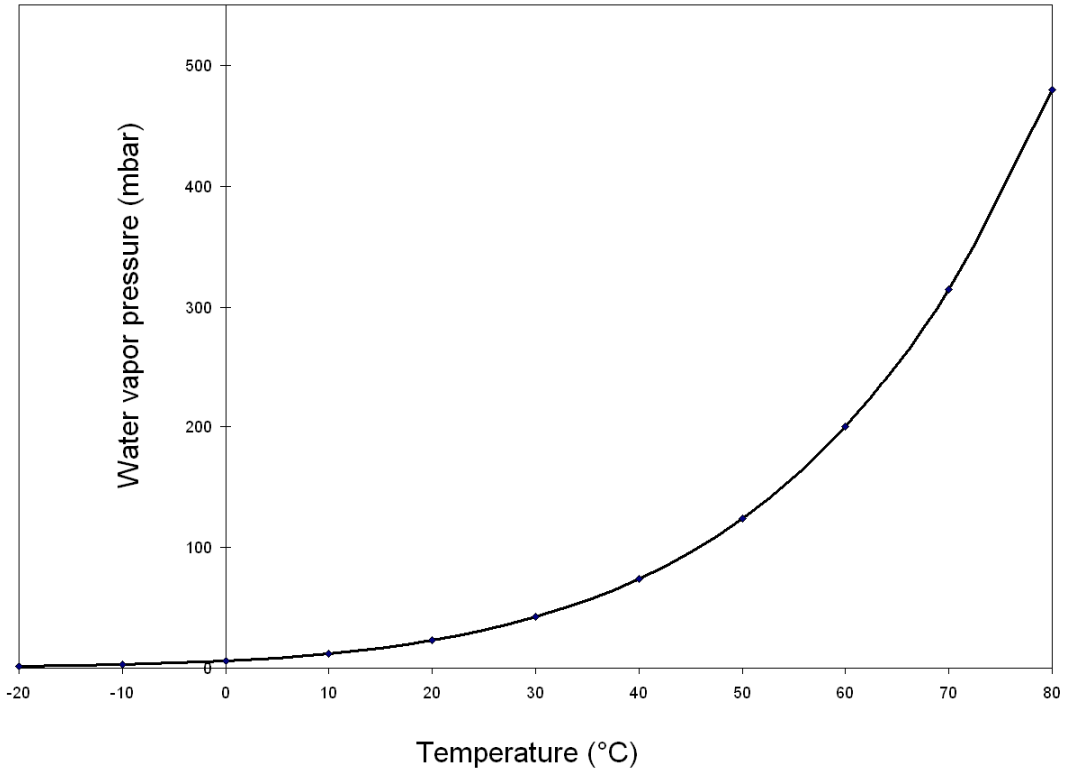

Figure 1.2. The saturated water vapor pressure at temperatures from -20 °C to 80 °C, calculated from equations provided in Buck (1981). Note the saturated vapor pressure is not zero below the freezing point of water.

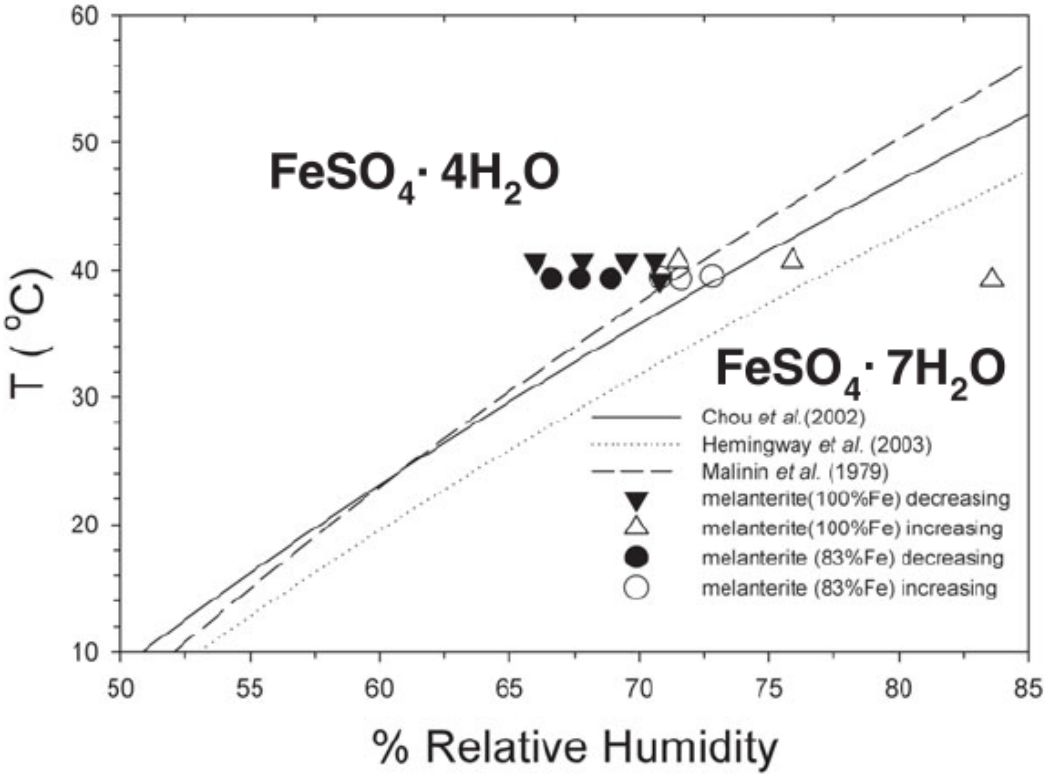

Figure 1.3. RH-T phase diagram for melanterite-rozenite from Peterson and Grant (2005). The solid, dashed and dotted lines represent this phase boundary measured in three independent studies from Chou et al. (2002), Malinin et al. (1979) and Hemingway et al. (2003).

Chapter 2

Phase Transitions of Ferric Sulfates at Room Temperature and Different Relative Humidity

This Chapter published as:

Xu, W.Q., Tosca, N.J., McLennan, S.M., and Parise, J.B. (2009) Humidity-induced phase transitions of ferric sulfate minerals studied by in situ and ex situ X-ray diffraction. American Mineralogist, 94(11-12), 1629-1637.

Abstract

Phases encountered in the hydration of monoclinic and trigonal anhydrous $Fe_2(SO_4)_3$ and evaporation of $Fe_2(SO_4)_3$ solutions were explored using *in situ* and *ex situ* X-ray diffraction (XRD) under dynamic relative humidity (RH) control at room temperature (22 – 25 °C). Both monoclinic and trigonal forms of $Fe_2(SO_4)_3$ remained anhydrous at 11% RH or below, and underwent the following phase evolution sequence: anhydrous $Fe_2(SO_4)_3$ → (ferricopiapite, rhomboclase) → kornelite → paracoquimbite at RH between 33% and 53% as a function of time. Evaporation of aqueous $Fe_2(SO_4)_3$ solutions at 40% < RH < 60% resulted in precipitation of ferricopiapite and rhomboclase, followed by a transition to kornelite and then paracoquimbite in post-evaporation aging processes at the same humidity levels. Evaporation at RH < 33% produced an amorphous ferric sulfate phase. The presence of some ferric sulfate hydrates and their stability under varying RH are not only determined by the final humidity level, but also

by the intermediate stages and hydration history (i.e, either ferricopiapite or paracoquimbite can be a stable phase at 62% RH depending on the hydration history). The sensitivity to humidity change and path-dependent transitions of ferric sulfates make them potentially valuable indicators of paleo-environmental conditions and past water activity on Mars. The phase relationships reported herein can help in understanding the diagenesis of ferric sulfate minerals, and are applicable to geochemical modeling of mineral solubility in multi-component systems, an endeavor hindered by the need for fundamental laboratory studies of ferric sulfate hydrates.

2.1. Introduction

An exciting result of recent Mars exploration is the observation of hydrated minerals (including hydrous sulfate minerals and phyllosilicates), that constitute an important fraction of sedimentary minerals on Mars (Bibring et al., 2005; Gendrin et al., 2005; McLennan and Grotzinger, 2008; Poulet et al., 2005; Squyres et al., 2004). The presence of these hydrated minerals implies water once played a significant role in Martian surficial evolution. Detailed understanding of the formation, stability and post-depositional evolution of these minerals is crucial in reconstructing ancient Martian environments.

Among these hydrated minerals, ferric sulfates are capable of yielding uniquely detailed information on the environmental conditions of the past and present Martian surface, because their stability is governed by important variables such as pH, redox conditions, temperature (T) and relative humidity (RH). To date, several ferric sulfate

minerals have been confirmed or strongly suspected at various places at the Spirit and Opportunity sites from Mossbauer or infrared spectroscopy data, including jarosite ($(Na,K,H_3O)^+Fe_3(SO_4)_2(OH)_6$), rhomboclase ($(H_3O^+)Fe(SO_4)_2 \cdot 3H_2O$), ferricopiapite ($Fe_{4.67}(SO_4)_6(OH)_2 \cdot 20H_2O$), fibroferrite ($Fe(OH)(SO_4) \cdot 5H_2O$), and schwertmannite ($Fe_{16}O_{16}(SO_4)_2(OH)_{12} \cdot 10H_2O$) (Farrand et al., 2007; Johnson et al., 2007; Klingelhofer et al., 2004; Lane et al., 2008; Morris et al., 2006; Poulet et al., 2008; Yen et al., 2008). The presence of sulfate minerals in evaporative settings implies a warmer, wetter and more acidic environment might have existed in Mar's early history (Bibring et al., 2006; Hurowitz and McLennan, 2007; King and McSween, 2005). Some workers have also suggested that the formation and distribution of ferric sulfate minerals on the Martian surface may be influenced by post-depositional diagenetic aqueous processes (Bibring et al., 2007; Tosca et al., 2008). In addition, ferric sulfates found within soils in the Columbia Hills and Inner Basin of Gusev Crater are likely associated with hydrothermal and fumarolic processes (Morris et al., 2008; Wang et al., 2008; Yen et al., 2008).

Sulfate minerals are known to display path-dependent phase transitions as a function of RH. For example, kieserite ($MgSO_4 \cdot H_2O$) transforms to hexahydrite ($MgSO_4 \cdot 6H_2O$) or epsomite ($MgSO_4 \cdot 7H_2O$) when exposed to humid air, while subsequent desiccation produces an amorphous phase rather than kieserite (Vaniman et al., 2004). These results suggest that kieserite might not occur in places influenced by surface cycles of hydration and dehydration (Vaniman et al., 2004). Similarly, Fe-sulfate minerals crystallize in multiple hydration states that are also sensitive to the changes in RH. Furthermore, as we show in this study, Fe(III) hydrolysis can significantly complicate hydration and dehydration reactions, and characterizing these complex

reaction pathways allows ferric sulfates to be used as important tracers of paleo-environmental conditions.

Two parallel experimental protocols were followed to study the phase stabilities and transformations in the ferric sulfate system: (1) *ex situ* RH equilibration of the sample followed by characterization with powder X-ray diffraction (XRD); (2) *in situ* monitoring of changes in the diffraction signature as RH was varied. While the *ex situ* method is well suited for the study of long-term stability, *in situ* XRD with dynamic RH control provides a more efficient way to examine the details of phase changes and to elucidate transient phases that may form over the course of the reaction. The RH-controlled *in situ* method was previously used to follow the phase transitions or structural change of inorganic clay minerals (Chipera, 1997) and sulfates, including Mg-sulfate (Vaniman et al., 2004), Fe(II)-sulfate (Peterson and Grant, 2005) and Na-sulfate (Linnow et al., 2006). Previous studies conducted by Chou and Seal (Chou and Seal, 2003a; Chou and Seal, 2003b; Chou and Seal, 2005a; Chou and Seal, 2005b; Chou and Seal, 2007; Chou et al., 2002) determined the equilibrium T and RH boundaries between neighboring hydration states of several bivalent metal sulfates by measuring the weight gain or loss caused by hydration or dehydration. To date, little work has been done to characterize the Fe(III)-sulfate interaction with water vapor, a common interaction in acid mine drainage (AMD) environments on Earth as well as on the Martian surface. In this study, we explored the stability and phase evolution among Fe(III)-sulfate hydrates as a function of RH at room temperature (22 – 25 °C). Results will also be used to establish a database which will enable a more thorough understanding of the X-ray scattering behavior of ferric sulfate

minerals in order to robustly interpret data from the CheMin instrument on the Mars Science Laboratory (Bish et al., 2007), which is scheduled to launch in 2011.

2.2. Experimental Methods

2.2.1. Sample preparation

Ferric sulfate ($Fe_2(SO_4)_3$) was selected as the starting material for hydration experiments. It has two polymorphs: a monoclinic and a trigonal phase (Christidis and Rentzeperis, 1975; Christidis and Rentzeperis, 1976). Only the trigonal phase has been found in nature as the mineral mikasaite (Miura et al., 1994). The monoclinic ferric sulfate (M-$Fe_2(SO_4)_3$) used in this study was purchased from Alfa-Aesar (Puratronic®, 99.998%, metals basis) and was used without further purification. The bulk sample was verified to be M-$Fe_2(SO_4)_3$ by powder XRD. The trigonal ferric sulfate (T-$Fe_2(SO_4)_3$) was prepared by heating the ferric sulfate hydrate from J. T. Baker (Baker Analyzed®, Assay $Fe_2(SO4)_3$ > 73.0%) at 350 °C for 2 hours. The purity and the anhydrous state of the prepared trigonal $Fe_2(SO4)_3$ were further confirmed by XRD and thermogravimetric analysis (TGA). The TG curve, shown in Figure 2.1, indicates a weight loss of less than 2% before the desulfation of the prepared trigonal $Fe_2(SO4)_3$ at 640 – 750 °C. The final desulfation product, determined to be pure hematite (α-Fe_2O_3) from XRD, weighted 39.5% of the initial sample weight. The weight is consistent with the theoretical value of 40% calculated from the ratio of molecular weights --- $MW_{Fe_2O_3} / MW_{Fe_2(SO_4)_3}$.

The reason for the selection of anhydrous $Fe_2(SO4)_3$ as the starting sample is two folded: first, it has the simplest stoichiometry in all ferric sulfates (Table 1.1 in Chapter

1); second, the Fe/S ratio of 2/3 is representative of quite a few important ferric sulfates including coquimbite ($Fe_2(SO_4)_3 \cdot 9H_2O$) and kornelite ($Fe_2(SO_4)_3 \cdot 7.25H_2O$). Coquimbite is the most commonly found ferric sulfate in AMD sites (Jambor et al., 2000). It is useful to explore the hydration of $Fe_2(SO_4)_3$ under different RH to form the more complex ferric sulfate hydrates. The result could be described with a phase evolution map (Levi, 1998), which is not necessarily related to the phase (equilibrium) diagram. Phase evolution maps also characterize the intermediate phases encountered as a function of time and other system variables (RH, T, Pressure, etc). The ferric sulfate hydration (or dehydration) evolution map will point out the different evolved ferric sulfate phases depending on the path taken during the evolution of RH.

2.2.2. *In situ* XRD with Dynamic RH control

Phase characterization was performed with two laboratory X-ray diffractometers, each of which was equipped with custom-built sample chambers capable of humidity control. A Bruker® General Area Detector Diffraction System (GADDS) equipped with a HI-STAR area detector was configured as shown in Figure 2.2. Co*K*α radiation (λ = 1.7903 Å), instead of the commonly used Cu*K*α radiation, was used to avoid Fe fluorescence from samples. The diffractometer has a *xyz* translation stage on which is mounted a Kapton® polyimide capillary enclosed in a sample environment chamber. A V-Gen II RH generator (InstruQuest®, not shown in the Figure 2.2) was used to dynamically control the humidity in the sample chamber. The RH generator uses a so-called two-temperature principle. The input gas, either air or N_2 gas, first flows into a water bath at temperature T_1, where the water vapor reaches saturation pressure at T_1.

The vapor-saturated gas then passes through a condenser chamber at temperature T_2 ($T_2 < T_1$). The gas is over-saturated at T_2 and part of the water vapor will be condensed into liquid. The water vapor in the condenser chamber is now at the saturated state at T_2. Then the gas is transported out of the condenser chamber to the sample chamber at temperature T_3 ($T_3 > T_2$). The RH in the sample chamber is determined by T_2 and T_3 following this equation:

$$RH = \frac{e_w^*(T_2)}{e_w^*(T_3)} \times 100\% \qquad \text{(Eq. 2.1)}$$

$e_w^*(T_2)$ is the saturated water vapor pressure at T_2, and $e_w^*(T_3)$ is the saturated water vapor pressure at T_3. $T_3 > T_2$ ensures $e_w^*(T_3) > e_w^*(T_2)$ so that no water vapor will be condensed in the sample chamber or on the sample (Fig. 1.2 in Chapter 1). In this study, T_3 is room temperature equals to ~23 ± 1 °C. The required RH is achieved by adjusting the T_2, which is program-controlled.

Humid air generated from the V-Gen II first passed through a heat-sealed transfer tube, through a manifold and finally into a polyimide capillary (1 mm in diameter) sealed in an 8 cm long Kapton® film chamber (Fig. 2.2). Sample powders, merged with the amorphous borosilicate glass wool substrates, were loaded in the top end of the capillary. The use of the substrate facilitates better contact with humid air by maximizing surface area, and avoided blocking the air flow. During the experiment, the airflow rate was set to 100 cc/min. A hygrometer was placed just above the capillary to measure both T and RH. To identify temperature gradients, an additional thermocouple was mounted in the manifold to measure the air temperature before it entered the capillary.

2.2.3. Humidity-buffer method

In addition to *in situ* studies, samples were also stored at a range of RH levels from 11% to 75% at room temperature (22 – 25 °C) to investigate reactions over prolonged time scales. The humidity-buffer method, where a saturated salt solution produces a stable RH, was used to control the RH inside the containers where powder samples were disseminated at the base of a trial and stored, as shown in Figure 2.3. The RH in the container is in equilibrium with the saturated salt solution (humidity buffer). The equilibrium RH is specific to the salt, and varies with temperature. Greenspan (Greenspan, 1977) evaluated previous experimental data on various saturated salt solutions, and estimated the equilibrium RH as a function of temperature. Table 2.1 lists humidity buffer salts used in this study, along with the documented and measured RH for each. The RH buffers were also used to test the calibration of RH probe (Rotronic®, Hygroclip SC05; accuracy: ± 1.5 %RH, ± 0.3 °C at 23 ± 5 °C), using a setup similar to Figure 2.3 except for provision of an opening in the cover for inserting the probe.

XRD patterns of the powder samples preserved in RH buffer cells were periodically collected and analyzed with the Scintag PAD-X X-ray diffractometer. The sample chamber on the Scintag (Fig. 2.4) differs from the one on the GADDS instrument in that it operates in Bragg-Brentano rather than Debye-Scherrer geometry. The chamber body is made from lucite with X-ray-transparent Kapton® film windows. The hygrometer is placed 1 cm above the sample plate through the opening in the front panel to monitor RH and T. Two other openings on the panel allow mounting of additional RH and T probes, or used as gas inlet and outlet when dynamic RH control is needed. Figure 2.4 shows the static RH control mode, achieved by simply placing a humidity buffer

inside the chamber. To collect XRD data, powder samples were quickly transferred into the chamber, in which the RH was pre-adjusted to match the condition inside the RH buffer cells, to prevent hydration or dehydration of the sample during data collection. Cu*K*α radiation (λ = 1.54178 Å) was used throughout experiments performed on the Scintag diffractometer which is able to discriminate Fe fluorescence. Data were collected using a step mode with a step size of 0.02° and a count rate of 3.0 seconds per step, and analyzed for phase information. Table 1.1 in Chapter 1 served as the primary database for phase identification. In cases there were peaks unable to be indexed to the phases listed in Table 1.1, an extensive search in Inorganic Crystal Structure Database (ICSD) and Powder Diffraction File (PDF) database would be performed. Phase quantification was done by a rough Rietveld refinement (Rietveld, 1969) of the powder XRD data using the programs GSAS (Larson and Von Dreele, 2000) and it is graphic interface EXPGUI (Toby, 2001), where scale factors for each crystalline phase were refined with adjusted cell parameters and specimen shift (zero correction) and peak profiles. An error of 10% in estimated phase percentage is normally expected.

2.3. Results

2.3.1. Long-term *ex situ* study using humidity-buffer method

2.3.1.1. Hydration of M-$Fe_2(SO_4)_3$

M-$Fe_2(SO_4)_3$ powder samples stored in different buffer cells at room T (22 – 25 °C) underwent different hydration pathways over time. Figure 2.5 shows the evolved ferric sulfate phases in different RH conditions versus storage time. For identified

crystalline phases, estimated weight proportions were given. Details of the phase evolution are described below.

The anhydrous state of M-$Fe_2(SO_4)_3$ appeared to remain stable over all reaction times at 11% RH. At 33% RH, a slow transition to a mixture of rhomboclase and ferricopiapite was observed. The mixture appeared to be a yellow aggregate showing the color of ferricopiapite. The crystallites were no larger than 2 μm, since no coherent domains could be discerned under microscope. Rhomboclase finely intergrew with ferricopiapite so that its white color could hardly be seen under microscope, but its presence was confirmed by XRD. The same transition also appeared in 43% and 53% RH cells but with an increased transition rate, as indicated by the proportions of rhomboclase and ferricopiapite in the samples at 25 days. At 43% and 53% RH, the mixture of rhomboclase and ferricopiapite subsequently transformed to kornelite then paracoquimbite over longer times, as the color of the sample turned from yellow to white and pinkish white that are colors of kornelite and paracoquimbite. Figure 2.6 shows the change of the sample XRD pattern along this transition at 53% RH. At 62% RH, ferricopiapite formed as a wet yellow paste less than two days after the hydration experiment started. However, rhomboclase, which co-formed with ferricopiapite at lower RH, did not appear, probably because rhomboclase, a highly soluble mineral (Tosca et al., 2007), was dissolved under this humidity level. This explanation was confirmed by an *in situ* experiment on the GADDS showing the deliquescence point of rhomboclase was between 58% and 60% RH at 25 °C. Also, the ferricopiapite paste with its coating liquid appeared to be stabilized at 62% RH, did not transform to kornelite as shown in 43% and

53% RH cells. At 75% RH, the sample was completely dissolved and a clear amber solution was formed.

2.3.1.2. Hydration of T-$Fe_2(SO_4)_3$

The phase evolution for T-$Fe_2(SO_4)_3$ at different RH levels involved the same hydrate phases as identified in the M-$Fe_2(SO_4)_3$ experiments --- ferricopiapite, rhomboclase, kornelite and paracoquimbite (Fig. 2.7). But this series was distinct from the hydration series of M-$Fe_2(SO_4)_3$ (Fig. 2.5) in two ways: first, the T-$Fe_2(SO_4)_3$ phase absorbed water much more rapidly than M-$Fe_2(SO_4)_3$. At 33%, 43%, 53% RH, T-$Fe_2(SO_4)_3$ turned to a solid-liquid suspensions within hours. Solid phases formed after 3 to 5 days. A higher water-absorbing rate could be related to a different surface structure or a smaller particle size thus larger specific surface area. The exact reason was not further investigated in this study. The second difference was that an unidentified intermediate phase(s) formed along with ferricopiapite and rhomboclase at 43% and 53% RH. Figure 2.8 shows the XRD patterns for the transformations at 53% RH containing this unknown phase. The XRD signature of this phase is further addressed in the discussion part in this chapter. The Crystal structure of the new phase is addressed in Appendix.

2.3.1.3. Dehydration from concentrated $Fe_2(SO_4)_3$ solution

To study the evaporation of ferric sulfate solution and the reversibility of the observed phase changes in the hydration experiments, the clear solution formed from T-$Fe_2(SO_4)_3$ in the 75% RH buffer cell was transferred to lower RH conditions. The

experimental set-up was as shown in Figure 2.3, except that the samples were liquid drops. The starting solution contains 41 wt. % $Fe_2(SO_4)_3$. The concentration is calculated by measuring the weight of starting T-$Fe_2(SO_4)_3$ and the resultant solution equilibrated in the 75% RH cell. Figure 2.9 shows the evolution of phases precipitated at different RH along with post-evaporation phase evolution.

At 62% RH, ferricopiapite precipitated as a yellow paste reminiscent of the sample observed at the same RH during the hydration process of both anhydrous forms of $Fe_2(SO_4)_3$. In the 53% and 43% RH cells, ferricopiapite and rhomboclase crystallized between 36 and 48 hours and no visible liquid phase remained. A slow transformation to kornelite and paracoquimbite occurred thereafter, but ferricopiapite and rhomboclase still dominated the overall phase assemblage after 60 days. At 33% RH, the liquid became extremely viscous and gradually (25 – 30 days) solidified to form a hard transparent amber-like amorphous material. Rhomboclase appeared after 50 days of subsequent reaction. At RH $\leq$ 11%, the amber-colored amorphous solid formed within 24 hours retaining the morphology of the starting liquid drops. No crystalline phases formed over two months of observation.

2.3.1.4. Dehydration of the ferricopiapite paste

The ferricopiapite paste stored in the 62% RH cell was loaded onto the Scintag Diffractometer with the RH inside the chamber stabilized at 53% by humidity buffer (Fig. 2.3). XRD patterns plotted in Figure 2.10 were collected over 72 hours without removing the sample. From beginning up to 12 hours, rhomboclase and kornelite formed and grew, while the ferricopiapite decreased. After 12 hours, rhomboclase XRD peak intensities

began decreasing while kornelite peak intensities continued to increase. After 60 hours, kornelite was the only phase in the product with the rhomboclase and the ferricopiapite phase both diminished. The kornelite product was then taken out of the diffractometer and re-preserved in the 62% RH buffer cell. The sample slowly rehydrated to paracoquimbite after months, instead of reverting to ferricopiapite paste with co-existing liquid (Fig. 2.11).

2.3.2. Short-term *In situ* study using RH generator

2.3.2.1. Hydration of M-$Fe_2(SO_4)_3$

Figure 2.12(a, b, c) shows the time-resolved XRD data collected on GADDS (Fig. 2.2) depicting the hydration of M-$Fe_2(SO_4)_3$ from 40% to 68% over 92 hours. The same phase evolution sequence was observed as in the *ex situ* studies: M-$Fe_2(SO_4)_3$ → (rhomboclase, ferricopiapite) → kornelite at RH ≤ 60%. At 68% RH, kornelite diminished while ferricopiapite increased. Note that kornelite generally transformed to paracoquimbite upon aging at 43% ≤ RH ≤ 62%, as reported in 2.3.1.1 to 2.3.1.4. The apparent transformation from kornelite to ferricopiapite at 68% was actually dissolution of kornelite followed by re-crystallization of ferricopiapite. XRD data shown in Figure 2.12(d) indicates the subsequent dehydration at 60 – 50% RH produced kornelite from the wet ferricopiapite, which is consistent with the result in 2.3.1.4.

2.3.2.2. Hydration of T-$Fe_2(SO_4)_3$

Figure 2.13 shows time-resolved XRD data collected on GADDS (Fig. 2.2) recording the hydration process of T-$Fe_2(SO_4)_3$ at 45% RH. The T-$Fe_2(SO_4)_3$ diffraction

peaks disappeared rapidly as the starting sample hydrated to form a suspension, as observed in the *ex situ* experiment. After 10 hours, both rhomboclase and ferricopiapite began crystallizing. The peak at 2θ = 12° could not be indexed to either rhomboclase or ferricopiapite. This reflection has the same d-spacing (8.4 Å) as the strongest reflection from the unknown phase observed in the ex situ experiment (Fig. 2.8). Note that the differences in 2θ values shown in Figure 2.8 and 2.13 are due to different X-ray wavelengths used on the Scintag (Cu*K*α) and GADDS (Co*K*α) instruments. These observations indicate this reflection very likely arises from the same unknown phase in both experiments. The *ex situ* experiment result discovered in section 2.3.1.2 was well reproduced.

2.4. Discussion

All experiments performed in this study were chemically constrained to the simplest Fe-SO_4-H_2O system: Molar ratio Fe/SO_4 was 2/3 as determined by the purity of the starting material, and the amount of H_2O was varied with RH.

2.4.1. Hydration series

At least five ferric sulfate hydrate phases were involved in the hydration of $Fe_2(SO_4)_3$ and subsequent dehydration experiments: ferricopiapite, rhomboclase, kornelite, paracoquimbite and an unknown phase particularly found in the hydration of T-$Fe_2(SO)_4$. One major difference from other metal sulfate hydrate systems is that the hydrolysis strongly affects the ferric sulfate phase evolution. This is manifested by the

formation of hydronium-bearing rhomboclase and hydroxyl-bearing ferricopiapite from anhydrous $Fe_2(SO_4)_3$ exposed to water vapor:

$$10\ Fe_2(SO_4)_3 + 90\ H_2O\ (g) \Longrightarrow 3\ Fe_{4.67}(SO_4)_6(OH)_2 \cdot 20H_2O + 6\ (H_3O)Fe(SO_4)_2 \cdot 3H_2O \quad \text{(Eq. 2.2)}$$

For the reaction with T-$Fe_2(SO_4)_3$, the product side should also include the unknown phase. The reverse reaction of equation 2.2 was not observed in this study. The mixture of the ferricopiapite and rhomboclase tends to neutralize each other to eventually form kornelite:

$$3\ Fe_{4.67}(SO_4)_6(OH)_2 \cdot 20H_2O + 6\ (H_3O)Fe(SO_4)_2 \cdot 3H_2O \Longleftrightarrow 10\ Fe_2(SO_4)_3 \cdot 7.25H_2O + 17.5\ H_2O(g) \quad \text{(Eq. 2.3)}$$

The forward reaction happens at modest RH from 33% to 53%. The reaction kinetics is dependent on the RH as higher RH facilitates the forward reaction. As indicated in Figure 2.5, the forward reaction proceeds more quickly at 53% RH than at 43% RH, but very slowly at 33% RH and was not able to reach equilibrium after 130 days. The reverse reaction happens when the RH is higher than the deliquescence point of kornelite but still lower than that of ferricopiapite (refer to section 2.3.2.1). While kornelite is not the most stable form at the modest RH conditions, it does finally transform to paracoquimbite:

$$Fe_2(SO_4)_3 \cdot 7.25H_2O + 1.75\ H_2O \Longrightarrow Fe_2(SO_4)_3 \cdot 9H_2O \quad \text{(Eq. 2.4)}$$

The RH-T boundary between kornelite and paracoquimbite was not a primary focus of the current study, although it can be concluded that the equilibrium RH should be below 43% at 22 to 25 °C, since the hydration transition was observed in this range (refer to section 2.3.1.1).

2.4.2. Path-dependant reactions

The particular ferric sulfate phases formed are determined not only by the RH, but also by the path taken to the final RH conditions. Results in sections 2.3.1.1 and 2.3.1.2 showed that one-step hydration of the anhydrous ferric sulfate at 62% RH produced the wet ferricopiapite paste, which was stable if there was no further change in RH. On the other hand, as shown in section 2.3.1.3, kornelite formed by dehydrating the ferricopiapite paste at 53% RH transformed to paracoquimbite rather than back to ferricopiapite when RH was re-elevated to 62%. We speculate that the difference in the pH of the coating solution might be responsible for ferricopiapite transforming to kornelite. When ferricopiapite was the only solid phase stabilized at 62% RH through a one-step hydration of $Fe_2(SO_4)_3$, the coating solution had to be acidic in order to balance the hydroxyls in ferricopiapite ($Fe_{4.67}(SO_4)_6(OH)_2 \cdot 20H_2O$), as the experiment system should have no net hydroxyls. The pH of the coating solution was probably still within the stability range of ferricopiapite, and therefore the paste could be well preserved. The paucity of coating solution and its close adsorption on ferricopiapite prohibited a precise measurement of pH by a probe method. The pH test paper attached onto the wet ferricopiapite indicated a pH value close to 1, fairly consistent with the predicted lower

pH boundary for ferricopiapite at about 0 in previous modeling work (Marion et al., 2008; Tosca et al., 2007). Reducing the RH to 53% evaporated more water, so that the coating solution finally became sufficiently acidic to convert ferricopiapite to kornelite.

2.4.3. Dehydration series

Evaporation of concentrated $Fe_2(SO_4)_3$ solution is also affected by environmental RH. At RH > 33%, ferricopiapite is the first solid phase to crystallize. Rhomboclase may or may not precipitate, depending on whether the RH is lower than the deliquescence point (58 – 60% at 25 °C). This precipitation process can also be described by Equation 2.1 in this chapter. Kornelite was not observed to crystallize directly from solution in this study, but forms by subsequent alteration of initially crystallized ferricopiapite. At RH conditions from 43% to 62%, kornelite gradually transforms to paracoquimbite over extended storage time (Fig. 2.5, 2.7 and 2.9), Paracoquimbite appears to be the most thermodynamically stable form of ferric sulfate hydrate at this RH range. This initial precipitation of ferricopiapite rather than kornelite or paracoquimbite may provide insight into the polymerization process in concentrated ferric sulfate solution. Evaporation at < 33% RH results in the formation of amorphous ferric sulfate. This may result from a high evaporation rate under low RH conditions which reduces the water activity of the solution so quickly that it inhibits the formation of any crystalline ferric sulfate hydrates. As the diurnal fluctuations of RH on the Martian surface range broadly from 10% to 90% (Peterson and Wang, 2006), ferric sulfate, if precipitated from a transient fluid phase formed under high RH condition, would most

likely stay as the initial precipitation phase like ferricopiapite or the amorphous ferric sulfate (Fig. 2.9).

2.4.4. The unindexed ferric sulfate phase

One of the transitional phases formed during the T-$Fe_2(SO_4)_3$ hydration process is not identified. This phase appears as a white powder, which has a fine intergrowth with ferricopiapite and rhomboclase, and is therefore difficult to obtain a pure phase powder. In the XRD data (Fig. 2.8) this unknown phase has two distinct low-angle peaks at d=16.7 Å and 8.4 Å). The relationship between the two d-spacings suggests the higher-angle peak probably has an index twice that of the lower one (2h 2k 2l). For comparison, ferricopiapite has peak 010 (d=18.3 Å) and 020 (d=9.2 Å) to the left of those of the unknown phase (Fig. 2.8). The unknown phase does not occur in the hydration of M-$Fe_2(SO_4)_3$, which may imply a different hydration mechanism, probably due to the structural difference of the two anhydrous ferric sulfate polymorphs. In Appendix, we show the unindexed phase can also be formed by evaporating concentrated ferric sulfate solution, though the synthesis was not reproducible. Crystal structure of this phase is also addressed in Appendix.

Some known ferric sulfate minerals were not yet found in this study, such as ferric sulfate pentahydrate ($Fe_2(SO_4)_3 \cdot 5H_2O$) (Majzlan et al., 2005), coquimbite [$(Fe, Al)_2(SO_4)_3 \cdot 9H_2O$] (Fang and Robinson, 1970) and quenstedtite ($Fe_2(SO_4)_3 \cdot 11H_2O$) (Thomas et al., 1974). Of these, ferric sulfate pentahydrate was later found as a phase primarily formed at elevated temperatures, which will be addressed in detail in Chapter 3; coquimbite, previously believed to be a polymorph of paracoquimbite, may actually

require the presence of aluminum in the structure, while paracoquimbite is a pure ferric phase (Majzlan et al., 2010). Furthermore, the relationship between M-$Fe_2(SO_4)_3$ and T-$Fe_2(SO_4)_3$ is not yet clear, and no direct conversion between the two phases has yet been found.

References:

Adams, J.R., and Merz, A.R. (1929) Hygroscopicity of fertilizer materials and mixtures. Industrial and Engineering Chemistry, 21, 305-307.

Bibring, J.P., Arvidson, R.E., Gendrin, A., Gondet, B., Langevin, Y., Le Mouelic, S., Mangold, N., Morris, R.V., Mustard, J.F., Poulet, F., Quantin, C., and Sotin, C. (2007) Coupled ferric oxides and sulfates on the Martian surface. Science, 317(5842), 1206-1210.

Bibring, J.P., Langevin, Y., Gendrin, A., Gondet, B., Poulet, F., Berthe, M., Soufflot, A., Arvidson, R., Mangold, N., Mustard, J., Drossart, P., and Team, O. (2005) Mars surface diversity as revealed by the OMEGA/Mars Express observations. Science, 307(5715), 1576-1581.

Bibring, J.P., Langevin, Y., Mustard, J.F., Poulet, F., Arvidson, R., Gendrin, A., Gondet, B., Mangold, N., Pinet, P., Forget, F., and Team, O. (2006) Global mineralogical and aqueous mars history derived from OMEGA/Mars express data. Science, 312(5772), 400-404.

Bish, D.L., Blake, D., Sarrazin, P., Treiman, A.H., Hoehler, T., Hausrath, E.M., Midtkandal, I., and Steele, A. (2007) Field XRD/XRF mineral analysis by the MSAL CheMin instrument. Lunar and Planetary Science XXXVIII, Abstract no. 1163.

Chipera, S.J., Carey, J.W., Bish, D. L. (1997) Controlled-humidity XRD analyses: Application to the study of smectite expansion/contraction. Adv. X-ray Anal., 39, 713-722.

Chou, I.M., and Seal, R.R. (2003a) Acquisition and evaluation of thermodynamic data for morenosite-retgersite equilibria at 0.1 MPa. American Mineralogist, 88(11-12), 1943-1948.

-. (2003b) Determination of epsomite-hexahydrite equilibria by the humidity-buffer technique at 0.1 MPa with implications for phase equilibria in the system $MgSO_4$-H_2O. Astrobiology, 3(3), 619-630.

-. (2005a) Acquisition and evaluation of thermodynamic data for bieberite-moorhouseite equilibria at 0.1 MPa. American Mineralogist, 90(5-6), 912-917.

-. (2005b) Determination of goslarite-bianchite equilibria by the humidity-buffer technique at 0.1 MPa. Chemical Geology, 215(1-4), 517-523.

-. (2007) Magnesium and calcium sulfate stabilities and the water budget of Mars. Journal of Geophysical Research-Planets, 112, E11004, DOI: 10.1029/2007JE002898.

Chou, I.M., Seal, R.R., and Hemingway, B.S. (2002) Determination of melanterite-rozenite and chalcanthite-bonattite equilibria by humidity measurements at 0.1 MPa. American Mineralogist, 87(1), 108-114.

Christidis, P.C., and Rentzeperis, P.J. (1975) Crystal-Structure of Monoclinic $Fe_2(SO_4)_3$. Zeitschrift Fur Kristallographie, 141(3-4), 233-245.

-. (1976) Crystal-Structure of Rhombohedral $Fe_2(SO_4)_3$. Zeitschrift Fur Kristallographie, 144(5-6), 341-352.

Fang, J.H., and Robinson, P.D. (1970) Crystal Structures and Mineral Chemistry of Hydrated Ferric Sulfates .1. Crystal Structure of Coquimbite. American Mineralogist, 55(9-10), 1534-1540.

Farrand, W.H., Bell, J.F., Johnson, J.R., Jolliff, B.L., Knoll, A.H., McLennan, S.M., Squyres, S.W., Calvin, W.M., Grotzinger, J.P., Morris, R.V., Soderblom, J., Thompson, S.D., Watters, W.A., and Yen, A.S. (2007) Visible and near-infrared multispectral analysis of rocks at Meridiani Planum, Mars, by the Mars Exploration Rover Opportunity. Journal of Geophysical Research-Planets, 112, E05S02, DOI: 10.1029/2006JE002773.

Gendrin, A., Mangold, N., Bibring, J.P., Langevin, Y., Gondet, B., Poulet, F., Bonello, G., Quantin, C., Mustard, J., Arvidson, R., and LeMouelic, S. (2005) Sulfates in martian layered terrains: the OMEGA/Mars Express view. Science, 307(5715), 1587-1591.

Greenspan, L. (1977) Humidity Fixed-Points of Binary Saturated Aqueous-Solutions. Journal of Research of the National Bureau of Standards Section a-Physics and Chemistry, 81(1), 89-96.

Hurowitz, J.A., and McLennan, S.M. (2007) A similar to 3.5 Ga record of water-limited, acidic weathering conditions on Mars. Earth and Planetary Science Letters, 260(3-4), 432-443.

Jambor, J.I., Nordstrom, D.K., and Alpers, C.N. (2000) Metal-sulfate Salts from Sulfide Mineral Oxidation. In C.N. Alpers, J.I. Jambor, and D.K. Nordstrom, Eds. Sulfate Minerals: Crystallography, Geochemistry, and Environmental Significance, Reviews in Mineralogy and Geochemistry, vol. 40, p. 305-350. Mineralogical Society of America, Geochemical Society, Washington, D. C.

Johnson, J.R., Bell, J.F., Cloutis, E., Staid, M., Farrand, W.H., Mccoy, T., Rice, M., Wang, A., and Yen, A. (2007) Mineralogic constraints on sulfur-rich soils from Pancam spectra at Gusev crater, Mars. Geophysical Research Letters, 34, L13202, DOI: 10.1029/2007GL029894.

King, P.L., and McSween, H.Y. (2005) Effects of H_2O, pH, and oxidation state on the stability of Fe minerals on Mars. Journal of Geophysical Research-Planets, 110, E12S10, DOI: 10.1029/2005JE002482.

Klingelhofer, G., Morris, R.V., Bernhardt, B., Schroder, C., Rodionov, D.S., de Souza, P.A., Yen, A., Gellert, R., Evlanov, E.N., Zubkov, B., Foh, J., Bonnes, U., Kankeleit, E., Gutlich, P., Ming, D.W., Renz, F., Wdowiak, T., Squyres, S.W., and Arvidson, R.E. (2004) Jarosite and hematite at Meridiani Planum from Opportunity's Mossbauer spectrometer. Science, 306(5702), 1740-1745.

Lane, M.D., Bishop, J.L., Dyar, M.D., King, P.L., Parente, M., and Hyde, B.C. (2008) Mineralogy of the Paso Robles soils on Mars. American Mineralogist, 93(5-6), 728-739.

Larson, A.C., and Von Dreele, R.B. (2000) "General Structure Analysis System (GSAS)". Los Alamos National Laboratory Report LAUR 86-748.

Levi, C.G. (1998) Metastability and microstructure evolution in the synthesis of inorganics from precursors. Acta Materialia, 46(3), 787-800.

Linnow, K., Zeunert, A., and Steiger, M. (2006) Investigation of sodium sulfate phase transitions in a porous material using humidity- and temperature-controlled X-ray diffraction. Analytical Chemistry, 78(13), 4683-4689.

Majzlan, J., Botez, C., and Stephens, P.W. (2005) The crystal structures of synthetics $Fe_2(SO_4)_3(H_2O)_5$ and the type specimen of lausenite. American Mineralogist, 90(2-3), 411-416.

Majzlan, J., Dordevic, T., Kolitsch, U., and Schefer, J. (2010) Hydrogen bonding in coquimbite, nominally $Fe_2(SO_4)_3\,9H_2O$, and the relationship between coquimbite and paracoquimbite. Mineralogy and Petrology, 100(3-4), 241-248.

Marion, G.M., Kargel, J.S., and Catling, D.C. (2008) Modeling ferrous-ferric iron chemistry with application to martian surface geochemistry. Geochimica Et Cosmochimica Acta, 72(1), 242-266.

McLennan, S.M., and Grotzinger, J.P. (2008) The Sedimentary Rock Cycle of Mars, in The Martian Surface: Compostion, Mineralogy, and Physical Properties. Cambridge Univ. Press (Cambridge) pp. 541-577.

Miura, H., Niida, K., and Hirama, T. (1994) Mikasaite, $(Fe^{3+}, Al)_2(SO_4)_3$, a New Ferric Sulfate Mineral from Mikasa City, Hokkaido, Japan. Mineralogical Magazine, 58(393), 649-653.

Morris, R.V., Klingelhofer, G., Schroder, C., Fleischer, I., Ming, D.W., Yen, A.S., Gellert, R., Arvidson, R.E., Rodionov, D.S., Crumpler, L.S., Clark, B.C., Cohen, B.A., Mccoy, T.J., Mittlefehldt, D.W., Schmidt, M.E., de Souza, P.A., and Squyres, S.W. (2008) Iron mineralogy and aqueous alteration from Husband Hill through Home Plate at Gusev Crater, Mars: Results from the Mossbauer instrument on the Spirit Mars Exploration Rover. Journal of Geophysical Research-Planets, 113, E12S42, DOI: 10.1029/2008JE003201.

Morris, R.V., Klingelhofer, G., Schroder, C., Rodionov, D.S., Yen, A., Ming, D.W., de Souza, P.A., Fleischer, I., Wdowiak, T., Gellert, R., Bernhardt, B., Evlanov, E.N., Zubkov, B., Foh, J., Bonnes, U., Kankeleit, E., Gutlich, P., Renz, F., Squyres, S.W., and Arvidson, R.E. (2006) Mossbauer mineralogy of rock, soil, and dust at Gusev crater, Mars: Spirit's journey through weakly altered olivine basalt on the plains and pervasively altered basalt in the Columbia Hills. Journal of Geophysical Research-Planets, 111, E02S13, DOI: 10.1029/2005JE002584.

Peterson, R.C., and Grant, A.H. (2005) Dehydration and crystallization reactions of secondary sulfate minerals found in mine waste: In situ powder-diffraction experiments. Canadian Mineralogist, 43, 1171-1181.

Peterson, R.C., and Wang, R.Y. (2006) Crystal molds on Mars: Melting of a possible new mineral species to create Martian chaotic terrain. Geology, 34(11), 957-960.

Poulet, F., Arvidson, R.E., Gomez, C., Morris, R.V., Bibring, J.P., Langevin, Y., Gondet, B., and Griffes, J. (2008) Mineralogy of Terra Meridiani and western Arabia Terra from OMEGA/MEx and implications for their formation. Icarus, 195(1), 106-130.

Poulet, F., Bibring, J.P., Mustard, J.F., Gendrin, A., Mangold, N., Langevin, Y., Arvidson, R.E., Gondet, B., Gomez, C., and Team, O. (2005) Phyllosilicates on Mars and implications for early martian climate. Nature, 438(7068), 623-627.

Rietveld, H.M. (1969) A Profile Refinement Method for Nuclear and Magnetic Structures. Journal of Applied Crystallography, 2, 65-&.

Squyres, S.W., Grotzinger, J.P., Arvidson, R.E., Bell, J.F., Calvin, W., Christensen, P.R., Clark, B.C., Crisp, J.A., Farrand, W.H., Herkenhoff, K.E., Johnson, J.R.,

Klingelhofer, G., Knoll, A.H., McLennan, S.M., McSween, H.Y., Morris, R.V., Rice, J.W., Rieder, R., and Soderblom, L.A. (2004) In situ evidence for an ancient aqueous environment at Meridiani Planum, Mars. Science, 306(5702), 1709-1714.

Thomas, J.N., Robinson, P.D., and Fang, J.H. (1974) Crystal-Structures and Mineral Chemistry of Hydrated Ferric Sulfates .4. Crystal-Structure of Quenstedtite. American Mineralogist, 59(5-6), 582-586.

Toby, B.H. (2001) EXPGUI, a graphical user interface for GSAS. Journal of Applied Crystallography, 34, 210-213.

Tosca, N.J., McLennan, S.M., Dyar, M.D., Sklute, E.C., and Michel, F.M. (2008) Fe oxidation processes at Meridiani Planum and implications for secondary Fe mineralogy on Mars. Journal of Geophysical Research-Planets, 113(E5), -.

Tosca, N.J., Smirnov, A., and McLennan, S.M. (2007) Application of the Pitzer ion interaction model to isopiestic data for the $Fe_2(SO_4)_3$-H_2SO_2-H_2O system at 298.15 and 323.15 K. Geochimica Et Cosmochimica Acta, 71(11), 2680-2698.

Vaniman, D.T., Bish, D.L., Chipera, S.J., Fialips, C.I., Carey, J.W., and Feldman, W.C. (2004) Magnesium sulphate salts and the history of water on Mars. Nature, 431(7009), 663-665.

Wang, A., Bell, J.F., Li, R., Johnson, J.R., Farrand, W.H., Cloutis, E.A., Arvidson, R.E., Crumpler, L., Squyres, S.W., McLennan, S.M., Herkenhoff, K.E., Ruff, S.W., Knudson, A.T., Chen, W., and Greenberger, R. (2008) Light-toned salty soils and coexisting Si-rich species discovered by the Mars Exploration Rover Spirit in Columbia Hills. Journal of Geophysical Research-Planets, 113, E12S40, DOI: 10.1029/2008JE003126.

Yen, A.S., Morris, R.V., Clark, B.C., Gellert, R., Knudson, A.T., Squyres, S., Mittlefehldt, D.W., Ming, D.W., Arvidson, R., Mccoy, T., Schmidt, M., Hurowitz, J., Li, R., and Johnson, J.R. (2008) Hydrothermal processes at Gusev Crater: An evaluation of Paso Robles class soils. Journal of Geophysical Research-Planets, 113, E06S10, DOI: 10.1029/2007JE002978.

Table 2.1. Humidity buffers used in this study

Humidity Buffer salts	Reported equilibrium RH (%)		RH measured in this study (±1% error)
	20°C	25°C	
LiCl	11.31 ± 0.31	11.30 ± 0.27	11.4 at 23.5°C
$MgCl_2$	33.07 ± 0.18	32.78 ± 0.16	33.7 at 22.8°C
$K_2(CO_3)_2$	43.16 ± 0.33	43.16 ± 0.39	42.9 at 24.3°C
$Mg(NO_3)_2$	54.38 ± 0.28	52.89 ± 0.22	53.0 at 22.4°C
NH_4NO_3	66.9*	62.7*	61.7 at 23.8°C
NaCl	75.47 ±0.14	75.29 ± 0.12	74.3 at 22.8°C

* data were adapted from (Adams and Merz, 1929); others were from (Greenspan, 1977)

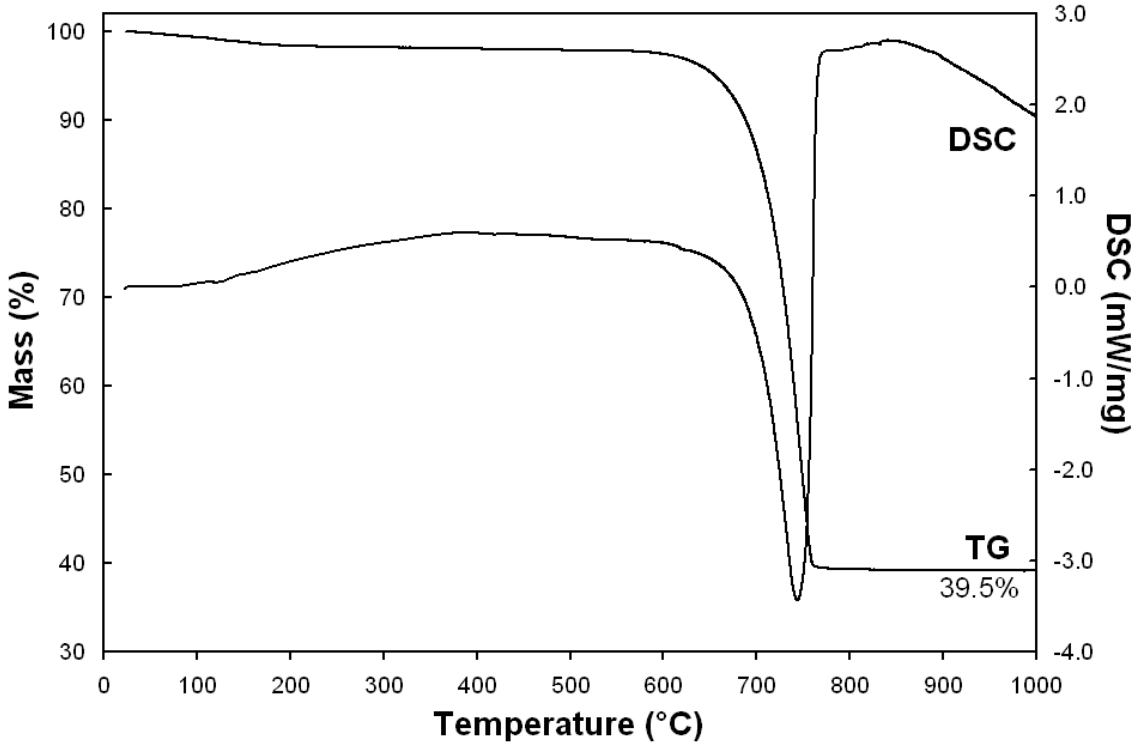

Figure 2.1. TG and DSC (Differential Scanning Calorimetric) data of the prepared trigonal $Fe_2(SO_4)_3$. A DSC endothermic peak correlates with a weight loss at around 640 to 750 °C, indicating the decomposition of $Fe_2(SO_4)_3$ forming hematite.

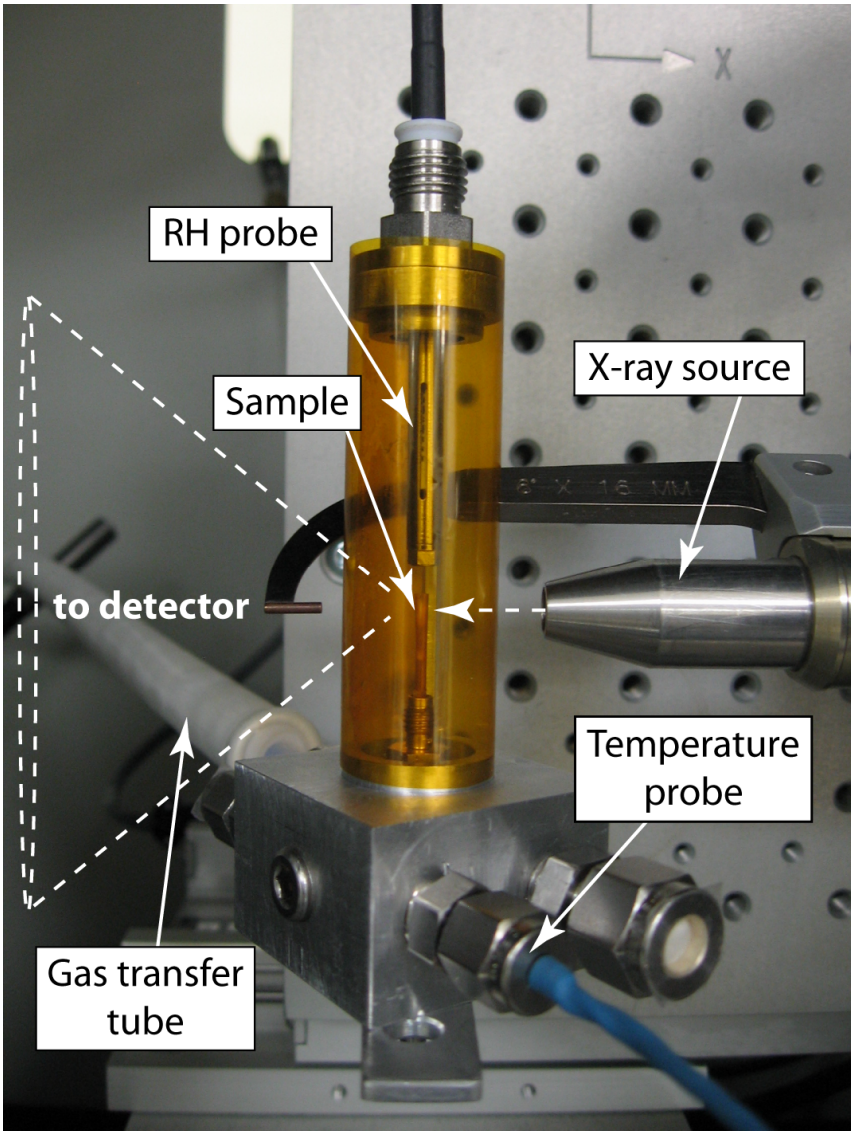

Figure 2.2. The humidity chamber on GADDS diffractometer with dynamic RH control

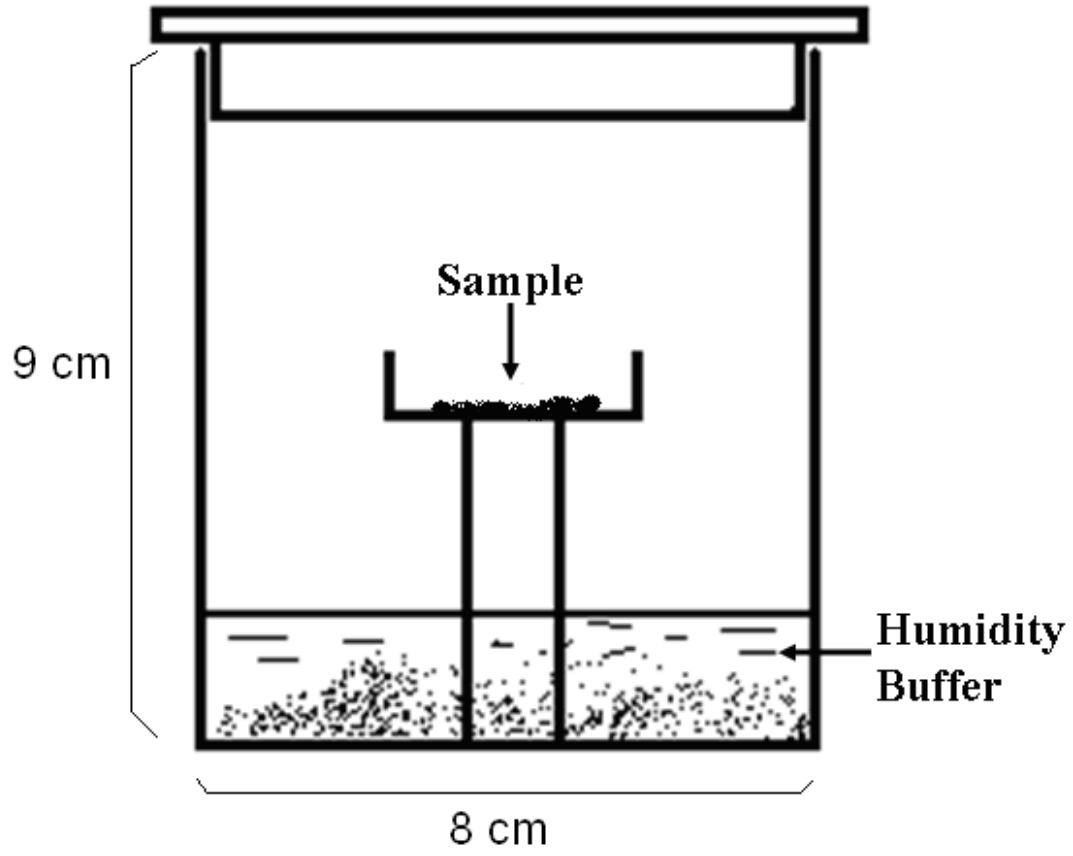

Figure 2.3. The scheme of the humidity container used to preserve samples under constant RH

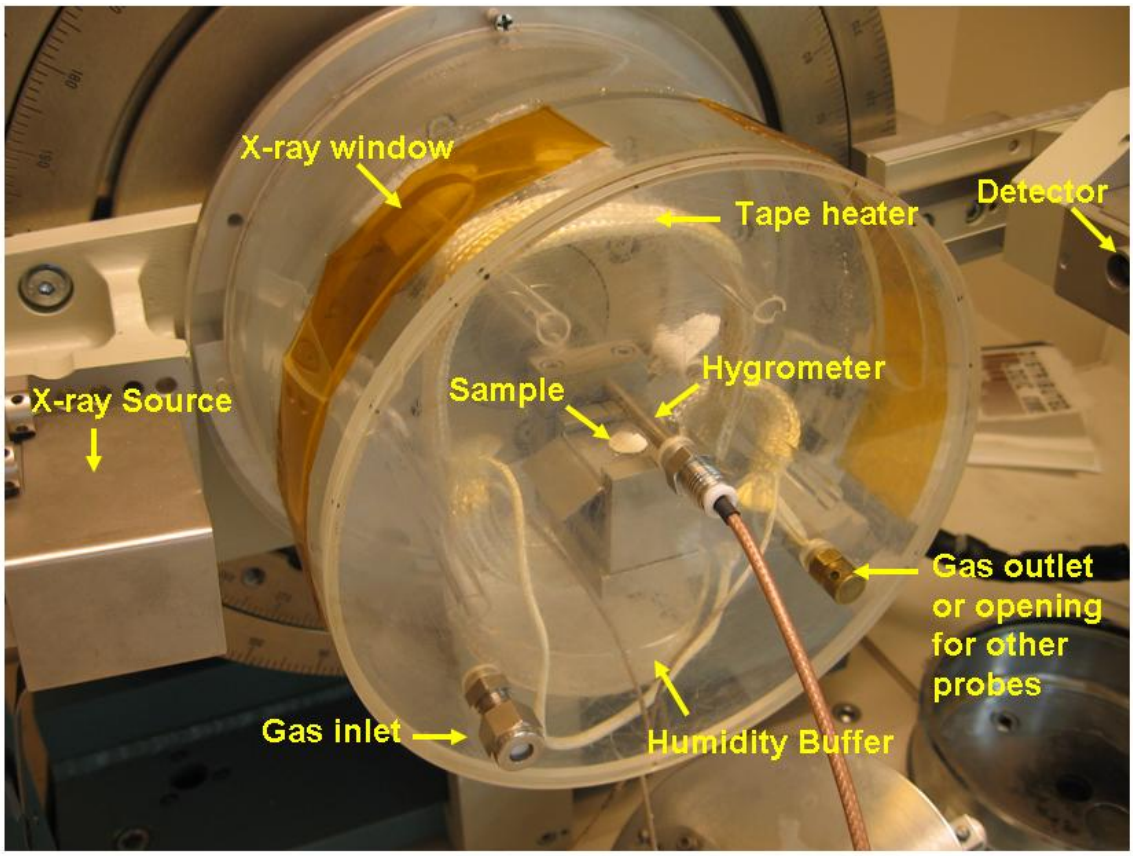

Figure 2.4. Set-up on Scintag Diffractometer using static RH control mode

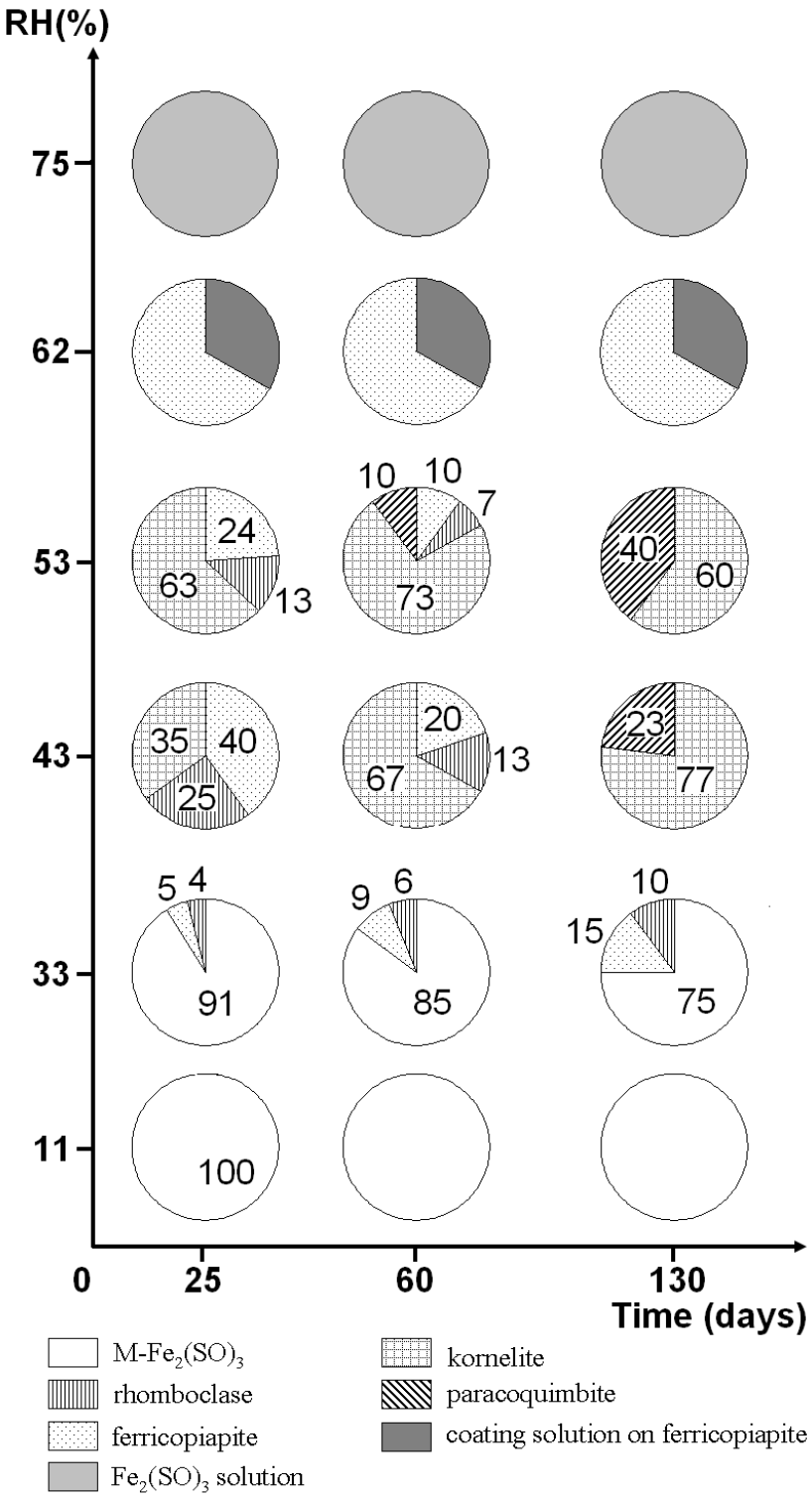

Figure 2.5. Phase evolution map of M-$Fe_2(SO_4)_3$ under static RH. Figures in the pie chart indicate the weight percentages of the phases present. These values are not given for liquid phases, or the crystalline phase that coexists with a liquid.

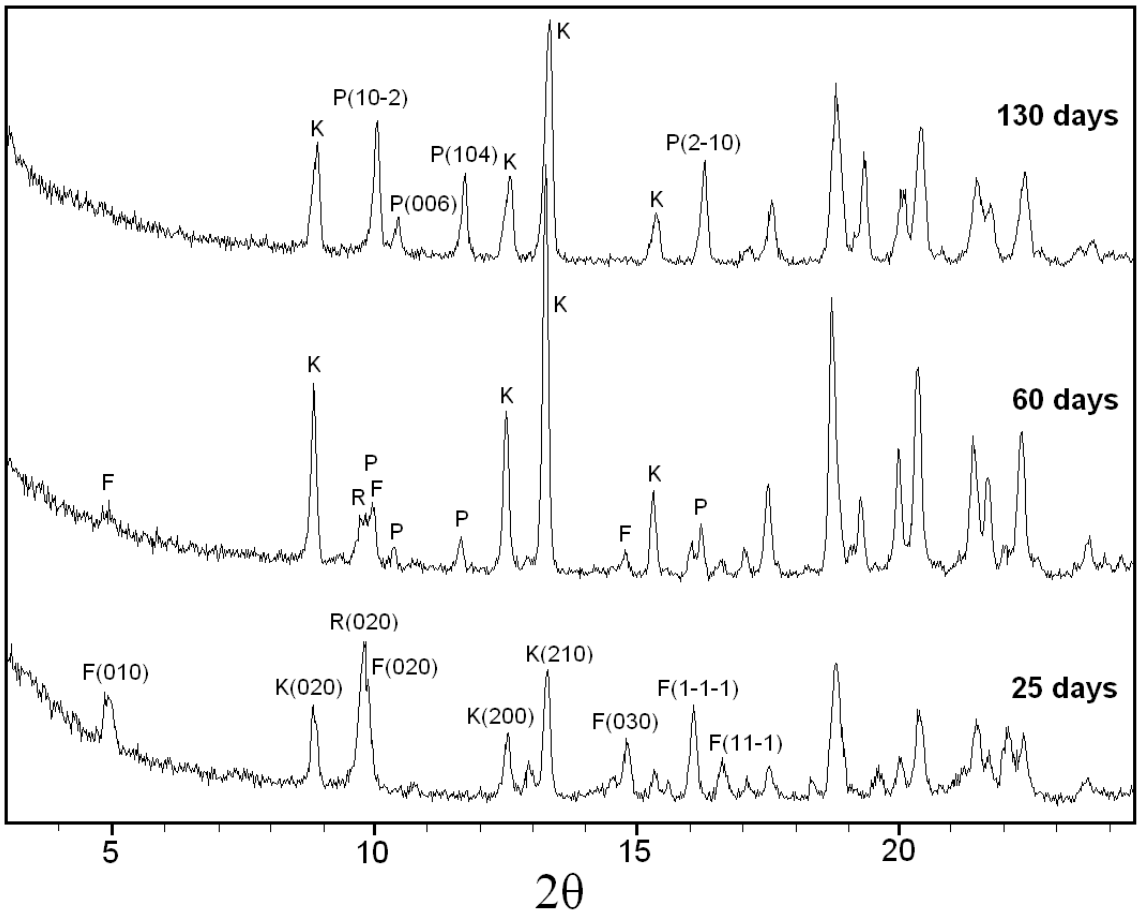

Figure 2.6. XRD data showing the hydration process of M-$Fe_2(SO_4)_3$ at 53% RH. Several peaks were marked with the initials of corresponding mineral names, either followed by the index numbers in parenthesis or not. **F**: Ferricopiapite; **R**: Rhomboclase; **K**: Kornelite; **P**: Paracoquimbite. The change of peak intensities clearly shows a phase transformation from ferricopiapite and rhomboclase to kornelite, then to paracoquimbite.

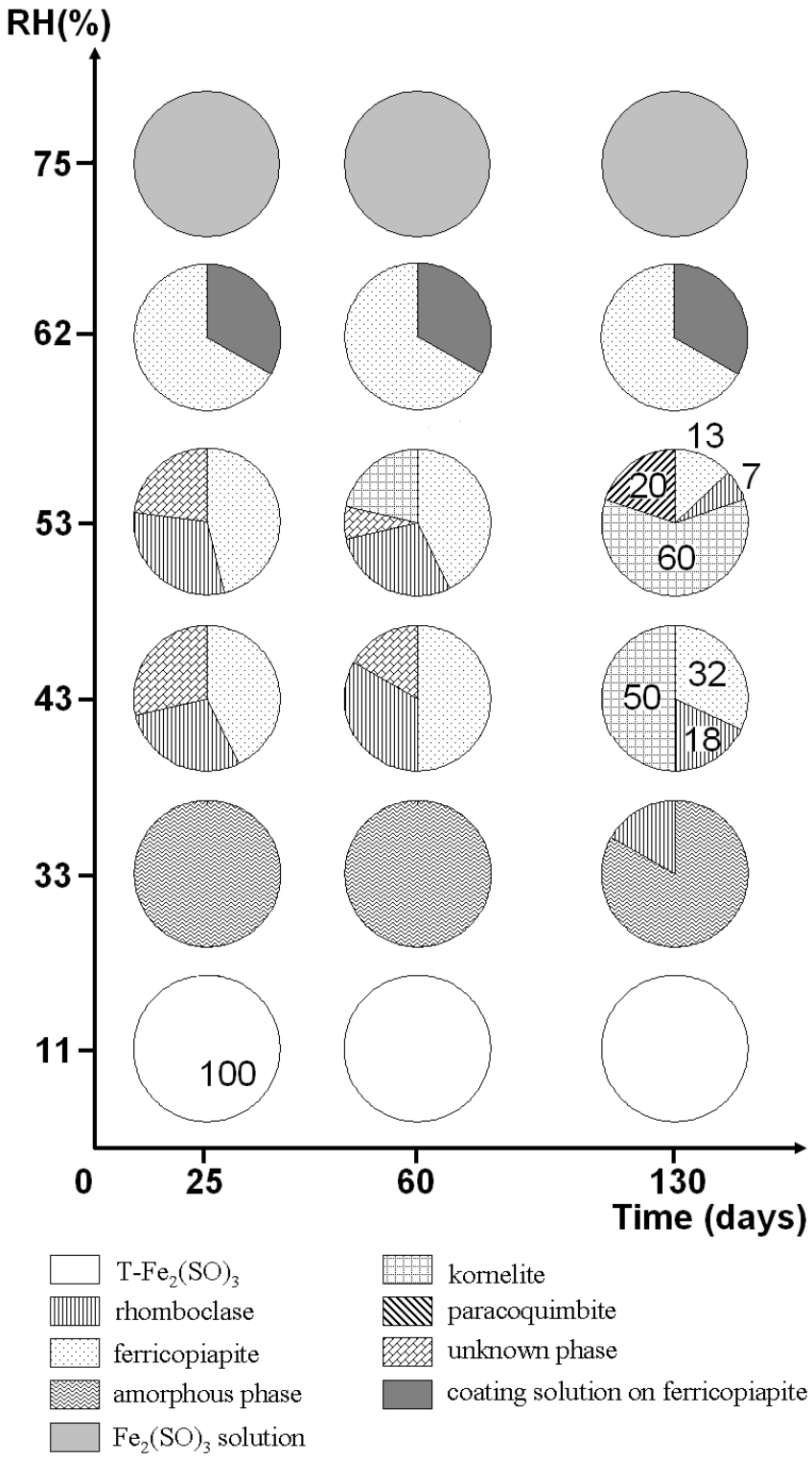

Figure 2.7. Phase evolution map of T-$Fe_2(SO_4)_3$ at different RH levels. Figures in the pie chart indicate the proportions of the phases present in weight percentages. These values are not given for amorphous, liquid or unknown phases, or the crystalline phases that coexist with them.

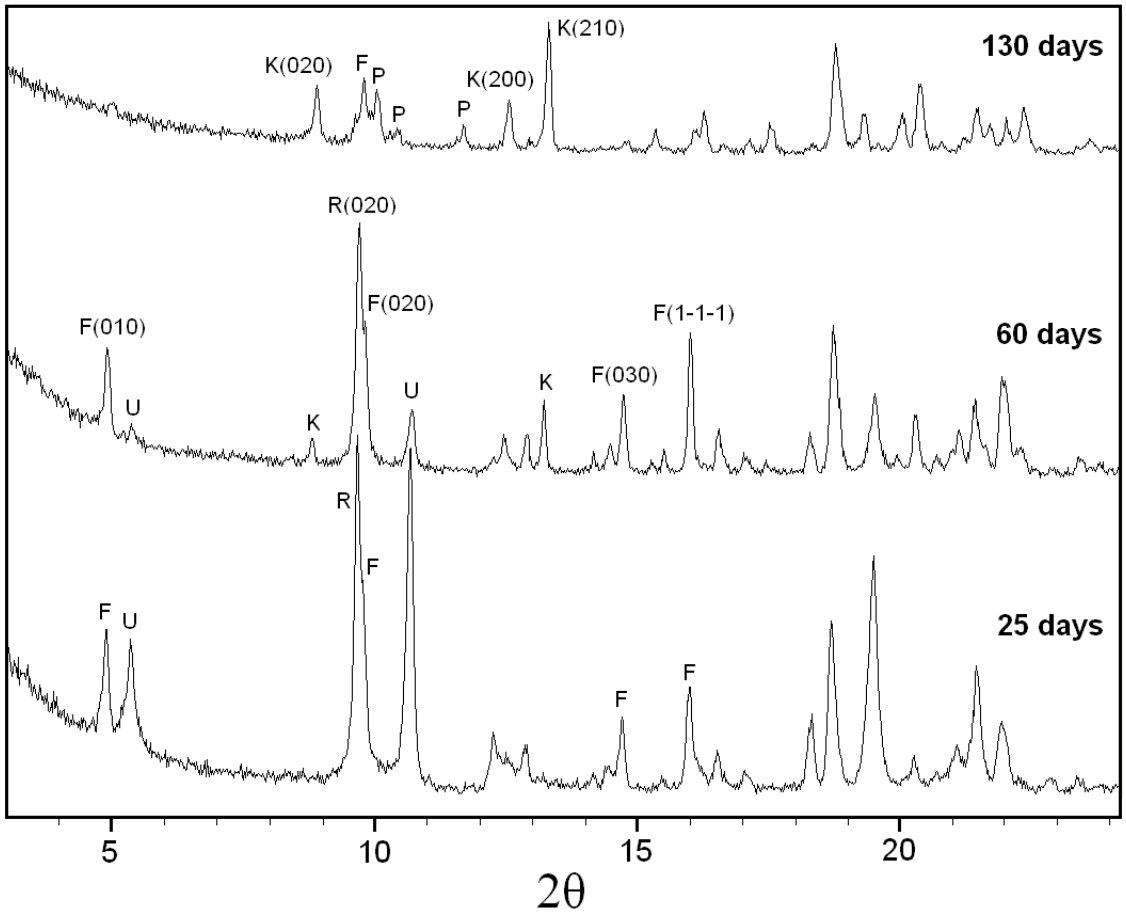

Figure 2.8. XRD data showing the hydration process of T-$Fe_2(SO_4)_3$ at 53% RH. **F**: Ferricopiapite; **R**: Rhomboclase; **K**: Kornelite; **P**: Paracoquimbite; **U**: Unknown phase.

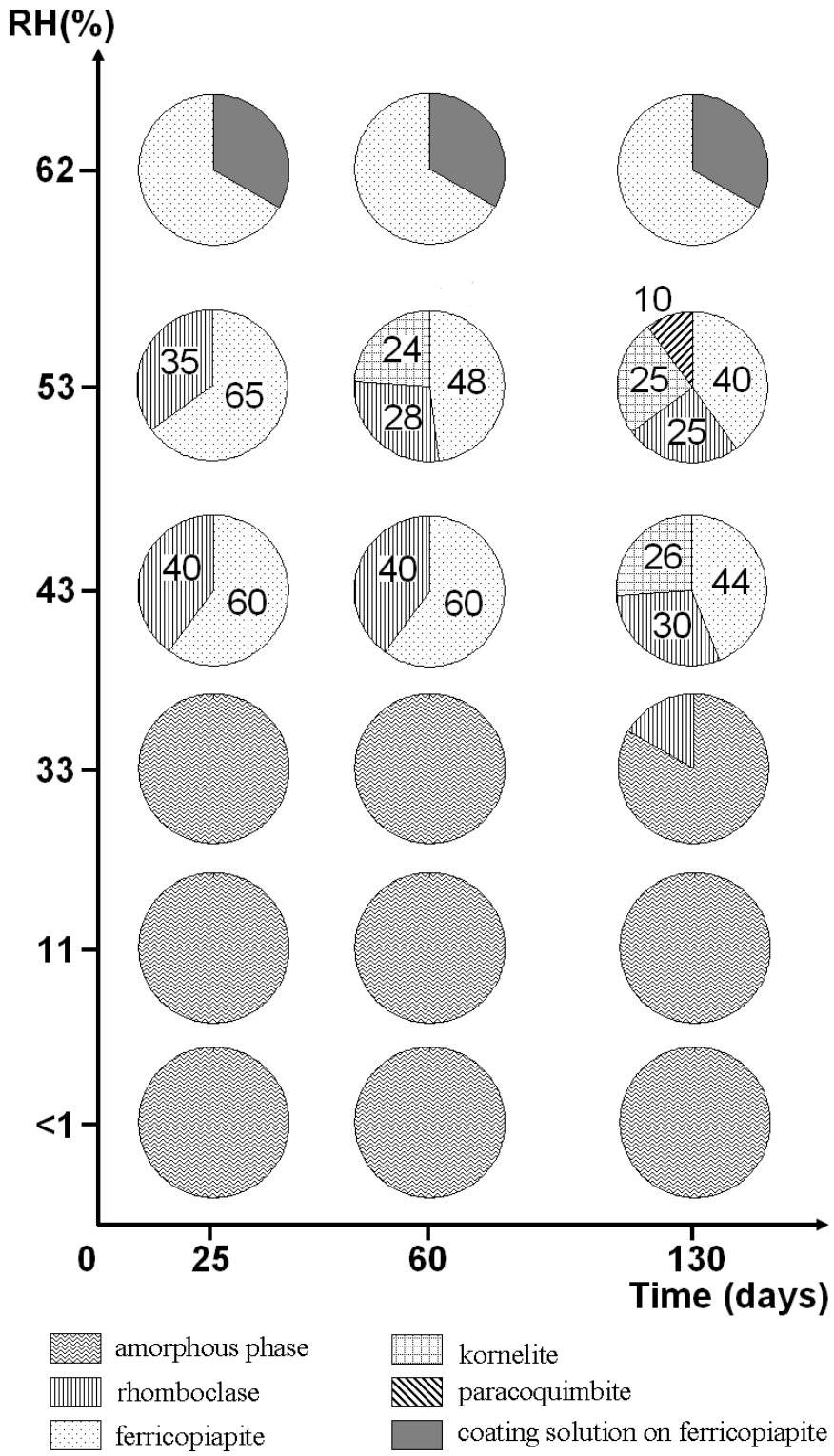

Figure 2.9. Phase evolution of concentrated ferric sulfate solution at different RH levels over time. Figures in the pie chart indicate the proportions of the phase in weight percentages. These values are not given for amorphous or liquid phases, or the crystalline phases that coexist with them.

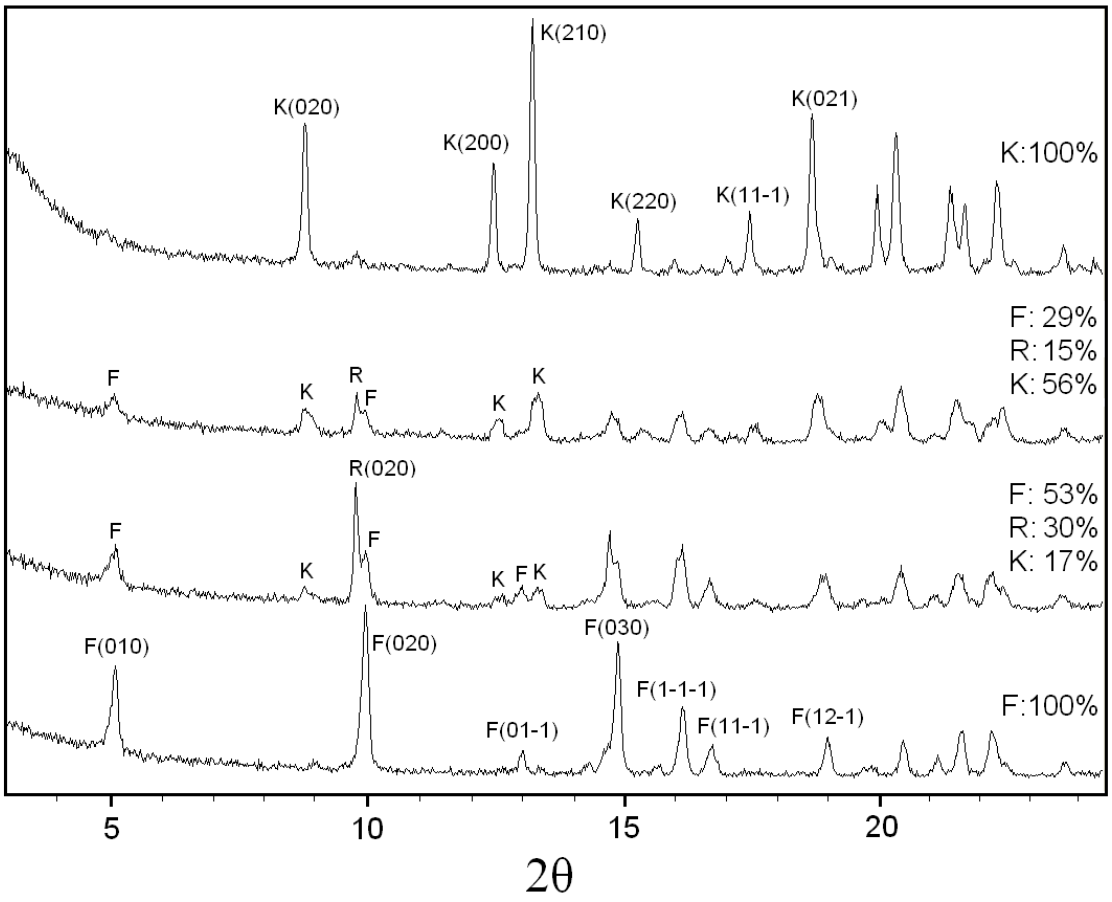

Figure 2.10. *In situ* XRD data showing the dehydration of the sample from 62% RH bottle at 53% RH. Four lines indicate 0, 12, 36 and 60 hours stay at 53% RH from bottom to top. Percentages are the weight proportions of each phase estimated from Rietveld refinement. **F**: Ferricopiapite; **R**: Rhomboclase; **K**: Kornelite. It can be seen that rhomboclase crystallized at the beginning, but converted to kornelite after 60 hours.

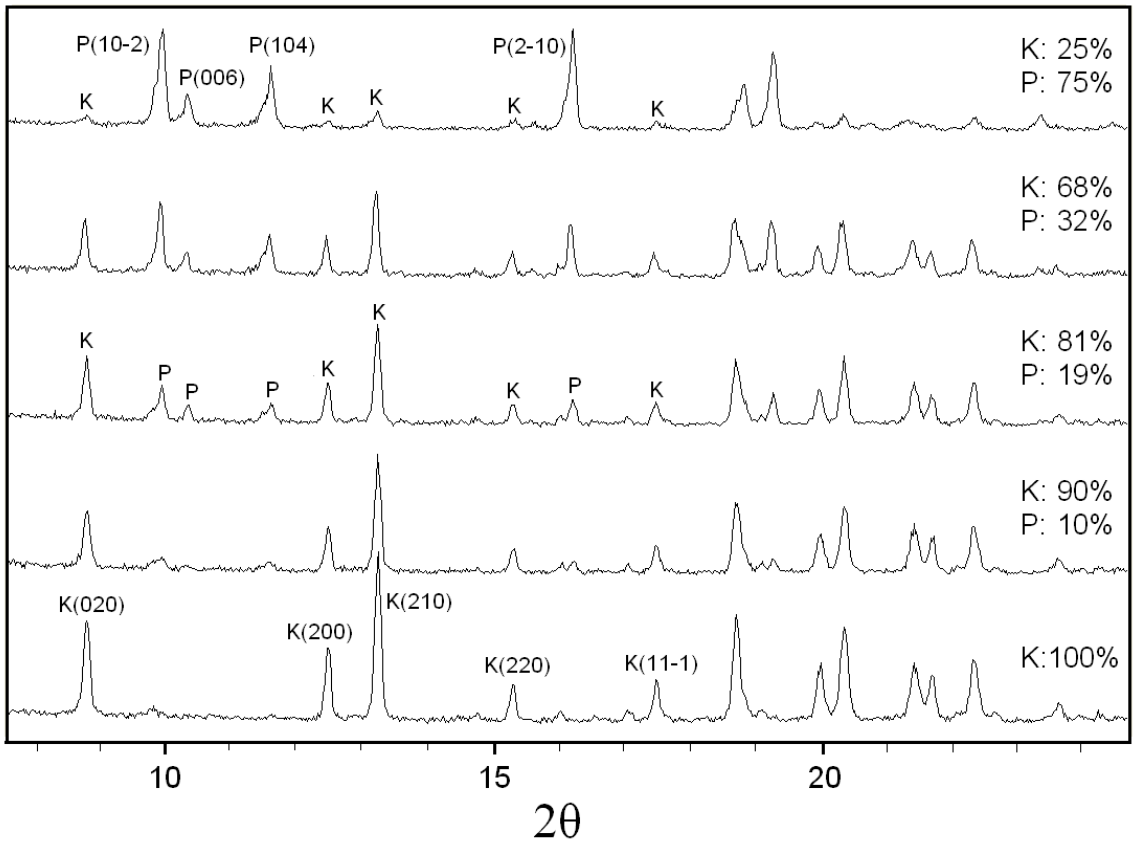

Figure 2.11. XRD data showing kornelite transforming to paracoquimbite at 62% RH. Five lines indicate 0, 7, 23, 43 and 79 days preservation of kornelite powders at 62% RH from bottom to top. Percentages are the weight proportions of each phase estimated from Rietveld refinement. **K**: Kornelite; **P**: Paracoquimbite.

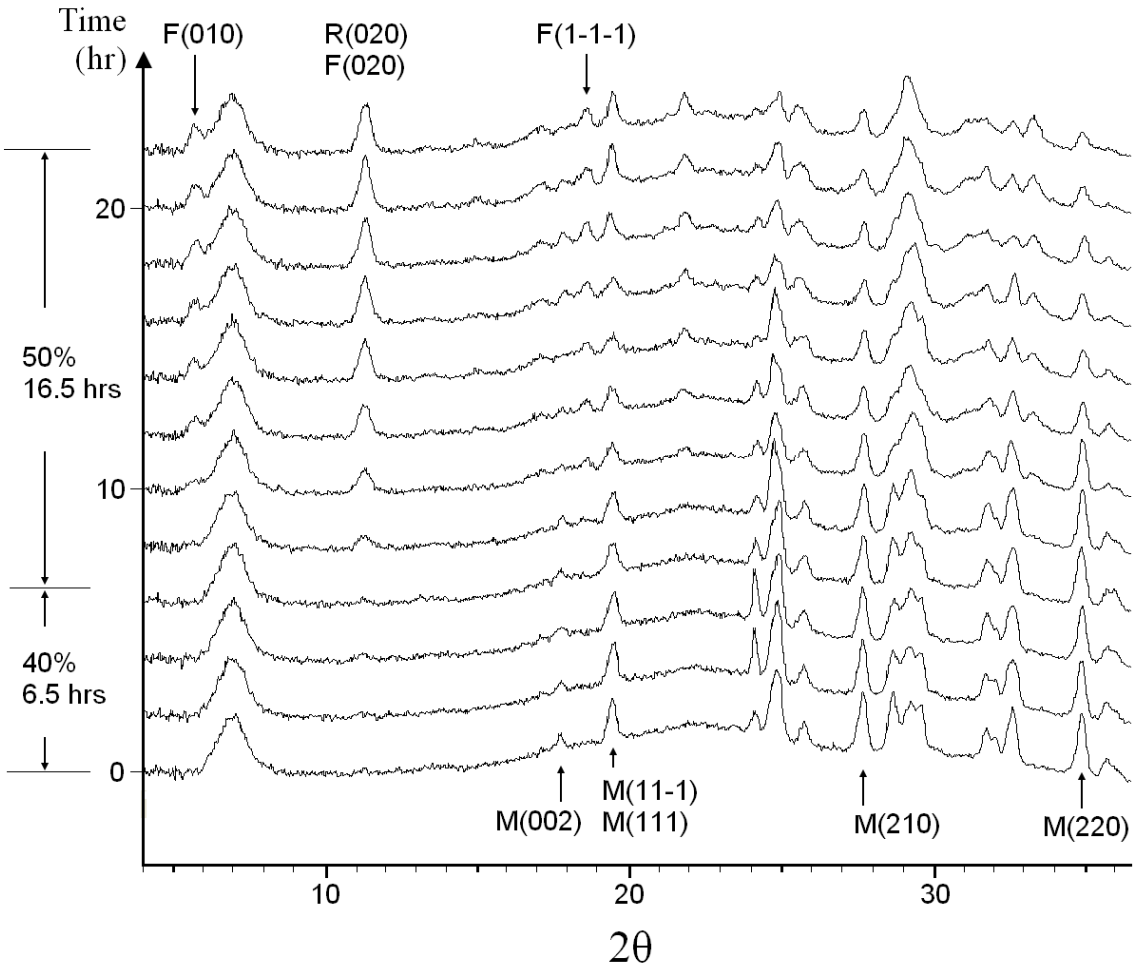

Figure 2.12. The hydration process of M-$Fe_2(SO_4)_3$ as recorded by time-resolved XRD data from the GADDS diffractometer. 2θ range from 4° to 36.5° is plotted on the horizontal axis. The vertical time axis is marked with the RH steps and their duration. Some peaks are marked with the initials of corresponding mineral names and diffraction index, **F**: Ferricopiapite; **R**: Rhomboclase; **K**: Kornelite, **P**: Paracoquimbite. Note that the broad peak at 7° is produced by the scattering from Kapton® capillary and the chamber wall. (a). M-$Fe_2(SO_4)_3$ transformed to ferricopiapite and rhomboclase at 50% RH.

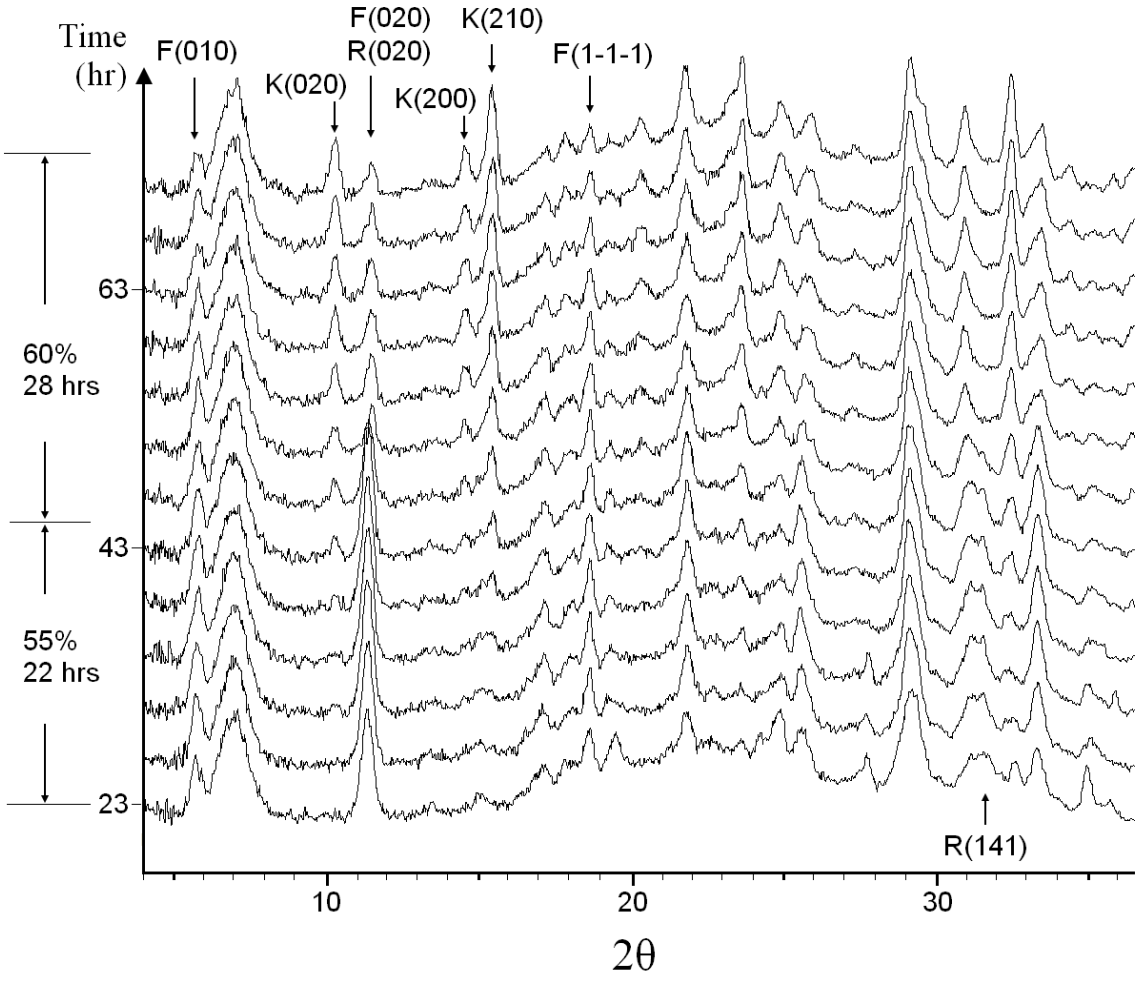

Figure 2.12(b). Kornelite crystallized at 55% RH. Rhomboclase quickly disappeared when RH was raised to 60%, indicated by a sudden drop of the peak intensity at 11.3° along with an apparent shift to higher 2θ, caused by the loss of R(020) contribution. Ferricopiapite diffraction peaks also decreased slowly in intensity at 60% RH as kornelite peaks intensified.

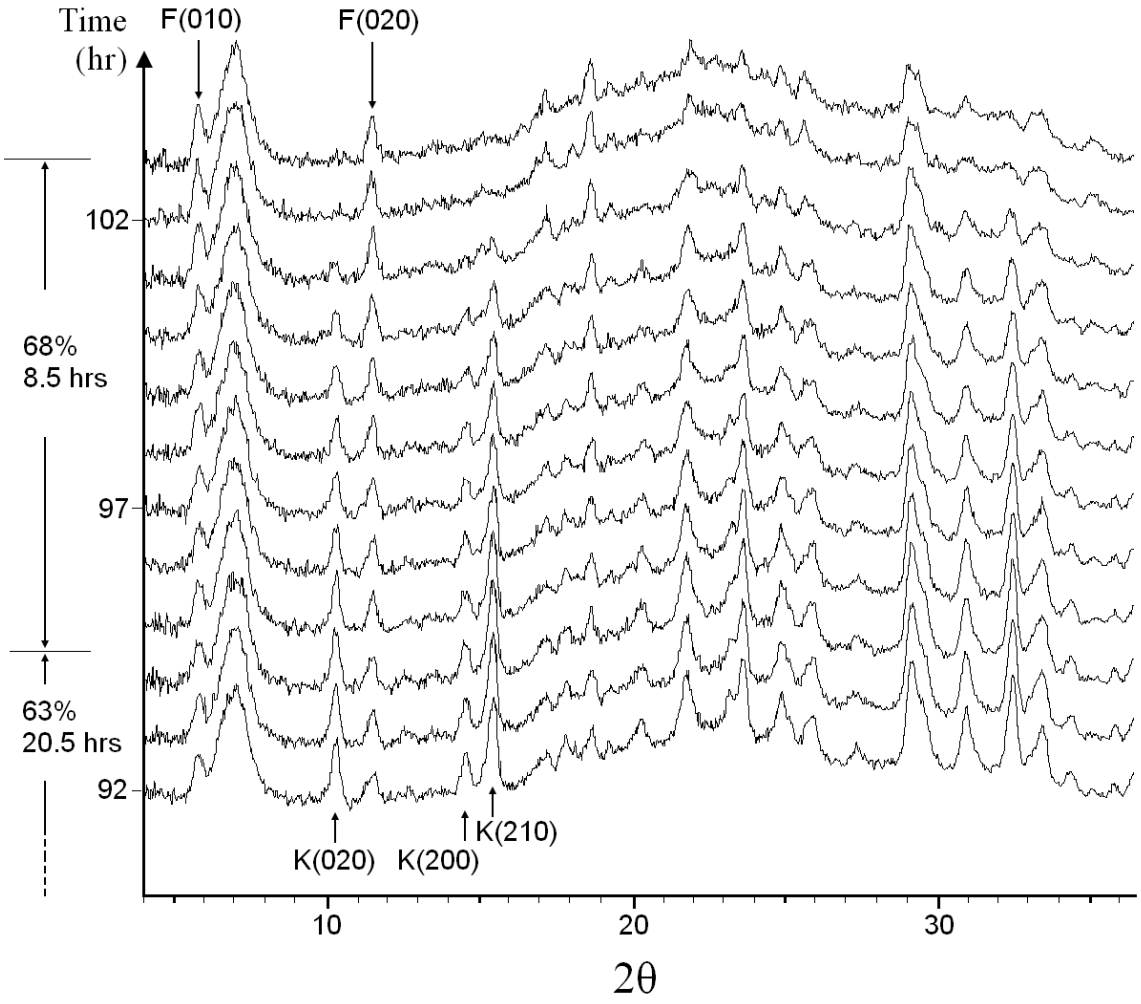

Figure 2.12(c). Kornelite dissolution and ferricopiapite crystallization with a residual solvent phase as RH increased to 68%.

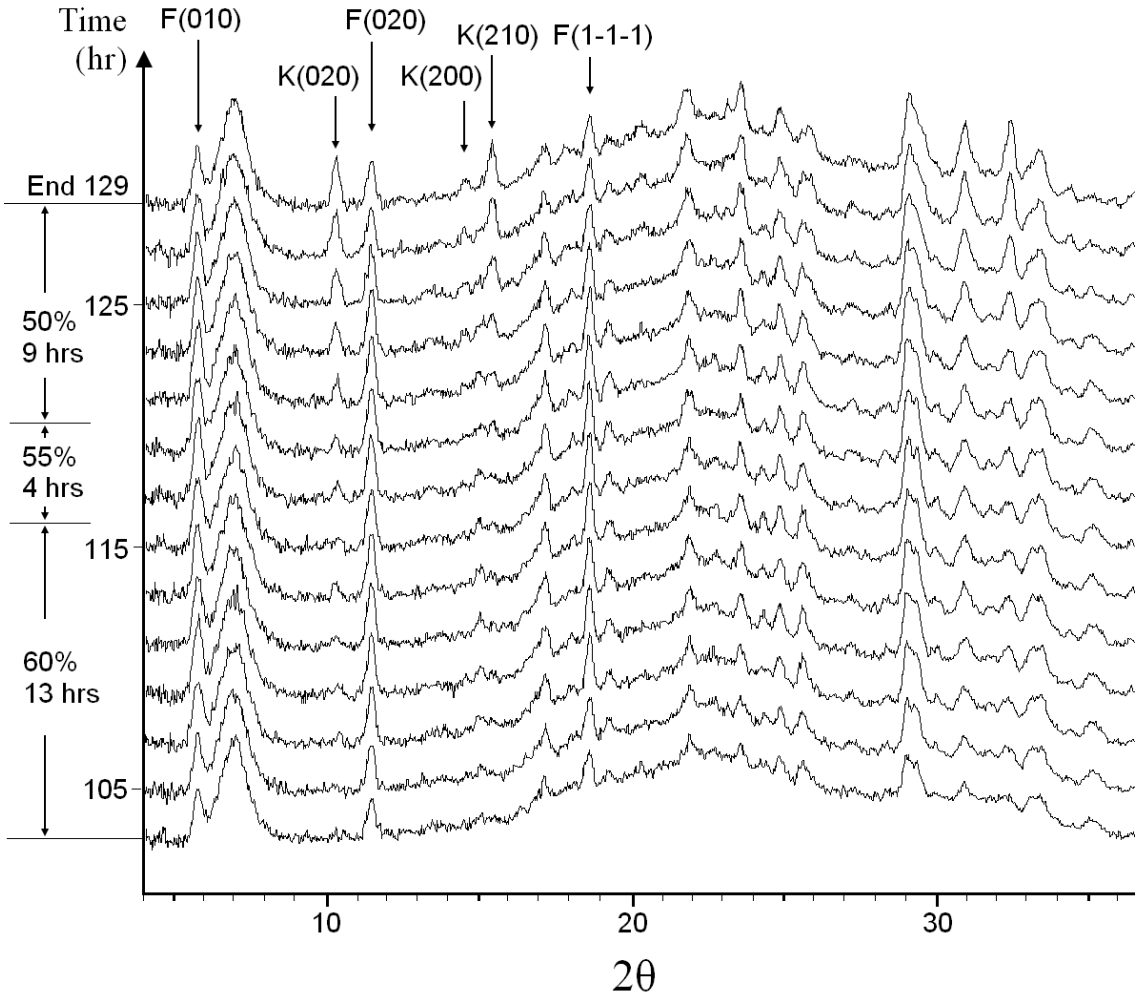

Figure 2.12(d). The subsequent dehydration process reversed the transition in (c) as ferricopiapite transformed to kornelite.

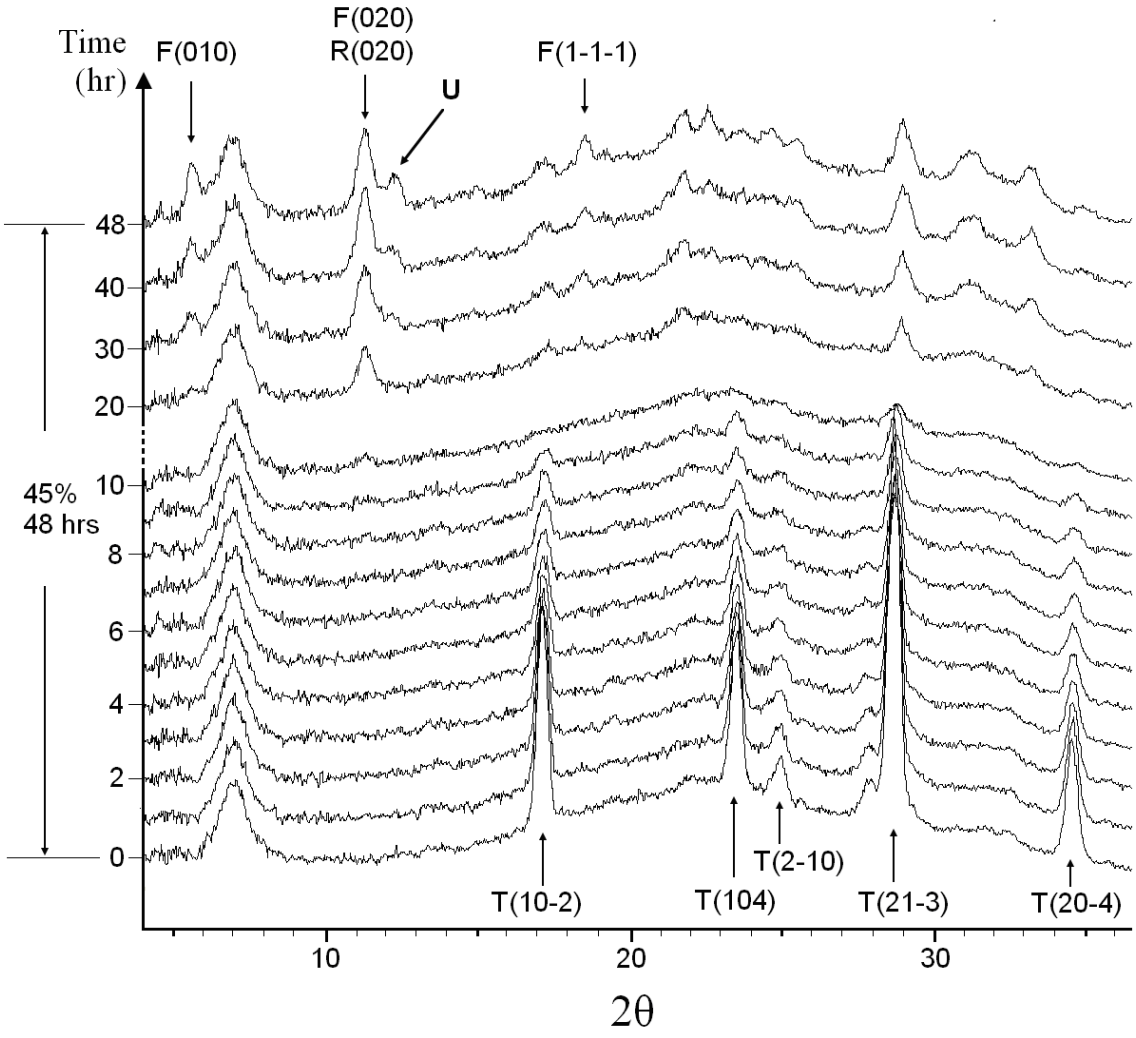

Figure 2.13. Time-resolved XRD data depicting the hydration of T-$Fe_2(SO_4)_3$ at 45% RH at room T. The starting T-$Fe_2(SO_4)_3$ dissolved quickly at 45% RH (lower patterns). At 10 hours, the XRD pattern has few diffraction peaks, indicating a lack of long-range order in the sample, which corresponds to the intermediate suspension phase. After 10 hours, Rhomboclase, ferricopiapite and a small amount of the unidentified phase(s) crystallized out (peak marked with U).

Chapter 3

Phase Transitions of Ferric Sulfates at non-Room Temperature and the RH – T phase diagram and phase evolution maps

Abstract

Evolution of concentrated $Fe_2(SO_4)_3$ solution, a process including both the evaporation of the solution and the post-evaporation aging of the precipitates, was studied at 2 °C and 50 °C under controlled relative humidity (RH). At 50 °C and RH from 42% to 47%, the starting solution underwent the following phase evolution sequence: $Fe_2(SO_4)_3$ solution → (ferricopiapite, rhomboclase) → kornelite at 42% RH, or paracoquimbite at 46 – 47% RH. At 2 °C and RH from 34% to 43%, the first step of the above sequence, the precipitation of ferricopiapite and rhomboclase was observed, but the subsequent combination, to form a single ferric sulfate hydrate phase, did not occur over 385 days. At both temperatures and RH ≤ 31%, amorphous ferric sulfate formed. The amorphous ferric sulfate was more stabilized at low RH conditions, e.g. RH ≤ 11%, than higher RH, at which it would transform to crystalline phases of rhomboclase and ferricopiapite, as observed at 31% RH and 50 °C. Combining these results with our previous study at room temperature (RT), the ferric sulfate phase evolution at 2 °C, 25 °C and 50 °C were mapped and compared. Temperature (T) strongly affects the ferric sulfate evolution kinetics, and low T may delay the evolution from reaching an

equilibrium state. Also, an RH and T-controlled *in situ* X-ray diffraction (RH-T-XRD) method was used to study phase transitions of ferric sulfate hydrates at 25 – 80 °C. A dehydration of paracoquimbite ($Fe_2(SO_4)_3 \cdot 9H_2O$) to form ferric sulfate pentahydrate ($Fe_2(SO_4)_3 \cdot 5H_2O$) was identified at 80 °C. These results are discussed with a previously constructed ferric sulfate RH – T phase diagram by Ackermann et al. (2009).

3.1. Introduction

Ferric sulfate minerals have been found at several localities on the surface of Mars, including Meridiani planum (Farrand et al., 2007; Klingelhofer et al., 2004; Poulet et al., 2008) and Gusev crater (Johnson et al., 2007; Lane et al., 2008; Yen et al., 2008) where *in situ* measurements were performed by rovers, and also locations such as Juventae Chasma (Bishop et al., 2009; Milliken et al., 2008) which were spectroscopically scanned by orbiters. Ferric sulfates may be more widely distributed within or near Valles Marineris (Milliken et al., 2008). On Earth, ferric sulfates are mostly found at acid mine drainage (AMD) regions as secondary minerals deposited from acidic sulfate waters formed by the oxidation or sulfide minerals (Hammarstrom et al., 2005; Jambor et al., 2000; Nordstrom and Alpers, 1999). As shown in Chapter 2, ferric sulfates are very hygroscopic and display complex phase transitions with change of humidity (Xu et al., 2009). These minerals exhibit the potential to be used to extract detailed information on depositional and post-depositional environments; this utility requires a comprehensive knowledge of the mineral stability and transitions as a function of environmental variables including temperature (T), relative humidity (RH), pressure

(P), atmospheric composition, etc. To date, most of the relevant phase relations are still to be established. Majzlan and colleagues recently reported thermodynamic data for a series of ferric sulfate minerals (Ackermann et al., 2009; Majzlan et al., 2006; Majzlan et al., 2005) and constructed an RH–T phase diagram (Ackermann et al., 2009; Majzlan et al., 2006; Majzlan et al., 2005). In Chapter 2, we reported the ferric sulfate phase transitions at room temperature (RT) under different RH conditions studied by *ex situ* and *in situ* X-ray diffraction (XRD) methods. Here, we explore the evaporation of ferric sulfate solutions and the subsequent phase changes at 2 °C and 50 °C using the same method, and built the phase evolution map for ferric sulfate at the three different temperatures as a function of time and RH.

3.2. Experimental Methods

3.2.1. Sample preparation and the *ex situ* method

Concentrated ferric sulfate solution was prepared by deliquescing anhydrous ferric sulfate at 84% RH and 25 °C in a potassium chloride humidity buffer cell. Humidity buffers are saturated solutions of a salt, e.g. KCl, which produces a constant RH in a closed space at equilibrium. The equilibrium RH is specific to the salt, and varies with temperature. The setup of the humidity cell used in this study was depicted in Figure 2.3. The anhydrous ferric sulfate, prepared using the method described in Chapter 2, quickly hydrated to become a slurry after a few hours at 84% RH, and finally turned to a clear brown solution with a constant weight after 7 days. The concentration of the solution was calculated to be 40 wt. % $Fe_2(SO_4)_3$. The solution was then stored in a

series of humidity buffer cells in a laboratory refrigerator and in an iso-temperature oven set to 50 °C. The amount of the solution in each humidity buffer cell was about 1.5 – 2.0 g. The temperature fluctuation in the refrigerator was measured as 0.5 to 2.5 °C, and that in the oven was measured as 51 to 52 °C. All humidity buffers used in this study are listed in table 3.1 with the reported and measured RH for each humidity buffer.

XRD patterns of the precipitates were collected on a Rigaku Ultima-IV diffractometer that operates in Bragg-Brentano geometry and uses Cu*K*α radiation (λ = 1.54178 Å). The diffractometer has a high-speed semiconductor element one-dimensional X-ray detector capable of energy discrimination to eliminate the effect of Fe fluorescence (Szczygiel et al., 2009). Due to its relatively short harvest time of a diffraction pattern, usually less than 10 minutes, no control of sample environment was used for general sample identity check. A second XRD pattern was collected immediately after the first pattern for the same sample to ensure the sample was not degrading or transforming to other phases during data collection. Phase quantifications were done with Rietveld refinement (Rietveld, 1969) using the programs GSAS (Larson and Von Dreele, 2000) and it is graphic interface EXPGUI (Toby, 2001). In these calculations scale factors, cell parameters, specimen shift and peak profile parameters for each crystalline phase were refined. Since determination of the phase fraction was the major objective, the atomic parameters for each phase were fixed at published values. References for published ferric sulfate structures are listed in Table 1.1 in Chapter 1.

3.2.2. *In situ* RH-T-XRD method

In situ RH-T-XRD experiments were performed on the Rigaku Ultima IV with a commercial environmental chamber and humidity control system installed (Kishi and Toraya, 2004). Target RH was achieved by mixing dry and water-saturated nitrogen gas of different proportions, and was under dynamic computer control. Target T was achieved by five cartridge heaters placed in the wall of the environmental chamber to maintain a homogeneous thermal field inside, when a temperature other than room T was needed. An RH probe was placed ~2 cm above the sample stage to measure the RH and T in the chamber. The sample stage was also a differential scanning calorimetry (DSC) device. In preparation of a specimen, sample powder was spread onto a 7×7×0.25 mm aluminum pan. Because ferric sulfate solution was found to oxidize aluminum at T > 70 °C, a kapton polyimide film was attached onto the aluminum pan to avoid direct contact of the sample powder with the pan. For experiments performed at high T, the gas T measured by the RH probe had to be maintained as close to the sample T measured by the DSC thermocouple as possible to avoid thermal gradients; RH is strongly dependent on T and the differential T was kept no larger than 1 °C throughout the experimental run. XRD data were continually collected during experiment with the 2-θ scanning range selected according to positions of the characteristic peaks of the phases of interest. The scanning speed was optimized depending on the trade-off between the signal to noise ratio in each scan and the time resolution needed to reveal the transition process.

3.3. Results

3.3.1. Dehydration of $Fe_2(SO_4)_3$ solution at 2 °C

Table 3.2 lists the phases evolved from the $Fe_2(SO_4)_3$ solution at 2 °C and different RH. The XRD patterns are shown in Figure 3.1. Yellow flower-like aggregates resembling the "ferricopiapite + rhomboclase" assemblage formed at 34% RH and 43% RH after a storage time of 40 days at 2 °C. Little change of the color or morphology of the yellow aggregates was observed thereafter. XRD taken on day 385 confirmed that the products were still ferricopiapite and rhomboclase with no other phases present. The small variation of peak intensities between the XRD patterns collected on day 265 and day 385, such as pattern **d** and pattern **e** in Figure 3.1, may be due to sample preparation, and not related to any real change of the amount of ferricopiapite and rhomboclase. Estimated weight proportions based on the Rietveld fitting of each pattern were given in table 3.2. At 57 % RH, a yellow ferricopiapite paste formed after 50 days, and did not evolve further in the remaining experiment time. The formation of ferricopiapite paste was also observed at 62% RH and RT (Fig. 2.9 in Chapter 2). The solutions stored at 73% and 75% RH remained liquid. The solutions stored at 0% and 11% RH transformed within 10 days to an amorphous solid retaining the morphology of the starting liquid drops, and stayed in the amorphous state without a trend of transforming to crystalline phases over 385 days (Fig. 3.1).

3.3.2. Dehydration of $Fe_2(SO_4)_3$ solution at 50 °C

Results of the dehydration of this solution are summarized in Table 3.3 and the XRD data are plotted in Figure 3.2. Similar to the experiments at RT and 2 °C, initial evaporation products from the $Fe_2(SO_4)_3$ solution were either ferricopiapite and rhomboclase or amorphous ferric sulfate, depending on the RH level. The amorphous

ferric sulfate formed at 0%, 11% and 31% RH, above which rhomboclase and ferricopiapite precipitated. At 31% RH, a clear amber-like solid first formed within 2 days, and then turned dark and less uniform in color and transparency. XRD data taken after 20 days indicated the growth of rhomboclase from the amorphous solid. After 40 days, ferricopiapite along with rhomboclase were observed in the sample. The crystallization of the amorphous ferric sulfate to rhomboclase was also found in a similar aging experiment at RT and 33% RH after 50 days (Fig. 2.9 in Chapter 2), where ferricopiapite was not found to have formed. Clearly, high temperature accelerated the crystallization of the amorphous ferric sulfate at 30% RH. The amorphous sulfate remained amorphous at 0% and 11% RH. At higher humidity, the initially precipitated rhomboclase and ferricopiapite combined to form kornelite at 42% RH or paracoquimbite at 46% and 47% RH. These transformations were also observed in studies at RT and similar RH levels (Fig. 2.5, 2.7 and 2.9 in Chapter 2).

3.3.3. *In situ* RH-T-XRD results

We attempted to reproduce transformations observed in *ex situ* studies in *in situ* experiments. RH and T can be adjusted continuously rather being restricted to the few RH levels set by humidity buffers. After phase evolution mapping by *ex situ* studies, *in situ* studies allow the transition boundaries to be studied in more detail. Paracoquimbite, kornelite, ferricopiapite and rhomboclase were studied. These samples were obtained from the products of previous *ex situ* humidity cell experiments. A total of six experiments were performed. RH-T steps in each experiment are listed in Table 3.4 to 3.9 along with the corresponding phase transitions. The selections of T, RH and duration

at each step were aimed at giving a representative coverage of the T-RH domain: T from 50 °C to 80 °C, RH from 0% to 90%.

3.3.3.1. Paracoquimbite

The paracoquimbite is stable at 40 °C and 60 °C over a total of 29 hours with RH ranging from 50% down to 4% (Table 3.4). At 80 °C, the transformation from paracoquimbite to crystalline $Fe_2(SO_4)_3 \cdot 5H_2O$ was observed. The structure of $Fe_2(SO_4)_3 \cdot 5H_2O$ was recently characterized and suspected to be same as a previously reported mineral, lausenite (Majzlan et al., 2005). To avoid any confusion, the crystalline $Fe_2(SO_4)_3 \cdot 5H_2O$ is named as pentahydrate in this study. The initial detection of pentahydrate formation was at 30% RH in the RH downslope from 50% to 3% at 80 °C, by the barely observable occurrence of the (021) reflection (Fig. 3.3). As RH continued down to 3%, the growth of pentahydrate apparently halted as the (021) reflection ceased to increase in intensity. Meanwhile, the paracoquimbite peaks continued to decrease, indicating the instability of paracoquimbite under this low RH condition. In the following increase in RH, the growth of pentahydrate resumed at 20% RH. The transformation was more rapid at medium RH (40 – 60%) and slowed down at higher RH (70 – 80%). The amount of paracoquimbite diminished after 18 hours exposure to air humidity above or equal to 70% RH (Fig. 3.4). The temperature was then decreased to 60 °C and RH was varied from 80% to 4%. No change in the pentahydrate formed under these conditions was found over 37 hours.

The paracoquimbite to pentahydrate transformation was repeated using a different RH-T route (Table 3.5, Fig. 3.5). The result is consistent with the first run. At 80 °C and

3% RH, the paracoquimbite peak intensity decreased with no pentahydrate or other crystalline phases forming, indicative of an amorphization process at this condition. The amorphization of paracoquimbite at the same RH and T condition was also observed in the first run (Table 3.4, Fig. 3.3), though the decrease of paracoquimbite peak intensity in Figure 3.3 was not as prominent as in Figure 3.5.

3.3.3.2. Paracoquimbite and rhomboclase

A sample consisting of a mixture of paracoquimbite and rhomboclase (Table 3.6) showed no change from 1% to 50% RH at 50 °C. The rhomboclase started dissolving at 60% RH, and the paracoquimbite remained and was not affected by the dissolution of rhomboclase.

3.3.3.3. Paracoquimbite and kornelite

A mixture of paracoquimbite and kornelite (Table 3.7) showed both phases remained at 30 °C from 10 to 68% RH. The kornelite gradually dissolved at 70% RH, while the paracoquimbite remained.

3.3.3.4. Ferricopiapite and rhomboclase

A mixture of ferricopiapite and rhomboclase crystallized from the $Fe_2(SO_4)_3$ solution showed that upon increasing RH at 26 °C, the rhomboclase dissolved at 65% RH and the ferricopiapite remained as a crystalline solid (Table 3.8; Fig. 3.6). Upon decreasing RH from 65% RH, paracoquimbite occurred at 55% RH along with the disappearance of the ferricopiapite (Fig. 3.7). The instability of wet ferricopiapite paste

at dehydration was also observed in the previous study at RT, where the ferricopiapite paste transformed to kornelite upon dehydration at 53% RH, as reported in section 2.3.1.4. Different from that study, the transition product here is paracoquimbite rather than kornelite. Direct transition from ferricopiapite and rhomboclase to paracoquimbite was also found in the *ex situ* experiment at 50 °C in this study. The formed paracoquimbite began dissolving at 80% RH. Before it was fully dissolved, RH was lowered. Below 65% RH, the paracoquimbite XRD peaks intensified, indicating a re-crystallization of paracoquimbite as a result of evaporation. After this step, T was raised to 50 °C. The paracoquimbite was deliquescent at 70 – 75% RH. The sample was then allowed to totally dissolve at 75% RH before RH was lowered down. Ferricopiapite and rhomboclase precipitated at 60% RH and 45% RH, respectively. This result is consistent with the observed phase evolution sequence in *ex situ* experiments, where ferricopiapite and rhomboclase were observed as the initial precipitates from $Fe_2(SO_4)_3$ solution.

The same starting sample, mixture of ferricopiapite and rhomboclase, was run under a different RH-T route. T was set to 50 °C throughout the experiment (Table 3.9). Paracoquimbite started to grow at 55% RH. At 60% RH, the amount of rhomboclase quickly diminished indicating deliquescence. The paracoquimbite growth continued while the amount of ferricopiapite decreased. At 70% RH, the paracoquimbite dissolved while the ferricopiapite remained. Upon decreasing RH, the amount of ferricopiapite increased slightly at 60% RH, and then decreased to zero at 50% and 40% RH. Paracoquimbite and rhomboclase appeared at 50% RH and 40% RH, respectively (Fig. 3.8). The extraordinarily strong intensity of the ferricopiapite (020) and (030) Bragg peaks and the weakness of the (01-1) and the (1-1-1) peaks at 60% RH were due to the

effects of preferred orientation (Fig. 3.8). Further, the difference in dehydrating the wet ferricopiapite in these two run is the formation of rhomboclase in the second run (Fig. 3.7 and 3.8). The mixture of rhomboclase and paracoquimbite was also observed in the *ex situ* experiment at 50 °C and 46% RH (Table 3.3). The presence of rhomboclase ($(H_5O_2^+)Fe(SO_4)_2 \cdot 2H_2O$) without ferricopiapite ($Fe_{4.67}(SO_4)_6(OH)_2 \cdot 20H_2O$) is difficult to understand, considering the starting $Fe_2(SO_4)_3$ solution has no net protons. This means if rhomboclase, which contains protons in its structure, crystallizes, an OH-bearing phase is supposed to form to keep the net protons in the system to be zero. One possible explanation is the presence of an OH-bearing amorphous phase in the mixture, which can not be easily verified by XRD.

3.4. Discussion

3.4.1. Phase evolution of $Fe_2(SO_4)_3$ solution

Figure 3.9 (a, b, c) illustrates the phase evolution of concentrated $Fe_2(SO_4)_3$ solution at 2 °C, 25 °C and 50 °C as a function of RH and time. At all three temperatures, depending on the RH, there are four initial states: (1) $Fe_2(SO_4)_3$ solution; (2) ferricopiapite + solution; (3) ferricopiapite + rhomboclase; (4) amorphous ferric sulfate. The first state, $Fe_2(SO_4)_3$ solution, is stable at RH > 70%. The second state, ferricopiapite + solution, forms at RH between about 60% and 70%, and could be stabilized if there were no further changes of RH. The remnant solution has to be acidic to balance the hydroxyl group in the ferricopiapite ($Fe_{4.67}(SO_4)_6(OH)_2 \cdot 20H_2O$) structure in order to maintain zero net hydroxyls in the system. The paucity of remnant solution

and its close adsorption on ferricopiapite prohibited an effective measurement of pH by a probe method. A pH test paper attached onto the wet ferricopiapite indicated a pH close to 1, higher than the predicted lower pH boundary for ferricopiapite formation at about 0 from previous modeling work (Marion et al., 2008; Tosca et al., 2007), which explains why the "ferricopiapite + solution" state could remain stable at this RH range. Note the "ferricopiapite + solution" state was not observed in the *ex situ* experiment at 50 °C, due to the limited RH levels set by available humidity buffers. But this state was observed in the *in situ* experiment (Table 3.7 and 3.8).

The third state, ferricopiapite + rhomboclase, formed at about 35% < RH < 55%, as an apparently homogeneous yellow aggregate. This state is not stable at the RH range it is formed, and will evolve to kornelite or paracoquimbite depending on the RH and T. The evolution kinetics is also affected by RH and T. At 25 °C and 50 °C, white tips were seen growing on the yellow aggregates after one to two months. These white minerals could be kornelite or paracoquimbite depending on the RH (Fig. 3.9). At 2 °C, the combination of ferricopiapite and rhomboclase could be preserved over a year without further transformation, indicating kinetic inhibition. The effect of RH on reaction kinetics is also remarkable. Within the RH range from 35% to 55%, higher RH always accelerates the reaction of ferricopiapite with rhomboclase. This reaction is probably a dissolution and recrystallization process in the microscopic scale, where locally dissolved rhomboclase releases strong acid that destabilized ferricopiapite. Higher RH increases the probability of local dissolution and thus facilitates the transformation to a more stable single hydrate phase like kornelite or paracoquimbite.

The fourth state, hydrated amorphous ferric sulfate, forms at RH <30%. An empirical formula of $Fe_2(SO_4)_3 \cdot 5.5\ H_2O$ is obtained by quantifying the water content with thermogravimetric analysis. This state was not observed to evolve to any crystalline phases at 11% RH or below, but at RH > 30%, rhomboclase and ferricopiapite form. This transformation proceeds more quickly at higher T.

3.4.2. RH-T phase diagram

Ackermann et al (2009) provided a RH-T phase diagram of $Fe_2(SO_4)_3$ based on thermodynamic measurements. Figure 3.10 is a reproduction of their diagram with the experimental data from this study overlain. Two rectangles at 80 °C mark the result of the *in situ* experiment on paracoquimbite. The one extending from 20% to 80% RH is the observed transition from paracoquimbite to pentahydrate. Another rectangle from 0 to 10% RH shows the amorphization of paracoquimbite. Also, the growth of pentahydrate was halted at this RH range. The squares at 50 °C mark the results of *ex situ* experiments. The open squares at 42% RH and 50 °C shows the evaporation of $Fe_2(SO_4)_3$ solution evolving to kornelite, consistent with the predicted kornelite stable field. The solid square marks the formation of paracoquimbite at 46% RH and 50 °C, which suggests paracoquimbite should be the stable phase at this condition. The phase boundary between the kornelite and paracoquimbite should go between the solid square and the open square. Two open triangles at 23 °C marks the formation of paracoquimbite observed in *ex situ* dehydration experiment at RT, and they are within the predicted paracoquimbite field. So our *ex situ* experiment results generally agree with the phase

diagram based on thermodynamic data, with the caveat that the kornelite-paracoquimbite phase boundary be moved to include the solid square in the paracoquimbite stable field.

The *in situ* experimental results at 80 °C, the transformation from paracoquimbite to pentahydrate from 20% to 80% RH, does not correlate well with the phase diagram by Ackermann et al. (2009), as the conditions transforming to pentahydrate apparently cross into the kornelite stability field (Fig. 3.10). It is possible that kornelite can not be formed through dehydrating paracoquimbite, which only produces pentahydrate. Therefore, these results do not reject the presence of a kornelite field at 80 °C. But the boundary between pentahydrate and kornelite certainly needs more characterization.

Also marked in Figure 3.10 are two solid triangles showing the deliquescence of paracoquimbite observed in *in situ* experiments. A deliquescence line should be placed around 70% to 80% RH to show the solid-liquid phase boundary.

3.4.3. Implication for ferric sulfates on Mars

The current Martian surface is exposed to temperature from -150 °C to 20 °C, ultraviolet radiation and relative humidity from 100% down to almost zero depending on latitude, season and time of day. The Martian atmosphere consists mostly of CO_2 and has an atmospheric pressure of 6 mbar with 50% variance. Of these environmental parameters, the CO_2 atmosphere is unlikely to affect the chemistry of the Fe(III) – SO_4 – H_2O system, since the concentrated $Fe_2(SO_4)_3$ solution is very acidic (pH ~ 1) and no carbonates can precipitate. The total atmospheric pressure should not be a direct factor affecting stability of hydrated minerals. Instead, the partial pressure of water vapor is likely to be the key factor. In our study, the water vapor pressure is parameterized as RH,

the vapor pressure divided by the saturated vapor pressure at a particular temperature. RH, which is also a better parameter to use than the absolute water vapor pressure because it represents water activity directly related to phase equilibrium. The ultraviolet radiation is not considered here, but has been investigated in a few studies showing no obvious effects on stabilities of hydrate minerals (Cloutis et al., 2008; Cloutis et al., 2007; Yen et al., 1999). Cloutis et al (2008) found ultraviolet light might enhance the dehydration of hexahydrite ($MgSO_4 \cdot 6H_2O$).

Temperature is surely an important factor to mineral stability and evolution. The current study only covers temperature above ice point, with some overlap with the highest temperatures found in Martian equatorial regions during summer noon time. Though not covering most of the temperature range present on Mars, the evaporation and phase transitions studied from 2 to 80 °C could be used to predict the behavior of ferric sulfates and the solution at lower T. An effect of low T is it dramatically slowed down or hindered the evaporation of $Fe_2(SO_4)_3$ solution and subsequent evolution to the final stable state, most probably paracoquimbite. As shown in the three evolution maps in Figure 3.9, the third initial evolution state, the mixture of ferricopiapite and rhomboclase, sustained for at least a year without further transitions at 2 °C. Even longer preservation of this initial state can be expected at lower T. The same effect was also observed for the transition from the amorphous ferric sulfate to crystalline phases. Hence these initial evolution phases, ferricopiapite, rhomboclase and amorphous ferric sulfate are very likely to be identified on Mars, though they do not appear in the phase diagram.

References:

Ackermann, S., Lazic, B., Armbruster, T., Doyle, S., Grevel, K.D., and Majzlan, J. (2009) Thermodynamic and crystallographic properties of kornelite [$Fe_2(SO_4)_3 \cdot 7.75H_2O$] and paracoquimbite [$Fe_2(SO_4)_3 \cdot 9H_2O$]. American Mineralogist, 94(11-12), 1620-1628.

Adams, J.R., and Merz, A.R. (1929) Hygroscopicity of fertilizer materials and mixtures. Industrial and Engineering Chemistry, 21, 305-307.

Bishop, J.L., Parente, M., Weitz, C.M., Dobrea, E.Z.N., Roach, L.H., Murchie, S.L., McGuire, P.C., McKeown, N.K., Rossi, C.M., Brown, A.J., Calvin, W.M., Milliken, R., and Mustard, J.F. (2009) Mineralogy of Juventae Chasma: Sulfates in the light-toned mounds, mafic minerals in the bedrock, and hydrated silica and hydroxylated ferric sulfate on the plateau. Journal of Geophysical Research-Planets, 114, E00D09, DOI: 10.1029/2009JE003352.

Cloutis, E.A., Craig, M.A., Kruzelecky, R.V., Jamroz, W.R., Scott, A., Hawthorne, F.C., and Mertzman, S.A. (2008) Spectral reflectance properties of minerals exposed to simulated Mars surface conditions. Icarus, 195(1), 140-168.

Cloutis, E.A., Craig, M.A., Mustard, J.F., Kruzelecky, R.V., Jamroz, W.R., Scott, A., Bish, D.L., Poulet, F., Bibring, J.P., and King, P.L. (2007) Stability of hydrated minerals on Mars. Geophysical Research Letters, 34, L20202, DOI: 10.1029/2007GL031267.

Farrand, W.H., Bell, J.F., Johnson, J.R., Jolliff, B.L., Knoll, A.H., McLennan, S.M., Squyres, S.W., Calvin, W.M., Grotzinger, J.P., Morris, R.V., Soderblom, J., Thompson, S.D., Watters, W.A., and Yen, A.S. (2007) Visible and near-infrared multispectral analysis of rocks at Meridiani Planum, Mars, by the Mars Exploration Rover Opportunity. Journal of Geophysical Research-Planets, 112, E05S02, DOI: 10.1029/2006JE002773.

Greenspan, L. (1977) Humidity Fixed-Points of Binary Saturated Aqueous-Solutions. Journal of Research of the National Bureau of Standards Section a-Physics and Chemistry, 81(1), 89-96.

Hammarstrom, J.M., Seal, R.R., Meier, A.L., and Kornfeld, J.M. (2005) Secondary sulfate minerals associated with acid drainage in the eastern US: recycling of metals and acidity in surficial environments. Chemical Geology, 215(1-4), 407-431.

Jambor, J.I., Nordstrom, D.K., and Alpers, C.N. (2000) Metal-sulfate salts from sulfide mineral oxidation. Sulfate Minerals - Crystallography, Geochemistry and Environmental Significance, 40, 303-350.

Johnson, J.R., Bell, J.F., Cloutis, E., Staid, M., Farrand, W.H., Mccoy, T., Rice, M., Wang, A., and Yen, A. (2007) Mineralogic constraints on sulfur-rich soils from Pancam spectra at Gusev crater, Mars. Geophysical Research Letters, 34, L13202, DOI: 10.1029/2007GL029894.

Kishi, A., and Toraya, H. (2004) Simultaneous measurements of X-ray diffraction (XRD) and differential scanning calorimetry (DSC) data under controlled humidity condition: Instrumentation and application to studies on hydration, dehydration, and rehydration processes of pharmaceutical compounds. Powder Diffraction, 19(1), 31-35.

Klingelhofer, G., Morris, R.V., Bernhardt, B., Schroder, C., Rodionov, D.S., de Souza, P.A., Yen, A., Gellert, R., Evlanov, E.N., Zubkov, B., Foh, J., Bonnes, U., Kankeleit, E., Gutlich, P., Ming, D.W., Renz, F., Wdowiak, T., Squyres, S.W., and Arvidson, R.E. (2004) Jarosite and hematite at Meridiani Planum from Opportunity's Mossbauer spectrometer. Science, 306(5702), 1740-1745.

Lane, M.D., Bishop, J.L., Dyar, M.D., King, P.L., Parente, M., and Hyde, B.C. (2008) Mineralogy of the Paso Robles soils on Mars. American Mineralogist, 93(5-6), 728-739.

Larson, A.C., and Von Dreele, R.B. (2000) "General Structure Analysis System (GSAS)". Los Alamos National Laboratory Report LAUR 86-748.

Majzlan, J., Navrotsky, A., McCleskey, R.B., and Alpers, C.N. (2006) Thermodynamic properties and crystal structure refinement of ferricopiapite, coquimbite, rhomboclase, and $Fe_2(SO_4)_3(H_2O)_5$. European Journal of Mineralogy, 18(2), 175-186.

Majzlan, J., Navrotsky, A., Stevens, R., Donaldson, M., Woodfield, B.F., and Boerio-Goates, J. (2005) Thermodynamics of monoclinic $Fe_2(SO_4)_3$. Journal of Chemical Thermodynamics, 37(8), 802-809.

Marion, G.M., Kargel, J.S., and Catling, D.C. (2008) Modeling ferrous-ferric iron chemistry with application to martian surface geochemistry. Geochimica Et Cosmochimica Acta, 72(1), 242-266.

Milliken, R.E., Swayze, G.A., Arvidson, R.E., Bishop, J.L., Clark, R.N., Ehlmann, B.L., Green, R.O., Grotzinger, J.P., Morris, R.V., Murchie, S.L., Mustard, J.F., and Weitz, C. (2008) Opaline silica in young deposits on Mars. Geology, 36(11), 847-850.

Nordstrom, D.K., and Alpers, C.N. (1999) Negative pH, efflorescent mineralogy, and consequences for environmental restoration at the Iron Mountain Superfund site, California. Proceedings of the National Academy of Sciences of the United States of America, 96(7), 3455-3462.

Poulet, F., Arvidson, R.E., Gomez, C., Morris, R.V., Bibring, J.P., Langevin, Y., Gondet, B., and Griffes, J. (2008) Mineralogy of Terra Meridiani and western Arabia Terra from OMEGA/MEx and implications for their formation. Icarus, 195(1), 106-130.

Rietveld, H.M. (1969) A Profile Refinement Method for Nuclear and Magnetic Structures. Journal of Applied Crystallography, 2, 65-70.

Szczygiel, R., Grybos, P., Maj, P., Tsukiyama, A., Matsushita, K., and Taguchi, T. (2009) Low-noise multichannel ASIC for high count rate X-ray diffractometry applications. Nuclear Instruments & Methods in Physics Research Section a-Accelerators Spectrometers Detectors and Associated Equipment, 607(1), 229-232.

Toby, B.H. (2001) EXPGUI, a graphical user interface for GSAS. Journal of Applied Crystallography, 34, 210-213.

Tosca, N.J., Smirnov, A., and McLennan, S.M. (2007) Application of the Pitzer ion interaction model to isopiestic data for the $Fe_2(SO_4)_3$-H_2SO_2-H_2O system at 298.15 and 323.15 K. Geochimica Et Cosmochimica Acta, 71(11), 2680-2698.

Xu, W.Q., Tosca, N.J., McLennan, S.M., and Parise, J.B. (2009) Humidity-induced phase transitions of ferric sulfate minerals studied by in situ and ex situ X-ray diffraction. American Mineralogist, 94(11-12), 1629-1637.

Yen, A.S., Morris, R.V., Clark, B.C., Gellert, R., Knudson, A.T., Squyres, S., Mittlefehldt, D.W., Ming, D.W., Arvidson, R., Mccoy, T., Schmidt, M., Hurowitz, J., Li, R., and Johnson, J.R. (2008) Hydrothermal processes at Gusev Crater: An evaluation of Paso Robles class soils. Journal of Geophysical Research-Planets, 113, E06S10, DOI: 10.1029/2007JE002978.

Yen, A.S., Murray, B., Rossman, G.R., and Grunthaner, F.J. (1999) Stability of hydroxylated minerals on Mars: A study on the effects of exposure to ultraviolet radiation. Journal of Geophysical Research-Planets, 104(E11), 27031-27041.

Table 3.1. Humidity buffers used in this study

RH buffer salt	Reported equilibrium RH (%) at different T					
	0 °C	5 °C	20 °C	25 °C	50 °C	55 °C
LiCl	11.23 ± 0.54	11.26 ± 0.47	11.31 ± 0.31	11.30 ± 0.27	11.10 ± 0.22	11.03 ± 0.23
$MgCl_2$	33.66 ± 0.33	33.60 ± 0.28	33.07 ± 0.18	32.78 ± 0.16	30.54 ± 0.14	29.93 ± 0.16
$K_2(CO_3)_2$	43.13 ± 0.66	43.13 ± 0.50	43.16 ± 0.33	43.16 ± 0.39	n/a	n/a
$Mg(NO_3)_2$	60.35 ± 0.55	58.86 ± 0.43	54.38 ± 0.28	52.89 ± 0.22	45.44 ± 0.60	n/a
NH_4NO_3	n/a	n/a	66.9*	62.7*	48.1*	n/a
$NaNO_3$	n/a	78.57 ± 0.52	75.36 ± 0.35	74.25 ± 0.32	69.04 ± 0.42	68.15 ± 0.49
NaCl	75.51 ± 0.34	75.65 ± 0.27	75.47 ±0.14	75.29 ± 0.12	74.43 ± 0.19	74.41 ± 0.24
KCl	88.61 ± 0.53	87.67 ± 0.45	85.11 ± 0.29	84.34 ± 0.26	81.20 ± 0.31	80.70 ± 0.35
	RH measured in this study (±1.5% error)					
LiCl	11.4 at 1.5 °C		11.4 at 23.5 °C		11.3 at 51.0 °C	
$MgCl_2$	34.0 at 1.7 °C		33.7 at 22.8 °C		31.1 at 51.5 °C	
$K_2(CO_3)_2$	43.3 at 1.6 °C		42.9 at 24.3 °C		42.4 at 52.1 °C	
$Mg(NO_3)_2$	57.4 at 1.7 °C		53.0 at 22.4 °C		45.9 at 51.8 °C	
NH_4NO_3	73.0 at 1.9 °C		61.7 at 23.8 °C		46.8 at 51.4 °C	
$NaNO_3$	n/a		n/a		69.0 at 51.0 °C	
NaCl	74.9 at 2.0 °C		74.3 at 22.8 °C		73.9 at 51.8 °C	
KCl	n/a		84.0 at 23.0 °C		n/a	
Drierite[$]	0.0 at 1.0 °C		0.0 at 22.1 °C		0.0 at 50.9 °C	

* data were adapted from (Adams and Merz, 1929); others were from (Greenspan, 1977)

[$] drierite is essentially $CaSO_4$, with $CoCl_2$ as a moisture indicator.

Table 3.2. Evolved phases from the $Fe_2(SO_4)_3$ solution at 2 °C and different RH.

RH (%)	**Phases at 265 days (wt. %)**	**Phases at 385 days (wt. %)**
0	amorphous ferric sulfate	amorphous ferric sulfate
11	amorphous ferric sulfate	amorphous ferric sulfate
34	rhomboclase (61) ferricopiapite (39)	rhomboclase (63) ferricopiapite (37)
43	rhomboclase (43) ferricopiapite (57)	rhomboclase (31) ferricopiapite (69)
57	ferricopiapite coating solution	ferricopiapite coating solution
73	solution	solution
75	solution	solution

Table 3.3. Evolved phases from the $Fe_2(SO_4)_3$ solution at 50 °C and different RH.

RH (%)	**Phases at 20 days (wt. %)**	**Phases at 40 days (wt. %)**
0	amorphous ferric sulfate	amorphous ferric sulfate
11	amorphous ferric sulfate	amorphous ferric sulfate
31	rhomboclase amorphous ferric sulfate	rhomboclase (86) pentahydrate (14)
42	rhomboclase (60) ferricopiapite (40)	rhomboclase (48) ferricopiapite (41) pentahydrate (11)
46	rhomboclase (50) ferricopiapite (50)	rhomboclase (35) paracoquimbite (65)
47	rhomboclase (42) ferricopiapite (58)	rhomboclase (13) paracoquimbite (87)
69	solution	solution
74	solution	solution

Table 3.4. In situ RH-T experiment --- paracoquimbite -1

T(°C)	**RH and time**	**Phase change**
40	50%, 2 hrs; 40%, 2 hrs; 30%, 2 hrs; 20%, 2 hrs; 10%, 2 hrs; 4%, 7 hrs	Starting: Paracoquimbite No change
60	50%, 2 hrs; 40%, 2 hrs; 30%, 2 hrs; 20%, 2 hrs; 10%, 2 hrs; 4%, 2 hrs	No change
80	50%, 2 hrs; 40%, 2 hrs; 30%, 2 hrs; 20%, 2 hrs; 10%, 2 hrs; 3%, 2 hrs	Paracoquimbite decreased slightly Pentahydrate formed at 30% RH (Fig. 3.3)
80	3%, 2 hrs; 10%, 2 hrs;	Paracoquimbite decreased slightly Pentahydrate growth halted
80	20%, 2 hrs	Paracoquimbite decreased slightly Pentahydrate continued to increase (Fig. 3.4)
80	30%, 2 hrs; 40%, 2 hrs; 50%, 2 hrs; 60%, 2 hrs	Paracoquimbite decreased Pentahydrate increased
80	70%, 2 hrs; 80%, 2 hrs; 70%, 3 hrs; 80%, 5 hrs	Paracoquimbite decreased slowly Pentahydrate increased slowly
80	70%, 6 hrs	Paracoquimbite diminished Pentahydrate remained (Fig. 3.4)
60	80% → 10%, 10% RH change per step, 3 hrs stay at each step	No change
60	4%, 3 hrs	No change
60	70%, 4 hrs; 75%, 7 hrs; 80%, 3 hrs	No change

Table 3.5. In situ RH-T experiment --- paracoquimbite -2

T(°C)	**RH and time**	**Phase transformation**
50	80% → 10%, 10% RH change per step, 2 hrs stay at each step	Starting: Paracoquimbite No change
50	5%, 2 hrs	No change
60	4%, 3 hrs	No change
70	3%, 3 hrs	No change
80	3%, 3 hrs	Paracoquimbite decreased (amorphization; Fig. 3.5)
80	10%, 3 hrs; 20%, 3 hrs	Paracoquimbite decreased
80	30%, 3 hrs; 40%, 3 hrs; 30%, 3 hrs	Paracoquimbite decreased Pentahydrate formed at 30% RH
80	20%, 3 hrs; 10%, 3 hrs; 1%, 3 hrs	Paracoquimbite decrease slightly Pentahydrate increase halted
60	10% → 80%, 10% RH change per step, 3 hrs stay at each step	No change
60	70%, 3 hrs; 60%, 3 hrs	No change
80	70%, 3 hrs; 80%, 3 hrs; 70%, 3 hrs	No change
80	60%, 3 hrs; 50%, 3 hrs; 40%, 7 hrs	Paracoquimbite decreased Pentahydrate increased

Table 3.6. In situ RH-T experiment --- paracoquimbite and rhomboclase

T(°C)	**RH and time**	**Phase change**
50	30%, 2 hrs; 20%, 2 hrs; 10%, 2 hrs; 1%, 4 hrs; 20%, 2 hrs; 30%, 2 hrs	Paracoquimbite and rhomboclase No change
50	40%, 2 hrs; 50%, 2 hrs; 60%, 2 hrs; 70%, 3 hrs	Paracoquimbite remained no change Rhomboclase diminished at 60% (deliquescence)

Table 3.7. In situ RH-T experiment --- paracoquimbite and kornelite

T(°C)	**RH and time**	**Phase change**
30	10%, 2 hrs; 20%, 2 hrs; 30%, 2 hrs; 40%, 2 hrs; 50%, 2 hrs; 60%, 2 hrs	Paracoquimbite and kornelite No change
29	68%, 2 hrs; 70%, 4 hrs	Paracoquimbite remained no change Kornelite diminished at 70% (deliquescence)

Table 3.8. In situ RH-T experiment --- Ferricopiapite and rhomboclase -1

T(°C)	**RH and time**	**Phase change**
26	60%, 2 hrs	Ferricopiapite and rhomboclase No change
26	65%, 2 hrs	Ferricopiapite remained no change Rhomboclase diminished (deliquescence) (Fig. 3.6)
26	70%, 2 hrs; 65%, 3 hrs; 60%, 3 hrs	Ferricopiapite remained no change
26	55%, 3 hrs	Ferricopiapite diminished Paracoquimbite formed (Fig. 3.7)
26	50%, 3 hrs; 45%, 3 hrs; 40%, 2 hrs; 30%, 3 hrs	No change, only paracoquimbite
26	60%, 1 hrs; 65%, 3 hrs; 70%, 3 hrs	No change
26	75%, 4 hrs; 80%, 3 hrs; 75%, 2 hrs; 70%, 2 hrs; 65%, 2 hrs	No change
28	80%, 2 hrs; 81%, 2 hrs	Paracoquimbite decreased slowly (deliquescence)
28	81%, 3 hrs; 84%, 2 hrs	Paracoquimbite decreased
26	75%, 3 hrs; 70%, 3 hrs	No change
26	65%, 3 hrs	Paracoquimbite increased
26	60%, 3 hrs; 55%, 3 hrs; 50%, 3 hrs	Paracoquimbite increased
50	30%, 2 hrs; 40%, 2 hrs; 50%, 2 hrs; 60%, 2 hrs, 63%, 2 hrs	No change, still paracoquimbite
50	70%, 6 hrs	Paracoquimbite decreased slowly (deliquescence)
50	75%, 6 hrs	Paracoquimbite diminished
50	70%, 2 hrs; 65%, 3 hrs	No change
50	60%, 4 hrs; 55%, 4 hrs; 50%, 4 hrs; 45%, 4 hrs; 40%, 20 hrs	Ferricopiapite formed at 60% RH Rhomboclase formed at 45% RH

Table 3.9. In situ RH-T experiment --- Ferricopiapite and rhomboclase -2

T(°C)	**RH and time**	**Phase change**
50	40%, 3 hrs; 45%, 3 hrs; 50%, 3 hrs	Ferricopiapite and rhomboclase No change
50	55%, 3 hrs	Paracoquimbite formed
50	60%, 3 hrs	Paracoquimbite increased Ferricopiapite decreased Rhomboclase diminished (deliquescence)
50	65%, 3 hrs	No change Only ferricopiapite and paracoquimbite
50	70%, 6 hrs	Paracoquimbite diminished Ferricopiapite remained
50	60%, 3 hrs	Ferricopiapite increased
50	50%, 3 hrs	Ferricopiapite decreased Paracoquimbite formed
50	40%, 3 hrs	Ferricopiapite diminished Paracoquimbite increased Rhomboclase formed

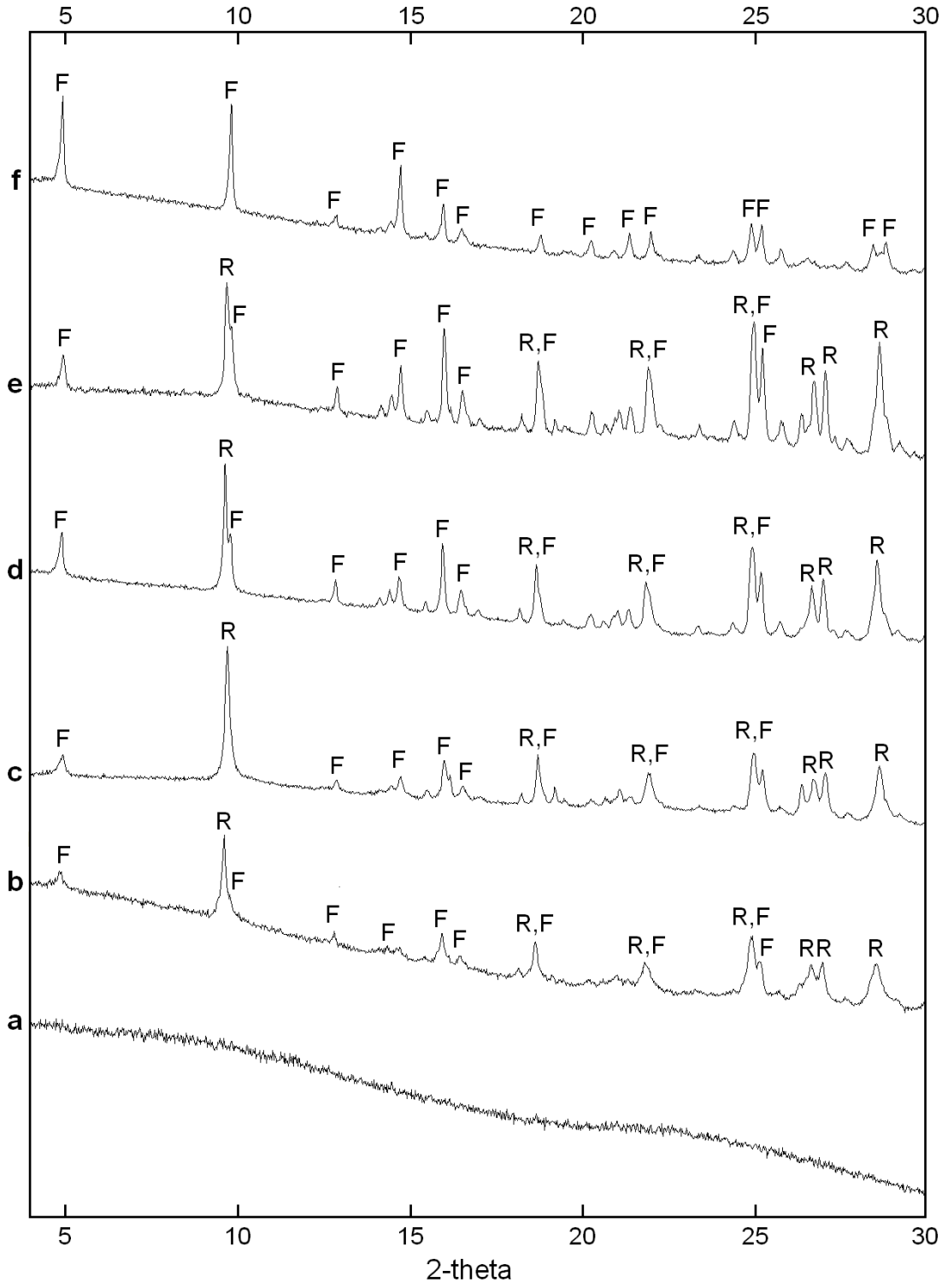

Figure 3.1. XRD data of the evolved phases at 2 °C. Pattern (a) 11% RH, Day 385; (b) 34% RH, Day 265; (c) 34% RH, Day 385; (d) 43% RH, Day 265; (e) 43% RH, Day 385; (f) 57% RH, Day 385. Peaks are marked with mineral name initials: R for rhomboclase, F for ferricopiapite.

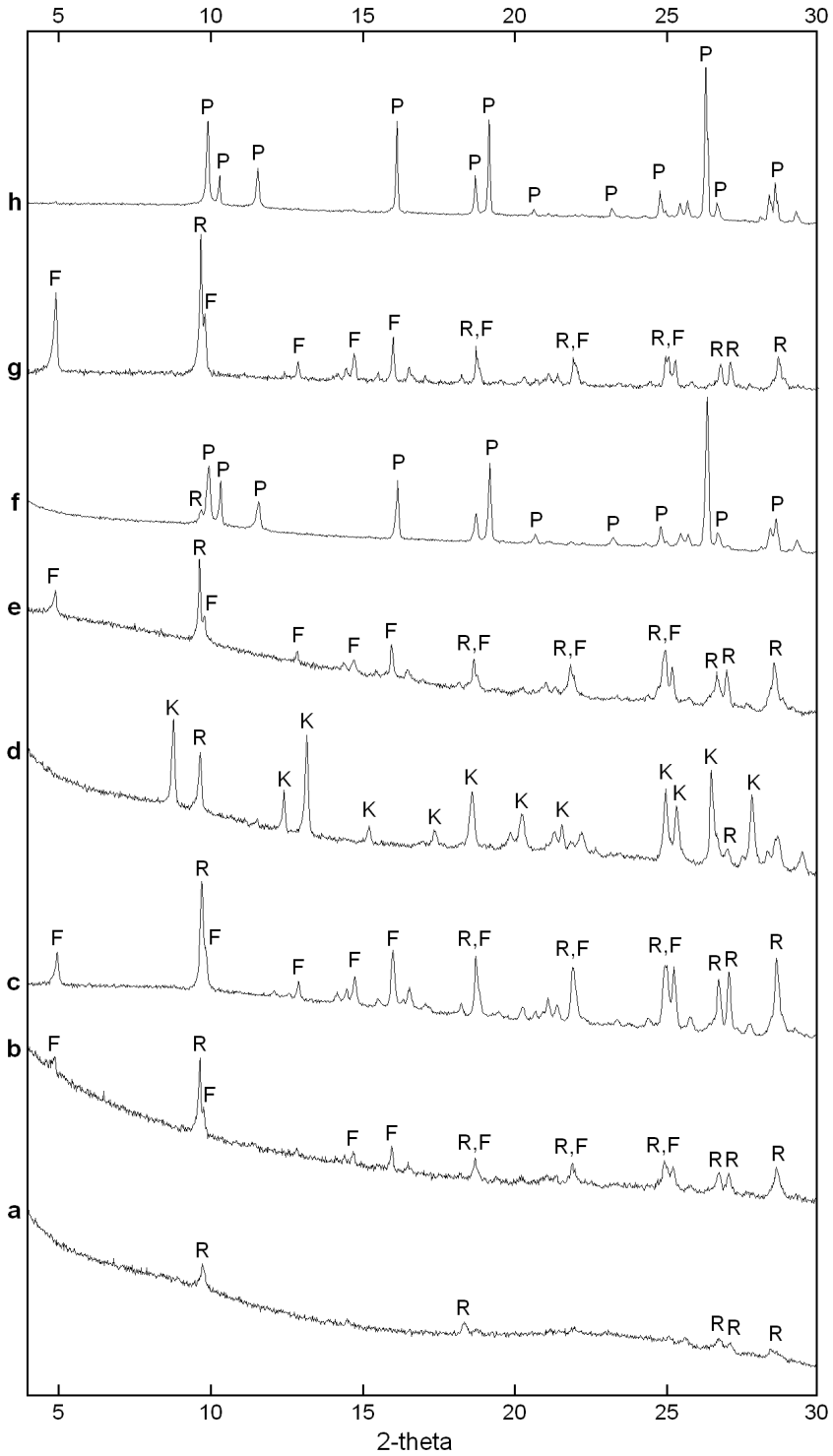

Figure 3.2. XRD data of the evolved phases at 50 °C. Pattern (a) 31% RH, Day 20; (b) 31% RH, Day 40; (c) 42% RH, Day 20; (d) 42% RH, Day 40; (e) 46% RH, Day 20; (f) 46% RH, Day 40; (e) 47% RH, Day 20; (f) 47% RH, Day 40. Peaks are marked with mineral name initials: R for rhomboclase, F for ferricopiapite, K for kornelite, P for paracoquimbite.

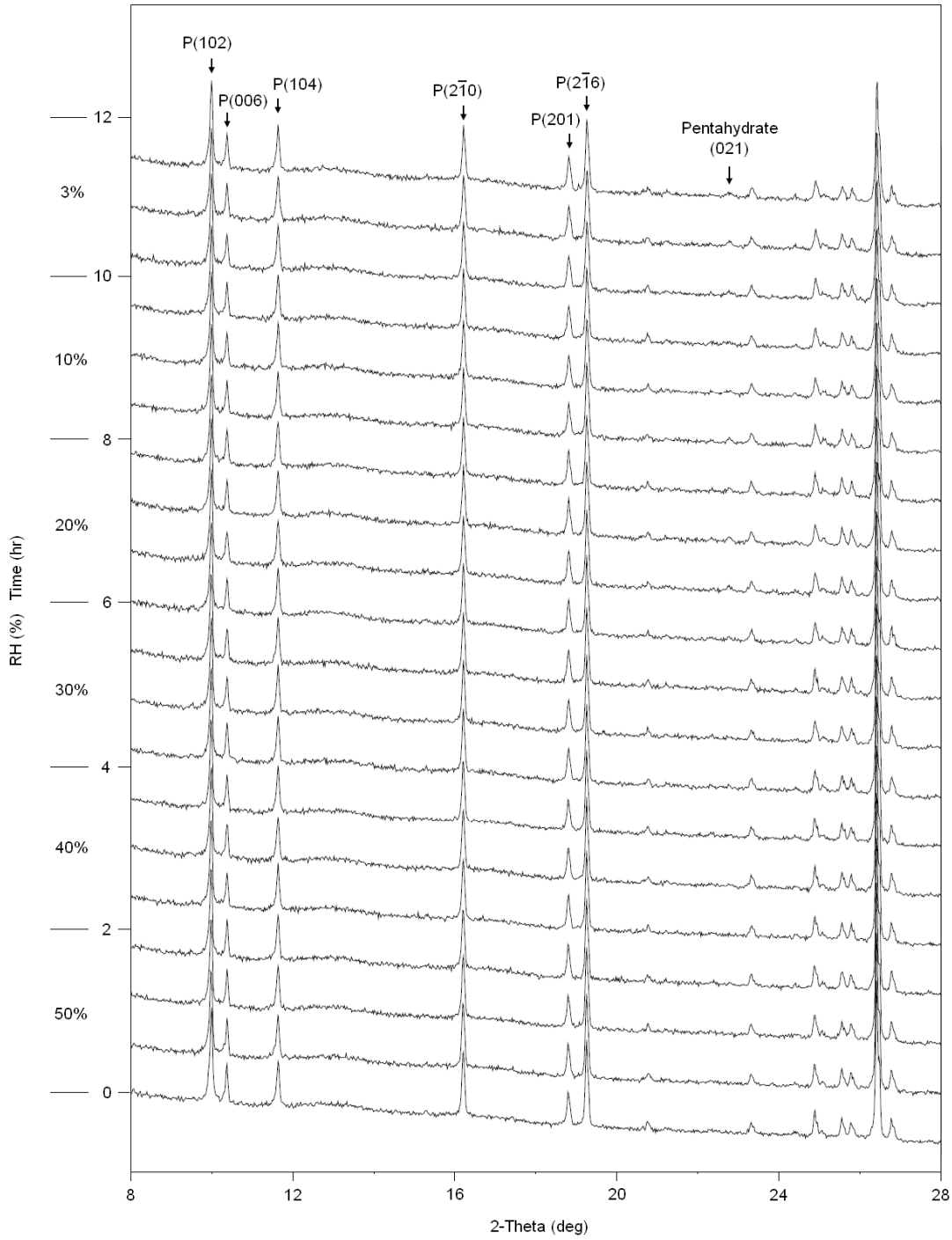

Figure 3.3. XRD patterns showing transformation of paracoquimbite-1 to pentahydrate at 80 °C and RH 50% down to 3%. Pentahydrate (021) peak is observed at 30% RH (not easy to see here due to the plot scale). Several paracoquimbite peaks are marked with letter P and their Miller indices.

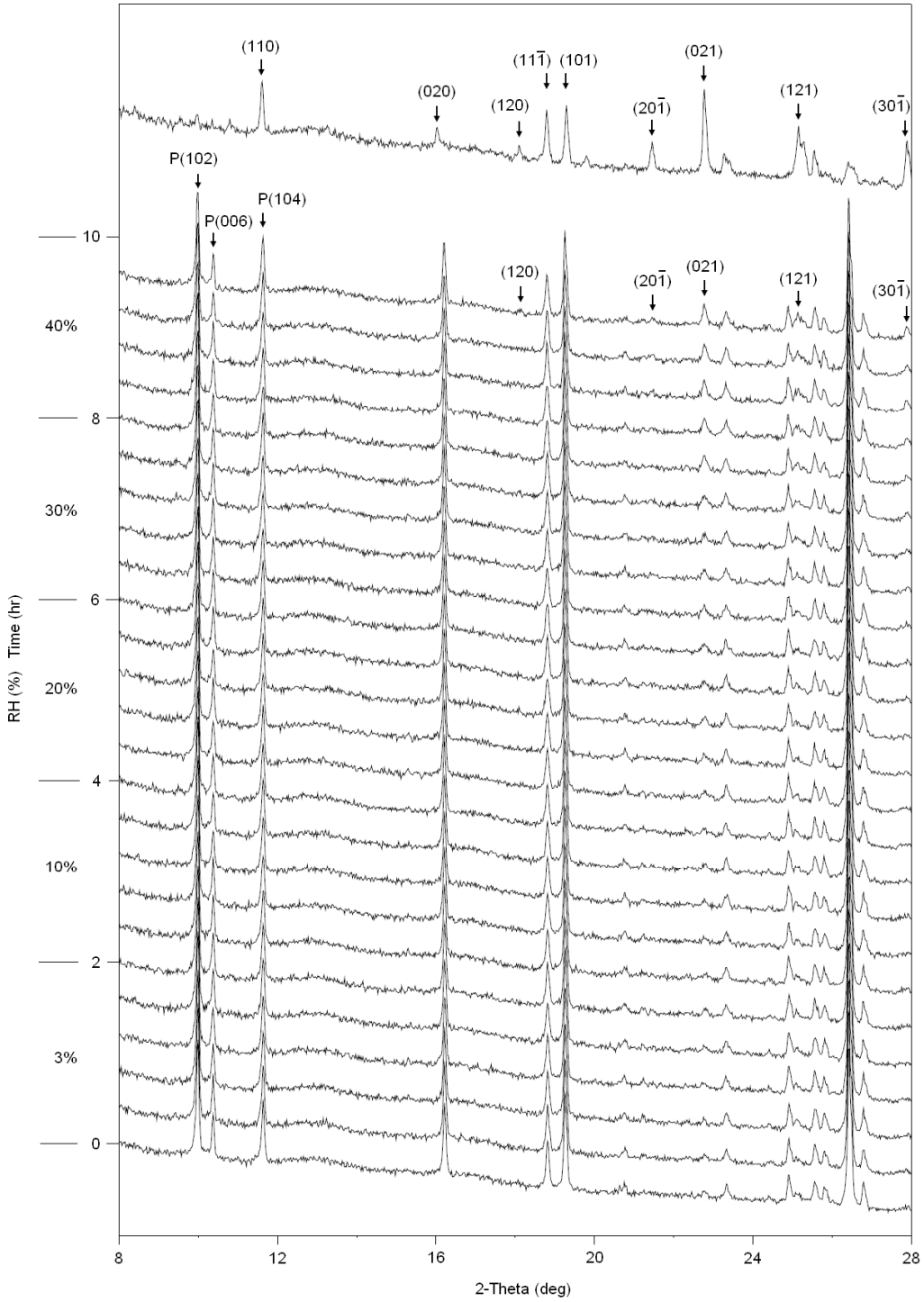

Figure 3.4. XRD patterns showing paracoquimbite-1 transforming to pentahydrate at 80 °C with increasing RH. Pentahydrate peaks are marked with their Miller indices. Paracoquimbite peaks are marked with letter P and the indices. The pattern at the top was collected at 70% RH showing the complete transformation to pentahydrate.

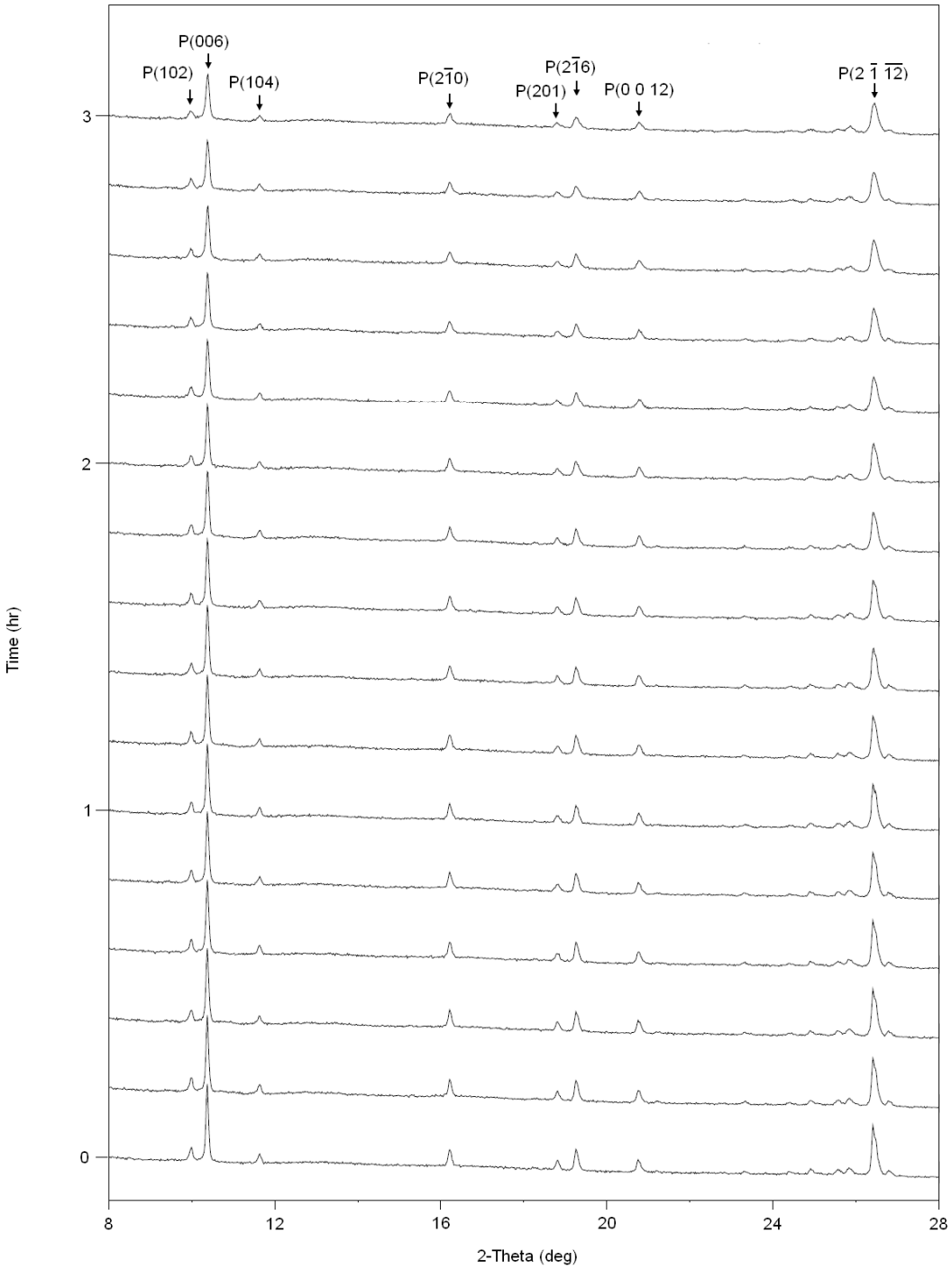

Figure 3.5. XRD patterns showing the paracoquimbite-2 destabilized at 80 °C and 3% RH over 3 hours. Paracoquimbite peaks, marked with letter P and the indices, decrease in intensity from bottom to top. Due to preferred orientation effect induced by the sample preparation, reflections perpendicular to *c* axis is stronger than normal, e.g. P(006).

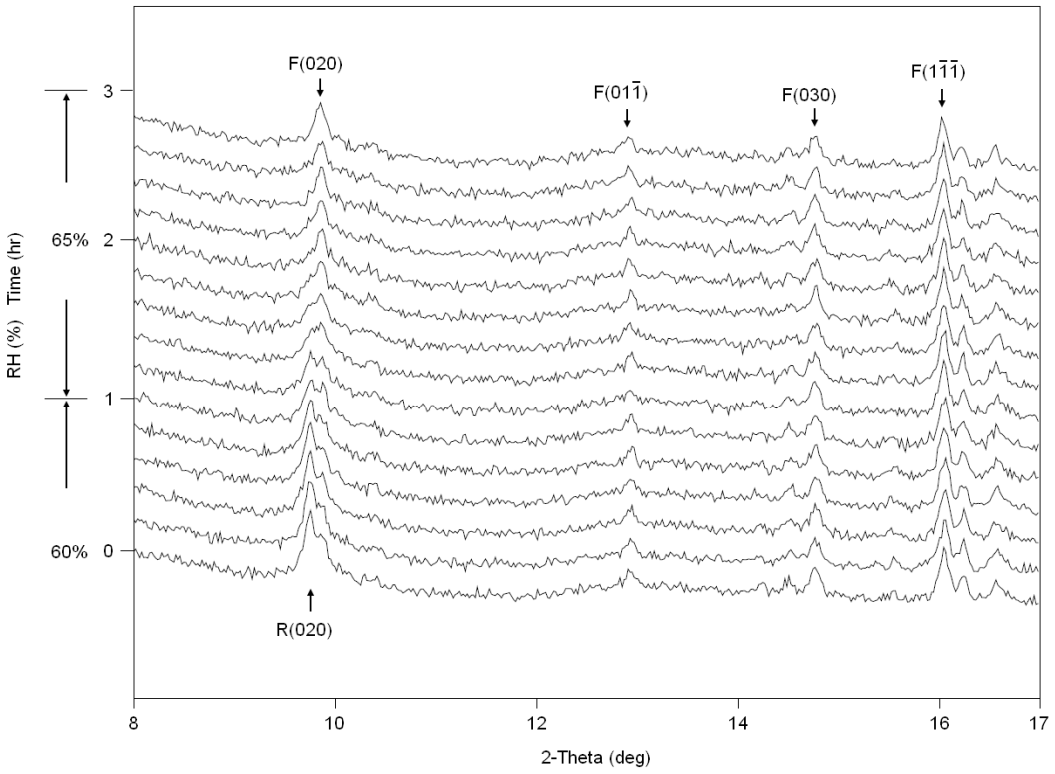

Figure 3.6. XRD patterns showing the deliquescence of rhomboclase and the retaining of ferricopiapite at 26 °C and 65% RH. Several peaks are marked with the mineral name initial and Miller indices.

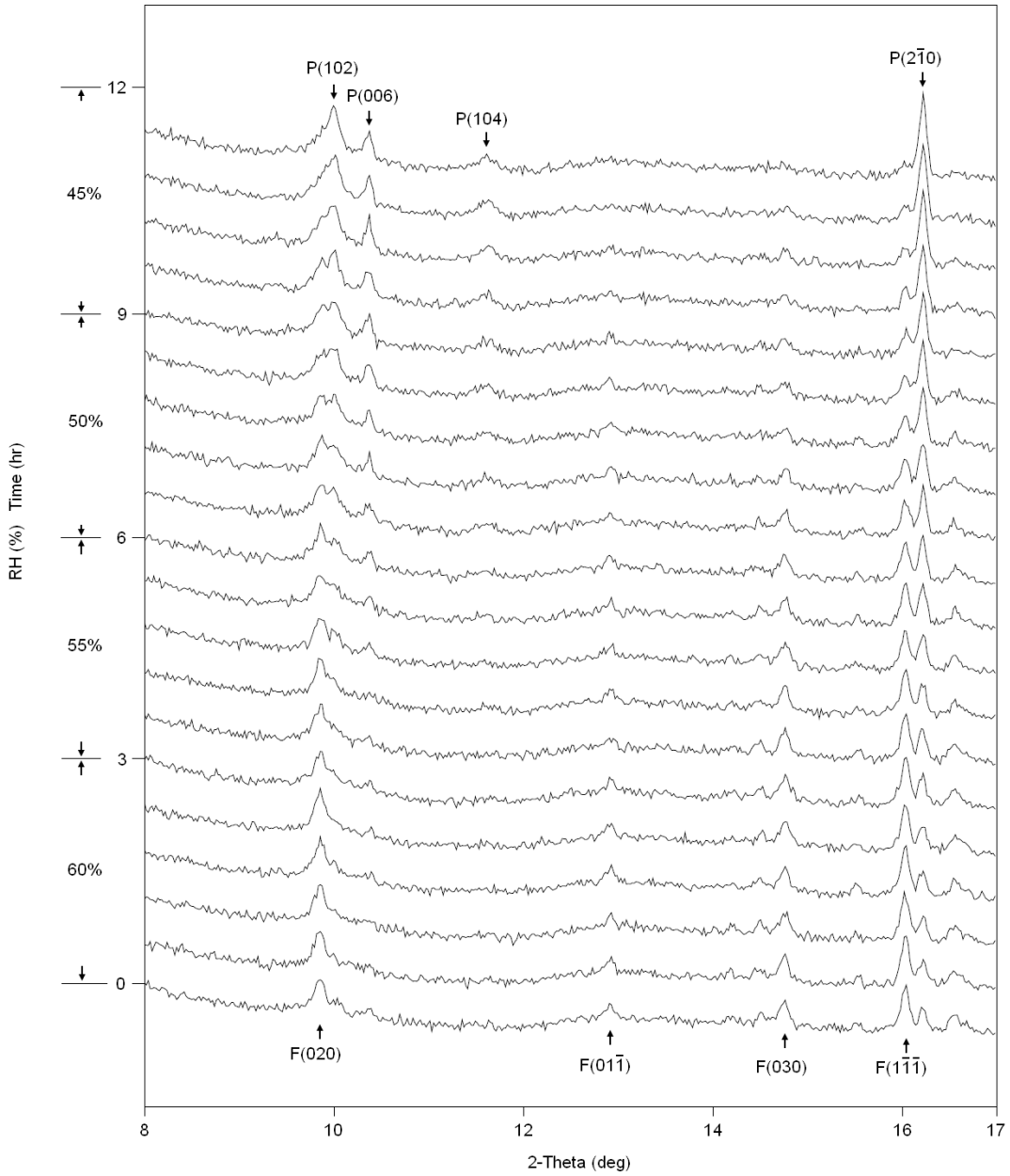

Figure 3.7. XRD patterns showing the formation of paracoquimbite out of the wet ferricopiapite at 26 °C with deceasing RH. Some peaks are marked with the mineral name initial and Miller indices.

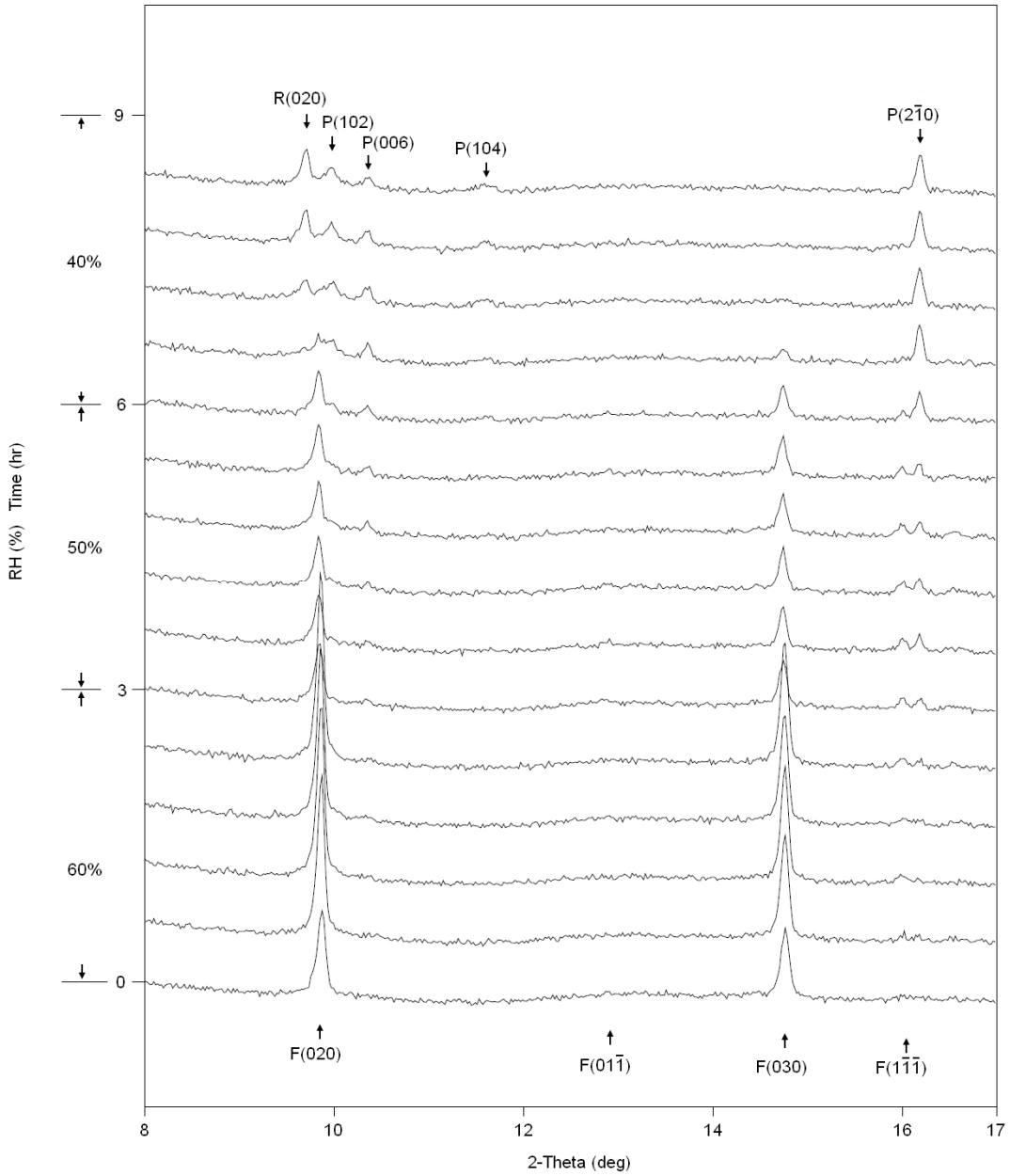

Figure 3.8. XRD patterns showing the formation of paracoquimbite and rhomboclase from the wet ferricopiapite at 50 °C with decreasing RH. Some peaks are marked with the mineral name initial and Miller indices.

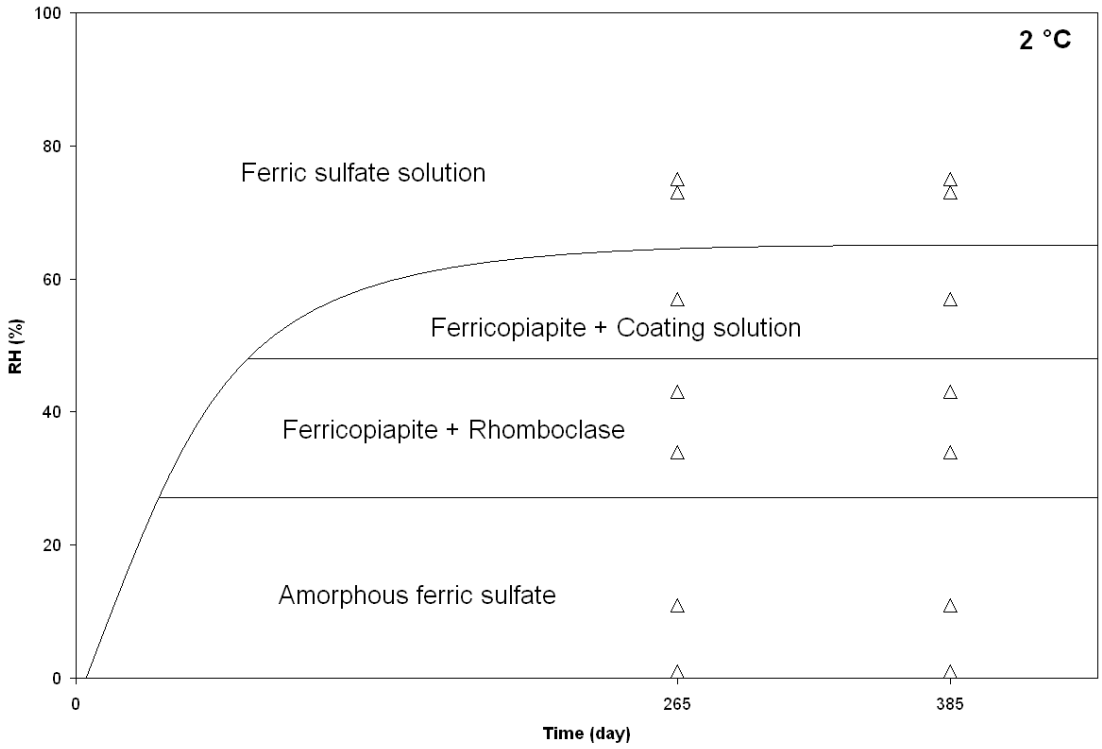

Figure. 3.9 (a) Phase evolution map of concentrated $Fe_2(SO_4)_3$ solution at (a) 2 °C, (b)25 °C and (c) 50 °C.

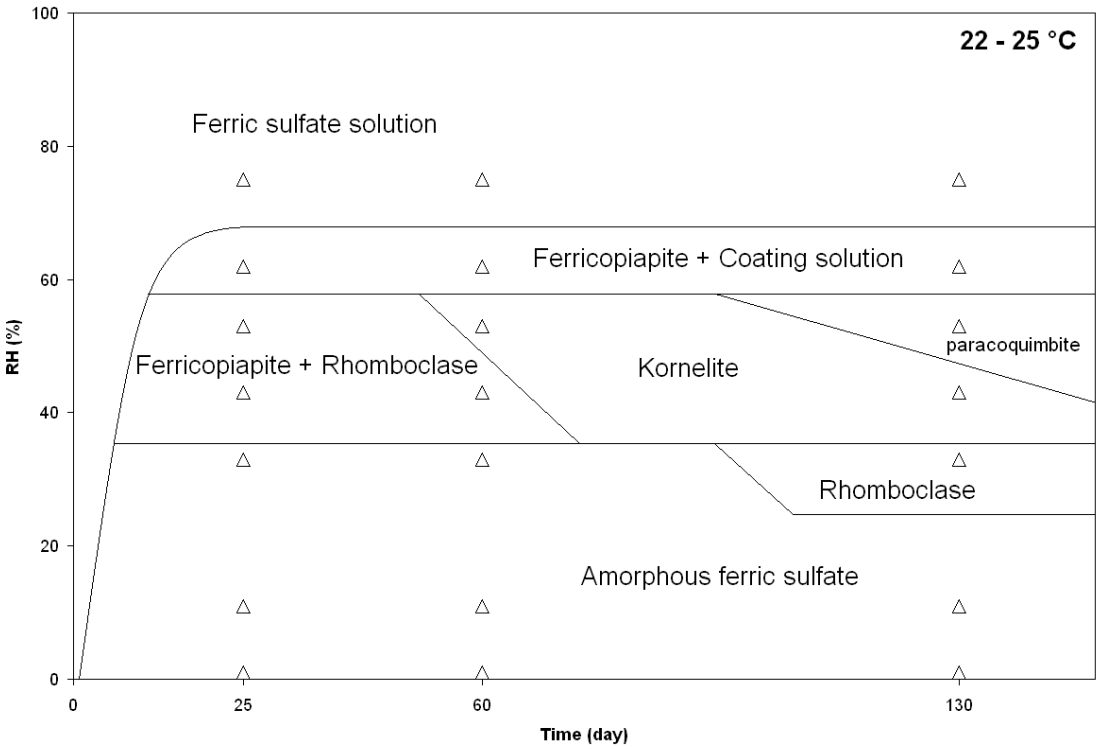

Figure 3.9 (b) Phase evolution map of concentrated $Fe_2(SO_4)_3$ solution at (a) 2 °C, (b)25 °C and (c) 50 °C. Note that slash boundaries show the occurrence of the phase on the right side, but do not mean extinction of the previously formed phases. For example, the triangle at 60 days and 53% RH drops in the region of kornelite, but the sample at this stage still contain ferricopiapite and rhomboclase, other than kornelite.

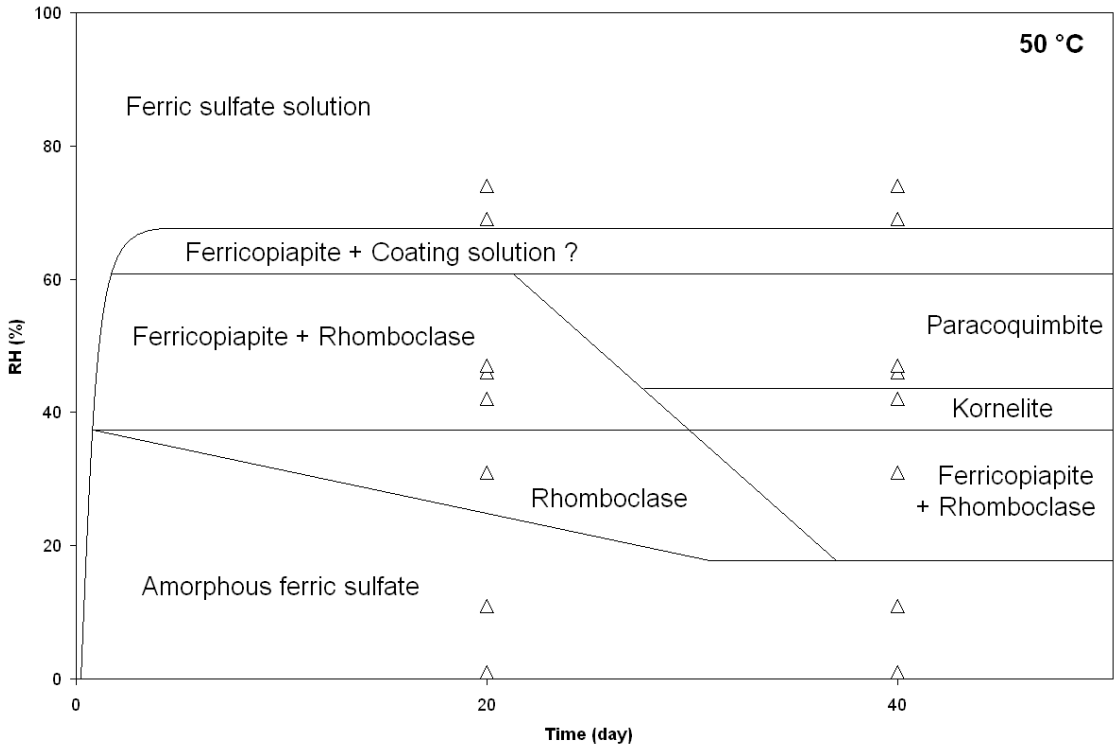

Figure 3.9 (c) Phase evolution map of concentrated $Fe_2(SO_4)_3$ solution at (a) 2 °C, (b)25 °C and (c) 50 °C.

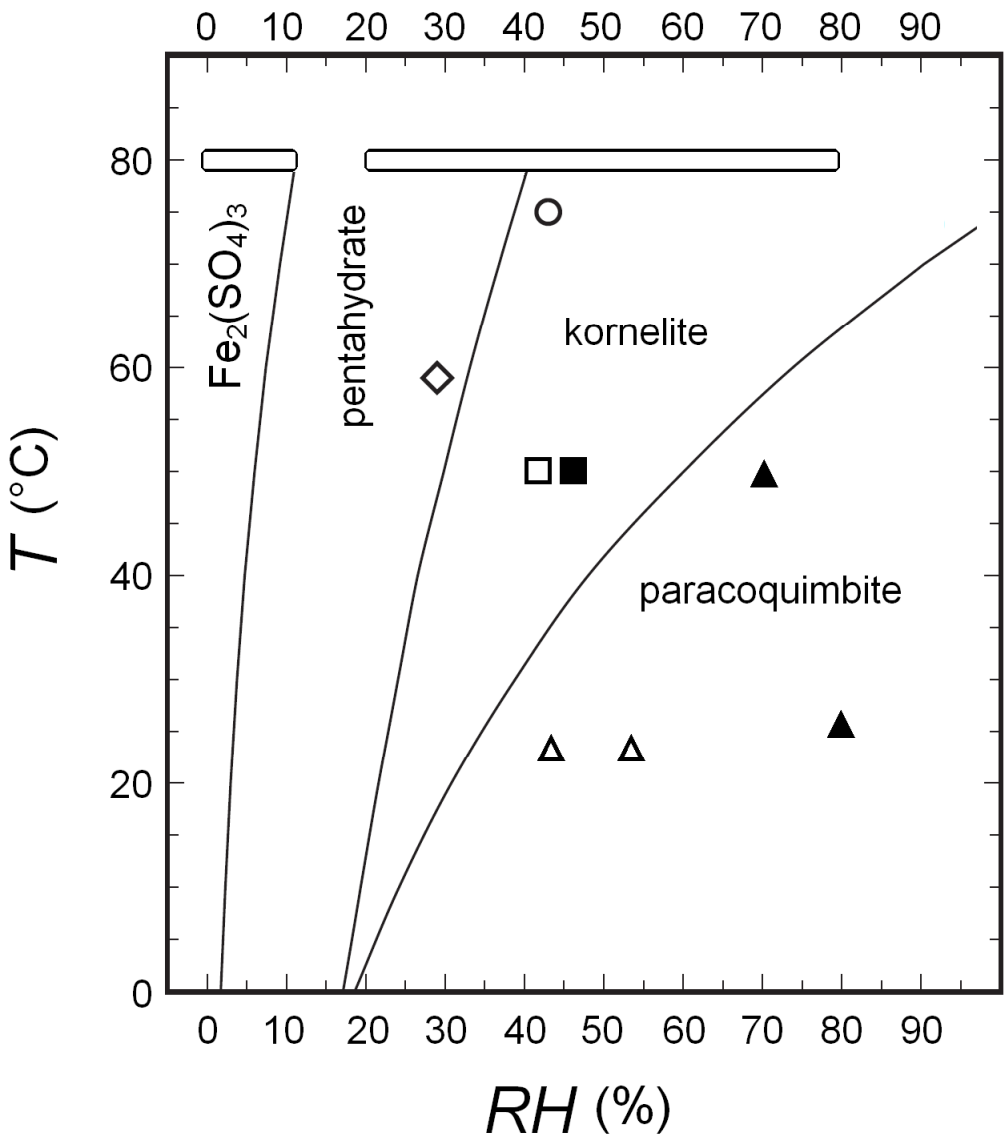

Figure 3.10. RH – T phase diagram for $Fe_2(SO_4)_3$ reproduced from Ackermann et al. (2009) with added observations in this study. The rectangle at 80 °C extending from 20% to 80% RH is the observed transition from paracoquimbite to pentahydrate. The rectangle from 0 to 10% RH is the amorphisation of paracoquimbite. Two open squares at 50 °C marks the evaporation of $Fe_2(SO_4)_3$ solution evolved to pentahydrate. The solid square at 50 °C shows the formation of paracoquimbite. Two open triangles at 23 °C marks the formation of paracoquimbite observed in *ex situ* dehydration experiment at RT. Two solid triangles showing the deliquescence of paracoquimbite observed in *in situ* experiments. The circle is the formation of kornelite as observed by Chipera et al. (2007). The diamond is the formation of pentahydrate as observed by Ackermann et al. (2009).

Chapter 4

$(H_3O)Fe(SO_4)_2$ Formed by Dehydrating Rhomboclase and Its Potential Existence on Mars

This Chapter published as:

Xu, W.Q., Parise, J.B. and Hanson, J. (2009) $(H_3O)Fe(SO_4)_2$ Formed by Dehydrating Rhomboclase and Its Potential Existence on Mars. American Mineralogist, 95(10), 1408-1412.

Abstract

The phase transitions in the 2 Fe(III) – 3 SO_4 – *n* H_2O system were described in Chapter 2 and Chapter 3. In this Chapter, we focus on the Fe(III) – 2 SO_4 – *n* H_2O system with a Fe/S ratio equal to ½. A representative phase in this system is rhomboclase with a formula $(H_5O_2)Fe(SO_4)_2 \cdot 2H_2O$. The stability of this mineral phase was explored under different temperature (T) and relative humidity (RH) conditions. The rhomboclase transforms to a solid crystalline phase, $(H_3O)Fe(SO_4)_2$ upon dehydration. The structure of $(H_3O)Fe(SO_4)_2$ is found to be the same as a recently reported structure determined from single crystal diffraction by Peterson et al. (2009), who synthesized the same compound using a hydrothermal method. The phase boundary between rhomboclase and $(H_3O)Fe(SO_4)_2$ as a function of T and RH was determined by environment-controlled *in situ* X-ray diffraction (XRD) method. The stability of $(H_3O)Fe(SO_4)_2$ vs rhomboclase was further evaluated under a simulated Martian condition of constant 50% RH, T = -

20 °C, and 6 mbar of CO_2. Both phases remained after 14 days with no observable transitions. This result suggests that hydrate ferric sulfate minerals might not respond to diurnal RH fluctuation under the extremely slowed kinetics expected on the Martian surface.

4.1. Introduction

Rhomboclase, $(H_5O_2)Fe(SO_4)_2 \cdot 2H_2O$, is a common secondary ferric sulfate mineral found in acid mine drainage (AMD) regions (Buckby et al., 2003; Hammarstrom et al., 2005; Jambor et al., 2000; Keith et al., 2001; Nordstrom and Alpers, 1999). This mineral is also suggested as a potential hydrated ferric sulfate in the sulfur-rich soils at Gusev Crater on Mars (Johnson et al., 2007; Lane et al., 2008; Yen et al., 2008). In laboratory studies, rhomboclase is found in evaporites of a brine from chemically weathering synthetic Martian basalts (Hurowitz et al., 2005; Tosca and McLennan, 2009; Tosca et al., 2004). Ferric sulfates, including rhomboclase, are sensitive to environmental changes such as relative humidity (RH) and temperature (T) and thus can act as mineral indicators of current and past sedimentary environments. Precipitates from aqueous Fe(III)-SO_4-H_2O systems were studied previously (Jonsson et al., 2006; King and McSween, 2005; Marion et al., 2008; Tosca et al., 2007). Rhomboclase precipitates at pH $\leq$ -1.8 (Marion et al., 2008), lower than the pH of solution from which ferricopiapite ($Fe_{4.67}(SO_4)_6(OH)_2 \cdot 20H_2O$) (-1 < pH < 1) and jarosite ($(K,Na,H_3O)Fe_3(OH)_6(SO4)_2$) (1 < pH < 3) precipitate (Jonsson et al., 2006; Tosca et al., 2008). In field studies, rhomboclase is found to be stable in contact with water -3.6 < pH

< 2.5 (Jambor et al., 2000). Though primarily precipitating at different pH conditions, a laboratory study has shown rhomboclase and ferricopiapite can co-precipitate by evaporation of a ferric sulfate solution with molar ratio Fe^{3+}/SO_4^{2-} = 2/3 (Xu et al., 2009). The mixture of rhomboclase and ferricopiapite may combine to form kornelite ($Fe_2(SO_4)_3 \cdot 7.25H_2O$) and paracoquimbite ($Fe_2(SO_4)_3 \cdot 9H_2O$) in the diagenesis process (Xu et al., 2009). Conversion of ferricopiapite to rhomboclase was also observed during the dehydration of ferricopiapite, probably due to a subtle change of environmental acidity (Freeman et al., 2009). Thermodynamic data for a series of ferric sulfates are recently reported by J. Majzlan and colleagues (Ackermann et al., 2009; Majzlan et al., 2006; Majzlan et al., 2005; Majzlan et al., 2004) and these data help explore the phase stability relations in the Fe(III)-SO_4-H_2O system. Here we evaluate the stability of rhomboclase with changes of RH and T, and find a transition to a dehydrated phase, $(H_3O)Fe(SO_4)_2$. Powder XRD shows the dehydrated phase has the same structure as that recently reported from a single crystal $(H_3O)Fe(SO_4)_2$ (Peterson et al., 2009), synthesized hydrothermally at 140 °C. Further experiments under simulated Martian conditions suggested the dehydrated phase may exist on the current Martian surface.

4.2. Experimental Methods

4.2.1. Sample preparation

Rhomboclase was synthesized according to methods described in the literature (Majzlan et al., 2006): mixing 2 g of anhydrous ferric sulfate, 2.5 g of water and 2.5 g of sulfuric acid (95.9% H_2SO_4 by mass) to produce a solution. The solution was evaporated

at ambient conditions (20 °C, 10-30% RH). A white solid forming after three days was confirmed as rhomboclase by XRD. The product was vacuum-filtered and rinsed with deionized water and ethanol to remove any surface H_2SO_4 and then dried in air. The yield was calculated as 68% based on the amount of Fe used in the synthesis. The preparation of anhydrous ferric sulfate was same as described in Chapter 2.

4.2.2. Thermal Analysis

Thermogravimetric (TG) and differential scanning calorimetric (DSC) analysis were performed on a Netzsch STA 449C Jupiter® simultaneous TG-DSC apparatus. Powder sample of freshly prepared rhomboclase was loaded in an alumina crucible with a hole in the cover for gas release, and heated from room temperature to 300 °C at a rate of 3 °C/min under N_2 flow.

4.2.3. Temperature-resolved XRD

In situ synchrotron XRD data were collected at the X7B beamline at the National Synchrotron Light Source, to follow the dehydration of rhomboclase under rising T. Sample powders were loaded into Kapton® polyimide capillaries with a 0.5 mm inner diameter. The X-ray beam height was matched to capillary diameter using variable slits. An air-blower type heater was used to control the temperature with the control thermocouple placed in contact with the outside of the capillary (Norby, 1996). The heater was programmed to heat in a range from 30 °C to 180 °C at a rate of 1 °C/min. XRD data were collected continuously on a MAR345 2-dimensional detector with 120 seconds exposure time, plus 80 seconds readout time before the start of the next

exposure. The time resolution was 200 seconds per exposure for the series of diffraction patterns. The sample-to-detector distance, X-ray beam center and the tilt of the detector relative to the incident beam were calibrated using a standard LaB_6 powder (NIST SRM 660a). The X-ray wavelength used was 0.31840(4) Å, also determined with the standard LaB_6 powder. The collected 2-D raw data were converted to traditional intensity versus 2θ plot using the program Fit2D (Hammersley et al., 1996). RH was not controlled in this experiment.

4.2.4. RH-resolved DSC-XRD

To investigate the combined effects of both RH and T on rhomboclase stability, *in situ* powder diffraction data were collected on a Rigaku® Ultima-IV diffractometer with a built-in environmental chamber and devices to control both T and RH (Kishi and Toraya, 2004). CuKα radiation (λ = 1.54178 Å) was used in conjunction with a high-speed semiconductor element one-dimensional X-ray detector capable of energy discrimination to eliminate the effect of Fe fluorescence in this experiment (Szczygiel et al., 2009). The same sample stage used for environment control also allows DSC measurement. In preparation of a specimen, sample powder was spread onto a 7×7×0.25 mm aluminum pan. The sample pan was placed onto the DSC heating stage beside a DSC reference pan. The DSC data were less sensitive compared to the TG-DSC apparatus due to the smaller sample size used and the open crucible necessitated by the simultaneous XRD measurement.

During the experiment, T was maintained at several arbitrary values between room T and 90 °C. At each T, RH was varied at a rate of 0.1% per minute to cross the

phase boundary from both sides. Five cartridge heaters placed in the wall of the sample chamber helped maintain a homogeneous thermal field inside. The thermocouple measuring the chamber T and the thermocouple below the sample pan indicated a T gradient of < 1 °C during the experiment. This is important since RH is strongly temperature dependent. XRD data were collected repeatedly spanning a 2θ range from 8° to 14° within a scan rate of 6 °/min. This 2θ range covers reflection (020) of rhomboclase and reflection (010) of the $(H_3O)Fe(SO_4)_2$ that are the most intense peaks of each phase.

Without using a RH control, a DSC-XRD experiment to study the thermal decomposition of rhomboclase was performed on Ultima-IV using a heating rate of 1 °C/min to 225 °C under 30 cc/min N_2 flow.

4.2.5. Simulating Martian conditions

Minerals on the Martian surface are exposed to an atmosphere consisting mainly of CO_2 with about 6 mbar pressure. A good simulation of the Martian atmosphere can be achieved using a simple vacuum line, with powder samples loaded into glass ampoules that can be attached and detached. To simulate Martian surface conditions, the whole vacuum system was first evacuated, and then filled with 6.1 mbar CO_2 and 0.8 mbar water vapor at room T (20 °C), which would create an atmosphere with 50% RH and 6 mbar atmospheric pressure at -20 °C. The sample container was then closed, disconnected from the vacuum line and kept in a freezer set at -20 °C. Because it is a sealed system, the RH in the container will drop or rise when water vapor is absorbed to or released from the sample. To maintain a constant RH and make it more like an open

system, the sample container was briefly reconnected to the vacuum line each day and the water vapor concentration was allowed to equilibrate. After 14 days, the samples were taken out and their XRD patterns were taken at ambient conditions (21 °C, 23% RH). There was about a 3-minute exposure of the sample to atmosphere for transporting the samples to the diffractometer and collecting XRD data; it turned out this short exposure did not induce any change of the sample phases (see below).

4.3. Results and Discussion

4.3.1. Thermal decomposition of rhomboclase

TG and DSC

Figure 4.1 shows the TG and DSC profiles for rhomboclase. Three endothermic events were recorded at 91, 150 and 195 °C, respectively. The first endotherm corresponded to a 17% weight loss, equal to the weight ratio of 3 H_2O molecules over rhomboclase: $3\times MW_{H_2O}/MW_{(H_5O_2)Fe(SO_4)_2\cdot 2H_2O}=16.8\%$. The compound after this dehydration step would have a nominal formula as $(H_3O)Fe(SO_4)_2$. This formula was later confirmed by the structural information obtained from *in situ* XRD data (see below). The second and third endotherms were overlapping with each other and the sample weight dropped continuously to 63.5% of the initial weight. The final product was monoclinic $Fe_2(SO_4)_3$ according to XRD. This is consistent with the TG result: $MW_{Fe_2(SO_4)_3}/\left(2\times MW_{(H_5O_2)Fe(SO_4)_2\cdot 2H_2O}\right)=62.3\%$. The reactions happening at the second step of weight loss could be written as:

$$2\ (H_3O)Fe(SO_4)_2 \Longrightarrow Fe_2(SO4)_3 + 2H_2O(g) + H_2SO_4 \qquad \text{(Eq. 4.1)}$$

This is both a dehydration and a desulfation process. The endotherm at 150 °C corresponds to the decomposition of $(H_3O)Fe(SO_4)_2$ to $Fe_2(SO4)_3$, as confirmed by DSC-XRD data (see below). No solid phase transition occurred during the third thermal event at 195 °C, but a continuous weight drop was recorded in TG. This is most likely due to the evaporation of sulfuric acid. Enthalpies of transition were calculated from the DSC data by integrating peak areas: -478.9 J/g, -164.1 J/g and -134.9 J/g for the three thermal events from low to high temperature.

In situ T-resolved synchrotron XRD

T-resolved XRD data on heating rhomboclase revealed a two-step structure change at 73 °C and 128 °C, shown in Figure 4.2. The intermediate phase between 73 °C and 128 °C was found to be $(H_3O)Fe(SO_4)_2$ according to XRD (Peterson et al., 2009). At 128 °C, $(H_3O)Fe(SO_4)_2$ decomposed to monoclinic $Fe_2(SO_4)_3$.

DSC-XRD data

Figure 4.3 shows the laboratory XRD series recording the thermal decomposition of rhomboclase along with the simultaneously collected DSC data. The same two-step transformation from rhomboclase to $(H_3O)Fe(SO_4)_2$ and then to monoclinic $Fe_2(SO_4)_3$ was revealed from XRD. Correspondingly, two endotherms at 95 °C and 157 °C were recorded in the DSC data at each transition point. A concave upward shape of the DSC curve between 150 min and 190 min was probably due to the evaporation of H_2SO_4, that

also caused the 195 °C endotherm in the DSC measurement shown in Figure 4.2. The shape difference was possibly caused by different DSC settings (see Experimental Methods).

4.3.2. RH-T phase diagram

A phase diagram showing the stability of rhomboclase and $(H_3O)Fe(SO_4)_2$ as a function of RH and T is plotted in Figure 4.4. Each data point was obtained from an RH-resolved DSC-XRD experiment, in which the dehydration or hydration was induced by varying RH while maintaining a constant temperature. Figure 4.5 shows the RH-induced dehydration of rhomboclase to $(H_3O)Fe(SO_4)_2$ at 72 °C. The transition to $(H_3O)Fe(SO_4)_2$ happened at 8% RH, as recorded by XRD and DSC. Each transition RH with the corresponding T is listed in Table 4.1. Notice in Figure 4.4 that there appears to be a hysteresis between the hydration RH and dehydration RH: the hydration RH is higher than the dehydration RH at the same T. The equilibrium RH should be within the domain confined by the measured points. The expected phase boundary is drawn in Figure 4.4.

Rhomboclase is commonly found in AMD regions, usually under very acidic conditions where pH could be as low as -3.6 (Nordstrom et al., 2000). But the dehydrated phase was never reported. This is expectable from the phase diagram (Fig. 4.4) where RH is required to reach 2 – 4 % or below to favor the transformation to the dehydrated phase at 20 – 50 °C. Such dry condition is not normally found in AMD regions. However, the dehydrated phase may still be present at high temperature spots, like close to fumaroles or under burial conditions. A good example is mikasaite, trigonal $(Fe, Al)_2(SO_4)_3$, an extremely hygroscopic mineral. It was discovered around coal gas

escape fractures, where temperatures are around 300 °C to keep the mineral from absorbing H_2O (Miura et al., 1994).

Also mapped in Figure 4.4 is the deliquescence boundary of rhomboclase. Rhomboclase is dissolved when RH reaches 60 – 65 % at 25 – 40 °C. The dissolution of rhomboclase will acidify streams due to Fe^{3+} hydrolysis and the release of hydronium ions (H_3O^+). In general, ferric sulfates have stronger acidification effect than other metal sulfates upon dissolution due to the Fe^{3+} hydrolysis. Other than acidity, the released metal ions like Zn^{2+} and Cu^{2+} also contaminate the aquatic system. Field observations show the water quality is worse in humid seasons than in dry seasons due to the dissolution or deliquescence of these efflorescent minerals (Hammarstrom et al., 2005). Mapping the deliquescence boundary for common ferric sulfates will be useful in predicting local water quality combined with a weather forecast.

4.3.3. Stability under simulated Martian condition

Both rhomboclase and the dehydrated samples were stored for 14 days under the simulated conditions of the Martian surface, 6 mbar air pressure, 50% RH and -20 °C. Neither was rhomboclase detected in the $(H_3O)Fe(SO_4)_2$ sample from XRD, nor was $(H_3O)Fe(SO_4)_2$ found in the rhomboclase sample. According to the RH-T phase diagram as shown in Figure 4.4, the experimental condition (-20 °C, 50% RH) should fall into the rhomboclase stability region, assuming the phase boundary line can be extrapolated to below 0 °C. So the absence of rhomboclase in the $(H_3O)Fe(SO_4)_2$ sample may be due to the extremely slow kinetics at -20 °C. Also, the absence of rhomboclase indicated there was little influence of the short exposure to the atmosphere during the XRD measurement,

as the ambient condition (21 °C, 23% RH) was supposed to favor the transformation to rhomboclase. Even though this experimental result did not confirm which species was more favored in the conditions used to simulate the Martian surface, it provided a lower limit of how slow the hydration or dehydration might be on Mars. Therefore, rhomboclase, or $(H_3O)Fe(SO_4)_2$, if present on the surface of Mars, will not respond to the diurnal fluctuation of RH, e.g. RH varies from <1% to 100% at the Viking Lander 1 site during summertime (Savijarvi, 1995). The suggestion that low T on Mars can dramatically slow down the kinetics is also supported by spectroscopic observations that sulfate deposits in East Candor did not show changes in hydration state over 2 years (Roach et al., 2009).

4.3.4. Comparison between the two Fe(III) – SO_4 – *n* H_2O systems

Mineral phases encountered in the 2 Fe(III) – 3 SO_4 – *n* H_2O system varied with RH and T were described in Chapter 2 and Chapter 3. In this chapter, phases in the Fe(III) – 2 SO_4 – *n* H_2O system are described. In the system with Fe/S = 2/3, electron charges are balanced between Fe^{3+} and SO_4^{2-} groups, and there are no net charges from the proton – hydroxyl pairs. In the system with Fe/S = 1/2, extra protons (or hydroniums) are required to compensate the positive charge deficiency, which makes this system more acidic than the 2 Fe(III) – 3 SO_4 – *n* H_2O system, thereby producing different ferric sulfate phases. In the 2 Fe(III) – 3 SO_4 – *n* H_2O system, neutral ferric sulfates like paracoquimbite, kornelite and pentahydrate are the thermodynamically stable phases, with rhomboclase and ferricopiapite also forming as intermediate phases. While in the Fe(III) – 2 SO_4 – *n* H_2O system, rhomboclase and its dehydrated version are the only

phases present in the RH-T phase diagram (Fig. 4.4). The different mineral assemblages evolved reflect the chemistry especially the pH in the two systems, which is consistent with field and laboratory studies of the precipitation pH of these minerals (Jambor et al., 2000; Marion et al., 2008; Tosca et al., 2008).

In a short summary, the combined RH-DSC-XRD method was used to study the thermal stability of rhomboclase. A transformation from rhomboclase to $(H_3O)Fe(SO_4)_2$ at high T or low RH conditions was observed, and mapped in the RH-T phase diagram. The successful application of the DSC-XRD technique provided a promising future for its use in exploring mineral stability and phase transition, in case complex heat signatures need to be deconvolved and correlated with structural changes.

References:

Ackermann, S., Lazic, B., Armbruster, T., Doyle, S., Grevel, K.D., and Majzlan, J. (2009) Thermodynamic and crystallographic properties of kornelite $[Fe_2(SO_4)_3 \cdot 7.75H_2O]$ and paracoquimbite $[Fe_2(SO_4)_3 \cdot 9H_2O]$. American Mineralogist, 94(11-12), 1620-1628.

Hammarstrom, J.M., Seal, R.R., Meier, A.L., and Kornfeld, J.M. (2005) Secondary sulfate minerals associated with acid drainage in the eastern US: recycling of metals and acidity in surficial environments. Chemical Geology, 215(1-4), 407-431.

Hammersley, A.P., Svensson, S.O., Hanfland, M., Fitch, A.N., and Hausermann, D. (1996) Two-dimensional detector software: From real detector to idealised image or two-theta scan. High Pressure Research, 14(4-6), 235-248.

Hurowitz, J.A., McLennan, S.M., Lindsley, D.H., and Schoonen, M.A.A. (2005) Experimental epithermal alteration of synthetic Los Angeles meteorite: Implications for the origin of Martian soils and identification of hydrothermal sites on Mars. Journal of Geophysical Research-Planets, 110, E07002, DOI: 10.1029/2004JE002391.

Jambor, J.I., Nordstrom, D.K., and Alpers, C.N. (2000) Metal-sulfate Salts from Sulfide Mineral Oxidation. In C.N. Alpers, J.I. Jambor, and D.K. Nordstrom, Eds. Sulfate Minerals: Crystallography, Geochemistry, and Environmental Significance, Reviews in Mineralogy and Geochemistry, vol. 40, p. 305-350. Mineralogical Society of America, Geochemical Society, Washington, D. C.

Johnson, J.R., Bell, J.F., Cloutis, E., Staid, M., Farrand, W.H., Mccoy, T., Rice, M., Wang, A., and Yen, A. (2007) Mineralogic constraints on sulfur-rich soils from Pancam spectra at Gusev crater, Mars. Geophysical Research Letters, 34, L13202, DOI: 10.1029/2007GL029894.

Jonsson, J., Jonsson, J., and Lovgren, L. (2006) Precipitation of secondary Fe(III) minerals from acid mine drainage. Applied Geochemistry, 21(3), 437-445.

Kishi, A., and Toraya, H. (2004) Simultaneous measurements of X-ray diffraction (XRD) and differential scanning calorimetry (DSC) data under controlled humidity condition: Instrumentation and application to studies on hydration, dehydration, and rehydration processes of pharmaceutical compounds. Powder Diffraction, 19(1), 31-35.

Lane, M.D., Bishop, J.L., Dyar, M.D., King, P.L., Parente, M., and Hyde, B.C. (2008) Mineralogy of the Paso Robles soils on Mars. American Mineralogist, 93(5-6), 728-739.

Majzlan, J., Navrotsky, A., McCleskey, R.B., and Alpers, C.N. (2006) Thermodynamic properties and crystal structure refinement of ferricopiapite, coquimbite, rhomboclase, and $Fe_2(SO_4)_3(H_2O)_5$. European Journal of Mineralogy, 18(2), 175-186.

Majzlan, J., Navrotsky, A., Stevens, R., Donaldson, M., Woodfield, B.F., and Boerio-Goates, J. (2005) Thermodynamics of monoclinic $Fe_2(SO_4)_3$. Journal of Chemical Thermodynamics, 37(8), 802-809.

Majzlan, J., Stevens, R., Boerio-Goates, J., Woodfield, B.F., Navrotsky, A., Burns, P.C., Crawford, M.K., and Amos, T.G. (2004) Thermodynamic properties, low-temperature heat-capacity anomalies, and single-crystal X-ray refinement of hydronium jarosite, $(H_3O)Fe_3(SO_4)_2(OH)_6$. Physics and Chemistry of Minerals, 31(8), 518-531.

Marion, G.M., Kargel, J.S., and Catling, D.C. (2008) Modeling ferrous-ferric iron chemistry with application to martian surface geochemistry. Geochimica Et Cosmochimica Acta, 72(1), 242-266.

Miura, H., Niida, K., and Hirama, T. (1994) Mikasaite, $(Fe^{3+}, Al)_2(SO_4)_3$, a New Ferric Sulfate Mineral from Mikasa City, Hokkaido, Japan. Mineralogical Magazine, 58(393), 649-653.

Norby, P. (1996) In-situ time resolved synchrotron powder diffraction studies of syntheses and chemical reactions. European Powder Diffraction: Epdic Iv, Pts 1 and 2, 228, 147-152.

Nordstrom, D.K., Alpers, C.N., Ptacek, C.J., and Blowes, D.W. (2000) Negative pH and extremely acidic mine waters from Iron Mountain, California. Environmental Science & Technology, 34(2), 254-258.

Peterson, R.C., Valyashko, E., and Wang, R.Y. (2009) The atomic structure of $(H_3O)Fe^{3+}(SO_4)_2$ and rhomboclase, $(H_5O_2)Fe^{3+}(SO_4)_2 \cdot 2H_2O$. Canadian Mineralogist, 47(3), 625-634.

Roach, L.H., Mustard, J.F., Murchie, S.L., Bibring, J.P., Forget, F., Lewis, K.W., Aharonson, O., Vincendon, M., and Bishop, J.L. (2009) Testing evidence of recent hydration state change in sulfates on Mars. Journal of Geophysical Research-Planets, 114, E00D02, DOI: 10.1029/2008JE003245.

Savijarvi, H. (1995) Mars Boundary-Layer Modeling - Diurnal Moisture Cycle and Soil Properties at the Viking-Lander-1 Site. Icarus, 117(1), 120-127.

Szczygiel, R., Grybos, P., Maj, P., Tsukiyama, A., Matsushita, K., and Taguchi, T. (2009) Low-noise multichannel ASIC for high count rate X-ray diffractometry applications. Nuclear Instruments & Methods in Physics Research Section a-Accelerators Spectrometers Detectors and Associated Equipment, 607(1), 229-232.

Tosca, N.J., and McLennan, S.M. (2009) Experimental constraints on the evaporation of partially oxidized acid-sulfate waters at the martian surface. Geochimica Et Cosmochimica Acta, 73(4), 1205-1222.

Tosca, N.J., McLennan, S.M., Dyar, M.D., Sklute, E.C., and Michel, F.M. (2008) Fe oxidation processes at Meridiani Planum and implications for secondary Fe mineralogy on Mars. Journal of Geophysical Research-Planets, 113, E05005, DOI: 10.1029/2007JE003019.

Tosca, N.J., McLennan, S.M., Lindsley, D.H., and Schoonen, M.A.A. (2004) Acid-sulfate weathering of synthetic Martian basalt: The acid fog model revisited. Journal of Geophysical Research-Planets, 109, E05003, DOI: 10.1029/2003JE002218.

Xu, W., Tosca, N., McLennan, S.M., and Parise, J.B. (2009) Humidity-induced phase transitions of ferric sulfate minerals studied by in situ and ex situ X-ray diffraction. American Mineralogist, 94(11-12), 1629-1637.

Yen, A.S., Morris, R.V., Clark, B.C., Gellert, R., Knudson, A.T., Squyres, S., Mittlefehldt, D.W., Ming, D.W., Arvidson, R., Mccoy, T., Schmidt, M., Hurowitz, J., Li, R., and Johnson, J.R. (2008) Hydrothermal processes at Gusev Crater: An evaluation of Paso Robles class soils. Journal of Geophysical Research-Planets, 113, E06S10, DOI: 10.1029/2007JE002978.

Table 4.1. Experimental transition RH and T between rhomboclase and $(H_3O)Fe(SO_4)_2$ and the deliquescence RH of rhomboclase.

Temp (±1 °C)	RH (±1.0%)		
	Dehydration	Hydration	Deliquescence
22	1.0	3.0	59.2
42	2.1	7.2	70.5
52	2.7	8.1	
62	5.2	11.8	
72	8.0	12.0	
82	12.4	16.0	
92	15.3	19.2	

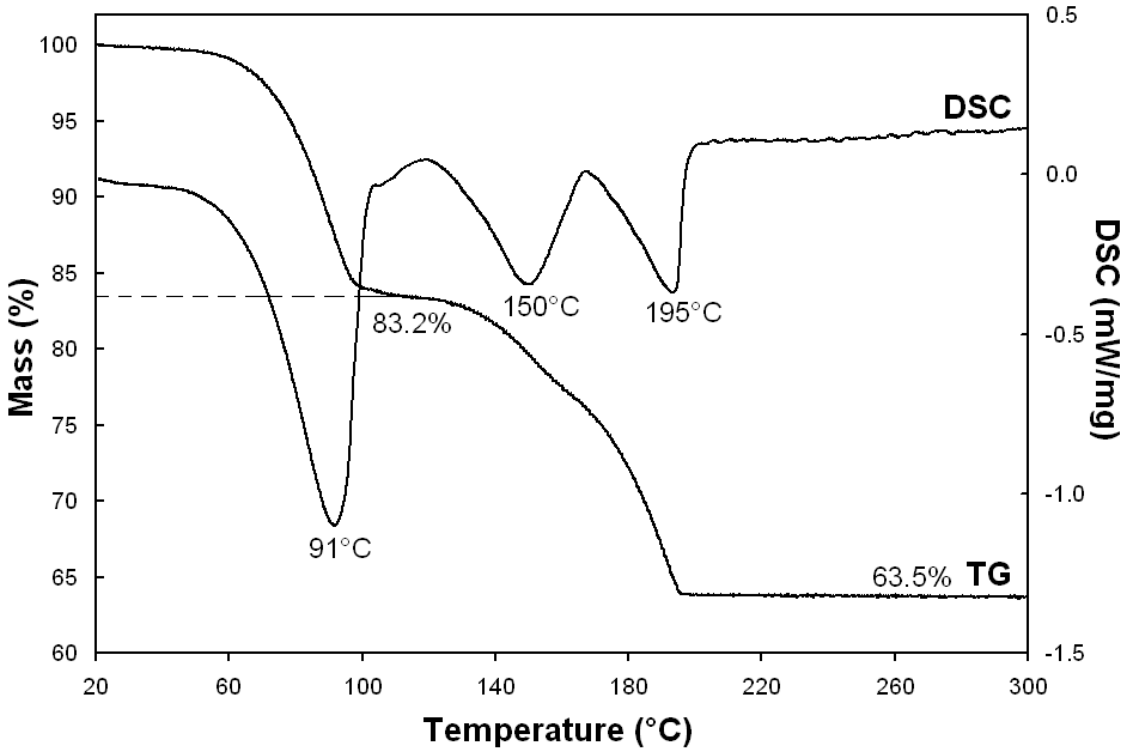

Figure 4.1. TG and DSC data for rhomboclase

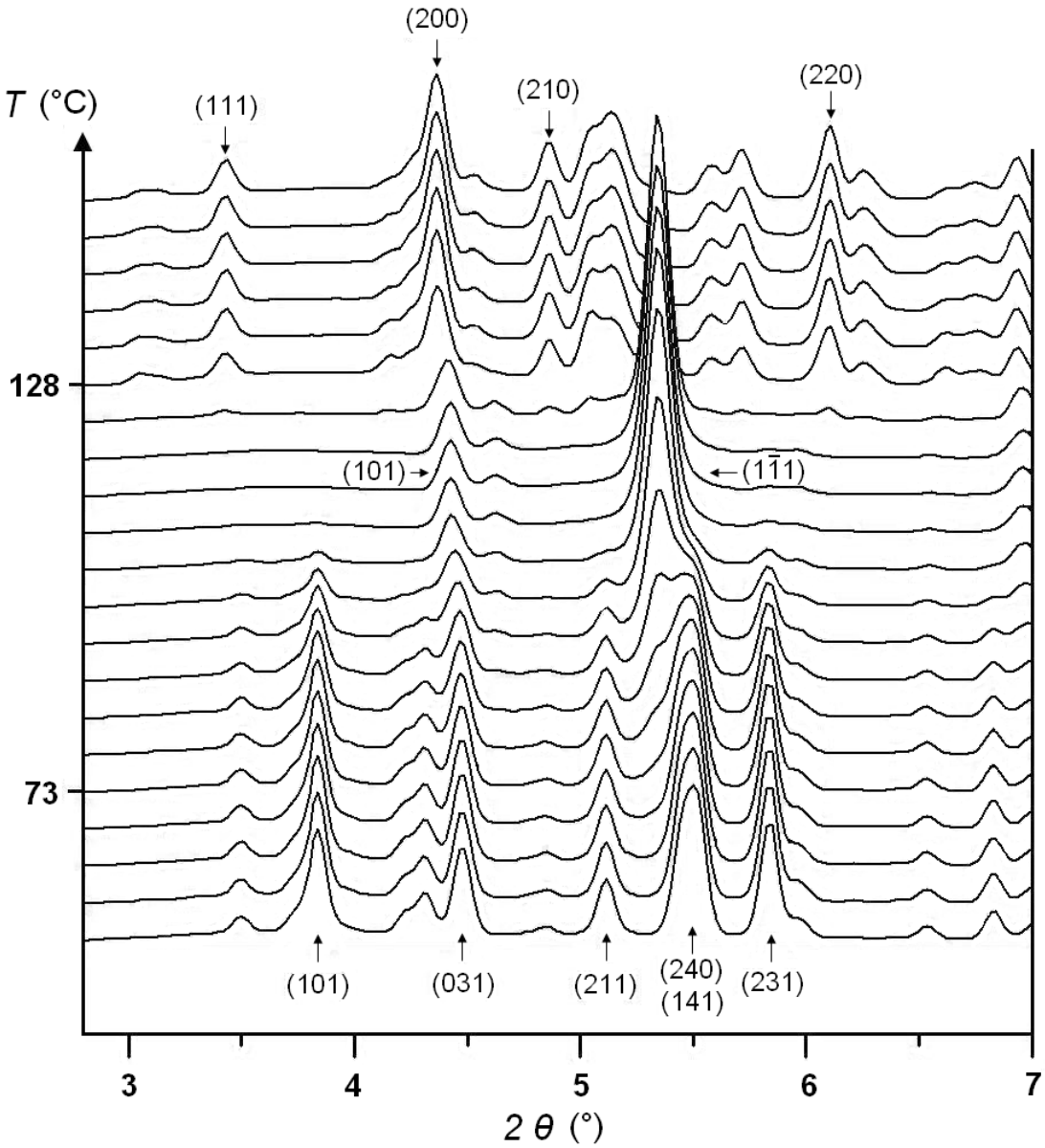

Figure 4.2. T-resolved synchrotron XRD data showing the thermal decomposition of rhomboclase to $(H_3O)Fe(SO_4)_2$ then to monoclinic $Fe_2(SO_4)_3$ at high T (no RH control). Some reflections are indexed for rhomboclase at the bottom, $(H_3O)Fe(SO_4)_2$ in the middle and monoclinic $Fe_2(SO_4)_3$ at the top.

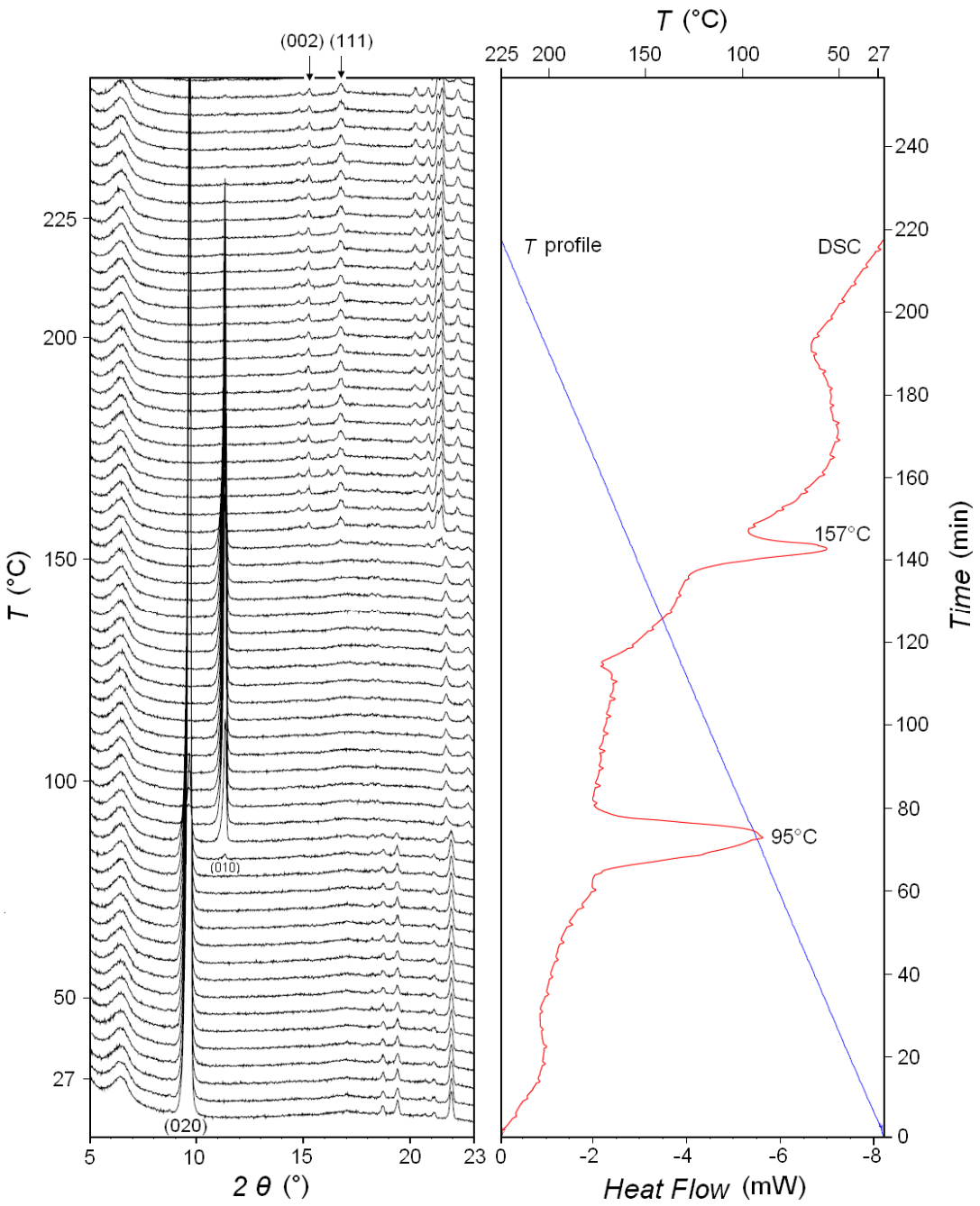

Figure 4.3. DSC-XRD data showing the thermal decomposition of rhomboclase to $(H_3O)Fe(SO_4)_2$ and to monoclinic $Fe_2(SO_4)_3$ (no RH control).

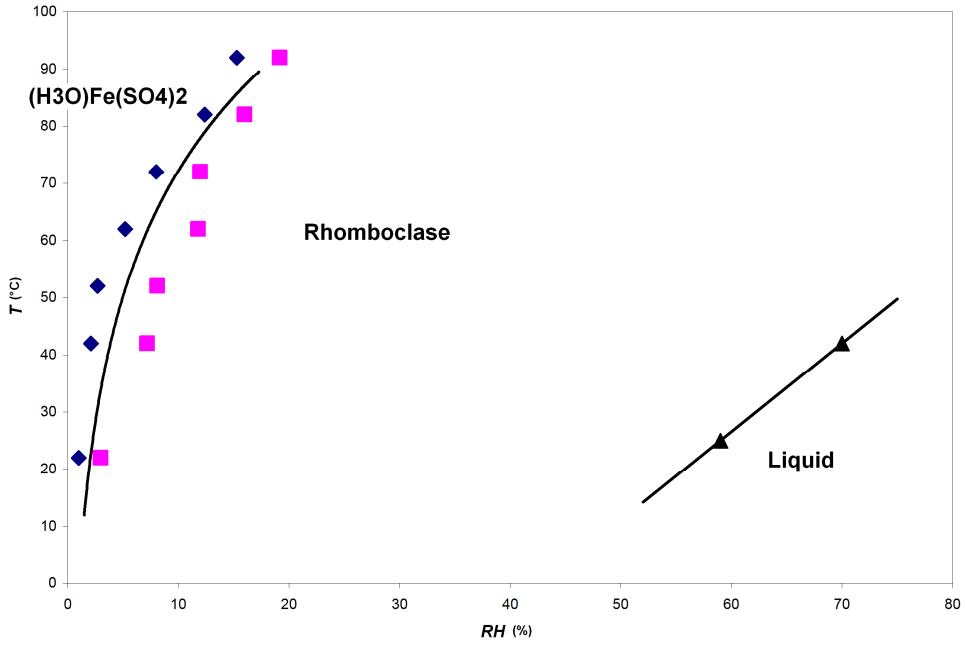

Figure 4.4. RH-T phase diagram of rhomboclase. Diamond spot represents the dehydration (RH, T) of rhomboclase; Square represents the hydration (RH, T) of $(H_3O)Fe(SO_4)_2$; Triangle represents the deliquescence (RH, T) of rhomboclase.

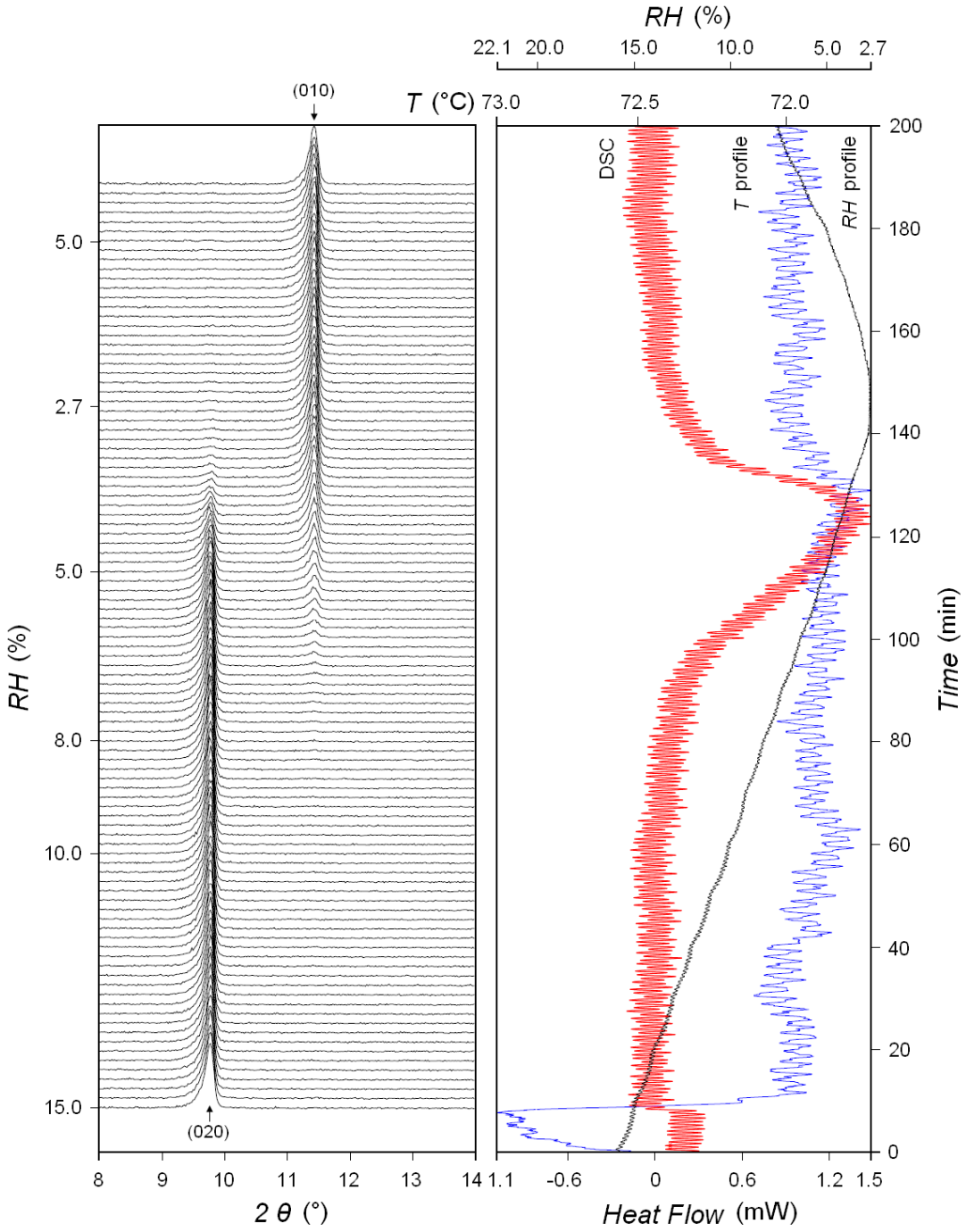

Figure 4.5. DSC-XRD data showing the RH-induced dehydration of rhomboclase to $(H_3O)Fe(SO_4)_2$ at 72°C

Chapter 5

Ferric sulfates under low temperature and low atmospheric pressure close to conditions on present day Martian surface

Abstract

A novel temperature (T) and atmospheric pressure (P) - controlled *in situ* powder X-ray diffraction method was developed and used to study the stability of hydrated ferric sulfates including ferricopiapite, rhomboclase, kornelite, paracoquimbite, ferric sulfate pentahydrate and an amorphous ferric sulfate under low atmospheric P (3.6 to 20.0 mbar) and low T (-30 °C). All sulfates studied retained their structures at -30 °C within the experiment timescale, 20 to 40 hours. Ferricopiapite showed signs of slight dehydration at -30 °C and 3.6 mbar and 15% relative humidity (RH). Upon increasing temperature, ferricopiapite was destabilized at ~6 °C and 3.6 mbar and 0.6% RH, and a new unidentified phase was formed; rhomboclase was destabilized at 20 °C and 3.6 mbar and 0% RH; kornelite, paracoquimbite, ferric sulfate pentahydrate and the amorphous ferric sulfate remained stable at 25 °C and $P \leq 6$ mbar for at least 10 hours. These results suggest ferricopiapite and rhomboclase, if present in Martian equatorial regions where temperature may reach above 0 °C during summer time, may be dehydrated to form other ferric sulfate phases not recorded in the present database. The new phases need to be further characterized in future work.

5.1. Introduction

The phase evolution maps based on results reported in Chapter 2 to 4 yield a rich set of results pertaining to the ferric sulfates phase diagenesis as a function of T and RH. However, these studies were performed at conditions of terrestrial atmospheric pressure and temperature above 0 °C. On Mars, atmospheric pressure is around 6 mbar; temperatures range from -150 °C to 20 °C depending on latitude, season and time of a day. The differences between the actual Martian environment and the simulated environment add difficulties in application of the laboratory results to interpreting or predicting the mineral phases on Mars. Clearly, the results reported in Chapter 2 and 3 need to be tested under conditions relevant to current Martian conditions.

Creating simultaneous low P, low T and controlled and measurable RH environments is particularly challenging at today's technology (Cloutis et al., 2007). One practical solution is to inject pure water vapor to the system while measuring the pressure of water vapor so that the RH can be calculated. This method was applied using the vacuum line setup to study the stability of rhomboclase, as described in Chapter 4. One difficulty with this setup is to cool the whole vacuum line down to a practical temperature relevant to Mars' surface. An alternative approach is to seal a sample vial, remove it from the vacuum line and store in a freezer. Repeatedly reconnecting the sample vial to the vacuum line day after day in order to make an approximation to an open system would inevitably raises complications such as the influence of temperature fluctuations. In this study, a new T and P - controlled *in situ* powder X-ray diffraction method was developed on the Rigaku Ultima diffractometer, and used to investigate the stability of

several important ferric sulfates at low T and low P that are typical of present conditions on Martian surface.

5.2. Experimental Methods

5.2.1. (T, P)-controlled *in situ* XRD

The *in situ* XRD experiments were performed on the Rigaku Ultima-IV diffractometer using Cu*K*α radiation (λ = 1.54178 Å). It is equipped with a one-dimensional X-ray detector working in Fe fluorescence reduction mode. A low-T stage is incorporated so that the samples can be cooled to as low as liquid N_2 temperature (-180 °C) under vacuum (Fig. 5.1). Powder samples are loaded into a copper sample holder that has a high thermal conductivity to allow quick transfer of heat from the sample. The thermocouple is shallowly buried into the copper stage in contact with the sample holder placed right on it. After loading the sample, the sample stage was enclosed in an aluminum cover used to enhance cooling performance (Fig. 5.1b). Liquid N_2 is injected from the back of the diffractometer to cool the stage, the aluminum cover and the sample. For the best cooling performance, a vacuum environment is required to avoid the heat transferring from the surrounding air to the sample. The vacuum is achieved with a cap sealing the sample stage connected to an air pump (Fig. 5.1c). X-ray windows on the cap are made of aluminum foil.

For the purpose of simulating a low-P (not vacuum) and open environment, the above set up was slightly modified. A digital air pressure meter was connected to the chamber through the gas release port at the bottom of the cap, so that the air pressure

inside the chamber could be monitored (Fig. 5.1c). The chamber was not fully sealed when the pressure meter was installed. An air flow rate of 2 cc/min into the chamber was estimated when the inside air pressure was below 100 mbar, based on measurement of the chamber volume and the recovery time from 0 mbar to 100 mbar. The target P in the chamber was achieved by adjusting the valve on the tube connected to the pump: a more open valve would result in lower P. During experiments, XRD patterns were continuously collected from 4° to 30° of 2-theta at a scanning speed of 0.5 °/min. Each scan took 52 minutes plus an interval time of 6 minutes between scans. The RH and T inside the diffractometer hutch were also recorded.

5.2.2. Sample preparation

Ferric sulfate samples were prepared by dehydrating ferric sulfate solution at different RH and T using the humidity buffer method introduced in Chapter 2. The sample of ferricopiapite ($Fe_{4.67}(SO_4)_6(OH)_2 \cdot 20H_2O$) mixed with rhomboclase ($(H_5O_2^+)Fe(SO_4)_2 \cdot 2H_2O$) and paracoquimbite ($Fe_2(SO_4)_3 \cdot 9H_2O$) was obtained by evaporating concentrated $Fe_2(SO_4)_3$ solution (40 wt. %) at 50 °C and 46% RH for 30 days. The amorphous ferric sulfate was prepared by dehydrating $Fe_2(SO_4)_3$ solution at 25 °C and 11% RH for 7 days. The mixture of pentahydrate ($Fe_2(SO_4)_3 \cdot 5H_2O$) and kornelite ($Fe_2(SO_4)_3 \cdot 7.25H_2O$) was prepared by heating the amorphous ferric sulfate hydrate to 90 °C in a sealed Teflon bottle for 5 days.

5.3. Results

5.3.1. Ferricopiapite, rhomboclase and paracoquimbite

The sample containing these three phases remained at -30 °C and low P for a total of 30 hours: 20.0 mbar for 10 hours, 8.3 mbar for 10 hours and 3.6 mbar for 10 hours. Figure 5.2 shows four patterns collected at the start of the experiment and at the end of each pressure step. A slight shift of the ferricopiapite peaks toward high 2-θ angles was observed at P = 3.6 mbar. The shift of the ferricopiapite (020) peak is 0.04°, small but clearly observed as it moved rightward and merged under the left shoulder of the paracoquimbite (102) peak (Fig. 5.2). The shift of peaks to higher angle indicated a contraction of the ferricopiapite unit cell, which might be caused by dehydration at this pressure (P = 3.6 mbar). The bulk structure of the ferricopiapite did not change.

The sample then warmed as the flow of liquid N_2 was stopped. The pressured was kept at 3.6 mbar. Figure 5.3 shows the recorded XRD patterns. Pattern (d) is the last scan before the warming sequence began. It is same as the pattern labeled (d) in Figure 5.2. Pattern (e) is the first scan collected while the sample T increased to 9.1 °C. Notice the drop of the ferricopiapite (1-40) peak at 2θ = 21.5° from pattern (d) to pattern (e), indicating decomposition of the ferricopiapite. The sample temperature at this point was 6.0 °C. So the ferricopiapite was not stable at P = 3.6 mbar and T = 6.0 °C. In the next scan, pattern (f), the ferricopiapite was seen fully decomposed and turned amorphous. Meanwhile, some weak peaks showed up but could not be related to any known ferric sulfate phases. These unidentified peaks include: U-1 at 2θ = 11.8°, U-2 at 2θ = 13.4° and U-3 at 2θ = 17.1°. Rhomboclase peaks intensities started to decrease in the third scan when T was increased to above 20 °C. The rhomboclase (020) peak was about ¼ of the

initial intensity after 15 hours staying at room temperature (25 °C), as shown in pattern (h). The paracoquimbite remained unchanged in the whole experiment.

5.3.2. Pentahydrate and kornelite

The pentahydrate and the kornelite were subjected to a similar low-T and low-P process as described above and did not show any sign of decomposition (Fig. 5.4). The sample was cooled to -30 °C, maintained under these conditions for 22 hours. It was then heated to 0 °C and maintained under this condition for 10 hours, and finally it was allowed to warm to room T (24.8 °C) and maintained for another 13 hours. The air pressure was kept at 6.0 mbar during the whole experiment. A peak at $2\theta = 9.7°$ appeared soon after the beginning of the experiment, and reached its maximum intensity after 4 hours, though still very weak (Fig. 5.4). During the rest of the experiment, this peak remained at a stable intensity until it was apparently reduced when the sample was warmed to room temperature. This new peak could possibly be the rhomboclase (020) peak. To be cautious, this peak was still marked as unidentified (U-4) in Figure 5.4. It should be noted that this unidentified phase was not transformed from the pentahydrate or the kornelite, whose peaks remained unchanged during the whole experiment. If it is a transformation from either of these two phases, the growth of the new phase should not be expected to stop after 4 hours while P/T conditions were not changed. It is most likely that this new phase formed from a small amount of amorphous material in the starting sample, which means the starting sample was not purely a mixture of kornelite and pentahydrate as expected.

5.3.3. Amorphous ferric sulfate

The amorphous ferric sulfate remained after 20 hours at -30 °C and another 13 hours at room T (24.7 °C), as shown in Figure 5.5. Pressure was maintained at 6 mbar during the experiment.

5.4. Discussion

5.4.1. Calculation of water vapor pressure and RH

The stability of a hydrated mineral with respect to a gas is governed by the water vapor pressure in the gas phase, assuming the gas is not reactive and the mineral stability is only affected by hydration or dehydration. In this study, the water vapor pressure in the sample chamber was not directly measured, by could be derived from the measured total air pressure and RH based on the following equation:

$$e_s = e_w(T_h) \cdot RH_h \cdot P_s / P_0 \qquad \text{(Eq. 5.1)}$$

In the above, e_s is the water vapor pressure inside the sample chamber. $e_w(T_h)$ is the saturated vapor pressure at T_h --- the temperature in the diffractometer hutch. RH_h is the measured relative humidity in the diffractometer hutch. The product of these two, $e_w(T_h) \cdot RH_h$, is the water vapor pressure in the diffractometer hutch. P_s is the measured pressure in the sample chamber. P_0 is the atmospheric pressure, equal to 1013 mbar. In calculation of $e_w(T_h)$, the following empirical equation from Buck (1981) was used:

$$e_w(T_h) = (1.0007 + 3.46 \times 10^{-6} P_0) \times 6.1121 \exp\left(\frac{17.502 T_h}{240.97 + T_h} \right) \qquad \text{(Eq. 5.2)}$$

With the value of e_s obtained, we calculate the RH inside the aluminum cover by dividing e_s by the saturated vapor pressure, $e_i(T_s)$. The equation used to calculate $e_i(T_s)$ is listed below, and is also given by Buck (1981).

$$e_i(T_s) = (1.0003 + 4.18\times10^{-6} P_s) \times 6.1115 \exp\left(\frac{22.452 T_s}{272.55 + T_s}\right) \quad \text{(Eq. 5.3)}$$

T_s in the above equation is the air temperature inside the aluminum cover (Fig. 5.1b). In practice, the sample temperature was used (e.g. -30 °C). This assumes the air in the aluminum cover reached the temperature of the sample. Table 5.1 listed the P/T conditions and the calculated RH for the experiments. The experimental observations can now be correlated with RH. At -30 °C, the hydration state of the ferricopiapite was maintained at above 35% RH; the slight dehydration occurred at 15% RH (Fig. 5.2). Upon increasing temperature, the ferricopiapite decomposed at 6 °C and 0.6% RH and the unknown ferric sulfate phase(s), indicated by peak U-1, U-2 and U-3, began to grow (Fig. 5.3). The rhomboclase decomposed at 20 °C and 0% RH. The paracoquimbite, pentahydrate, kornelite and the amorphous ferric sulfate were apparently stable at the conditions listed in Table 5.1 (Fig. 5.4 and Fig. 5.5).

5.4.2. Implications for Martian ferric sulfates

Ferricopiapite has been proposed as a ferric sulfate species contained in Paso Robles soils in Gusev crater (Bishop et al., 2008; Johnson et al., 2007) and in sulfate sediments in and nearing Valles Marineris (Bishop et al., 2009; Mangold et al., 2008; Milliken et al., 2008). As shown in this study, ferricopiapite dehydrates and transforms to an unidentified phase, when the surface temperature is above 6 °C and the humidity is below 15%, a condition present on the surface of current Mars (Fig 5.3). However,

whether this dehydration process actually occurred on Mars can not be confirmed, until the unidentified phase is better characterized, especially with infrared (IR) spectroscopy, the spectroscopic method used in most remote sensing rovers to Mars in commission.

Rhomboclase and paracoquimbite were also suggested as candidate components in Paso Robles soils based on the visible to infrared spectra from the Spirit Rover (Johnson et al., 2007). According to this study, rhomboclase decomposes and transforms to an amorphous state at 0% RH and around 20 °C (Fig. 5.3). Rhomboclase was also found to dehydrate to form crystalline $(H_3O)Fe(SO_4)_2$ at RH below 4% at 20 °C in a previous experiment (see Fig. 4.4 in Chapter 4). The different dehydration products, the amorphous material versus crystalline $(H_3O)Fe(SO_4)_2$, are probably due to the slight difference in RH, where the vacuum set up in this study could effectively draw the RH down to zero, while the range of RH < 1% was not covered using the humidity generator in the previous study. The dehydration of rhomboclase to crystalline $(H_3O)Fe(SO_4)_2$ or further to the amorphous state is possible on Mar during summer afternoons when the dehydration RH and T conditions may be satisfied. Paracoquimbite showed no change in the studied conditions, and would probably remain unchanged if present on Mars.

References:

Bishop, J.L., Lane, M.D., Dyar, M.D., Parente, M., Roach, L.H., Murchie, S.L., and Mustard, J.F. (2008) Sulfates on Mars: How recent discoveries from CRISM, OMEGA and the MERs are changing our view of the planet. Geochimica Et Cosmochimica Acta, 72(12), A86-A86.

Bishop, J.L., Parente, M., Weitz, C.M., Dobrea, E.Z.N., Roach, L.H., Murchie, S.L., McGuire, P.C., McKeown, N.K., Rossi, C.M., Brown, A.J., Calvin, W.M., Milliken, R., and Mustard, J.F. (2009) Mineralogy of Juventae Chasma: Sulfates

in the light-toned mounds, mafic minerals in the bedrock, and hydrated silica and hydroxylated ferric sulfate on the plateau. Journal of Geophysical Research-Planets, 114, E00D09, DOI: 10.1029/2009JE003352.

Buck, A.L. (1981) New Equations for Computing Vapor-Pressure and Enhancement Factor. Journal of Applied Meteorology, 20(12), 1527-1532.

Cloutis, E.A., Craig, M.A., Mustard, J.F., Kruzelecky, R.V., Jamroz, W.R., Scott, A., Bish, D.L., Poulet, F., Bibring, J.P., and King, P.L. (2007) Stability of hydrated minerals on Mars. Geophysical Research Letters, 34, L20202, DOI: 10.1029/2007GL031267.

Johnson, J.R., Bell, J.F., Cloutis, E., Staid, M., Farrand, W.H., Mccoy, T., Rice, M., Wang, A., and Yen, A. (2007) Mineralogic constraints on sulfur-rich soils from Pancam spectra at Gusev crater, Mars. Geophysical Research Letters, 34, L13202, DOI: 10.1029/2007GL029894.

Mangold, N., Gendrin, A., Gondet, B., LeMouelic, S., Quantin, C., Ansan, V., Bibring, J.P., Langevin, Y., Masson, P., and Neukum, G. (2008) Spectral and geological study of the sulfate-rich region of West Candor Chasma, Mars. Icarus, 194(2), 519-543.

Milliken, R.E., Swayze, G.A., Arvidson, R.E., Bishop, J.L., Clark, R.N., Ehlmann, B.L., Green, R.O., Grotzinger, J.P., Morris, R.V., Murchie, S.L., Mustard, J.F., and Weitz, C. (2008) Opaline silica in young deposits on Mars. Geology, 36(11), 847-850.

Table 5.1. T, P and RH conditions for the three experiment runs

Step / elapse(hours)	T_s (°C)	P_s (mbar)	T_h (°C)	RH_h (%)	Calculated RH (%)
		Ferricopiapite, rhomboclase and paracoquimbite			
1 / 10	-30.0	20.0	24.7 – 25.4	53 – 58	86 – 98
2 / 10	-30.0	8.3	24.6 – 24.9	52 – 54	35 – 37
3 / 10	-30.0	3.6	24.8 – 24.9	50 – 55	15 – 16
4 / 20	-30.0 to 24.9	3.6	24.8 – 24.9	52 – 53	16 to 0
		Pentahydrate and kornelite			
1 / 22	-30.0	6.0	24.0 – 24.8	51 – 57	24 – 28
2 / 10	0	6.0	24.8 – 24.9	53 – 54	1.6 – 1.7
3 / 13	0 to 24.9	6.0	24.8 – 24.9	53 – 54	1.7 to 0
		Amorphous ferric sulfate			
1 / 20	-30.0	6.0	23.6 – 24.0	60 – 63	27 – 29
2 / 13	-30.0 to 24.7	6.0	24.0 – 24.7	60 – 63	29 to 0

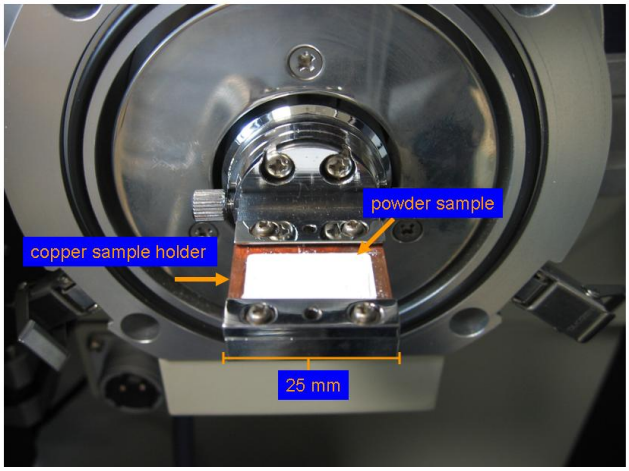

a

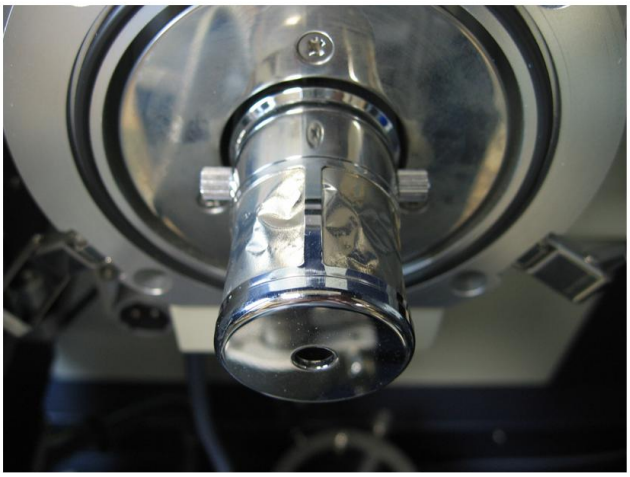

b

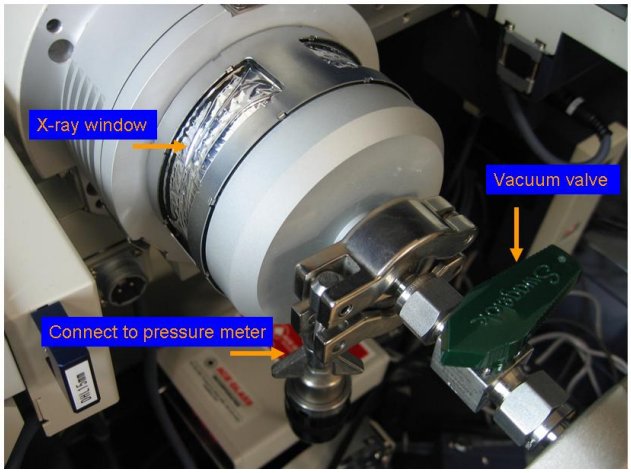

c

Figure 5.1. The low-T and low-P setup on the diffractometer. **a**, sample stage; **b**, sample stage enclosed in an aluminum cover; **c**, the pressure meter and the vacuum pump connected to the stage.

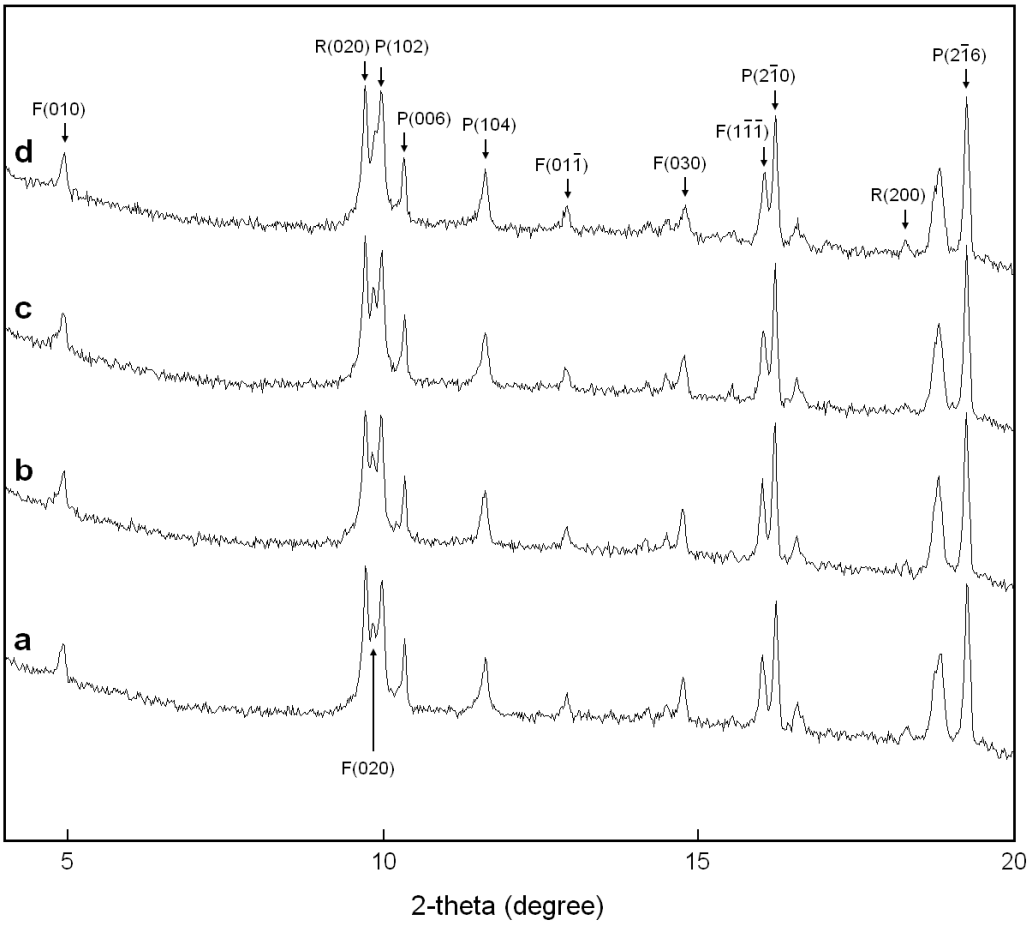

Figure 5.2. XRD patterns of ferricopiapite, rhomboclase and paracoquimbite at -30 °C and low P: (a) the 1st scan at P = 20.0 mbar; (b) the 10th scan after 10 hours at P = 20.0 mbar; (c) the 20th scan after another 10 hours at P = 8.3 mbar; (d) the 30th scan after another 10 hours at P = 3.6 mbar. Some peaks are marked with mineral name initials (**R** for rhomboclase, **P** for paracoquimbite, **F** for ferricopiapite) and miller indices. CuKα radiation was used.

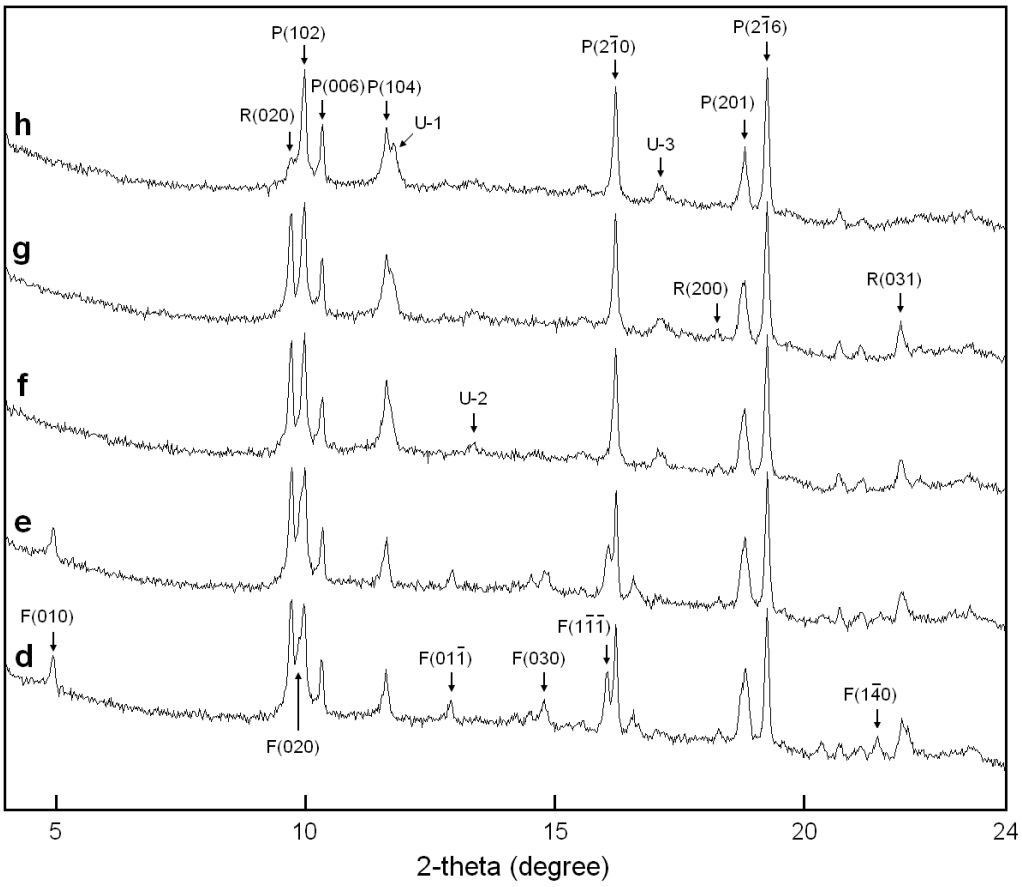

Figure 5.3. XRD patterns of the sample recorded during the natural warming process at P = 3.6 mbar: (d) before the warming process, the same (d) pattern shown in Figure 5-1; (e) the 1st scan with T increased from -27.2 °C to 9.1 °C; (f) the 2nd scan with T increased from 12.0 °C to 20.0 °C; (g) the 3rd scan with T increased from 20.5 °C to 22.7 °C; (h) the 15th scan, T at 24.5 °C. Some peaks are marked with mineral name initials (**R** for rhomboclase, **P** for paracoquimbite, **F** for ferricopiapite) and miller indices. Unidentified peaks are labeled as U-1, U-2 and U-3.

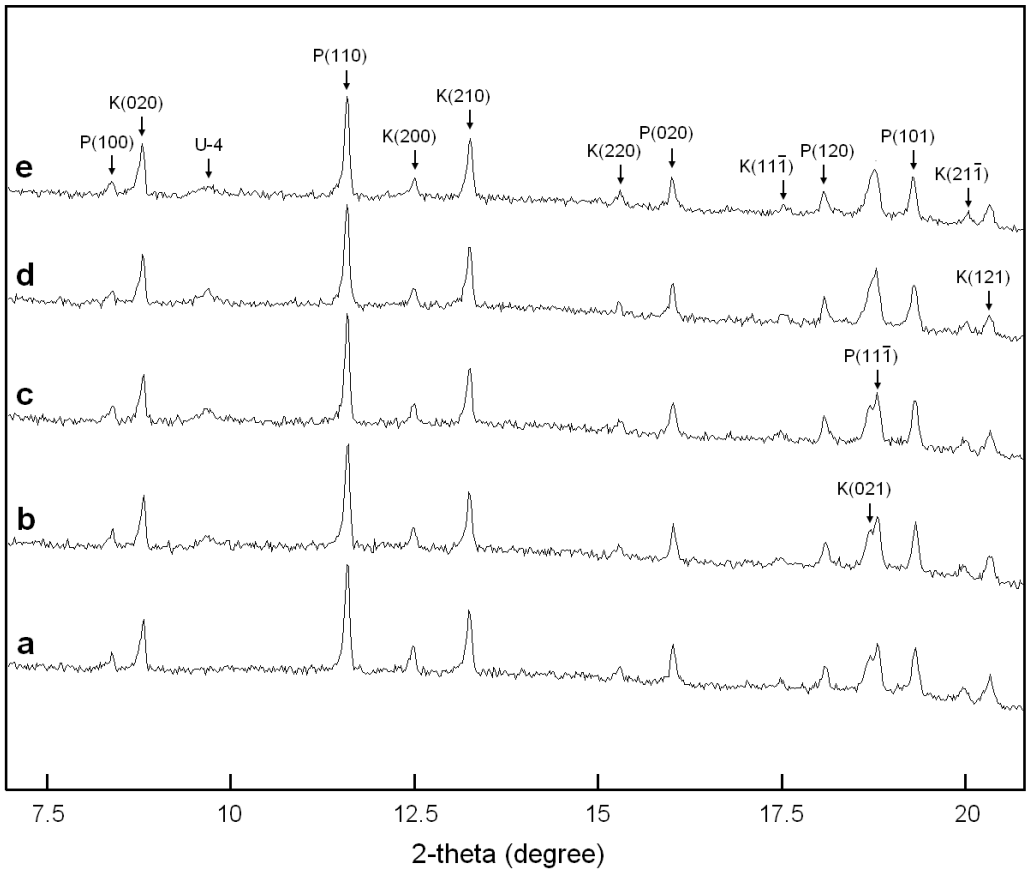

Figure 5.4 XRD patterns of the pentahydrate and the kornelite at 6.0 mbar and -30 °C to room T: (a) the 1st scan at T = -30 °C; (b) the 5th scan after 4 hours at T = -30 °C; (c) the 22nd scan after 21 hours at T = -30 °C; (d) the 32nd scan after anther 10 hours at T = 0 °C; (e) the 45th scan after another 13 hours at room T. Some peaks are marked with mineral name initials (**K** for kornelite, **P** for pentehydrate) and miller indices. U-4 marks an unidentified peak.

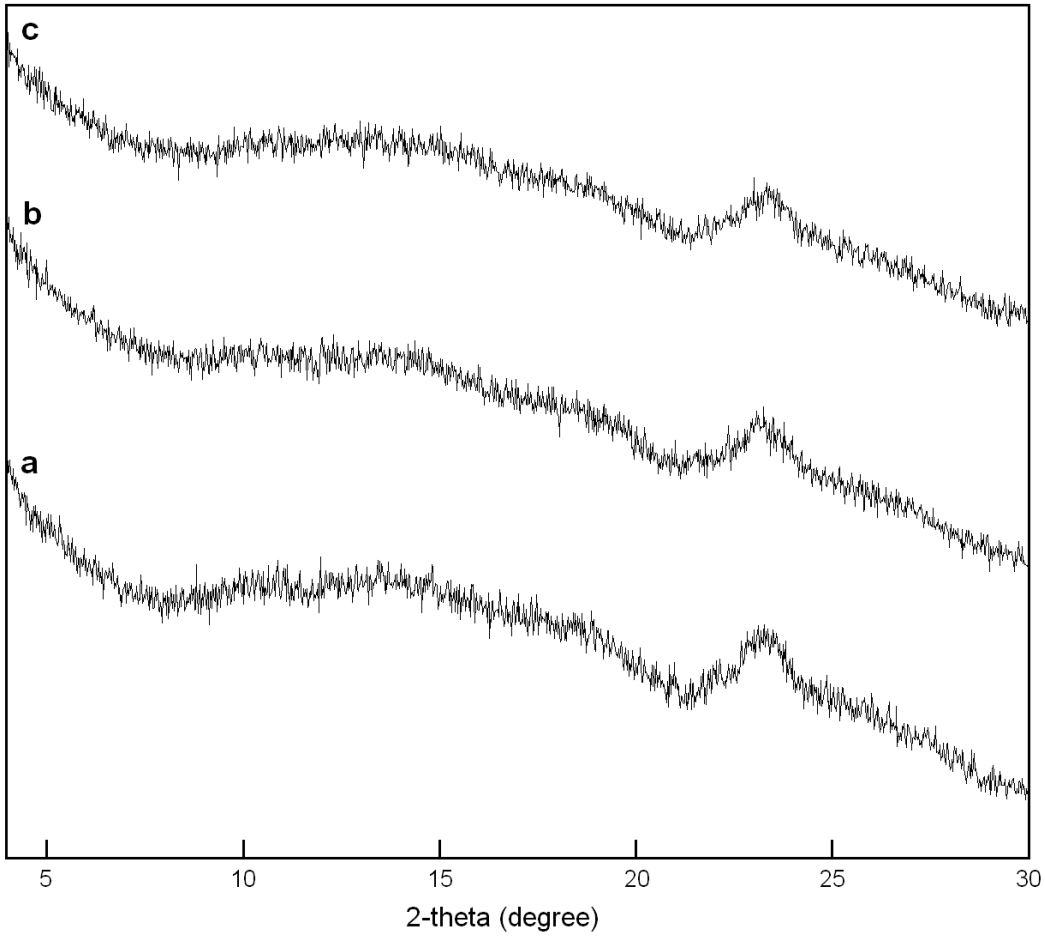

Figure 5.5 XRD patterns of the amorphous ferric sulfate at 6.0 mbar and -30 °C and room T: (a) the 1st scan at T = -30 °C; (b) the 20th scan after 19 hours at T = -30 °C; (c) the 33rd scan after another 13 hours at room T.

Chapter 6

Structural Water in Ferrihydrite and Constraints This Provides on Possible Structure Models

This Chapter published as:

Xu, W.Q., Hausner, D.B, Harrington, R., Lee, P.L., Strongin, D.R. and Parise, J.B. (2011) Structural water in ferrihydrite and constraints this provides on possible structure models. American Mineralogist, in press.

Abstract

Ferrihydrite, a nanocrystalline ferric oxyhydroxide, is ubiquitous on Earth and has been positively identified on Mars. The dry thermal transformation of ferrihydrite to hematite was investigated using combinations of thermogravimetric (TG) and differential scanning calorimetric (DSC) analysis, along with *in situ* DSC and pair distribution function (PDF) analysis of X-ray total scattering data and *in situ* temperature controlled infrared (IR) spectroscopy. TG data show a 25.6 ± 0.1% weight loss below 300 °C, ascribed to the removal of surface water since PDF analysis shows no change in the structure of ferrihydrite up to this temperature. The transformation to hematite occurs at a DSC peak temperature of 415 ± 1 °C at a heating rate of 10 °C/min, with no obvious weight change during or after the transformation. *In situ* PDF analysis indicates the ferrihydrite bulk structure remained intact up to the direct transition to crystalline hematite, with no intermediate phases, crystalline or amorphous, formed. *In situ* IR data

shows the extent of absorption attributable to OH stretching in ferrihydrite at 215 °C dropped to 10% of its room temperature value. These results suggest ferrihydrite contains very little structural OH: the molar ratio of OH/Fe is 0.18 ± 0.01. A recently proposed akdalaite-like ferrihydrite model has an OH/Fe equal to 0.2, consistent with this result. The 3-phase model proposed by Drits et al has an average formula close to FeOOH, with an OH/Fe equal to 1.0, far more than suggested by our experiments. Based on the constraints set by the estimated water content and the PDF signatures, we examined possible anion packing types and local structural motifs in ferrihydrite, and demonstrate that ABAC is the only feasible packing type and that a peak at 3.44(2) Å in PDF provides indirect evidence for the presence of tetrahedral Fe.

6.1. Introduction

Ferrihydrite is a widely occurring nanocrystalline iron oxyhydroxide mineral, also referred as "colloidal ferric oxide", "ferric hydroxide" and "hydrous ferric oxide" in the literature. Found in weathered rocks and sediments, ferrihydrite plays a crucial role in iron cycling on earth and controls the iron concentration in aquatic systems: it forms as the immediate precipitate by fast polymerization and nucleation of hydrolyzed ferric ions as pH increases (Schwertmann et al., 1999). Ferrihydrite is often a precursor to more crystalline iron oxides and oxyhydroxides such as hematite (α-Fe_2O_3) and goethite (α-FeOOH) (Schwertmann et al., 1999). The presence of ferrihydrite on Mars has been suggested in previous studies (Bishop et al., 1993; Klingelhofer et al., 2004), and may have a diagenetic relationship with ferric sulfates such as schwertmannite (Tosca et al.,

2008). Ferrihydrite has a large surface area and strong affinity for a wide range of metal ions, so it functions as a sorbent of toxic contaminants such as Pb, Cd, and As (Jambor and Dutrizac, 1998; Harrington et al., 2010). In industry, ferrihydrite is used in catalysis and metallurgical processing (Jambor and Dutrizac, 1998). Ferrihydrite is also believed to form the core of ferritin, a biological iron storage protein (Harrison et al., 1967), although positive structural characterization of the ferritin core is lacking.

Despite its importance to industry and environment remediation, the structure of ferrihydrite has been an issue of debate for a long time. Several chemical formulae for ferrihydrite have been reported, including widely cited ones such as $5Fe_2O_3 \cdot 9H_2O$ (Schwertmann and Cornell, 1991) and $Fe_5HO_8 \cdot 4H_2O$ (Towe and Bradley, 1967). Due to its nanocrystallinity, a clear structure determination from the broad Bragg reflections in the X-ray diffraction (XRD) pattern has proved difficult and controversial. Ferrihydrite is conventionally named as "2-line" or "6-line" based on the number of characteristic broad Bragg peaks in the XRD pattern. The XRD peak positions are reproduced by a hexagonal unit cell (a = 5.08 Å, c = 9.4 Å) with closest packing of anions (Towe and Bradley, 1967). In other proposed cells, 2.96 Å and 5.95 Å are used for the length of **a** (Harrison et al., 1967; Eggleton and Fitzpatrick, 1988; Michel et al., 2007a), but they are inherently related by a sub- or super-lattice relationship (Drits et al., 1993). Drits et al. (1993) evaluated previous models based on the similarity of the simulated and experiment XRD patterns and extended X-ray absorption fine structure (EXAFS) data (Manceau and Drits, 1993), proposing a three-component model containing a defect-free ferrihydrite, a defective ferrihydrite and an ultradispersed hematite phase. These authors suggested the dimension of coherent scattering domains

(CSD) as the main difference between the 2-line and 6-line ferrihydrite. The structural similarity of 2-line and 6-line variants of ferrihydrite and the CSD difference was confirmed by transmission electron microscopy (TEM) and pair distribution function (PDF) analysis of X-ray total scattering data (Michel et al., 2007b).

Prior tests of proposed structure models for ferrihydrite have attempted to fit laboratory-based diffraction data and concentrated on fitting the Bragg data alone, including the peak broadening. Generally the peaked elastic diffuse scattering contributions from atoms in the nano-particle scattering coherently is difficult to distinguish from the inelastic scattering and other diffuse scattering that is usually folded into the background corrections. Fitting just to the Bragg component inherently limits our ability to discriminate between competing models for the atomic arrangements when the observed data to parameters needed to describe the model is small, as they are in the case of ferrihydrite where some proposed models are multi-phasic.

In principle, the total elastic scattering (Bragg + diffuse) contains all elastic scattering from relevant short, intermediate and long-range atom correlations. The pair distribution function, G(r), is derived by Fourier transforming the experimentally observed total structure factor (Waseda, 1980), S(Q), derived from the normalized observed total elastic scattering: $G(r)_{exp} = (2/\pi) \int Q[S(Q) - 1]sin(Qr)dQ$, where Q is the magnitude of the wave vector, $Q = 4\pi\sin\theta/\lambda$. This is an experimentally observable function. The atomic PDF is defined as $G(r)_{model} = 4\pi r[\rho(r)-\rho_0]$ where $\rho(r)$ and ρ_0 are the local and average atomic number densities, respectively, and r is the radial distance. $G(r)_{model}$ is the probability of finding an atom at a distance r from a reference atom weighted by the number of interatomic distances and the relative scattering power of the

atoms involved. This quantity can be derived from a model of proposed atomic arrangements and can be compared to the $G(r)_{exp}$ derived experimentally. Full-profile fitting of the PDF has proven to be a powerful technique; it is used routinely to test proposed models for atomic arrangements in nano-crystalline materials and serves as a basis for structure refinement (Proffen and Billinge, 1999; Petkov et al., 2002; Billinge and Kanatzidis, 2004). Specifically for ferrihydrite, the PDF is a real space 1-D map of interatomic distances that is more information rich than the 2- or 6-line XRD pattern. Because it inherently has a higher data to parameter ratio than when Bragg data alone are considered, the PDF is more sensitive to dramatic differences in proposed models and can be fitted with appropriate models with a high level of confidence. PDF has a proven track record in discerning the structure of nanoparticles (Michel et al., 2005; Paglia et al., 2006; Billinge, 2008; Petkov et al., 2009).

Michel et al (2007) found that the PDF calculated from the three-component model of Drit's et al (1993) – designated as the D-model here – did not reproduce the experimental PDF measured from ferrihydrite prepared by several techniques. Instead a new single phase model (Michel et al., 2007a) – the M-model – with an ideal formula $Fe_{10}O_{14}(OH)_2$, structurally similar to a natural alumina hydrate, akdalaite ($Al_{10}O_{14}(OH)_2$) was proposed. The PDF derived from this model reproduces features of the experimental PDF very well. This new model is refuted (Rancourt and Meunier, 2008; Manceau, 2009; Hiemstra and Van Riemsdijk, 2009), with one debate centering on the presence, absence and extent of tetrahedral Fe (tet-Fe) in ferrihydrite. While the M-model contains 20% of Fe in tetrahedral sites, previous X-ray absorption near edge structure (XANES) and extended X-ray absorption fine structure (EXAFS) studies tend to dismiss the existence

of tet-Fe (Manceau and Drits, 1993, Manceau and Gates, 1997), although the presence of tet-Fe on the surface has been shown to be a possibility (Zhao et al., 1994).

Besides tet-Fe, a major difference between the D- and M-models concerns the amount of structural OH: the D-model has a molar ratio of OH/Fe roughly equal to 1.0, while this ratio for the M-model is 0.22. Thus, accurately measuring the amount of structural OH in ferrihydrite, as opposed to surface absorbed water, is critical in constraining possible structure models. Studies in the last few decades did not clarify this issue but rather led to more open questions. Towe and Bradley (1967) found the absence or limited amount of hydroxyl water by IR and DTA and believed water in ferrihydrite existed as either absorbed or chemically combined molecular water. Their IR measuring procedure, involving the use of KBr disks, was later questioned by Russell (1979), who found the amount of OH groups in ferrihydrite was about half of the amount in akaganeite (β-FeOOH). Stanjek and Weidler (1992) dehydrated ferrihydrite without transformation to a more crystalline phase, although the humps in their XRD patterns became a little sharper, and derived a formula of $Fe_{1.75}O_{2.26}(OH)_{0.74}$ with the OH/Fe ratio equal to 0.42. Childs et al (1993) questioned the necessity of H_2O and OH in ferrihydrite at all, based on the observation that the OH/Fe ratio could be reduced to less than 0.1 with no phase change being manifested in the XRD pattern. Weidler (1997) reported that under low humidity condition a small portion of ferrihydrite (<3%) transformed to hematite and goethite after hours of heating at 170 °C, while high humidity would accelerate the transition. Hiemstra and Van Riemsdijk (2009) developed a surface structural model for ferrihydrite and estimated the ferrihydrite core had an average composition close to FeOOH, with a mass density about 4.15 g/cm^3, consistent with the

D-model, but less than the 4.9 g/cm^3 calculated from the M-model. Most recently, Michel et al (2010) revised the M-model by inserting 45 - 50% vacancy to the Fe2 and Fe3 sites. Those vacancies were suspected to be filled with protons as hydroxyls to balance the total charge. The revised model has a formula $Fe_{8.2}O_{8.5}(OH)_{7.4} \cdot 3H_2O$, satisfying the above estimated density. Michel et al (2010) also found the vacancy defects could be filled by hydrothermal treatment of a citrate-containing ferrihydrite suspension, producing a low-defect phase named "ferrifh", having the same ferrihydrite structure with the Fe sites almost fully occupied.

In this study, we investigate the dry transformation of 2-line ferrihydrite to hematite using thermogravimetric and differential scanning calorimetric analysis (TG and DSC), temperature controlled infrared spectroscopy and an *in situ* DSC-PDF method. These techniques allow us to follow the reaction in an attempt to quantify the amount of structural H_2O/OH in ferrihydrite and provide further constraints on the ferrihydrite structural model. It should be noted that using the *in situ* DSC-PDF method has an advantage over traditional XRD method on studying the ferrihydrite transformation. If ferrihydrite transforms to an intermediate nanocrystalline phase before changing to hematite, it would be difficult for XRD to characterize or even to detect this phase, because the structural change will be reflected by the change of diffuse scattering signatures mostly immersed in the background. XRD using Cu radiation generally resolves to Q = 6 Å^{-1} range, insufficient to disclose detailed local structure information. PDF analysis uses total scattering data with Q up to 25 - 30 Å^{-1}, especially sensitive to subtle structural changes in local (< 5 Å) and intermediate (< 15 Å) range.

6.2. Experimental Methods

Samples of 2-line ferrihydrite were prepared by modification of the method of Schwertmann and Cornell (1991). Briefly, 0.1 M solutions of anhydrous ferric chloride were neutralized using 1 M sodium hydroxide solution, resulting in the formation of a suspension of 2-line ferrihydrite. Samples were centrifuged and washed with deionized water (18 MΩ) then dried at room temperature. Ferrihydrite samples were characterized by XRD and TEM. XRD showed two broad diffraction maxima corresponding to d-spacings of approximately 0.25 and 0.15 nm. TEM confirmed that the 2-line particles were nominally 2 nm in diameter.

TG and DSC measurement was performed on a Netzsch STA 449C Jupiter® simultaneous TG-DSC apparatus. Samples loaded in alumina crucibles were heated from room temperature to 1000 °C at a rate of 10 °C/min under nitrogen flow.

In situ DSC-PDF measurements were preformed using a modified Linkam® DSC 600 device mounted on synchrotron beamline 1-ID-C at the Advanced Photon Source (APS) at Argonne National Laboratory, IL (Fig. 6.1). Designed for operating with an optical microscope, the DSC furnace has a 2 mm hole in the center of both the cover and the bottom. The furnace is enclosed in an aluminum stage by removable lids at both sides with glass windows. During data collection, both glass windows were removed and a 3 mm hole was drilled in the base of the aluminum crucible to allow X-ray access to the sample and to avoid parasitic scattering. The sensitivity of DSC measurement is inevitably degraded due to air convection. However, the DSC measurements made concurrently with collection of the total scattering data does allow us to correlate changes

in the more precise measurements in the laboratory apparatus with measurements at the APS.

For measurements at the beamline, finely powdered ferrihydrite samples were packed in a 5.5 mm long Kapton® capillary capped with glass wool at both ends (Fig. 6.1). The length of the capillary matched the aluminum crucible diameter so that the specimen was locked at the center of the crucible. It should be noted that locking the capillary in the crucible did not seal the sample, nor did the glass wool seal the sample. Water vapor was free to escape out of the capillary upon heating. When closed, the furnace cover added a gentle press to the crucible, which ensured an intimate contact between the crucible and the DSC element in the base. Samples were heated to 380 °C at a rate of 4 °C/min and held at this temperature for one hour. The 380 °C upper limit was set by the decomposition temperature of Kapton® film (400 °C). For PDF analysis, an empty capillary heated using the above strategy provided the blanks to subtract out contributions from the sample container. Throughout the heating process, 2-dimensional scattering data were collected using an amorphous-Si area detector continuously with a 20 second exposure time per frame (Chupas et al., 2007). The sample-to-detector distance, X-ray beam center and the tilt of the detector relative to the incident beam were calibrated using a CeO_2 standard (NIST diffraction intensity standard set 674a). The X-ray wavelength was 0.1241(2) Å. Raw datasets were converted to a traditional intensity versus 2θ (or Q) plot using the program Fit2D (Hammersley et al., 1996).

The G(r) curves were generated using the program PDFgetX2 (Qiu et al., 2004). This process includes a subtraction of background scattering from the converted raw data (Intensity versus Q), followed by corrections for sample absorption, secondary scattering,

Compton scattering, Laue diffuse scattering and weighting correction to obtain the structure function S(Q). Experimentally, the resolution of G(r) is restricted by the cutoff value of Q for the Fourier transform. In this experiment, data were useable to a Q_{max} of 25 $Å^{-1}$.

In situ IR data were collected using a Golden Gate Attenuated Total Reflectance (ATR) (Specac) accessory capable of heating to 300 °C and a Nicolet 670 spectrometer (Thermo Scientific) equipped with a MCT-detector. Spectra were collected as single beam spectra of 100 co-added scans reprocessed against the clean diamond at the appropriate temperature. Samples were placed on the ATR element at room temperature from solution and dried under a stream of nitrogen using a home built gas flow cell. Flow of dry nitrogen was maintained through heating and drying of the samples.

6.3. Results

TG and DSC

Figure 6.2 shows both the TG and DSC curves for ferrihydrite heated to 1000°C. The endothermic peak below 300 °C corresponding to a weight loss of 25.6 ± 0.1% indicates the removal of surface-adsorbed water without disruption of the ferrihydrite structure (see PDF results below). An exothermic event occurred at 415 ± 1 °C (peak temperature), which is conventionally assigned to the transformation to hematite (Towe and Bradley, 1967). Note there is no apparent abrupt weight loss related to this event. Rather, the total gradual weight loss from 300 °C to 1000 °C is 1.5 ± 0.1% of the initial sample weight, equal to an OH/Fe ratio of 0.18 ± 0.01. Additional DSC data collected *in*

situ on the APS synchrotron beamline (DSC-PDF) showed the first dehydration endotherm (Fig. 6.3), but did not show the exotherm corresponding to the hematite transition as the transition occurred during the 380 °C holding period and went too slowly to be detected by this less sensitive DSC-PDF apparatus. The poorer sensitivity compared to the laboratory instrument is due to the smaller quantity of sample and poor insulation required to allow adequate X-ray access. Despite these difficulties, the recorded temperature profile shows good temperature control throughout the experiment (Fig. 6.3).

Temperature-resolved XRD and PDF

A stack plot of raw *in situ* temperature resolved XRD lines from 30 °C to 380 °C is shown in Figure 6.4. The time interval between two neighboring profiles is about 330 seconds, representing a temperature increase of 21 ~ 22 °C. Reflections assignable to hematite appear at about 380 °C; this is the only crystalline phase formed. Prior to this transition, the only change in the XRD signature of 2-line ferrihydrite is that the two broad reflections become slightly sharper, consistent with previous reports (Stanjek and Weidler, 1992).

Figure 6.5 shows a cascade plot of the reduced PDF as a function of temperature. Up to 380 °C, all the atom pair correlations remain the same, indicating no change of the basic ferrihydrite structure, although slight peak shifts were observed. The shifting of peak apexes was tracked in Figure 6.5b. The peaks at 1.99(2) Å, 3.07(2) Å and 3.44(2) Å are generally assigned to the first shell Fe-O distance, Fe-Fe distance between edge-sharing FeO_6 octahedra, and Fe-Fe distance between corner-sharing FeO_6 octahedra,

respectively. Upon heating, the Fe-O distance shortened slightly. The $d(Fe\text{-}Fe)_{edge}$ increased a little while $d(Fe\text{-}Fe)_{corner}$ decreased. These subtle changes probably reflect minor structural distortions caused by removal of surface water and heating. During the transition to hematite, $d(Fe\text{-}Fe)_{edge}$ was decreased from 3.07(2) Å down to 2.98(2) Å, while the $(Fe\text{-}Fe)_{corner}$ peak split into features at 3.39(2) Å and 3.66(2) Å. In a standard hematite structure, each oct-Fe is surrounded by 1 face-sharing (d = 2.90 Å), 3 edge-sharing (d = 2.97 Å), and 9 corner-sharing oct-Fe (d =3.36 and 3.71 Å). Values in parentheses are calculated based on the known hematite structure (Blake et al., 1966). Due to the limited Q_{max} (25 $Å^{-1}$) available in these experiments, the generated PDFs are not of high enough resolution to distinguish the Fe-Fe distance of face-sharing octahedra from that of edge-sharing ones. The single peak at 2.98 Å represents contributions from both. Therefore, the shift of the $(Fe\text{-}Fe)_{edge}$ peak is probably due to the addition of face-sharing oct-Fe when ferrihydrite transforms to hematite. This indicates that ferrihydrite may normally contain much less face-sharing oct-Fe moieties than the hematite does. It should be noted that the absolute positions of these peaks could be biased by calibration or experimental settings, but the relative movements are reliable since data were collected *in situ* on the same sample and processed in the same manner.

Figure 6.6 is an extension of the PDF data in Figure 6.5a to a higher **r**, in order to follow the changes in crystallinity. The crystallites grew at the beginning of the 380 °C holding period, the same time that the local structure rearranged to hematite. This is consistent with the sole exotherm at 415 °C in the DSC plot (Fig. 6.2). Previous studies have found two exotherms and attributed the latter one to hematite crystallite growth (Campbell et al., 1997).

Temperature-resolved IR

In-situ ATR-FTIR was used to observe the mid infrared OH stretching region. Samples were heated to 215°C, held there for 30 minutes and returned to room temperature. These conditions were chosen based on the results obtained in the DSC-PDF study, in order to dehydrate ferrihydrite while keeping it from transforming to hematite. Figure 6.7 shows the obtained spectra. There is approximately a 90% loss of adsorption area in the spectrum taken at 215°C compared with the spectrum prior to heating.

6.4. Discussion

6.4.1. Water in ferrihydrite

TG and DSC analysis indicated that ferrihydrite lost all water and most hydroxyls prior to the transition to hematite, while the transition itself involved no more than a 2 wt.% change, equal to an OH/Fe ratio of 0.18. The *in situ* PDF study showed the bulk ferrihydrite structure was maintained until its transformation to hematite. This is further confirmed by *in situ* IR measurements with T control, which indicated that approximately 90% of the OH stretch signal is removed at 215 °C where ferrihydrite does not transform to hematite. From these experiments we infer that most of the water associated with ferrihydrite is surface-adsorbed water, and its loss does not affect the basic structure. Structural OH per mole Fe is no more than 0.18. These results do not favor any structural model with an OH/Fe ratio significantly higher than 0.18.

In the D-model (the three-component model), the defective phase has a hexagonal ABACA layer stacking sequence with cavities for water molecules and Fe randomly occupying 50 % of the octahedral sites. This gives a formula $FeOOH \bullet nH_2O$. The defect-free phase is similar to feroxyhite (δ-FeOOH) thus has a formula FeOOH. Both phases have an OH/Fe ratio no less than 1.0. The third component is an ultradispersed phase, which could be nanocrystalline hematite or maghemite. The formula of this third phase should be Fe_2O_3 with no structural water. Since the third component is a minor phase, the mixture of the three should still have an average OH/Fe ratio of about 1.0. This ratio is contradictory to our TG results, which indicate the OH/Fe ratio should be close to 0.18. For comparison, one can check the TG data of goethite (a-FeOOH) in the supporting material of Cole et al (2004), which clearly shows a 10 wt.% drop at the transition point, as predicted by the stoichiometry. The model of Michel et al (2007) has an ideal formula of $Fe_{10}O_{14}(OH)_2$ with an OH/Fe ratio of 0.2, very close to the result in this study.

One issue in the ferrihydrite structural debate is the discrepancy between calculated densities from proposed models and those obtained from experiment. Rancourt and Meunier (2008) pointed out that the M-model has a calculated density of 4.90 g/cm^3, much greater than the measured value of 3.96 g/cm^3 from Towe and Bradley (Rancourt and Meunier, 2008). This discrepancy may be caused by surface-absorbed water, which is not included in the M-model, but based on this study accounts for 25 wt.% of a typical ferrihydrite sample. It is expected that adsorbed water will reduce the bulk density of ferrihydrite compared to the density of the particle core. This effect has also been discussed by Hiemstra and Van Riesmdijk (2009) in their modeling of the

ferrihydrite surface structure. Their study showed the mineral core had a density of 4.15 ± 0.1 g/cm^3, not much higher than the measured value, 3.96 g/cm^3 from Towe and Bradley (1967). Recently, Michel et al (2010) revised the model by incorporating more vacancies in the Fe sites, and proposed a new formula of ferrihydrite core, $Fe_{8.2}O_{8.5}(OH)_{7.4}$. This revised model gives a more consistent density, but also includes more OH in the structure with the OH/Fe ratio reaching 0.90, much higher than the predicted structural OH/Fe ratio (0.18) in this study. Michel et al (2010) also found hydrothermal aging of a citrate-containing ferrihydrite suspension transformed the ferrihydrite to a low-defect "ferrifh" phase. In this process, structural hydroxyls were replaced by iron in the vacant sites. A CSD growth was also indicated by PDF data. This 2-line ferrihydrite → ferrifh → hematite transformation process does not occur in the dry heating of ferrihydrite studied here. Unlike the PDF data in Michel et al (2010) paper showing obvious changes in the short range correlations when ferrihydrite transformed to ferrifh, the *in situ* PDF data in this study did not reveal any pronounced changes in those correlations (Fig. 6.5) or the growth of the CSD (Fig. 6.6) prior to the transformation to hematite.

6.4.2. Structure analysis

Hexagonal close packing of oxygen atoms has been suggested for the ferrihydrite structure from XRD indexing (Towe and Bradley, 1967) and TEM data (Janney et al., 2000; Janney et al., 2001), at least for the major component. Therefore, solving the ferrihydrite structure involves finding a proper anion packing type and then filling the octahedral and tetrahedral interstices created with the stoichiometric amount of Fe atoms.

Starting with a three-layer unit, two packing types are available: ABA and ABC, as shown in Figure 6.8. When filling in Fe atoms, we begin with simplifying assumptions: 1) Fe only goes to octahedral sites, since tet-Fe has not been positively confirmed; 2) oct-Fe coordination polyhedra do not share faces with one another, as face-sharing is not supported by the PDF result.

(1) ABA stacking

Figure 6.8a illustrates three layers in ABA packing. The central O atom has 6 octahedral sites around it, each filled with a Fe atom. At most 3 of the 6 sites can be filled without face-sharing. If every O atom bonds to 3 Fe atoms, extending the ABA 3-layer stack to large particle sizes, say > 100 nm, gives an effectively infinite ABAB sequence and an overall Fe/O ratio equal to ½; if this sequence is finite, say < 2 nm as it might be for ferrihydrite, then the Fe/O ratio is less than ½. So the ideal formula for this stacking sequence is FeOOH. Goethite (α-FeOOH) is an example of this packing type with ½ of the octahedral interstices occupied forming alternating double strips of Fe-O_6 octahedra. As discussed above, the stoichiometry FeOOH contains too much structural OH to explain the experimentally observed TG or IR signatures for ferrihydrite. Reducing the amount of OH requires a higher Fe/O ratio from charge balance consideration. The calculated OH/Fe ratio of 0.18 requires a Fe/O ratio equal to 0.63. Since the coordination number of Fe is set to be 6, oxygen needs to bond with 3.8 Fe atoms on average; this would necessitate face-sharing oct-Fe. So ABA packing is not appropriate.

(2) ABC

Figure 6.8b shows the ABC packing type. Each O atom connects with 6 octahedral sites as in ABA, but none share a face. In the figure only four sites are occupied. With the ABC packing, the required O atom bonding to 3.8 Fe atoms can be easily satisfied, but the ABC packing can not produce the 3.44 Å peak observed in the experimental PDF (Fig. 6.5) for the following reason. There is only one kind of corner-sharing oct-Fe in this packing type, Fe1-O-Fe2, as shown in Figure 6.8b. Ideally, the distance between Fe1 and Fe2 is equal to twice of the Fe-O bond length, which would be 3.9 ~ 4.0 Å. However, the PDF data (Fig. 6.5) have the corner-sharing peak at 3.44 Å. At 4 Å in the PDF is a negative peak, indicating a pair-electron density much lower than the average. So ABC packing is not appropriate.

Based on the preceding discussion both packing types are rejected. This is not possible as any three adjacent layers must fall into one type or the other. It can only be that one or both of our limiting assumptions, that tetrahedral Fe-coordination is not present and that there is no polyhedral face sharing, are incorrect. Face-sharing oct-Fe appeared in the double-chain structure model proposed by Janney et al (2000). But the current *in situ* PDF data provide strong evidence that face-sharing oct-Fe in not present in ferrihydrite. The remaining explanation, the presence of tet-Fe, produces the required Fe/O ratio.

The Fe-Fe peak at 3.44 Å in the PDF (Fig. 6.5) can be produced by three types of corner-sharing configurations, as shown in Figure 6.9. Two require the presence of tet-Fe (Fig. 6.9a and b). The configuration in 9b is found in maghemite and magnetite. The third type is a bent corner-sharing oct-Fe in the ABA packing type shown in 9c, found in

hematite and goethite (for illustration purpose, a six member ring as found in hematite is drawn, but not required for this configuration). Since the ABA packing can not accommodate enough Fe in octahedral sites without sharing a face, one or both of the configurations in 9a and 9b have to be present. The 3.44 Å peak serves as indirect proof to the presence of tet-Fe. The M-model employed the structure motifs shown in Figure 6.9a and c.

Indexing of XRD and of TEM data suggested a cell length of 9.4 Å in the c direction (Towe and Bradley, 1967; Harrison et al., 1967; Drits et al., 1993; Eggleton and Fitzpatrick, 1988; Janney et al., 2000). Considering the distance between neighboring oxygen layers is 2.3 ~ 2.4 Å, there will be 4 layers of oxygen in a repeat unit if we use this cell length. This leaves two types of packing in total: ABAB or ABAC. As discussed above, the ABAB packing can not accommodate enough Fe to reach the required Fe/O ratio of 0.63, even if tet-Fe is allowed. Figure 6.9a illustrates the ABA packing with a tet-Fe. If there is another B layer above it, the tet-Fe will share three top edges with three octahedral sites above. Tet-Fe sharing an edge with Oct-Fe is not energetically favorable, nor is it proposed or supported from PDF data or other experimental evidence. Leaving those sites unoccupied will cause too many vacancies in the framework and will not give the required Fe/O ratio.

If the packing sequence is ABAC, the tet-Fe will share corners with the octahedral sites above it, just like the tetrahedral site in δ-Al_{13} Keggin cluster (Casey, 2006). Therefore ABAC packing is the only choice, and indeed this packing type is used in most proposed structure models for ferrihydrite, including the D- and M-models (Drits et al., 1993; Michel et al., 2007a).

With the ABAC packing sequence established and the c-axis length equal to the thickness of four oxygen layers (9 to 9.4 Å), there remains some ambiguity over the length of the hexagonal a-axis. Different values of 2.96 Å, 5.08 Å and 5.95 Å have been proposed, all consistent with hexagonal closest packing. In seeking an appropriate a-axis length for the structure model, there is no need to use a large cell if a smaller one provides a structure solution that serves all the experimental data equally well. The M-model (Michel et al., 2007a) has the longest a-axis length and the largest cell volume in all proposed ferrihydrite models so far: a = 5.95 Å, c = 9.04 Å. So the authors first chose this unit cell and the ABAC anion packing sequence, and attempted to explore the possibility of alternative Fe atom arrangements. Placing Fe atoms in the octahedral or tetrahedral interstices must satisfy three requirements: (1) one or more of the structure motifs shown in Figure 6.9 have to be present in the alternative structure model to produce the 3.44 Å peak in PDF; (2) no face-sharing octahedral sites or tetrahedral sites could be occupied at the same time; (3) a Fe/O ratio close to 0.63. These requirements greatly limited the freedom of filling Fe atoms in the cell. It turned out there were no other possible Fe atom arrangements. The M-model provides the sole structure solution consistent with this unit cell. Next, does an equally good structure solution exist in a smaller unit cell? We argue that the answer is no. The smaller the unit cell is the more difficult for the required structure motifs drawn in Figure 6.9 to fit in the cell due to the size. It takes little effort to rule out the possibility of an equally good structure model with a smaller cell.

6.4.3. The debate over ferrihydrite structure

A growing body of evidence suggests the atomic arrangement in ferrihydrite, regardless of grain size, synthesis conditions, surface reconstruction, morphology, site-disorder and defect density can be described by a single model (Drits et al, 1993; Michel et al, 2007b; Michel et al, 2010). The nature of that model is the subject of considerable debate however. The most recently proposed model by Michel et al (2007) consists of a single phase while that proposed by Drits et al (1993) and defended by Rancourt and Meunier (2008) and Manceau (2009) consists of three phases. Neither model fits significant features perfectly in either the laboratory XRD data or PDFs derived from synchrotron X-ray and neutron diffraction data. For example, while the M-model is supported by PDF analysis, it is criticized for its prediction of strong Bragg intensity where weak peaks are observed in the diffraction data (Manceau, 2009). While the M-model provides robust fits to PDFs derived from a wide variety of synthetic conditions, calculation of the Bragg data alone from this model, using a fully periodic structure, is bound to be misleading. Such a calculation produces, unsurprisingly, sharp diffraction features (Manceau, 2009), in a pattern with no diffuse scattering due to intermediate range ordering, anisotropic peak broadening and other diffraction effects due to grain size, grain morphology and surface reconstruction. The M-model, consisting of a single phase, does require elaboration. However it is clearly parameterized, if somewhat ideally, and the algorithms used for the calculation of the PDF are both well known and readily available (Proffen and Neder, 1997; Qiu et al, 2004). Elaborations of the M-model to date suggest it is useful, even if it does not reveal the full picture (Pinney et al., 2009).

In the case of the D-model (Drits et al, 1993), the parameterization and algorithms used to calculate diffraction data from those models, are neither clearly stated nor are

they readily available. It is clear from the measurement of thermal and physical properties discussed here that the multiphase model proposed is far too water rich, and even with the larger degrees of freedom inherent in fitting data with three rather than one phase, at best fits the available data only as well as the M-model. We combined TGA and *in situ* PDF methods to quantify the structural OH in ferrihydrite, and found the OH/Fe ratio close to 0.18. The M-model with the OH/Fe = 0.2 is consistent with this result, while the D-model has much more structural OH than observed. We demonstrated that ABAC is the only feasible packing type based on the estimated structural OH content and PDF signatures, and provided three structure motifs that could explain the 3.44 Å peak in PDF data, which is indirect evidence for the presence of tetrahedral Fe in ferrihydrite.

References:

Billinge, S.J.L. (2008) Nanoscale structural order from the atomic pair distribution function (PDF): There's plenty of room in the middle. Journal of Solid State Chemistry, 181(7), 1695-1700.

Billinge, S.J.L., and Kanatzidis, M.G. (2004) Beyond crystallography: the study of disorder, nanocrystallinity and crystallographically challenged materials with pair distribution functions. Chemical Communications(7), 749-760.

Bishop, J.L., Pieters, C.M., and Burns, R.G. (1993) Reflectance and Mossbauer-Spectroscopy of Ferrihydrite-Montmorillonite Assemblages as Mars Soil Analog Materials. Geochimica Et Cosmochimica Acta, 57(19), 4583-4595.

Blake, R.L., Hessevic.Re, Zoltai, T., and Finger, L.W. (1966) Refinement of Hematite Structure. American Mineralogist, 51(1-2), 123-129.

Campbell, A.S., Schwertmann, U., and Campbell, P.A. (1997) Formation of cubic phases on heating ferrihydrite. Clay Minerals, 32(4), 615-622.

Casey, W.H. (2006) Large aqueous aluminum hydroxide molecules. Chemical Reviews, 106(1), 1-16.

Childs, C.W., Kanasaki, N., and Yoshinaga, N. (1993) Effects of Heating in Air on Si and Ge-containing Ferrihydrites. Clay Science, 9(2), 65-80.

Chupas, P.J., Chapman, K.W., and Lee, P.L. (2007) Applications of an amorphous silicon-based area detector for high-resolution, high-sensitivity and fast time-resolved pair distribution function measurements. Journal of Applied Crystallography, 40, 463-470.

Cole, K.E., Paik, Y., Reeder, R.J., Schoonen, M., and Grey, C.P. (2004) H-2 MAS NMR studies of deuterated goethite (alpha-FeOOD). Journal of Physical Chemistry B, 108(22), 6938-6940.

Drits, V.A., Sakharov, B.A., Salyn, A.L., and Manceau, A. (1993) Structural Model for Ferrihydrite. Clay Minerals, 28(2), 185-207.

Eggleton, R.A., and Fitzpatrick, R.W. (1988) New Data and a Revised Structural Model for Ferrihydrite. Clays and Clay Minerals, 36(2), 111-124.

Hammersley, A.P., Svensson, S.O., Hanfland, M., Fitch, A.N., and Hausermann, D. (1996) Two-dimensional detector software: From real detector to idealised image or two-theta scan. High Pressure Research, 14(4-6), 235-248.

Harrington, R., Hausner, D.B., Bhandari, N., Strongin, D.R., Chapman, K.W., Chupas, P.J., Middlemiss, D.S., Grey, C.P., and Parise, J.B. (2010) Investigation of Surface Structures by Powder Diffraction: A Differential Pair Distribution Function Study on Arsenate Sorption on Ferrihydrite. Inorganic Chemistry, 49(1), 325-330.

Harrison, P.M., Fischbac.Fa, Hoy, T.G., and Haggis, G.H. (1967) Ferric Oxyhydroxide Core of Ferritin. Nature, 216(5121), 1188-1190.

Hiemstra, T., and Van Riemsdijk, W.H. (2009) A surface structural model for ferrihydrite I: Sites related to primary charge, molar mass, and mass density. Geochimica Et Cosmochimica Acta, 73(15), 4423-4436.

Jambor, J.L., and Dutrizac, J.E. (1998) Occurrence and constitution of natural and synthetic ferrihydrite, a widespread iron oxyhydroxide. Chemical Reviews, 98(7), 2549-2585.

Janney, D.E., Cowley, J.M., and Buseck, P.R. (2000) Structure of synthetic 2-line ferrihydrite by electron nanodiffraction. American Mineralogist, 85(9), 1180-1187.

-. (2001) Structure of synthetic 6-line ferrihydrite by electron nanodiffraction. American Mineralogist, 86(3), 327-335.

Klingelhofer, G., Morris, R.V., Bernhardt, B., Schroder, C., Rodionov, D.S., de Souza, P.A., Yen, A., Gellert, R., Evlanov, E.N., Zubkov, B., Foh, J., Bonnes, U., Kankeleit, E., Gutlich, P., Ming, D.W., Renz, F., Wdowiak, T., Squyres, S.W., and Arvidson, R.E. (2004) Jarosite and hematite at Meridiani Planum from Opportunity's Mossbauer spectrometer. Science, 306(5702), 1740-1745.

Manceau, A. (2009) Evaluation of the structural model for ferrihydrite derived from real-space modelling of high-energy X-ray diffraction data. Clay Minerals, 44(1), 19-34.

Manceau, A., and Drits, V.A. (1993) Local-Structure of Ferrihydrite and Feroxyhite by Exafs Spectroscopy. Clay Minerals, 28(2), 165-184.

Manceau, A. and Gates, W. P. (1997) Surface structural model for ferrihydrite. Clays and Clay Minerals, 45(3), 448-460.

Michel, F.M., Antao, S.M., Chupas, P.J., Lee, P.L., Parise, J.B., and Schoonen, M.A.A. (2005) Short- to medium-range atomic order and crystallite size of the initial FeS precipitate from pair distribution function analysis. Chemistry of Materials, 17(25), 6246-6255.

Michel, F.M., Barron, V., Torrent, J., Morales, M.P., Serna, C.J., Boily, J.F., Liu, Q.S., Ambrosini, A., Cismasu, A.C., and Brown, G.E. (2010) Ordered ferrimagnetic form of ferrihydrite reveals links among structure, composition, and magnetism. Proceedings of the National Academy of Sciences of the United States of America, 107(7), 2787-2792.

Michel, F.M., Ehm, L., Antao, S.M., Lee, P.L., Chupas, P.J., Liu, G., Strongin, D.R., Schoonen, M.A.A., Phillips, B.L., and Parise, J.B. (2007a) The structure of ferrihydrite, a nanocrystalline material. Science, 316(5832), 1726-1729.

Michel, F.M., Ehm, L., Liu, G., Han, W.Q., Antao, S.M., Chupas, P.J., Lee, P.L., Knorr, K., Eulert, H., Kim, J., Grey, C.P., Celestian, A.J., Gillow, J., Schoonen, M.A.A., Strongin, D.R., and Parise, J.B. (2007b) Similarities in 2-and 6-line ferrihydrite based on pair distribution function analysis of X-ray total scattering. Chemistry of Materials, 19(6), 1489-1496.

Paglia, G., Bozin, E.S., and Billinge, S.J.L. (2006) Fine-scale nanostructure in gamma-Al2O3. Chemistry of Materials, 18(14), 3242-3248.

Petkov, V., Billinge, S.J.L., Larson, P., Mahanti, S.D., Vogt, T., Rangan, K.K., and Kanatzidis, M.G. (2002) Structure of nanocrystalline materials using atomic pair distribution function analysis: Study of LiMoS2. Physical Review B, 65(9), -.

Petkov, V., Ren, Y., Saratovsky, I., Pasten, P., Gurr, S.J., Hayward, M.A., Poeppelmeier, K.R., and Gaillard, J.F. (2009) Atomic-Scale Structure of Biogenic Materials by Total X-ray Diffraction: A Study of Bacterial and Fungal MnOx. Acs Nano, 3(2), 441-445.

Pinney, N., Kubicki, J.D., Middlemiss, D.S., Grey, C.P., and Morgan, D. (2009) Density Functional Theory Study of Ferrihydrite and Related Fe-Oxyhydroxides. Chemistry of Materials, 21(24), 5727-5742.

Proffen, T., and Billinge, S.J.L. (1999) PDFFIT, a program for full profile structural refinement of the atomic pair distribution function. Journal of Applied Crystallography, 32, 572-575.

Proffen, T., and Neder, R.B. (1997) DISCUS: A program for diffuse scattering and defect-structure simulation. Journal of Applied Crystallography, 30, 171-175.

Qiu, X., Thompson, J.W., and Billinge, S.J.L. (2004) PDFgetX2: a GUI-driven program to obtain the pair distribution function from X-ray powder diffraction data. Journal of Applied Crystallography, 37(4), 678.

Rancourt, D.G., and Meunier, J.F. (2008) Constraints on structural models of ferrihydrite as a nanocrystalline material. American Mineralogist, 93(8-9), 1412-1417.

Russell, J.D. (1979) Infrared Spectroscopy of Ferrihydrite - Evidence for the Presence of Structural Hydroxyl-Groups. Clay Minerals, 14(2), 109-114.

Schwertmann, U., and Cornell, R.M. (1991) Iron Oxides in the Laboratory: Preperation and Characterization. Wiley-VCH, New York, p105.

Schwertmann, U., Friedl, J., and Stanjek, H. (1999) From Fe(III) ions to ferrihydrite and then to hematite. Journal of Colloid and Interface Science, 209(1), 215-223.

Stanjek, H., and Weidler, P.G. (1992) The Effect of Dry Heating on the Chemistry, Surface-Area, and Oxalate Solubility of Synthetic 2-Line and 6-Line Ferrihydrites. Clay Minerals, 27(4), 397-412.

Tosca, N.J., McLennan, S.M., Dyar, M.D., Sklute, E.C., and Michel, F.M. (2008) Fe oxidation processes at Meridiani Planum and implications for secondary Fe mineralogy on Mars. Journal of Geophysical Research-Planets, 113, E05005, DOI: 10.1029/2007JE003019.

Towe, K.M., and Bradley, W.F. (1967) Mineralogical Constitution of Colloidal Hydrous Ferric Oxides. Journal of Colloid and Interface Science, 24(3), 384-392.

Waseda, Y. (1980) The structure of Non-crystalline Materials. McGraw-Hill, New York.

Weidler, P.G. (1997) BET Sample Pretreatment of Synthetic Ferrihydrite and its Influence on the Determination of Surface Area and Porosity. Journal of Porous Materials, 4(3), 165-169.

Zhao, J.M., Huggins, F.E., Feng, Z., and Huffman, G.P. (1994) Ferrihydrite - Surface-Structure and Its Effects on Phase-Transformation. Clays and Clay Minerals, 42(6), 737-746.

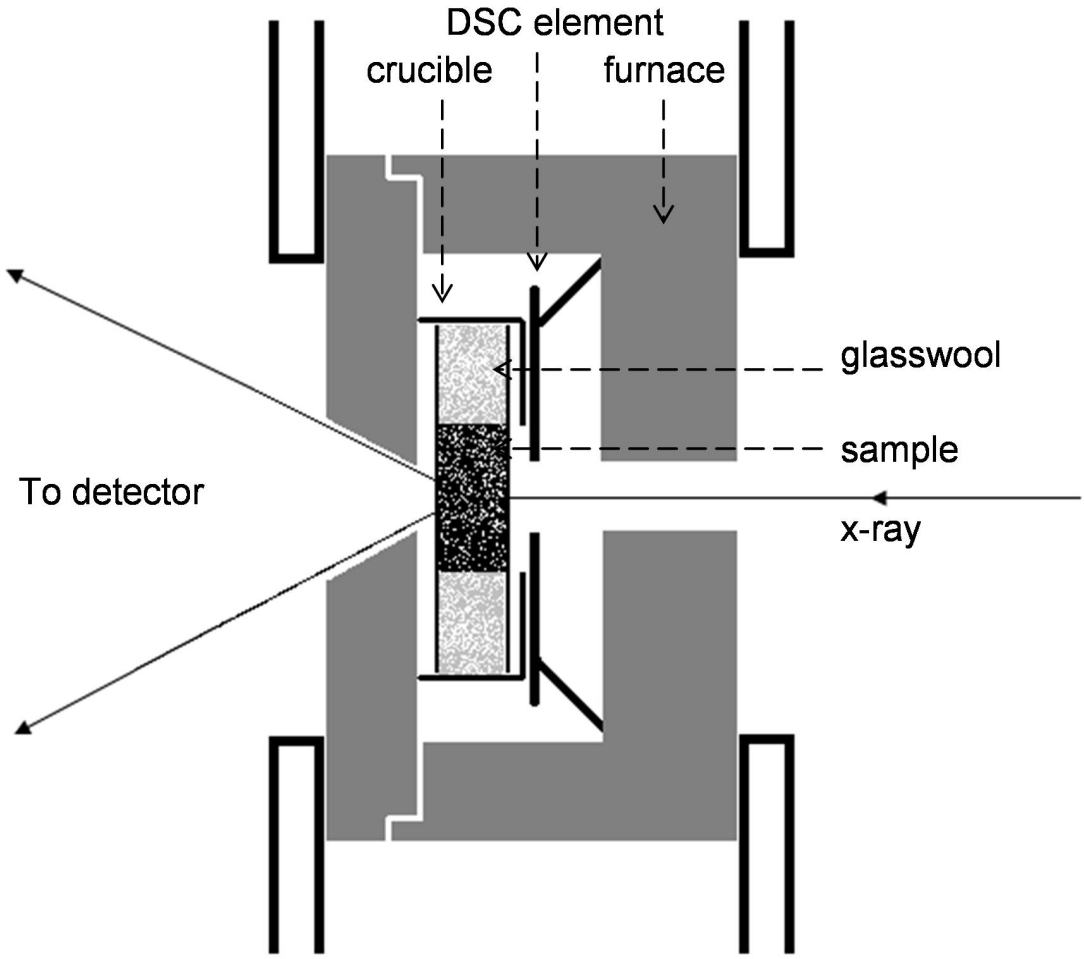

Figure 6.1. The schematic diagram of the DSC device for the DSC-PDF experiment

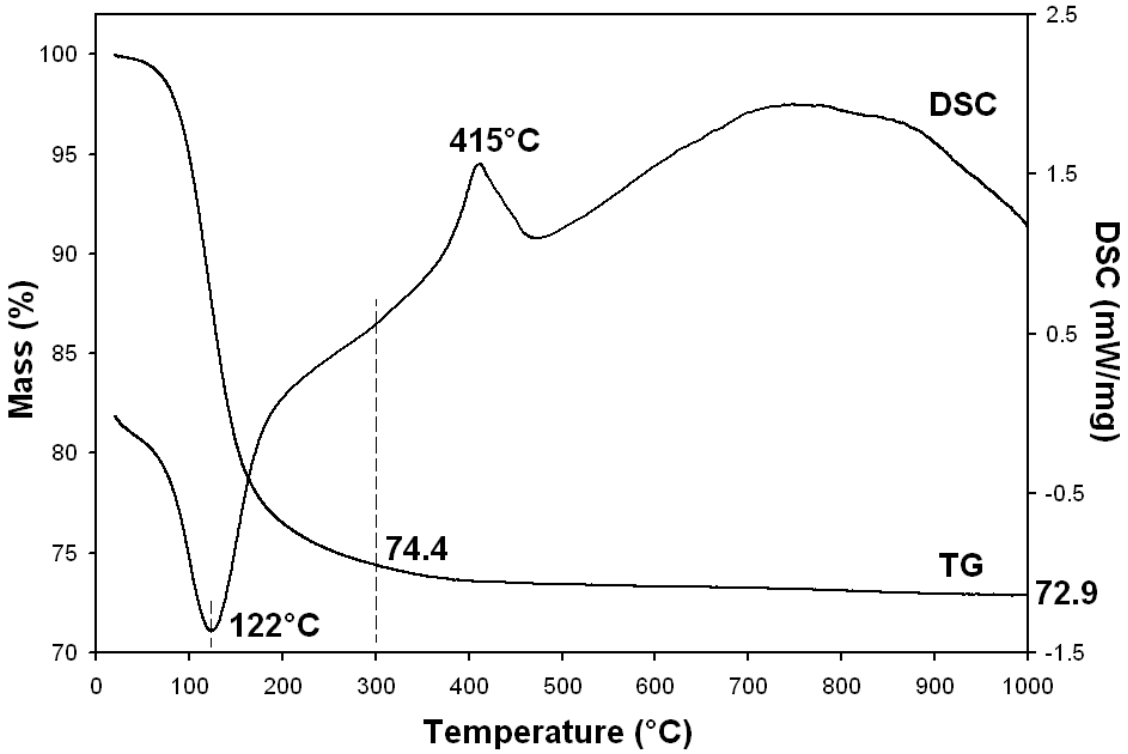

Figure 6.2. TG and DSC data for 2-line ferrihydrite. Sample weight dropped to 74.4% at 300°C, and to 72.9% at 1000°C. The broad hump over 750°C in the DSC curve is due to a common baseline drift, not related to a real thermal event.

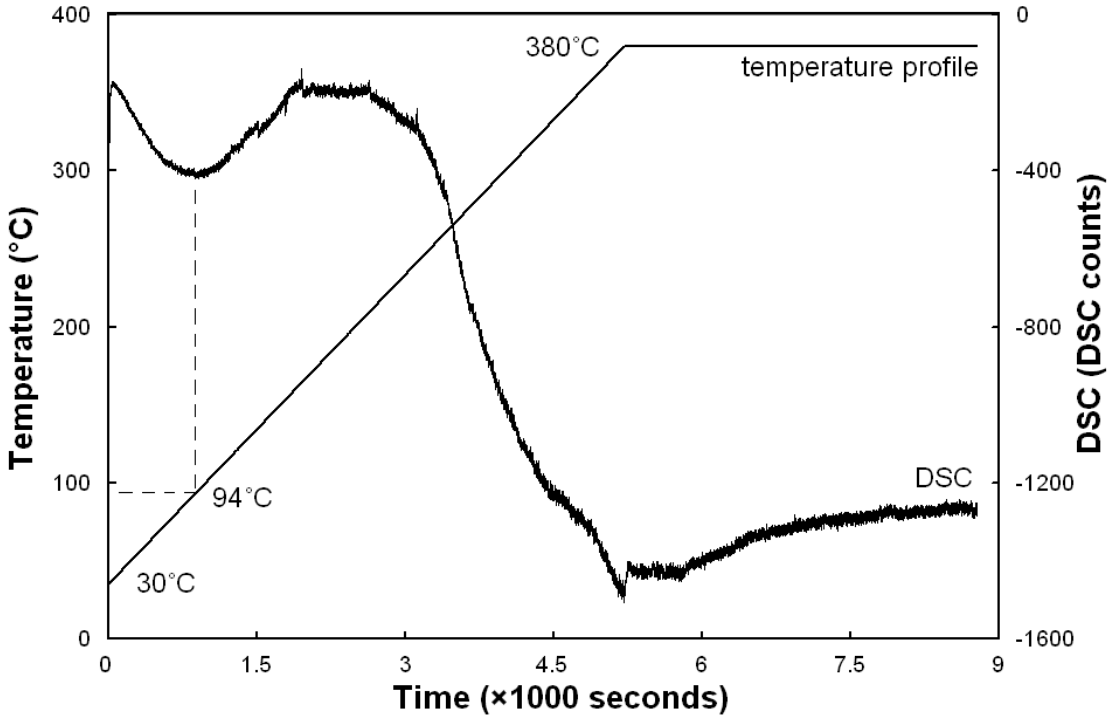

Figure 6.3. Temperature profile and DSC data collected in the *in situ* DSC-PDF experiment. The endotherm at 94°C corresponds to the removal of adsorbed water. From 3000 second, there is an enormous baseline drift which makes the DSC data above 200°C not informative. The kink at 5200 second is due to a change from heating to holding sample temperature.

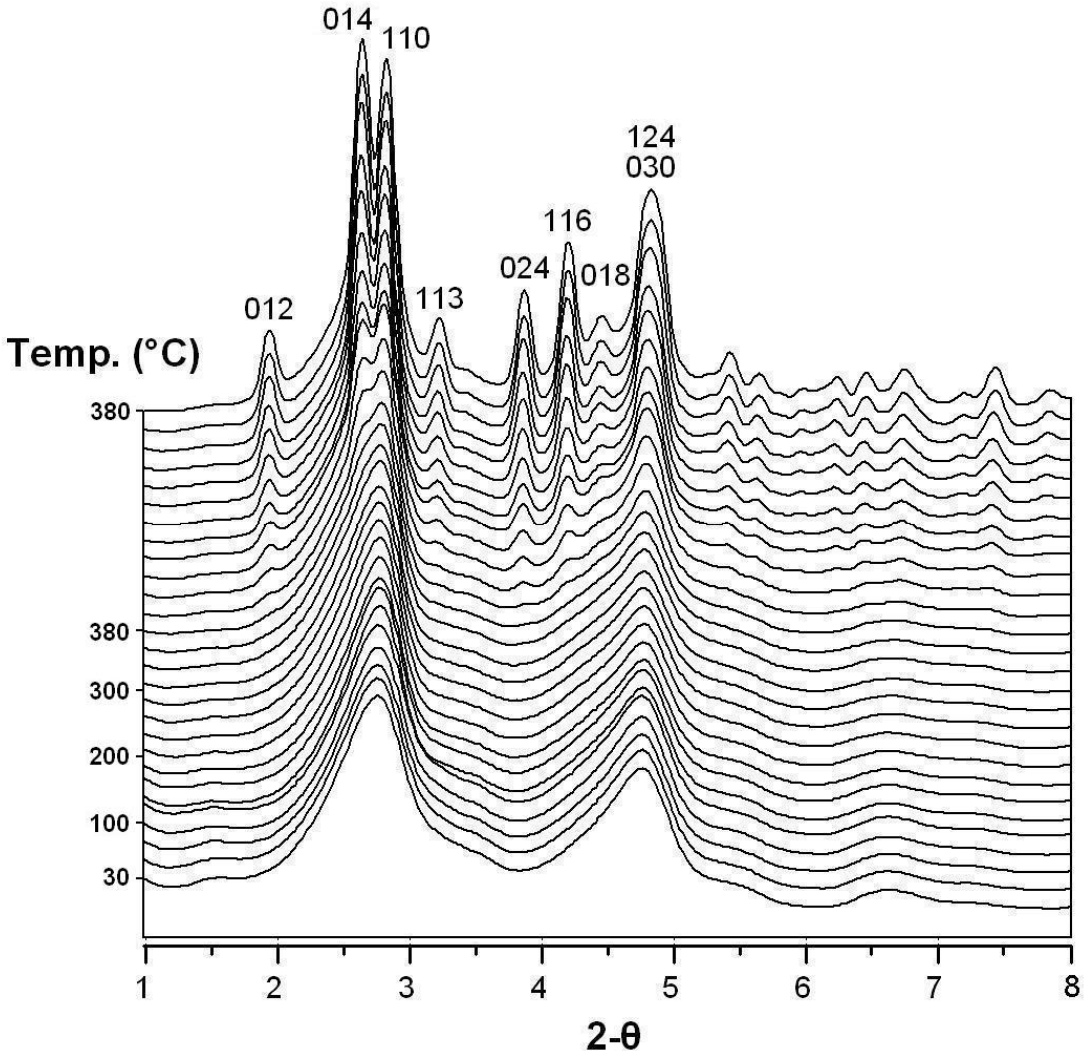

Figure 6.4. In situ X-ray scattering data showing the change of 2-line ferrihydrite to hematite. Hematite reflections indexes are shown at the top.

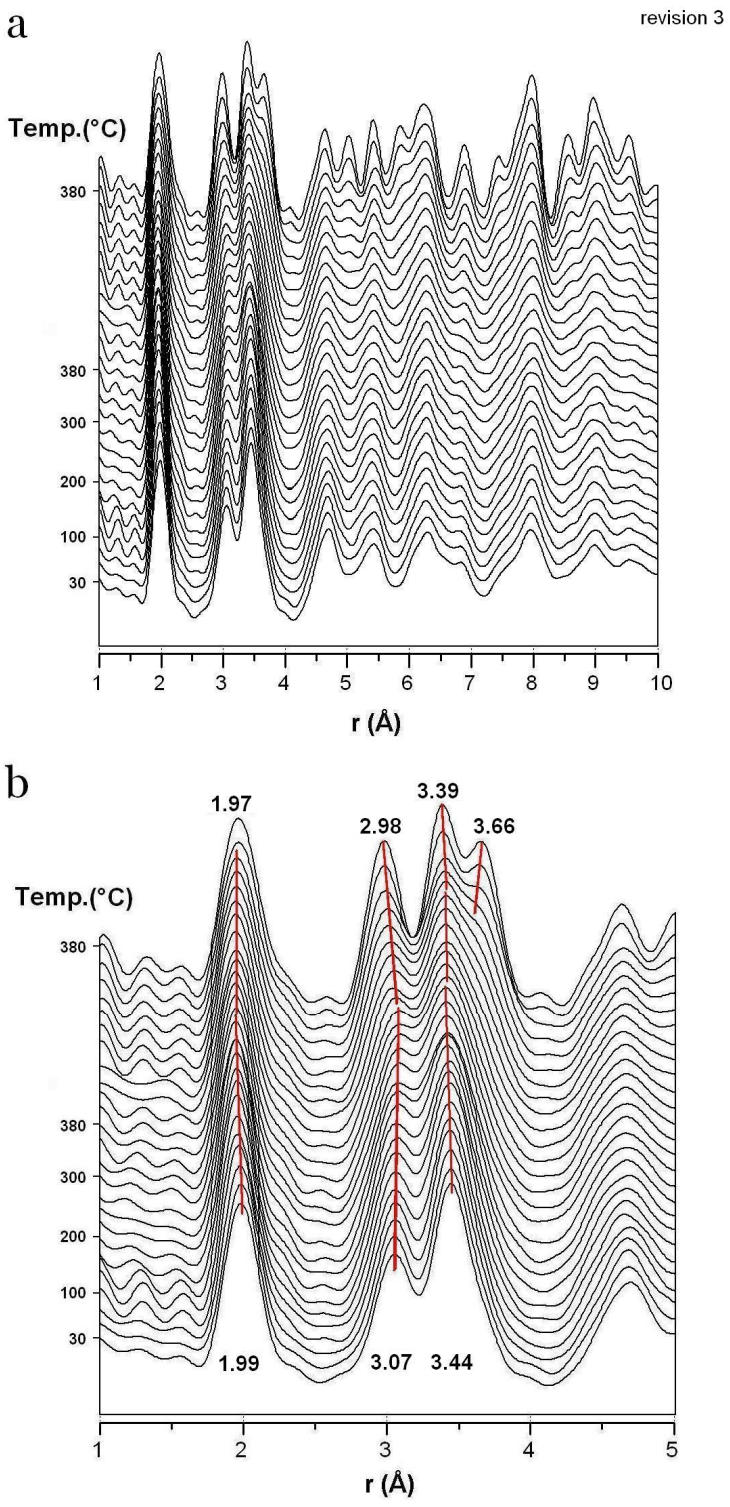

Figure 6.5. PDF data series showing the local structural change of ferrihydrite transforming to hematite

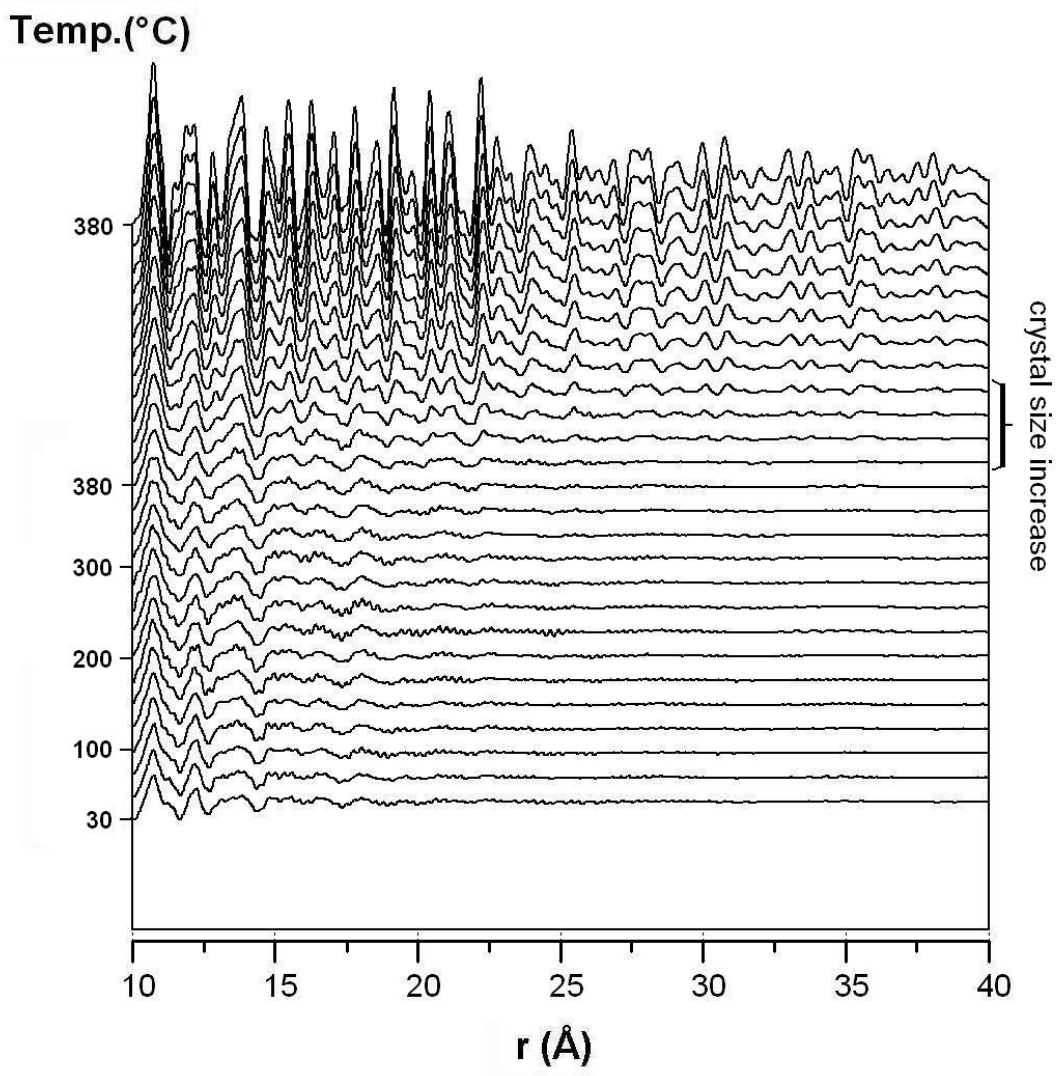

Figure 6.6. PDF data extended to 40Å to show the mid-range structure. Correlations between 20 to 40 Å started to show up at 380˚C, the same time hematite began to form.

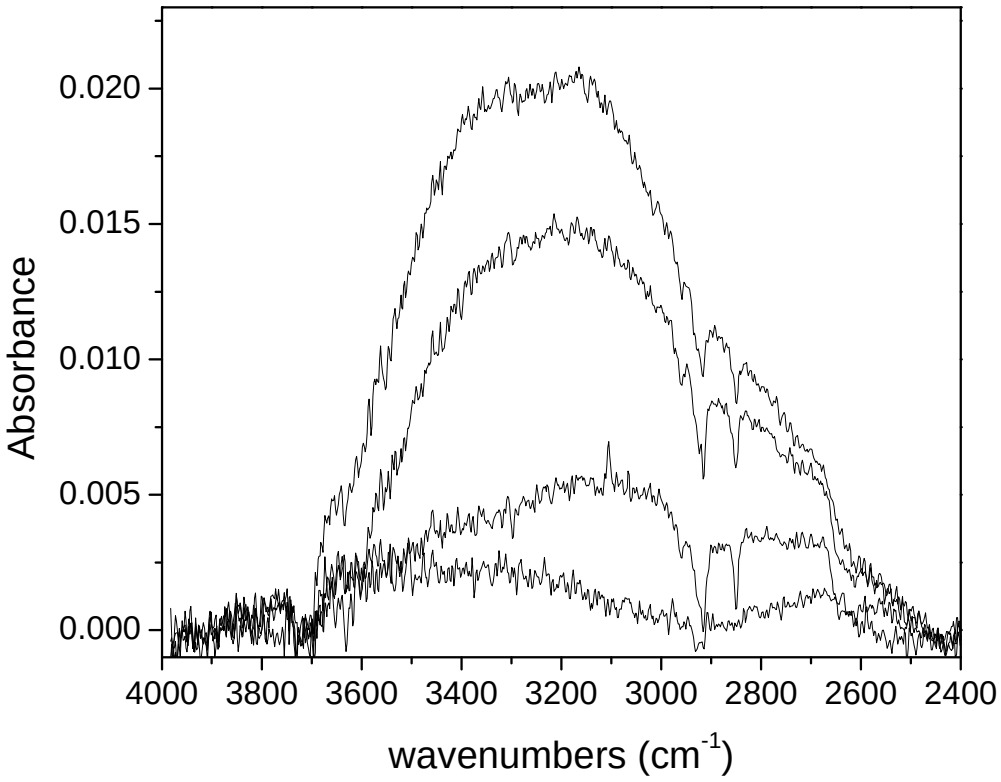

Figure 6.7. In situ ATR-FTIR of ferrihydrite, from top to bottom: under N_2 flow at 25°C, after heating to 215°C for 30 mins then cooled to 25°C and exposed to atmospheric moisture, after heating to 215°C for 30 mins then cooled to 25°C under N2 flow, 215°C under N_2 flow. The sharp absorption bands around 2850 and 2920 cm^{-1} come from the diamond ATR element and mismatches in some lattice absorption within the diamond.

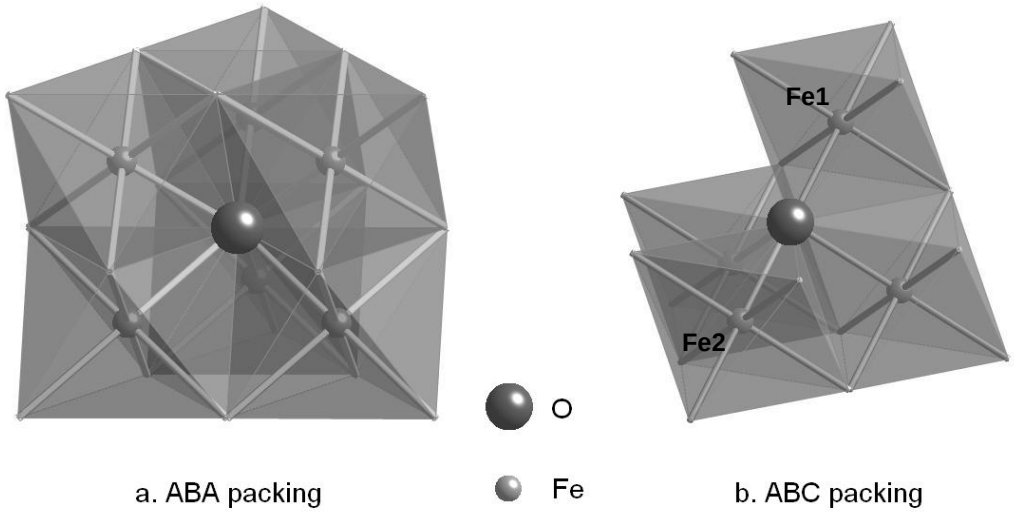

Figure 6.8. Octahedral Fe sites in ABA and ABC packing type.

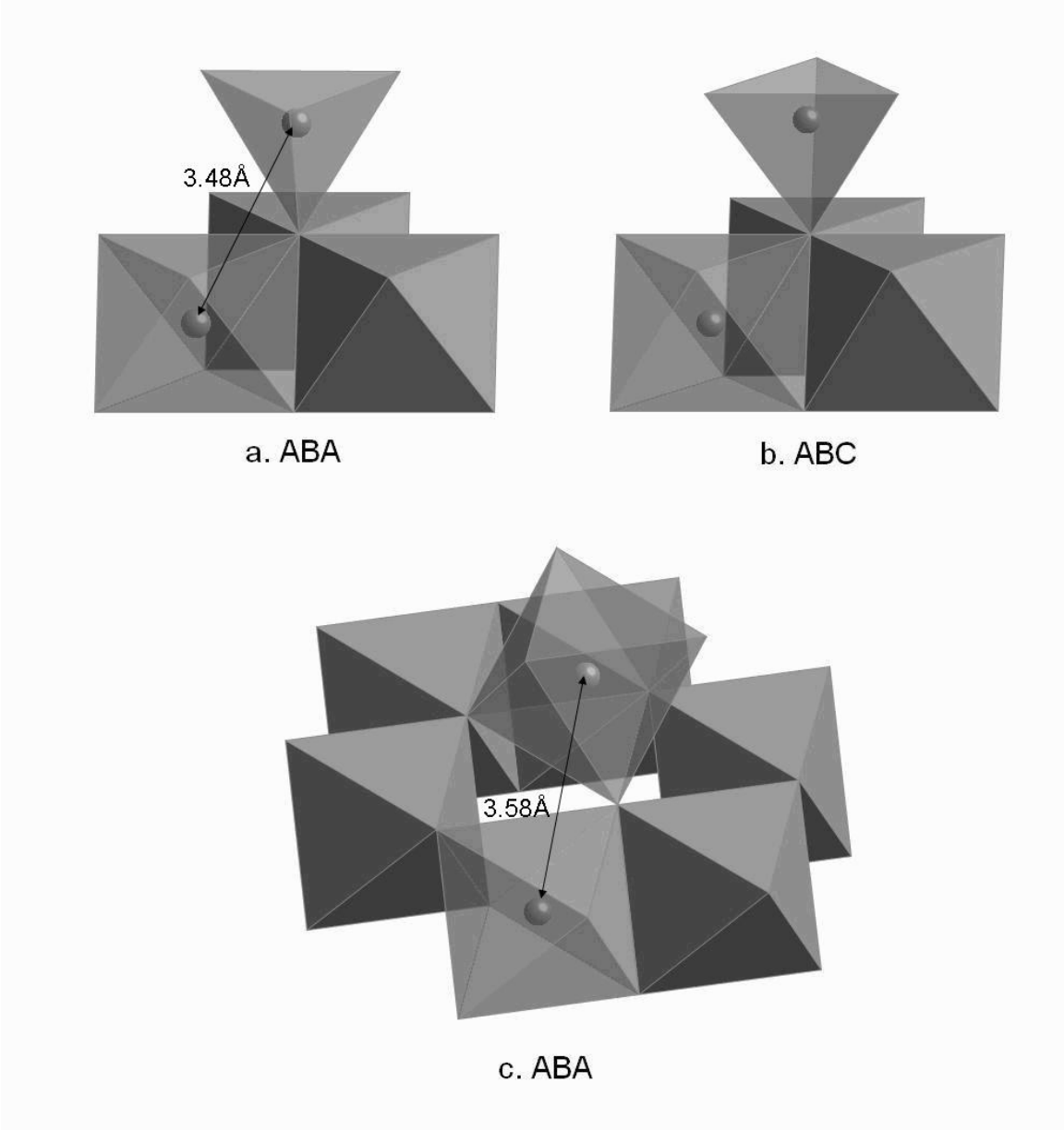

Figure 6.9. Three types of configurations able to produce the 3.44 Å Fe-Fe. Distances shown in the figure are calculated assuming no structural distortions and Fe-O bond length equal to 1.96 Å.

Chapter 7

Conclusions

The stability and transformation of ferric sulfates as functions of relative humidity (RH), temperature (T) and atmospheric pressure (P) were resolved in this research. This leads to a more detailed understanding of the behavior of this group of minerals, their formation and interaction with moist air. This information provides the basis for interpretation of ferric sulfate minerals on Mars, and provides mineralogical constraints for recovering information on local paleo-environments. Nonetheless, the ferric sulfate systems studied here, including the "2 Fe(III) – 3 SO_4 – *n* H_2O" and "Fe(III) – 2 SO_4 – *n* H_2O" systems, are still too basic to reflect the real sulfate brine chemistry on early Mars. The effects of other cations (e.g Mg^{2+}, Ca^{2+}) and anions (e.g. Cl^-) on the speciation and evolution of ferric sulfates should be studied in future research.

7.1. Achievements

Phases encountered in the two ferric sulfate hydrate systems, 2 Fe(III) – 3 SO_4 – *n* H_2O and Fe(III) – 2 SO_4 – *n* H_2O, were characterized with RH and T in Chapter 2, 3 and 4. Low T and low P effects on ferric sulfates stability were addressed in Chapter 5. Below is a brief summary of major scientific achievements in this research.

(1) 2 Fe(III) – 3 SO_4 – n H_2O phase evoluiton

The evaporation of concentrated $Fe_2(SO_4)_3$ solution and subsequent diagenetic transformations of precipitated ferric sulfates were studied in a series of *ex situ* and *in situ* experiments performed at T ranging from ~ 0 °C to 80 °C and RH ranging from 0% to 80%. Results from *ex situ* experiments were plotted in RH-Time phase evolution maps (Fig. 3.8 in Chapter 3). The evolution of $Fe_2(SO4)_3$ solution displays the following major features: (a) at mid-RH, ~ 40% to ~ 60%, ferricopiapite and rhomboclase are the initial precipitates; they combine to form single ferric sulfate hydrates such as kornelite (Fig. 3.8b), paracoquimbite (Fig. 3.8b and 3.8c) or ferric sulfate pentahydrate (Fig. 3.8c) in the post-precipitation evolution (diagenetic process), depending on RH and T; (b) at low-RH, < 30%, the $Fe_2(SO4)_3$ solution evolves to an amorphous solid without crystallizing; the amorphous ferric sulfate remains at 0% and 11% RH, but slowly transforms to crystalline rhomboclase at ~ 30% RH.

(2) Fe(III) – 2 SO_4 – n H_2O phase map

Studies of the RH-T phase diagram for the Fe(III) – 2 SO_4 – *n* H_2O system show reversible transformation between rhomboclase and $(H_3O)Fe(SO_4)_2$, as well as the deliquescence boundary of rhomboclase (Fig. 4.4). This transformation was kinetically inhibited at -20 °C.

(3) Ferric sulfates at Low T and Low P

Results reported in Chapter 5 indicate that under simulated low-T and low-P conditions, ferricopiapite was not stable at 6 °C and 3.6 mbar and 0.6% RH, and transformed to a new phase which was not identified. Rhomboclase transformed to an

amorphous phase at 20 °C and 3.6 mbar and 0% RH. Other ferric sulfates including kornelite, paracoquimbite, ferric sulfate pentahydrate and the amorphous ferric sulfate remained stable at 25 °C and P ≤ 6 mbar. All the above mentioned ferric sulfates were apparently stable at -30 °C against variations of RH. It is expected that these ferric sulfates will remain stable at even lower temperature.

7.2. Limitations

The research contributes to fundamental knowledge of ferric sulfate stabilities and phase transitions as functions of RH and T. However, application of the results to interpretation or prediction of Martian ferric sulfates is limited by the differences between the simulated environmental conditions and the actual conditions on Mars, as well as the differences in chemistry between the studied ferric sulfate solution and the sulfate brine on ancient Mars.

(1) Difference in chemistry

The explored ferric sulfate hydrate systems, 2 Fe(III) – 3 SO_4 – *n* H_2O and Fe(III) – 2 SO_4 – *n* H_2O, are too simple to be close to a Martian sulfate brine that consists of significant amount of extra ions. For example, ferric sulfates observed on Mars generally coexist with Mg- sulfates and Ca- sulfates. The presence of Mg^{2+} and Ca^{2+} is likely to alter the ferric sulfate speciation, e.g. Mg-copiapite may be favored to precipitate over ferricopiapite.

The pH of the studied concentrated ferric sulfate solution was below 1. Sulfate brines of a similar pH is supposed to occur at the last stage of the hypothesized aqueous

sedimentary history on Mars (Bibring et al., 2006), where water is mostly evaporated and pH is very low. Therefore, the evolved ferric sulfates studied in this research only represent part of the ferric sulfate group minerals observed on Mars that primarily precipitate at pH < 1, e.g. ferricopiapite and rhomboclase. Jarosite and schwertmannite, also confirmed or suggested on Mars, were not studied in this research due to their high formation pH, e.g. 2 < pH < 4 for jarosite, 4 < pH < 6 for schwertmannite (Tosca et al., 2007). Jarosite and schwertmannite should be covered in future RH-T studies.

(2) Difference in environmental parameters

There are four differences between the simulated conditions in this research and actual Martian conditions: (1) the atmospheric composition; (2) the low atmospheric pressure on Mars; (3) the low temperature on Mars; (4) the presence of stronger ultraviolet radiation than on Earth. The influences of these environmental parameters on ferric sulfate stability and chemistry have been discussed in detail in Chapter 3, section 3.4.3. For the first aspect, the difference in atmospheric composition is not expected to affect speciation and stability of ferric sulfates. No experiments were done under CO_2 or Martian atmospheric contents in this research, except the one studying rhomboclase stability using the vacuum line setup, which does not reveal any effect of CO_2 on rhomboclase (Section 4.3.3). For the second aspect, the difference in atmospheric pressure should not be directly related to the stability of hydrated minerals. Instead, water vapor pressure or RH is directly related and its effect has been thoroughly investigated in this research. For the third aspect, the low temperature on Mars could dramatically slow down the reaction kinetics. This effect was observed in the *ex situ*

experiments from ~ 0 °C to 50 °C presented in Chapter 3. Direct characterization of several ferric sulfate phases at low temperature (-30 °C) was also performed in Chapter 5. However, due to the slower kinetics, extensive direct studies on sulfate brine evaporation at low temperature are not realistic. For the fourth aspect, the effect of ultraviolet light was not included in the current research. Exposure to UV was suspected to affect the hydration states of Mg-sulfate in a previous study (Cloutis et al., 2007). The ultraviolet light effect should be incorporated in future studies.

(3) Unidentified ferric sulfate phases

At least two new crystalline ferric sulfate phases were discovered in this research. One is an intermediate phase formed along with ferricopiapite and rhomboclase during the hydration of trigonal $Fe_2(SO4)_3$ or the evaporation of $Fe_2(SO4)_3$ solution (Chapter 2 and Appendix). The synthesis of this phase is not completely reproducible, probably due to an as yet to be discovered optimal synthesis route has not been discovered. Its structure is mostly determined with single crystal diffraction data and reported in some detail in Appendix. The other new phase was found as a dehydration product of ferricopiapite at 6 °C and 3.6 mbar (Chapter 5). No crystal structure characterization was attempted on this phase. There are more unidentified ferric sulfate phases reported by other scientists (Chipera et al., 2007; Freeman et al., 2009). The phase diagram will not be complete without identifying these unknown phases and their stability field.

7.3. Future directions

Two main directions are proposed here for future research in this field of laboratory simulation of Martian sulfate mineralogy and sedimentary history: (1) continue study of basic ferric sulfate chemistry, e.g. completing phase diagrams and characterizing the unknown phases; (2) improved the simulation of Martian conditions in laboratory based research, especially by adding ultraviolet radiation in *ex situ* and *in situ* experiments. In detail, three projects are listed below:

(1) Systematic study of Fe(III) – SO_4 – H_2O speciation

Posnjak and Merwin (1922) published a paper that examined the speciation of ferric sulfate and ferric oxide and oxyhydroxide in the system, $Fe_2O_3 – SO_3 – H_2O$. They proposed a $Fe_2O_3 – SO_3 – H_2O$ ternary phase diagram. This work provided useful information on various ferric sulfate stability conditions. With much advanced technology at present days and more comprehensive knowledge of ferric sulfate chemistry and crystallography, it is necessary to reevaluate the $Fe_2O_3 – SO_3 – H_2O$ system. This study is also expected lead to discovery unidentified phases and their stability conditions.

Methods: Initial slurries are prepared by mixing Fe_2O_3, 98% sulfuric acid and water of different ratios, then loading and sealed in Teflon bombs stored at 50 °C to 200 °C for enough long time, 5 to 20 days depending on temperature, to let the system reach equilibrium. The solid and liquid phases produced will be analyzed for speciation and ion concentration. A total of 150 to 200 hydrothermal reactions are expected to complete the mapping of the ternary phase diagrams at different temperature from 50 °C to 200 °C. This work is right now being conducted.

(2) Ferric and ferrous sulfates hydration and dehydration under ultraviolet radiation

Ultraviolet light is one potentially important environmental factor that affects the stability of hydrate mineral (Cloutis et al., 2007), but has not been considered in the current research. This project is going to aim at investigating the effect of ultraviolet radiation on ferric sulfate hydrates, with *in situ* and *ex situ* XRD methods similar to used in this research. Ferrous sulfates should also be included in the study for their diagenetic relationships with ferric sulfate.

Reference:

Bibring, J.P., Langevin, Y., Mustard, J.F., Poulet, F., Arvidson, R., Gendrin, A., Gondet, B., Mangold, N., Pinet, P., Forget, F., and Team, O. (2006) Global mineralogical and aqueous mars history derived from OMEGA/Mars express data. Science, 312(5772), 400-404.

Bishop, J.L., Lane, M.D., Dyar, M.D., Parente, M., Roach, L.H., Murchie, S.L., and Mustard, J.F. (2008) Sulfates on Mars: How recent discoveries from CRISM, OMEGA and the MERs are changing our view of the planet. Geochimica Et Cosmochimica Acta, 72(12), A86-A86.

Bishop, J.L., Parente, M., Weitz, C.M., Dobrea, E.Z.N., Roach, L.H., Murchie, S.L., McGuire, P.C., McKeown, N.K., Rossi, C.M., Brown, A.J., Calvin, W.M., Milliken, R., and Mustard, J.F. (2009) Mineralogy of Juventae Chasma: Sulfates in the light-toned mounds, mafic minerals in the bedrock, and hydrated silica and hydroxylated ferric sulfate on the plateau. Journal of Geophysical Research-Planets, 114, E00D09, DOI: 10.1029/2009JE003352.

Chipera, S.J., Vaniman, D.T., and Bish, D.L. (2007) The effect of temperature and water on ferric-sulfates. Lunar and Planetary Science XXXVIII, Abstract no. 1409.

Cloutis, E.A., Craig, M.A., Mustard, J.F., Kruzelecky, R.V., Jamroz, W.R., Scott, A., Bish, D.L., Poulet, F., Bibring, J.P., and King, P.L. (2007) Stability of hydrated minerals on Mars. Geophysical Research Letters, 34, L20202, DOI: 10.1029/2007GL031267.

Freeman, J.J., Wang, A., and Ling, Z.C. (2009) Ferric sulfates on Mars: Mission observations and laboratory investigations. Lunar and Planetary Science XXXX, Abstract no. 2284.

Gendrin, A., Mangold, N., Bibring, J.P., Langevin, Y., Gondet, B., Poulet, F., Bonello, G., Quantin, C., Mustard, J., Arvidson, R., and LeMouelic, S. (2005) Sulfates in martian layered terrains: the OMEGA/Mars Express view. Science, 307(5715), 1587-1591.

Jambor, J.I., Nordstrom, D.K., and Alpers, C.N. (2000) Metal-sulfate Salts from Sulfide Mineral Oxidation. In C.N. Alpers, J.I. Jambor, and D.K. Nordstrom, Eds. Sulfate Minerals: Crystallography, Geochemistry, and Environmental Significance, Reviews in Mineralogy and Geochemistry, vol. 40, p. 305-350. Mineralogical Society of America, Geochemical Society, Washington, D. C.

Lane, M.D., Bishop, J.L., Dyar, M.D., King, P.L., Parente, M., and Hyde, B.C. (2008) Mineralogy of the Paso Robles soils on Mars. American Mineralogist, 93(5-6), 728-739.

Majzlan, J., and Kiefer, B. (2006) An X-ray- and neutron-diffraction study of synthetic ferricopiapite, $Fe_{14/3}(SO_4)_6(OD,OH)_2(D_2O,H_2O)_{20}$, and ab initio calculations on the structure of magnesiocopiapite, $MgFe_4(SO_4)_6(OH)_2(H_2O)_{20}$. Canadian Mineralogist, 44, 1227-1237.

Squyres, S.W., Knoll, A.H., Arvidson, R.E., Clark, B.C., Grotzinger, J.P., Jolliff, B.L., McLennan, S.M., Tosca, N., Bell, J.F., Calvin, W.M., Farrand, W.H., Glotch, T.D., Golombek, M.P., Herkenhoff, K.E., Johnson, J.R., Klingelhofer, G., McSween, H.Y., and Yen, A.S. (2006) Two years at Meridiani Planum: Results from the Opportunity Rover. Science, 313(5792), 1403-1407.

References

Adams, J.R., and Merz, A.R. (1929) Hygroscopicity of fertilizer materials and mixtures. Industrial and Engineering Chemistry, 21, 305-307.

Ackermann, S., Lazic, B., Armbruster, T., Doyle, S., Grevel, K.D., and Majzlan, J. (2009) Thermodynamic and crystallographic properties of kornelite [$Fe_2(SO_4)_3 \cdot 7.75H_2O$] and paracoquimbite [$Fe_2(SO_4)_3 \cdot 9H_2O$]. American Mineralogist, 94(11-12), 1620-1628.

Alpers, C.N., Nordstrom, D.K., and Thompson, J.M. (1994) Seasonal-Variations of Zn/Cu Ratios in Acid-Mine Water from Iron-Mountain, California. Environmental Geochemistry of Sulfide Oxidation, 550, 324-344.

Arvidson, R.E., Poulet, F., Bibring, J.P., Wolff, M., Gendrin, A., Morris, R.V., Freeman, J.J., Langevin, Y., Mangold, N., and Bellucci, G. (2005) Spectral reflectance and morphologic correlations in eastern Terra Meridiani, Mars. Science, 307(5715), 1591-1594.

Arvidson, R.E., Ruff, S.W., Morris, R.V., Ming, D.W., Crumpler, L.S., Yen, A.S., Squyres, S.W., Sullivan, R.J., Bell, J.F., Cabrol, N.A., Clark, B.C., Farrand, W.H., Gellert, R., Greenberger, R., Grant, J.A., Guinness, E.A., Herkenhoff, K.E., Hurowitz, J.A., Johnson, J.R., Klingelhofer, G., Lewis, K.W., Li, R., McCoy, T.J., Moersch, J., McSween, H.Y., Murchie, S.L., Schmidt, M., Schroder, C., Wang, A., Wiseman, S., Madsen, M.B., Goetz, W., and McLennan, S.M. (2008) Spirit Mars Rover Mission to the Columbia Hills, Gusev Crater: Mission overview and selected results from the Cumberland Ridge to Home Plate. Journal of Geophysical Research-Planets, 113, E12S33, DOI: 10.1029/2008JE003183.

Bibring, J.P., Arvidson, R.E., Gendrin, A., Gondet, B., Langevin, Y., Le Mouelic, S., Mangold, N., Morris, R.V., Mustard, J.F., Poulet, F., Quantin, C., and Sotin, C. (2007) Coupled ferric oxides and sulfates on the Martian surface. Science, 317(5842), 1206-1210.

Bibring, J.P., Langevin, Y., Gendrin, A., Gondet, B., Poulet, F., Berthe, M., Soufflot, A., Arvidson, R., Mangold, N., Mustard, J., Drossart, P., and Team, O. (2005) Mars surface diversity as revealed by the OMEGA/Mars Express observations. Science, 307(5715), 1576-1581.

Bibring, J.P., Langevin, Y., Mustard, J.F., Poulet, F., Arvidson, R., Gendrin, A., Gondet, B., Mangold, N., Pinet, P., Forget, F., and Team, O. (2006) Global mineralogical and aqueous mars history derived from OMEGA/Mars express data. Science, 312(5772), 400-404.

Bigham, J.M., Schwertmann, U., Traina, S.J., Winland, R.L., and Wolf, M. (1996) Schwertmannite and the chemical modeling of iron in acid sulfate waters. Geochimica Et Cosmochimica Acta, 60(12), 2111-2121.

Billinge, S.J.L. (2008) Nanoscale structural order from the atomic pair distribution function (PDF): There's plenty of room in the middle. Journal of Solid State Chemistry, 181(7), 1695-1700.

Billinge, S.J.L., and Kanatzidis, M.G. (2004) Beyond crystallography: the study of disorder, nanocrystallinity and crystallographically challenged materials with pair distribution functions. Chemical Communications(7), 749-760.

Bish, D.L., Blake, D., Sarrazin, P., Treiman, A.H., Hoehler, T., Hausrath, E.M., Midtkandal, I., and Steele, A. (2007) Field XRD/XRF mineral analysis by the MSAL CheMin instrument. Lunar and Planetary Science XXXVIII, Abstract no. 1163.

Bishop, J.L., Lane, M.D., Dyar, M.D., Parente, M., Roach, L.H., Murchie, S.L., and Mustard, J.F. (2008) Sulfates on Mars: How recent discoveries from CRISM, OMEGA and the MERs are changing our view of the planet. Geochimica Et Cosmochimica Acta, 72(12), A86-A86.

Bishop, J.L., Parente, M., Weitz, C.M., Dobrea, E.Z.N., Roach, L.H., Murchie, S.L., McGuire, P.C., McKeown, N.K., Rossi, C.M., Brown, A.J., Calvin, W.M., Milliken, R., and Mustard, J.F. (2009) Mineralogy of Juventae Chasma: Sulfates in the light-toned mounds, mafic minerals in the bedrock, and hydrated silica and hydroxylated ferric sulfate on the plateau. Journal of Geophysical Research-Planets, 114, E00D09, DOI: 10.1029/2009JE003352.

Bishop, J.L., Pieters, C.M., and Burns, R.G. (1993) Reflectance and Mossbauer-Spectroscopy of Ferrihydrite-Montmorillonite Assemblages as Mars Soil Analog Materials. Geochimica Et Cosmochimica Acta, 57(19), 4583-4595.

Blake, R.L., Hessevic.Re, Zoltai, T., and Finger, L.W. (1966) Refinement of Hematite Structure. American Mineralogist, 51(1-2), 123-129.

Buck, A.L. (1981) New Equations for Computing Vapor-Pressure and Enhancement Factor. Journal of Applied Meteorology, 20(12), 1527-1532.

Burns, R.G. (1987) Ferric Sulfates on Mars. Journal of Geophysical Research-Solid Earth and Planets, 92(B4), E570-E574.

Burns, R.G., and Fisher, D.S. (1990) Iron-Sulfur Mineralogy of Mars - Magmatic Evolution and Chemical-Weathering Products. Journal of Geophysical Research-Solid Earth and Planets, 95(B9), 14415-14421.

Campbell, A.S., Schwertmann, U., and Campbell, P.A. (1997) Formation of cubic phases on heating ferrihydrite. Clay Minerals, 32(4), 615-622.

Casey, W.H. (2006) Large aqueous aluminum hydroxide molecules. Chemical Reviews, 106(1), 1-16.

Childs, C.W., Kanasaki, N., and Yoshinaga, N. (1993) Effects of Heating in Air on Si and Ge-containing Ferrihydrites. Clay Science, 9(2), 65-80.

Chipera, S.J., Carey, J.W., Bish, D. L. (1997) Controlled-humidity XRD analyses: Application to the study of smectite expansion/contraction. Adv. X-ray Anal., 39, 713-722.

Chou, I.M., and Seal, R.R. (2003a) Acquisition and evaluation of thermodynamic data for morenosite-retgersite equilibria at 0.1 MPa. American Mineralogist, 88(11-12), 1943-1948.

-. (2003b) Determination of epsomite-hexahydrite equilibria by the humidity-buffer technique at 0.1 MPa with implications for phase equilibria in the system $MgSO_4$-H_2O. Astrobiology, 3(3), 619-630.

-. (2005a) Acquisition and evaluation of thermodynamic data for bieberite-moorhouseite equilibria at 0.1 MPa. American Mineralogist, 90(5-6), 912-917.

-. (2005b) Determination of goslarite-bianchite equilibria by the humidity-buffer technique at 0.1 MPa. Chemical Geology, 215(1-4), 517-523.

-. (2007) Magnesium and calcium sulfate stabilities and the water budget of Mars. Journal of Geophysical Research-Planets, 112, E11004, DOI: 10.1029/2007JE002898.

Chou, I.M., Seal, R.R., and Hemingway, B.S. (2002) Determination of melanterite-rozenite and chalcanthite-bonattite equilibria by humidity measurements at 0.1 MPa. American Mineralogist, 87(1), 108-114.

Christensen, P.R., Wyatt, M.B., Glotch, T.D., Rogers, A.D., Anwar, S., Arvidson, R.E., Bandfield, J.L., Blaney, D.L., Budney, C., Calvin, W.M., Faracaro, A., Fergason, R.L., Gorelick, N., Graff, T.G., Hamilton, V.E., Hayes, A.G., Johnson, J.R., Knudson, A.T., McSween, H.Y., Mehall, G.L., Mehall, L.K., Moersch, J.E., Morris, R.V., Smith, M.D., Squyres, S.W., Ruff, S.W., and Wolff, M.J. (2004) Mineralogy at Meridiani Planum from the Mini-TES experiment on the Opportunity Rover. Science, 306(5702), 1733-1739.

Christidis, P.C., and Rentzeperis, P.J. (1975) Crystal-Structure of Monoclinic $Fe_2(SO_4)_3$. Zeitschrift Fur Kristallographie, 141(3-4), 233-245.

-. (1976) Crystal-Structure of Rhombohedral $Fe_2(SO_4)_3$. Zeitschrift Fur Kristallographie, 144(5-6), 341-352.

Chupas, P.J., Chapman, K.W., and Lee, P.L. (2007) Applications of an amorphous silicon-based area detector for high-resolution, high-sensitivity and fast time-resolved pair distribution function measurements. Journal of Applied Crystallography, 40, 463-470.

Clark, B.C., Baird, A.K., Weldon, R.J., Tsusaki, D.M., Schnabel, L., and Candelaria, M.P. (1982) Chemical-Composition of Martian Fines. Journal of Geophysical Research, 87(Nb12), 59-67.

Clark, B.C., Morris, R.V., McLennan, S.M., Gellert, R., Jolliff, B., Knoll, A.H., Squyres, S.W., Lowenstein, T.K., Ming, D.W., Tosca, N.J., Yen, A., Christensen, P.R., Gorevan, S., Bruckner, J., Calvin, W., Dreibus, G., Farrand, W., Klingelhoefer, G., Waenke, H., Zipfel, J., Bell, J.F., Grotzinger, J., McSween, H.Y., and Rieder, R. (2005) Chemistry and mineralogy of outcrops at Meridiani Planum. Earth and Planetary Science Letters, 240(1), 73-94.

Clark, B.C., and Vanhart, D.C. (1981) The Salts of Mars. Icarus, 45(2), 370-378.

Cloutis, E.A., Craig, M.A., Kruzelecky, R.V., Jamroz, W.R., Scott, A., Hawthorne, F.C., and Mertzman, S.A. (2008) Spectral reflectance properties of minerals exposed to simulated Mars surface conditions. Icarus, 195(1), 140-168.

Cloutis, E.A., Craig, M.A., Mustard, J.F., Kruzelecky, R.V., Jamroz, W.R., Scott, A., Bish, D.L., Poulet, F., Bibring, J.P., and King, P.L. (2007) Stability of hydrated minerals on Mars. Geophysical Research Letters, 34, L20202, DOI: 10.1029/2007GL031267.

Cole, K.E., Paik, Y., Reeder, R.J., Schoonen, M., and Grey, C.P. (2004) H-2 MAS NMR studies of deuterated goethite (alpha-FeOOD). Journal of Physical Chemistry B, 108(22), 6938-6940.

Drits, V.A., Sakharov, B.A., Salyn, A.L., and Manceau, A. (1993) Structural Model for Ferrihydrite. Clay Minerals, 28(2), 185-207.

Dutrizac, J.E., and Jambor, J.I. (2000) Jarosites and Their Application in Hydrometallurgy. In C.N. Alpers, J.I. Jambor, and D.K. Nordstrom, Eds. Sulfate Minerals: Crystallography, Geochemistry, and Environmental Significance, Reviews in Mineralogy and Geochemistry, vol. 40, p. 405-452. Mineralogical Society of America, Geochemical Society, Washington, D. C.

Eggleton, R.A., and Fitzpatrick, R.W. (1988) New Data and a Revised Structural Model for Ferrihydrite. Clays and Clay Minerals, 36(2), 111-124.

Fanfani, L., Nunzi, A., and Zanazzi, P.F. (1970) The crystal structure of roemerite. American Mineralogist, 55(1-2), 78-89.

-. (1971) Crystal Structure of Butlerite. American Mineralogist, 56(5-6), 751-757.

Fanfani, L., Nunzi, A., Zanazzi, P.F., and Zanzari, A.R. (1973) Copiapite Problem - Crystal-Structure of a Ferrian Copiapite. American Mineralogist, 58(3-4), 314-322.

Fang, J.H., and Robinson, P.D. (1970) Crystal Structures and Mineral Chemistry of Hydrated Ferric Sulfates .1. Crystal Structure of Coquimbite. American Mineralogist, 55(9-10), 1534-1540.

Farrand, W.H., Bell, J.F., Johnson, J.R., Jolliff, B.L., Knoll, A.H., McLennan, S.M., Squyres, S.W., Calvin, W.M., Grotzinger, J.P., Morris, R.V., Soderblom, J., Thompson, S.D., Watters, W.A., and Yen, A.S. (2007) Visible and near-infrared multispectral analysis of rocks at Meridiani Planum, Mars, by the Mars Exploration Rover Opportunity. Journal of Geophysical Research-Planets, 112, E05S02, DOI: 10.1029/2006JE002773.

Farrand, W.H., Glotch, T.D., Rice, J.W., Hurowitz, J.A., and Swayze, G.A. (2009) Discovery of jarosite within the Mawrth Vallis region of Mars: Implications for the geologic history of the region. Icarus, 204(2), 478-488.

Fernandez-Martinez, A., Timon, V., Roman-Ross, G., Cuello, G.J., Daniels, J.E., and Ayora, C. (2010) The structure of schwertmannite, a nanocrystalline iron oxyhydroxysulfate. American Mineralogist, 95(8-9), 1312-1322.

Freeman, J.J., Wang, A., and Ling, Z.C. (2009) Ferric sulfates on Mars: Mission observations and laboratory investigations. Lunar and Planetary Science XXXX, Abstract no. 2284.

Gellert, R., Rieder, R., Bruckner, J., Clark, B.C., Dreibus, G., Klingelhofer, G., Lugmair, G., Ming, D.W., Wanke, H., Yen, A., Zipfel, J., and Squyres, S.W. (2006) Alpha particle X-ray spectrometer (APXS): Results from Gusev crater and calibration report. Journal of Geophysical Research-Planets, 111, E02S05, DOI: 10.1029/2005JE002555.

Gendrin, A., Mangold, N., Bibring, J.P., Langevin, Y., Gondet, B., Poulet, F., Bonello, G., Quantin, C., Mustard, J., Arvidson, R., and LeMouelic, S. (2005) Sulfates in martian layered terrains: the OMEGA/Mars Express view. Science, 307(5715), 1587-1591.

Giere, R., Sidenko, N.V., and Lazareva, E.V. (2003) The role of secondary minerals in controlling the migration of arsenic and metals from high-sulfide wastes (Berikul gold mine, Siberia). Applied Geochemistry, 18(9), 1347-1359.

Glotch, T. D., Bandfield, J. L., Christensen, P. R., Calvin, W. M., McLennan, S. M., Clark, B. C., Rogers, A. D. & Squyres, S. W. (2006). Journal of Geophysical Research-Planets 111, E12S03, DOI: 10.1029/2005JE002672.

Gooding, J.L., Wentworth, S.J., and Zolensky, M.E. (1988) Calcium-Carbonate and Sulfate of Possible Extraterrestrial Origin in the Eeta-79001 Meteorite. Geochimica Et Cosmochimica Acta, 52(4), 909-915.

Greenspan, L. (1977) Humidity Fixed-Points of Binary Saturated Aqueous-Solutions. Journal of Research of the National Bureau of Standards Section a-Physics and Chemistry, 81(1), 89-96.

Hammarstrom, J.M., Seal, R.R., Meier, A.L., and Kornfeld, J.M. (2005) Secondary sulfate minerals associated with acid drainage in the eastern US: recycling of metals and acidity in surficial environments. Chemical Geology, 215(1-4), 407-431.

Hammersley, A.P., Svensson, S.O., Hanfland, M., Fitch, A.N., and Hausermann, D. (1996) Two-dimensional detector software: From real detector to idealised image or two-theta scan. High Pressure Research, 14(4-6), 235-248.

Harrington, R., Hausner, D.B., Bhandari, N., Strongin, D.R., Chapman, K.W., Chupas, P.J., Middlemiss, D.S., Grey, C.P., and Parise, J.B. (2010) Investigation of Surface Structures by Powder Diffraction: A Differential Pair Distribution Function Study on Arsenate Sorption on Ferrihydrite. Inorganic Chemistry, 49(1), 325-330.

Harrison, P.M., Fischbac.Fa, Hoy, T.G., and Haggis, G.H. (1967) Ferric Oxyhydroxide Core of Ferritin. Nature, 216(5121), 1188-1190.

Hawthorne, F.C., Krivovichev, S.V., and Burns, P.C. (2000) The Crystal Chemistry of Sulfate Minerals. In C.N. Alpers, J.I. Jambor, and D.K. Nordstrom, Eds. Sulfate Minerals: Crystallography, Geochemistry, and Environmental Significance, Reviews in Mineralogy and Geochemistry, vol. 40, p. 1-112. Mineralogical Society of America, Geochemical Society, Washington, D. C.

Hiemstra, T., and Van Riemsdijk, W.H. (2009) A surface structural model for ferrihydrite I: Sites related to primary charge, molar mass, and mass density. Geochimica Et Cosmochimica Acta, 73(15), 4423-4436.

Hurowitz, J.A., McLennan, S.M., Lindsley, D.H., and Schoonen, M.A.A. (2005) Experimental epithermal alteration of synthetic Los Angeles meteorite: Implications for the origin of Martian soils and identification of hydrothermal sites on Mars. Journal of Geophysical Research-Planets, 110, E07002, DOI: 10.1029/2004JE002391.

Hurowitz, J.A., and McLennan, S.M. (2007) A similar to 3.5 Ga record of water-limited, acidic weathering conditions on Mars. Earth and Planetary Science Letters, 260(3-4), 432-443.

Inami, T., Nishiyama, M., Maegawa, S., and Oka, Y. (2000) Magnetic structure of the kagome lattice antiferromagnet potassium jarosite $KFe_3(OH)_6(SO_4)_2$. Physical Review B, 61(18), 12181-12186.

Jambor, J.I., Nordstrom, D.K., and Alpers, C.N. (2000) Metal-sulfate Salts from Sulfide Mineral Oxidation. In C.N. Alpers, J.I. Jambor, and D.K. Nordstrom, Eds. Sulfate Minerals: Crystallography, Geochemistry, and Environmental Significance, Reviews in Mineralogy and Geochemistry, vol. 40, p. 305-350. Mineralogical Society of America, Geochemical Society, Washington, D. C.

Jamieson, H.E., Robinson, C., Alpers, C.N., McCleskey, R.B., Nordstrom, D.K., and Peterson, R.C. (2005) Major and trace element composition of copiapite-group minerals and coexisting water from the Richmond mine, Iron Mountain, California. Chemical Geology, 215(1-4), 387-405.

Janney, D.E., Cowley, J.M., and Buseck, P.R. (2000) Structure of synthetic 2-line ferrihydrite by electron nanodiffraction. American Mineralogist, 85(9), 1180-1187.

-. (2001) Structure of synthetic 6-line ferrihydrite by electron nanodiffraction. American Mineralogist, 86(3), 327-335.

Jonsson, J., Jonsson, J., and Lovgren, L. (2006) Precipitation of secondary Fe(III) minerals from acid mine drainage. Applied Geochemistry, 21(3), 437-445.

Johnson, J.R., Bell, J.F., Cloutis, E., Staid, M., Farrand, W.H., Mccoy, T., Rice, M., Wang, A., and Yen, A. (2007) Mineralogic constraints on sulfur-rich soils from Pancam spectra at Gusev crater, Mars. Geophysical Research Letters, 34, L13202, DOI: 10.1029/2007GL029894.

King, P.L., and McSween, H.Y. (2005) Effects of H_2O, pH, and oxidation state on the stability of Fe minerals on Mars. Journal of Geophysical Research-Planets, 110, E12S10, DOI: 10.1029/2005JE002482.

Kishi, A., and Toraya, H. (2004) Simultaneous measurements of X-ray diffraction (XRD) and differential scanning calorimetry (DSC) data under controlled humidity condition: Instrumentation and application to studies on hydration, dehydration, and rehydration processes of pharmaceutical compounds. Powder Diffraction, 19(1), 31-35.

Klingelhofer, G., Morris, R.V., Bernhardt, B., Schroder, C., Rodionov, D.S., de Souza, P.A., Yen, A., Gellert, R., Evlanov, E.N., Zubkov, B., Foh, J., Bonnes, U., Kankeleit, E., Gutlich, P., Ming, D.W., Renz, F., Wdowiak, T., Squyres, S.W., and Arvidson, R.E. (2004) Jarosite and hematite at Meridiani Planum from Opportunity's Mossbauer spectrometer. Science, 306(5702), 1740-1745.

Klingelhofer, G., Morris, R.V., De Souza, P.A., Rodionov, D., and Schroder, C. (2006) Two earth years of Mossbauer studies of the surface of Mars with MIMOS II. Hyperfine Interactions, 170(1-3), 169-177.

Kounaves, S.P., Hecht, M.H., Kapit, J., Gospodinova, K., DeFlores, L., Quinn, R.C., Boynton, W.V., Clark, B.C., Catling, D.C., Hredzak, P., Ming, D.W., Moore, Q., Shusterman, J., Stroble, S., West, S.J., and Young, S.M.M. (2010) Wet Chemistry experiments on the 2007 Phoenix Mars Scout Lander mission: Data analysis and results. Journal of Geophysical Research-Planets, 115, E00E10, DOI: 10.1029/2009JE003424.

Lane, M.D., Bishop, J.L., Dyar, M.D., King, P.L., Parente, M., and Hyde, B.C. (2008) Mineralogy of the Paso Robles soils on Mars. American Mineralogist, 93(5-6), 728-739.

Langevin, Y., Poulet, F., Bibring, J.P., and Gondet, B. (2005) Sulfates in the north polar region of Mars detected by OMEGA/Mars express. Science, 307(5715), 1584-1586.

Larson, A.C., and Von Dreele, R.B. (2000) "General Structure Analysis System (GSAS)". Los Alamos National Laboratory Report LAUR 86-748.

Levi, C.G. (1998) Metastability and microstructure evolution in the synthesis of inorganics from precursors. Acta Materialia, 46(3), 787-800.

Linnow, K., Zeunert, A., and Steiger, M. (2006) Investigation of sodium sulfate phase transitions in a porous material using humidity- and temperature-controlled X-ray diffraction. Analytical Chemistry, 78(13), 4683-4689.

Madden, M.E.E., Bodnar, R.J., and Rimstidt, J.D. (2004) Jarosite as an indicator of water-limited chemical weathering on Mars. Nature, 431(7010), 821-823.

Majzlan, J., Botez, C., and Stephens, P.W. (2005) The crystal structures of synthetics $Fe_2(SO_4)_3(H_2O)_5$ and the type specimen of lausenite. American Mineralogist, 90(2-3), 411-416.

Majzlan, J., Dordevic, T., Kolitsch, U., and Schefer, J. (2010) Hydrogen bonding in coquimbite, nominally $Fe_2(SO_4)_3\,9H_2O$, and the relationship between coquimbite and paracoquimbite. Mineralogy and Petrology, 100(3-4), 241-248.

Majzlan, J., and Kiefer, B. (2006) An X-ray- and neutron-diffraction study of synthetic ferricopiapite, $Fe_{14/3}(SO_4)_6(OD,OH)_2(D_2O,H_2O)_{20}$, and ab initio calculations on the structure of magnesiocopiapite, $MgFe_4(SO_4)_6(OH)_2(H_2O)_{20}$. Canadian Mineralogist, 44, 1227-1237.

Majzlan, J., and Michallik, R. (2007) The crystal structures, solid solutions and infrared spectra of copiapite-group minerals. Mineralogical Magazine, 71(5), 553-569.

Majzlan, J., Navrotsky, A., McCleskey, R.B., and Alpers, C.N. (2006) Thermodynamic properties and crystal structure refinement of ferricopiapite, coquimbite, rhomboclase, and $Fe_2(SO_4)_3(H_2O)_5$. European Journal of Mineralogy, 18(2), 175-186.

Majzlan, J., Navrotsky, A., Stevens, R., Donaldson, M., Woodfield, B.F., and Boerio-Goates, J. (2005) Thermodynamics of monoclinic $Fe_2(SO_4)_3$. Journal of Chemical Thermodynamics, 37(8), 802-809.

Majzlan, J., Stevens, R., Boerio-Goates, J., Woodfield, B.F., Navrotsky, A., Burns, P.C., Crawford, M.K., and Amos, T.G. (2004) Thermodynamic properties, low-temperature heat-capacity anomalies, and single-crystal X-ray refinement of hydronium jarosite, $(H_3O)Fe_3(SO_4)_2(OH)_6$. Physics and Chemistry of Minerals, 31(8), 518-531.

Manceau, A. (2009) Evaluation of the structural model for ferrihydrite derived from real-space modelling of high-energy X-ray diffraction data. Clay Minerals, 44(1), 19-34.

Manceau, A., and Drits, V.A. (1993) Local-Structure of Ferrihydrite and Feroxyhite by Exafs Spectroscopy. Clay Minerals, 28(2), 165-184.

Manceau, A. and Gates, W. P. (1997) Surface structural model for ferrihydrite. Clays and Clay Minerals, 45(3), 448-460.

Mangold, N., Gendrin, A., Gondet, B., LeMouelic, S., Quantin, C., Ansan, V., Bibring, J.P., Langevin, Y., Masson, P., and Neukum, G. (2008) Spectral and geological study of the sulfate-rich region of West Candor Chasma, Mars. Icarus, 194(2), 519-543.

Marion, G.M., Kargel, J.S., and Catling, D.C. (2008) Modeling ferrous-ferric iron chemistry with application to martian surface geochemistry. Geochimica Et Cosmochimica Acta, 72(1), 242-266.

McLennan, S.M., Bell, J.F., Calvin, W.M., Christensen, P.R., Clark, B.C., de Souza, P.A., Farmer, J., Farrand, W.H., Fike, D.A., Gellert, R., Ghosh, A., Glotch, T.D., Grotzinger, J.P., Hahn, B., Herkenhoff, K.E., Hurowitz, J.A., Johnson, J.R., Johnson, S.S., Jolliff, B., Klingelhofer, G., Knoll, A.H., Learner, Z., Malin, M.C.,

McSween, H.Y., Pocock, J., Ruff, S.W., Soderblom, L.A., Squyres, S.W., Tosca, N.J., Watters, W.A., Wyatt, M.B., and Yen, A. (2005) Provenance and diagenesis of the evaporite-bearing Burns formation, Meridiani Planum, Mars. Earth and Planetary Science Letters, 240(1), 95-121.

McLennan, S.M., and Grotzinger, J.P. (2008) The Sedimentary Rock Cycle of Mars, in The Martian Surface: Compostion, Mineralogy, and Physical Properties. Cambridge Univ. Press (Cambridge) pp. 541-577.

Mereiter, K. (1974) Die Kristallstruktur von Rhomboklas $H_5O_2Fe(SO_4)_2 \cdot 2H2O$. Tschermaks Mineralogische Und Petrographische Mitteilungen, 21, 216-232.

Michel, F.M., Antao, S.M., Chupas, P.J., Lee, P.L., Parise, J.B., and Schoonen, M.A.A. (2005) Short- to medium-range atomic order and crystallite size of the initial FeS precipitate from pair distribution function analysis. Chemistry of Materials, 17(25), 6246-6255.

Michel, F.M., Barron, V., Torrent, J., Morales, M.P., Serna, C.J., Boily, J.F., Liu, Q.S., Ambrosini, A., Cismasu, A.C., and Brown, G.E. (2010) Ordered ferrimagnetic form of ferrihydrite reveals links among structure, composition, and magnetism. Proceedings of the National Academy of Sciences of the United States of America, 107(7), 2787-2792.

Michel, F.M., Ehm, L., Antao, S.M., Lee, P.L., Chupas, P.J., Liu, G., Strongin, D.R., Schoonen, M.A.A., Phillips, B.L., and Parise, J.B. (2007a) The structure of ferrihydrite, a nanocrystalline material. Science, 316(5832), 1726-1729.

Michel, F.M., Ehm, L., Liu, G., Han, W.Q., Antao, S.M., Chupas, P.J., Lee, P.L., Knorr, K., Eulert, H., Kim, J., Grey, C.P., Celestian, A.J., Gillow, J., Schoonen, M.A.A., Strongin, D.R., and Parise, J.B. (2007b) Similarities in 2-and 6-line ferrihydrite based on pair distribution function analysis of X-ray total scattering. Chemistry of Materials, 19(6), 1489-1496.

Milliken, R.E., Swayze, G.A., Arvidson, R.E., Bishop, J.L., Clark, R.N., Ehlmann, B.L., Green, R.O., Grotzinger, J.P., Morris, R.V., Murchie, S.L., Mustard, J.F., and Weitz, C. (2008) Opaline silica in young deposits on Mars. Geology, 36(11), 847-850.

Ming, D.W., Mittlefehldt, D.W., Morris, R.V., Golden, D.C., Gellert, R., Yen, A., Clark, B.C., Squyres, S.W., Farrand, W.H., Ruff, S.W., Arvidson, R.E., Klingelhofer, G., McSween, H.Y., Rodionov, D.S., Schroder, C., de Souza, P.A., and Wang, A. (2006) Geochemical and mineralogical indicators for aqueous processes in the Columbia Hills of Gusev crater, Mars. Journal of Geophysical Research-Planets, 111, E02S12, DOI: 10.1029/2005JE002560.

Miura, H., Niida, K., and Hirama, T. (1994) Mikasaite, $(Fe^{3+}, Al)_2(SO_4)_3$, a New Ferric Sulfate Mineral from Mikasa City, Hokkaido, Japan. Mineralogical Magazine, 58(393), 649-653.

Morris, R.V., Klingelhofer, G., Schroder, C., Fleischer, I., Ming, D.W., Yen, A.S., Gellert, R., Arvidson, R.E., Rodionov, D.S., Crumpler, L.S., Clark, B.C., Cohen, B.A., Mccoy, T.J., Mittlefehldt, D.W., Schmidt, M.E., de Souza, P.A., and Squyres, S.W. (2008) Iron mineralogy and aqueous alteration from Husband Hill through Home Plate at Gusev Crater, Mars: Results from the Mossbauer instrument on the Spirit Mars Exploration Rover. Journal of Geophysical Research-Planets, 113, E12S42, DOI: 10.1029/2008JE003201.

Morris, R.V., Klingelhofer, G., Schroder, C., Rodionov, D.S., Yen, A., Ming, D.W., de Souza, P.A., Fleischer, I., Wdowiak, T., Gellert, R., Bernhardt, B., Evlanov, E.N., Zubkov, B., Foh, J., Bonnes, U., Kankeleit, E., Gutlich, P., Renz, F., Squyres, S.W., and Arvidson, R.E. (2006a) Mossbauer mineralogy of rock, soil, and dust at Gusev crater, Mars: Spirit's journey through weakly altered olivine basalt on the plains and pervasively altered basalt in the Columbia Hills. Journal of Geophysical Research-Planets, 111, E02S13, DOI: 10.1029/2005JE002584.

Morris, R.V., Klingelhofer, G., Schroder, C., Rodionov, D.S., Yen, A., Ming, D.W., de Souza, P.A., Wdowiak, T., Fleischer, I., Gellert, R., Bernhardt, B., Bonnes, U., Cohen, B.A., Evlanov, E.N., Foh, J., Gutlich, P., Kankeleit, E., McCoy, T., Mittlefehldt, D.W., Renz, F., Schmidt, M.E., Zubkov, B., Squyres, S.W., and Arvidson, R.E. (2006b) Mossbauer mineralogy of rock, soil, and dust at Meridiani Planum, Mars: Opportunity's journey across sulfate-rich outcrop, basaltic sand and dust, and hematite lag deposits. Journal of Geophysical Research-Planets, 111, E12S15, DOI: 10.1029/2006JE002791.

Nordstrom, D.K., and Alpers, C.N. (1999) Negative pH, efflorescent mineralogy, and consequences for environmental restoration at the Iron Mountain Superfund site, California. Proceedings of the National Academy of Sciences of the United States of America, 96(7), 3455-3462.

Nordstrom, D.K., Alpers, C.N., Ptacek, C.J., and Blowes, D.W. (2000) Negative pH and extremely acidic mine waters from Iron Mountain, California. Environmental Science & Technology, 34(2), 254-258.

Paglia, G., Bozin, E.S., and Billinge, S.J.L. (2006) Fine-scale nanostructure in gamma-Al2O3. Chemistry of Materials, 18(14), 3242-3248.

Peterson, R.C., and Grant, A.H. (2005) Dehydration and crystallization reactions of secondary sulfate minerals found in mine waste: In situ powder-diffraction experiments. Canadian Mineralogist, 43, 1171-1181.

Peterson, R.C., Valyashko, E., and Wang, R.Y. (2009) The atomic structure of $(H_3O)Fe^{3+}(SO_4)_2$ and rhomboclase, $(H_5O_2)Fe^{3+}(SO_4)_2 \cdot 2H_2O$. Canadian Mineralogist, 47(3), 625-634.

Peterson, R.C., and Wang, R.Y. (2006) Crystal molds on Mars: Melting of a possible new mineral species to create Martian chaotic terrain. Geology, 34(11), 957-960.

Petkov, V., Billinge, S.J.L., Larson, P., Mahanti, S.D., Vogt, T., Rangan, K.K., and Kanatzidis, M.G. (2002) Structure of nanocrystalline materials using atomic pair distribution function analysis: Study of LiMoS2. Physical Review B, 65(9), -.

Petkov, V., Ren, Y., Saratovsky, I., Pasten, P., Gurr, S.J., Hayward, M.A., Poeppelmeier, K.R., and Gaillard, J.F. (2009) Atomic-Scale Structure of Biogenic Materials by Total X-ray Diffraction: A Study of Bacterial and Fungal MnOx. Acs Nano, 3(2), 441-445.

Pinney, N., Kubicki, J.D., Middlemiss, D.S., Grey, C.P., and Morgan, D. (2009) Density Functional Theory Study of Ferrihydrite and Related Fe-Oxyhydroxides. Chemistry of Materials, 21(24), 5727-5742.

Poulet, F., Arvidson, R.E., Gomez, C., Morris, R.V., Bibring, J.P., Langevin, Y., Gondet, B., and Griffes, J. (2008) Mineralogy of Terra Meridiani and western Arabia Terra from OMEGA/MEx and implications for their formation. Icarus, 195(1), 106-130.

Poulet, F., Bibring, J.P., Mustard, J.F., Gendrin, A., Mangold, N., Langevin, Y., Arvidson, R.E., Gondet, B., Gomez, C., and Team, O. (2005) Phyllosilicates on Mars and implications for early martian climate. Nature, 438(7068), 623-627.

Proffen, T., and Billinge, S.J.L. (1999) PDFFIT, a program for full profile structural refinement of the atomic pair distribution function. Journal of Applied Crystallography, 32, 572-575.

Proffen, T., and Neder, R.B. (1997) DISCUS: A program for diffuse scattering and defect-structure simulation. Journal of Applied Crystallography, 30, 171-175.

Qiu, X., Thompson, J.W., and Billinge, S.J.L. (2004) PDFgetX2: a GUI-driven program to obtain the pair distribution function from X-ray powder diffraction data. Journal of Applied Crystallography, 37(4), 678.

Rancourt, D.G., and Meunier, J.F. (2008) Constraints on structural models of ferrihydrite as a nanocrystalline material. American Mineralogist, 93(8-9), 1412-1417.

Rietveld, H.M. (1969) A Profile Refinement Method for Nuclear and Magnetic Structures. Journal of Applied Crystallography, 2, 65-&.

Roach, L.H., Mustard, J.F., Murchie, S.L., Bibring, J.P., Forget, F., Lewis, K.W., Aharonson, O., Vincendon, M., and Bishop, J.L. (2009) Testing evidence of recent hydration state change in sulfates on Mars. Journal of Geophysical Research-Planets, 114, E00D02, DOI: 10.1029/2008JE003245.

Robinson, P.D., and Fang, J.H. (1971) Crystal Structures and Mineral Chemistry of Hydrated Ferric Sulphates .2. Crystal Structure of Paracoquimbite. American Mineralogist, 56(9-10), 1567-1572.

-. (1973) Crystal-Structures and Mineral Chemistry of Hydrated Ferric Sulfates .3. Crystal-Structure of Kornelite. American Mineralogist, 58(5-6), 535-539.

Romero, A., Gonzalez, I., and Galan, E. (2006) The role of efflorescent sulfates in the storage of trace elements in stream waters polluted by acid mine-drainage: The case of Pena del Hierro, southwestern Spain. Canadian Mineralogist, 44, 1431-1446.

Russell, J.D. (1979) Infrared Spectroscopy of Ferrihydrite - Evidence for the Presence of Structural Hydroxyl-Groups. Clay Minerals, 14(2), 109-114.

Savijarvi, H. (1995) Mars Boundary-Layer Modeling - Diurnal Moisture Cycle and Soil Properties at the Viking-Lander-1 Site. Icarus, 117(1), 120-127.

Schwertmann, U., and Cornell, R.M. (1991) Iron Oxides in the Laboratory: Preperation and Characterization. Wiley-VCH, New York, p105.

Schwertmann, U., Friedl, J., and Stanjek, H. (1999) From Fe(III) ions to ferrihydrite and then to hematite. Journal of Colloid and Interface Science, 209(1), 215-223.

Scordari, F. (1981) Fibroferrite - a Mineral with a $Fe(OH)(H_2O)_2SO_4$ Spiral Chain and Its Relationship to $Fe(OH)SO_4$, Butlerite and Parabutlerite. Tschermaks Mineralogische Und Petrographische Mitteilungen, 28(1), 17-29.

Scordari, F., Ventruti, G., and Gualtieri, A.F. (2004) The structure of metahohmannite, $Fe^{3+}_2[O(SO_4)_2] \cdot 4H_2O$, by in situ synchrotron powder diffraction. American Mineralogist, 89(2-3), 365-370.

Squyres, S.W., Grotzinger, J.P., Arvidson, R.E., Bell, J.F., Calvin, W., Christensen, P.R., Clark, B.C., Crisp, J.A., Farrand, W.H., Herkenhoff, K.E., Johnson, J.R., Klingelhofer, G., Knoll, A.H., McLennan, S.M., McSween, H.Y., Morris, R.V., Rice, J.W., Rieder, R., and Soderblom, L.A. (2004) In situ evidence for an ancient aqueous environment at Meridiani Planum, Mars. Science, 306(5702), 1709-1714.

Squyres, S.W., and Knoll, A.H. (2005) Sedimentary rocks at Meridiani Planum: Origin, diagetiesis, and implications for life on Mars. Earth and Planetary Science Letters, 240(1), 1-10.

Squyres, S.W., Knoll, A.H., Arvidson, R.E., Clark, B.C., Grotzinger, J.P., Jolliff, B.L., McLennan, S.M., Tosca, N., Bell, J.F., Calvin, W.M., Farrand, W.H., Glotch, T.D., Golombek, M.P., Herkenhoff, K.E., Johnson, J.R., Klingelhofer, G., McSween, H.Y., and Yen, A.S. (2006) Two years at Meridiani Planum: Results from the Opportunity Rover. Science, 313(5792), 1403-1407.

Stanjek, H., and Weidler, P.G. (1992) The Effect of Dry Heating on the Chemistry, Surface-Area, and Oxalate Solubility of Synthetic 2-Line and 6-Line Ferrihydrites. Clay Minerals, 27(4), 397-412.

Stoffregen, R.E., Alpers, C.N., and Jambor, J.I. (2000) Alunite-Jarosite Crystallography, Thermodynamics, and Geochronology. In C.N. Alpers, J.I. Jambor, and D.K. Nordstrom, Eds. Sulfate Minerals: Crystallography, Geochemistry, and Environmental Significance, Reviews in Mineralogy and Geochemistry, vol. 40, p. 453-480. Mineralogical Society of America, Geochemical Society, Washington, D. C.

Susse, P. (1972) Crystal-Structure and Hydrogen-Bonding of Copiapite. Zeitschrift Fur Kristallographie Kristallgeometrie Kristallphysik Kristallchemie, 135(1-2), 34-55.

Szczygiel, R., Grybos, P., Maj, P., Tsukiyama, A., Matsushita, K., and Taguchi, T. (2009) Low-noise multichannel ASIC for high count rate X-ray diffractometry applications. Nuclear Instruments & Methods in Physics Research Section a-Accelerators Spectrometers Detectors and Associated Equipment, 607(1), 229-232.

Thomas, J.N., Robinson, P.D., and Fang, J.H. (1974) Crystal-Structures and Mineral Chemistry of Hydrated Ferric Sulfates .4. Crystal-Structure of Quenstedtite. American Mineralogist, 59(5-6), 582-586.

Toby, B.H. (2001) EXPGUI, a graphical user interface for GSAS. Journal of Applied Crystallography, 34, 210-213.

Tosca, N.J., and McLennan, S.M. (2009) Experimental constraints on the evaporation of partially oxidized acid-sulfate waters at the martian surface. Geochimica Et Cosmochimica Acta, 73(4), 1205-1222.

Tosca, N.J., McLennan, S.M., Dyar, M.D., Sklute, E.C., and Michel, F.M. (2008) Fe oxidation processes at Meridiani Planum and implications for secondary Fe mineralogy on Mars. Journal of Geophysical Research-Planets, 113(E5), -.

Tosca, N.J., Smirnov, A., and McLennan, S.M. (2007) Application of the Pitzer ion interaction model to isopiestic data for the $Fe_2(SO_4)_3$-H_2SO_2-H_2O system at 298.15 and 323.15 K. Geochimica Et Cosmochimica Acta, 71(11), 2680-2698.

Toulmin, P., Baird, A.K., Clark, B.C., Keil, K., Rose, H.J., Christian, R.P., Evans, P.H., and Kelliher, W.C. (1977) Geochemical and Mineralogical Interpretation of Viking Inorganic Chemical Results. Journal of Geophysical Research, 82(28), 4625-4634.

Towe, K.M., and Bradley, W.F. (1967) Mineralogical Constitution of Colloidal Hydrous Ferric Oxides. Journal of Colloid and Interface Science, 24(3), 384-392.

Vaniman, D.T., Bish, D.L., Chipera, S.J., Fialips, C.I., Carey, J.W., and Feldman, W.C. (2004) Magnesium sulphate salts and the history of water on Mars. Nature, 431(7009), 663-665.

Wang, A., Bell, J.F., Li, R., Johnson, J.R., Farrand, W.H., Cloutis, E.A., Arvidson, R.E., Crumpler, L., Squyres, S.W., McLennan, S.M., Herkenhoff, K.E., Ruff, S.W., Knudson, A.T., Chen, W., and Greenberger, R. (2008) Light-toned salty soils and coexisting Si-rich species discovered by the Mars Exploration Rover Spirit in Columbia Hills. Journal of Geophysical Research-Planets, 113, E12S40, DOI: 10.1029/2008JE003126.

Waseda, Y. (1980) The structure of Non-crystalline Materials. McGraw-Hill, New York.

Weidler, P.G. (1997) BET Sample Pretreatment of Synthetic Ferrihydrite and its Influence on the Determination of Surface Area and Porosity. Journal of Porous Materials, 4(3), 165-169.

Xu, W.Q., Tosca, N.J., McLennan, S.M., and Parise, J.B. (2009) Humidity-induced phase transitions of ferric sulfate minerals studied by in situ and ex situ X-ray diffraction. American Mineralogist, 94(11-12), 1629-1637.

Yen, A.S., Morris, R.V., Clark, B.C., Gellert, R., Knudson, A.T., Squyres, S., Mittlefehldt, D.W., Ming, D.W., Arvidson, R., Mccoy, T., Schmidt, M., Hurowitz, J., Li, R., and Johnson, J.R. (2008) Hydrothermal processes at Gusev Crater: An evaluation of Paso Robles class soils. Journal of Geophysical Research-Planets, 113, E06S10, DOI: 10.1029/2007JE002978.

Yen, A.S., Murray, B., Rossman, G.R., and Grunthaner, F.J. (1999) Stability of hydroxylated minerals on Mars: A study on the effects of exposure to ultraviolet radiation. Journal of Geophysical Research-Planets, 104(E11), 27031-27041.

Zhao, J.M., Huggins, F.E., Feng, Z., and Huffman, G.P. (1994) Ferrihydrite - Surface-Structure and Its Effects on Phase-Transformation. Clays and Clay Minerals, 42(6), 737-746.

Appendix

Crystal structure of a new ferric sulfate hydrate $(H_3O)Fe_2(OH)(SO_4)_3 \cdot 7H_2O$

Abstract

A new phase precipitates from concentrated $Fe_2(SO_4)_3$ solutions along with ferricopiapite ($Fe_{4.67}(SO_4)_6(OH)_2 \cdot 20H_2O$) and rhomboclase ($(H_3O)Fe(SO_4)_2 \cdot 3H_2O$) at room temperature (RT) and 43% relative humidity (RH). Its crystal structure was determined from synchrotron single-crystal X-ray diffraction data. This new phase is triclinic, space group $P\bar{1}$, with cell parameters a = 7.563(2) Å, b = 15.075(3) Å, c = 16.387 (3) Å, α = 94.969(7)°, β = 91.851(7)°, γ = 89.998(7)°, V = 1835.6(7) Å^3, Z = 4. The structure is composed of $[Fe_2(SO_4)_2(OH)(H_2O)_6]^+$ clusters, isolated SO_4^{2-} anions, disordered water molecules and hydronium ions. However, the site assignment of water molecules and hydronium ions remains ambiguous. This new phase was previously observed as an intermediate hydration product of trigonal $Fe_2(SO_4)_3$, as shown in Figure 2.8 in Chapter 2.

A1. Synthesis and Characterization

Anhydrous $Fe_2(SO_4)_3$ was prepared by heating ferric sulfate hydrate from J. T. Baker (Baker Analyzed, Assay $Fe_2(SO_4)_3$ > 73.0%) at 340°C for 2 hours. Thermogravimetric analysis (TGA) confirmed its anhydrous state, and powder XRD indicated it as pure triclinic $Fe_2(SO_4)_3$ (ICSD-22368). For a typical synthesis, 1.34 g $Fe_2(SO_4)_3$ was mixed with 1.74 g distilled water to produce a clear dark brown solution formed after sonication for 0.5 hours. This solution was then evaporated at 43% RH and room T (~22°C). The stable RH condition was achieved by the humidity buffer method described in Chapter 2: the sample was preserved in a closed container with saturated K_2CO_3 solution and an excess of solid K_2CO_3. A yellow precipitate formed after 10 days.

Powder X-ray diffraction (XRD) pattern of the yellow product was taken on a Rigaku Ultima IV diffractometer using CuKα radiation (λ = 1.54178 Å) and a high-speed semiconductor element one-dimensional detector capable of Fe fluorescence suppression. Preliminary XRD results suggest the product was composed of ferricopiapite, rhomboclase and the new iron sulfate phase that was previously observed in *ex situ* hydration experiments on trigonal $Fe_2(SO_4)_3$ (Fig. 2.8 in Chapter 2). The three phases were not evenly distributed in the vial, with the new phase agglomerated at the bottom 10% (volume estimate) of the precipitate where ferricopiapite was very rare (Fig. A1). Single crystals of the new phase are plate-like with the shortest dimension no larger than 5 µm. Crystals tend to form piles, strongly bond along the shortest dimension and are not easily separated, making it very difficult to find an single crystal. A microcrystal of this phase (5 × 29 × 136 µm) was taken to the Advanced Photon Source and data were collected at ChemMatCars (beamline No. 15-IDB), using a three-circle Bruker D8 diffractometer equipped with an APEXII detector. The radiation wavelength was 0.41328(1) Å. The raw data were processed using the APEX-II suite of software

(Bruker, 2006). The crystal was found to be a 50/50 twin with the two individuals related by a 180.0° rotation about the real axis [1 0 0]. The data were integrated based on the two components. Absorption correction was performed using TWINABS. The structure was solved and refined using SHELXL97 (Sheldrick, 2008).

Combined thermogravimetric and differential scanning calorimetric analysis (TG and DSC) was conducted on a Netzsch STA 449C Jupiter simultaneous TG-DSC apparatus, in order to constrain the water content in the structure. 9.0 mg powder sample used to collect XRD data shown in Figure A1 was loaded into an alumina crucible, and heated from room temperature to 800°C at a rate of 10°C/min under N_2 protection.

A2. Results and Discussion

A2.1. Crystal Structure

The crystal structure of the new iron sulfate phase consists of isolated $[Fe_2(SO_4)_2(OH)(H_2O)_6]^+$ clusters and $[SO_4]^{2-}$ groups, disordered H_2O and H_3O^+, as shown in Figure A2. H atoms on the cluster were not located from the XRD data, but their association with O is consistent with the calculations of bond valence shown in Table A3 (Brown and Altermatt, 1985). In the cation cluster, each Fe^{3+} is octahedrally coordinated by three H_2O molecules, two O atoms from two $[SO_4]^{2-}$ groups in cis configuration and one OH bridging to the other Fe^{3+}. A similar structure motif exists in copiapite group minerals, except that the clusters in copiapite are linked by $[SO_4]^{2-}$. Seven O sites, designated from O39 to O45 in Table A2, are distributed on the z = 0 plane (Fig. A2). The occupancies of these sites were assigned to disordered H_2O and H_3O^+ based on the scattering powder and charge balance calculation. The seven sites can be divided into two groups based on the inter-atomic distances, with O39 to O42 in one group and O43 to O45 in the other. The total site occupancy of each group was constrained to 2 during the refinement, which gave reasonable displacement parameters for all sites. This assignment of total occupancy was in agreement with the TG data shown below. However, unrealistically short O-O distances, e.g. d(O39-O44) is 1.43 Å, requires that a maximum summed occupancy of 1 be assigned to each group. Refinement of this model for total occupancy resulted in non-positive thermal parameters, suggesting the sites contain atoms heavier than oxygen, possibly sulfur. The shape of the two groups of sites resembles SO_2 and SO_3, and the S-O bond can be as short as 1.43 Å. However, these sites can not be SO_2 and SO_3 or SO_3^{2-}, because there was no reductant for reducing SO_4^{2-} in the starting materials: ferric sulfate and water. Besides, for the purpose of charge balance, these two groups of sites need to be positively charged. The current structure solution still assumes those sites are disordered H_2O and H_3O^+, but it is not conclusive due to the reasons discussed above. The ambiguity is probably due to the quality of XRD data that is limited by the quality of the single crystal. The crystals grown in this study had a platy morphology with a thickness smaller than 5 μm. Most of the crystals show undulatory extinctions under crossed polars.

A2.2. Thermal properties

TG and DSC data were plotted in Figure A3. Three weight loss events were recorded in TG with a total weight loss equal to 72.0%. XRD of the heating product confirmed it as pure hematite (α-Fe_2O_3). Two more heating runs to 200°C and 400°C

were performed. The heating products up to these intermediate temperatures were amorphous indicated by XRD. Since Fe was conserved in the solid phases throughout the heating, the percentage of Fe in the initial sample was calculated to be 19.6% based on the resultant hematite. This value could be further used to estimate the water content in the new phase. The estimation takes account of the fact that the starting sample was a mixture of the new phase, rhomboclase and ferricopiapite. To get the proportions of each phase, quantitative Rietveld analysis was performed with TOPAS 4.1 (Bruker, 2008; Rietveld, 1969). Scale factors and specimen shift were refined. The weight percentages were 82% for the new phase, 15% for rhomboclase and 3% for ferricopiapite. Since the percentage of Fe in rhomboclase and ferricopiapite are 17.4% and 21.2% based on their formulas, the percentage of Fe in the new phase was calculated to be 19.9%. Applying this value to the formula, $[Fe_2(SO_4)_2(OH)(H_2O)_6]^+$ $(H_3O)^+$ $SO_4^{2-} \cdot x\ H_2O$, x was then calculated to be 1.0. The formula could be rewritten as $(H_3O)Fe_2(OH)(SO_4)_3 \cdot 7H_2O$. The TG result supports the occupancy assignment for the disordered H_2O sites discussed earlier.

A2.3. Diagenetic relations with other ferric sulfates

In the previous study, the same three phase mixture including ferricopiapite, rhomboclase and the new ferric sulfate phase was also observed at the initial hydration stage of trigonal $Fe_2(SO_4)_3$ at 43% and 53% RH and room T. The mixture transformed to kornelite ($Fe_2(SO_4)_3 \cdot 7.25H_2O$) then paracoquimbite ($Fe_2(SO_4)_3 \cdot 9H_2O$) after months. That hydration condition was the same as the precipitation condition used in the current study - 43% RH and room T (~22°C). It should be noted that this preparation condition does not guarantee the formation of this new ferric sulfate phase. In fact, this is the only time that this new phase was successfully made of totally three attempts using the same preparation method, with the other two times only crystallizing ferricopiapite and rhomboclase. Even in this successful synthesis, the new phase only took a small part of all the precipitates in which ferricopiapite and rhomboclase still dominated. The optimal crystallization condition of the new phase is not clear. Its close association with ferricopiapite is understandable considering they share similar structure motif $[Fe_2(SO_4)_2(OH)(H_2O)_6]^+$. The new phase, like ferricopiapite, is also a metastable phase in the evolution of ferric sulfate solution, which will finally evolve to paracoquimbite under the condition of synthesis, 43% RH and 22 °C.

References:

Brown, I.D., and Altermatt, D. (1985) Bond-Valence Parameters Obtained from a Systematic Analysis of the Inorganic Crystal-Structure Database. Acta Crystallographica Section B-Structural Science, 41(Aug), 244-247.

Bruker. (2006) Apex-II. Bruker AXS Inc. Madison.

-. (2008) TOPAS 4 Technical Reference, Bruker AXS GmbH, Karlsruhe, Germany.

Rietveld, H.M. (1969) A Profile Refinement Method for Nuclear and Magnetic Structures. Journal of Applied Crystallography, 2, 65-75.

Sheldrick, G.M. (2008) A short history of SHELX. Acta Crystallographica Section A, 64, 112-122.

Table A1. Crystallographic information for $(H_3O)Fe_2(OH)(SO_4)_3 \cdot 7H_2O$

Empirical formula	$(H_3O)Fe_2(OH)(SO_4)_3 \cdot 7H_2O$
Formula weight	544.31
Collection temperature (K)	298
Wavelength (Å)	0.41328(2)
Symmetry	Triclinic
Space group	P -1
Unit cell dimensions (Å and °)	a = 7.463(2)
	b = 15.075(3)
	c = 16.387(3)
	α = 94.969(7)
	β = 91.851(7)
	γ = 89.998(7)
Volume ($Å^3$)	1835.6(7)
Z	4
Calculated density (g/cm^3)	1.969
Absorption coefficient (mm^{-1})	0.417
F(000)	1073
Goodness of fit	1.040
R [I/s >2]	R = 0.0707
	wR = 0.1788
R (all reflections)	R = 0.0977
	wR = 0.1973

Table A2. Coordinates and displacement parameters of atoms

Atom	*x*	*y*	*z*	U_{eq}	*Occ.*
Fe1	0.34879(16)	0.89577(7)	0.30290(8)	0.0143(3)	1
Fe2	0.84661(16)	0.56957(7)	0.30185(7)	0.0133(3)	1
Fe3	1.16177(16)	0.40161(7)	0.28476(7)	0.0139(3)	1
Fe4	0.66517(16)	1.06116(7)	0.29151(7)	0.0140(3)	1
S1	0.7611(3)	0.38654(13)	0.19375(13)	0.0151(4)	1
S2	0.2667(3)	1.06255(13)	0.20099(13)	0.0159(4)	1
S3	0.6829(3)	0.87599(13)	0.18522(13)	0.0166(4)	1
S4	0.7869(3)	0.85619(13)	0.50473(13)	0.0160(4)	1
S5	1.1736(3)	0.56835(12)	0.17694(13)	0.0150(4)	1
S6	0.2866(3)	0.63954(13)	0.50397(13)	0.0161(4)	1
O1	0.6448(8)	0.3120(4)	0.2059(4)	0.0257(15)	1
O2	0.9459(8)	0.3626(4)	0.2182(4)	0.0229(14)	1
O3	0.7051(8)	0.4650(3)	0.2515(4)	0.0208(14)	1
O4	0.7530(10)	0.4088(5)	0.1107(4)	0.0365(18)	1
O5	0.2088(8)	0.9946(4)	0.2561(4)	0.0207(14)	1
O6	0.2624(10)	1.0253(5)	0.1178(4)	0.0348(17)	1
O7	0.1480(8)	1.1382(4)	0.2133(4)	0.0249(15)	1
O8	0.4507(8)	1.0940(4)	0.2273(4)	0.0255(15)	1
O9	0.7791(9)	0.8190(4)	0.2395(5)	0.0333(17)	1
O10	0.7059(10)	0.8510(5)	0.0994(4)	0.0389(19)	1
O11	0.4868(8)	0.8703(4)	0.2000(4)	0.0205(14)	1
O12	0.7413(8)	0.9694(4)	0.2051(4)	0.0242(15)	1
O13	0.7499(9)	0.7925(4)	0.4343(4)	0.0349(19)	1
O14	0.6886(9)	0.9387(4)	0.4921(4)	0.0267(15)	1
O15	0.7276(9)	0.8209(4)	0.5798(4)	0.0300(16)	1
O16	0.9825(9)	0.8716(5)	0.5134(4)	0.0298(16)	1
O17	1.2382(8)	0.4804(4)	0.2016(4)	0.0217(14)	1
O18	0.9800(8)	0.5775(4)	0.1981(4)	0.0193(13)	1
O19	1.1811(10)	0.5697(4)	0.0897(4)	0.0293(15)	1
O20	1.2775(9)	0.6388(4)	0.2218(4)	0.0291(16)	1
O21	0.2554(9)	0.6879(5)	0.4307(5)	0.0369(19)	1
O22	0.1871(9)	0.5555(4)	0.4919(4)	0.0262(15)	1
O23	0.2229(9)	0.6903(4)	0.5776(4)	0.0313(17)	1
O24	0.4802(8)	0.6247(4)	0.5145(4)	0.0278(15)	1
O25	0.4534(8)	0.7889(4)	0.3510(4)	0.0210(13)	1
O26	0.2076(9)	0.9246(4)	0.4059(4)	0.0227(14)	1
O27	0.1530(8)	0.8107(4)	0.2542(4)	0.0220(14)	1
O28	0.5345(8)	0.9754(4)	0.3493(3)	0.0168(12)	1
O29	0.7087(9)	0.5589(4)	0.4048(4)	0.0261(14)	1
O30	0.6527(8)	0.6504(4)	0.2566(4)	0.0241(14)	1
O31	0.9589(9)	0.6833(4)	0.3508(4)	0.0221(14)	1
O32	1.0348(8)	0.4968(4)	0.3441(3)	0.0172(13)	1
O33	1.1082(9)	0.3202(4)	0.3720(5)	0.0331(17)	1
O34	1.2910(9)	0.3010(4)	0.2198(4)	0.0256(15)	1
O35	1.3996(8)	0.4309(4)	0.3456(4)	0.0255(15)	1
O36	0.7961(9)	1.1549(4)	0.2349(4)	0.0286(16)	1
O37	0.8998(8)	1.0401(4)	0.3505(4)	0.0244(14)	1

O38	0.6144(9)	1.1540(4)	0.3833(5)	0.0344(18)	1
O39	0.391(2)	0.8860(15)	-0.0400(10)	0.051(7)	0.44(2)
O40	0.042(4)	0.8834(15)	-0.0201(14)	0.099(12)	0.48(3)
O41	0.261(3)	0.7796(11)	0.0436(14)	0.051(8)	0.38(2)
O42	0.1538(19)	0.3502(9)	1.0171(9)	0.047(5)	0.60(2)
O43	0.405(2)	0.4026(10)	0.9429(9)	0.057(5)	0.61(2)
O44	0.2642(18)	0.8673(7)	0.0202(7)	0.055(5)	0.75(3)
O45	0.2210(12)	0.4211(6)	0.9707(6)	0.032(3)	0.79(2)

Atom	U_{11}	U_{22}	U_{33}	U_{23}	U_{13}	U_{12}
Fe1	0.0110(7)	0.0110(5)	0.0214(7)	0.0031(4)	0.0028(5)	-0.0019(5)
Fe2	0.0110(7)	0.0104(5)	0.0187(6)	0.0011(4)	0.0029(5)	0.0002(4)
Fe3	0.0091(7)	0.0120(5)	0.0211(7)	0.0034(5)	0.0009(5)	0.0005(4)
Fe4	0.0093(7)	0.0104(5)	0.0226(7)	0.0014(5)	0.0022(5)	-0.0023(4)
S1	0.0112(11)	0.0124(9)	0.0214(11)	0.0000(8)	-0.0003(8)	-0.0013(8)
S2	0.0126(11)	0.0129(9)	0.0226(12)	0.0036(8)	0.0012(9)	0.0019(8)
S3	0.0150(11)	0.0134(9)	0.0211(11)	-0.0004(8)	0.0035(9)	0.0004(8)
S4	0.0127(11)	0.0153(9)	0.0199(11)	0.0004(8)	-0.0001(9)	-0.0004(8)
S5	0.0131(11)	0.0118(8)	0.0205(11)	0.0014(8)	0.0056(9)	-0.0026(8)
S6	0.0129(11)	0.0175(9)	0.0183(11)	0.0043(8)	0.0011(8)	-0.0014(8)
O1	0.007(3)	0.018(3)	0.052(5)	-0.001(3)	0.004(3)	-0.004(2)
O2	0.005(3)	0.020(3)	0.043(4)	-0.004(3)	0.001(3)	0.003(2)
O3	0.024(4)	0.010(2)	0.028(4)	-0.007(2)	0.005(3)	-0.002(2)
O4	0.044(5)	0.037(4)	0.027(4)	-0.004(3)	-0.001(3)	0.007(3)
O5	0.018(3)	0.013(3)	0.034(4)	0.011(2)	0.004(3)	0.001(2)
O6	0.043(5)	0.037(4)	0.024(4)	0.000(3)	-0.001(3)	-0.003(3)
O7	0.014(4)	0.014(3)	0.048(4)	0.012(3)	0.005(3)	0.004(2)
O8	0.010(3)	0.025(3)	0.043(4)	0.014(3)	-0.004(3)	-0.003(2)
O9	0.022(4)	0.018(3)	0.062(5)	0.016(3)	-0.006(3)	0.004(3)
O10	0.039(5)	0.044(4)	0.033(4)	-0.010(3)	0.019(3)	-0.005(3)
O11	0.015(3)	0.023(3)	0.023(3)	-0.002(3)	0.007(3)	-0.006(2)
O12	0.020(4)	0.018(3)	0.035(4)	0.000(3)	0.011(3)	-0.005(3)
O13	0.026(4)	0.034(4)	0.040(4)	-0.022(3)	-0.008(3)	0.006(3)
O14	0.034(4)	0.022(3)	0.023(3)	0.002(3)	-0.009(3)	0.012(3)
O15	0.020(4)	0.035(4)	0.038(4)	0.021(3)	0.012(3)	0.005(3)
O16	0.013(4)	0.045(4)	0.032(4)	-0.001(3)	0.006(3)	-0.009(3)
O17	0.013(3)	0.019(3)	0.034(4)	0.007(3)	0.008(3)	0.007(2)
O18	0.011(3)	0.025(3)	0.022(3)	0.003(3)	0.010(2)	0.003(2)
O19	0.038(4)	0.031(3)	0.020(3)	0.009(3)	0.010(3)	-0.001(3)
O20	0.022(4)	0.018(3)	0.046(4)	-0.008(3)	0.000(3)	-0.004(3)
O21	0.020(4)	0.052(4)	0.043(5)	0.031(4)	-0.014(3)	-0.011(3)
O22	0.030(4)	0.022(3)	0.025(3)	-0.001(3)	-0.007(3)	-0.009(3)
O23	0.033(4)	0.030(3)	0.030(4)	-0.011(3)	0.023(3)	-0.008(3)
O24	0.013(4)	0.043(4)	0.029(4)	0.006(3)	0.003(3)	0.005(3)
O25	0.018(3)	0.020(3)	0.026(4)	0.009(3)	0.001(3)	-0.003(2)
O26	0.022(4)	0.025(3)	0.022(3)	-0.001(3)	0.012(3)	-0.004(3)
O27	0.017(4)	0.016(3)	0.032(4)	-0.001(3)	0.002(3)	-0.004(2)
O28	0.018(3)	0.018(3)	0.015(3)	0.004(2)	0.004(2)	0.000(2)
O29	0.024(4)	0.029(3)	0.027(4)	0.008(3)	0.013(3)	0.001(3)
O30	0.014(4)	0.021(3)	0.037(4)	0.004(3)	-0.003(3)	0.005(2)

O31	0.023(4)	0.016(3)	0.026(4)	-0.005(2)	-0.001(3)	-0.003(2)
O32	0.017(3)	0.020(3)	0.015(3)	0.006(2)	0.004(2)	0.010(2)
O33	0.017(4)	0.039(4)	0.048(5)	0.028(3)	0.014(3)	0.003(3)
O34	0.021(4)	0.016(3)	0.040(4)	0.000(3)	0.010(3)	0.005(3)
O35	0.012(4)	0.039(4)	0.026(4)	0.006(3)	-0.001(3)	-0.001(3)
O36	0.017(4)	0.021(3)	0.051(5)	0.018(3)	0.006(3)	0.000(3)
O37	0.015(4)	0.031(3)	0.028(4)	0.000(3)	-0.001(3)	-0.001(3)
O38	0.022(4)	0.023(3)	0.055(5)	-0.018(3)	0.015(3)	-0.008(3)
O39	0.018(10)	0.104(17)	0.028(10)	-0.005(10)	0.010(7)	-0.023(9)
O40	0.16(3)	0.073(16)	0.063(17)	-0.003(13)	-0.055(16)	-0.004(16)
O41	0.068(17)	0.018(9)	0.069(17)	0.021(9)	-0.035(12)	-0.031(9)
O42	0.040(9)	0.043(8)	0.058(10)	-0.010(6)	0.020(7)	-0.007(6)
O43	0.056(11)	0.061(9)	0.057(10)	0.019(8)	0.024(7)	0.016(7)
O44	0.090(11)	0.034(6)	0.042(8)	0.000(5)	0.019(6)	0.000(6)
O45	0.029(6)	0.032(5)	0.035(6)	0.006(4)	-0.010(4)	-0.002(4)

Table A3. Bond lengths and bond valence calculation

Bond	Bond length (Å)	Bond valence	Atom	Bond valence sum	H atom attached
Fe1-O28	1.927(6)	0.635	Fe1	3.106	
Fe1-O25	2.002(6)	0.519	Fe4	3.198	
Fe1-O5	2.011(6)	0.506	S2	6.149	
Fe1-O11	2.013(6)	0.503	S3	6.100	
Fe1-O26	2.034(6)	0.476	**O28**	**1.235**	**1**
Fe1-O27	2.041(6)	0.467	O25	0.519	2
Fe4-O28	1.948(6)	0.600	O5	1.919	0
Fe4-O8	1.974(6)	0.559	O11	1.924	0
Fe4-O12	1.989(6)	0.537	O26	0.476	2
Fe4-O38	2.009(6)	0.509	O27	0.467	2
Fe4-O37	2.011(6)	0.506	O8	1.992	0
Fe4-O36	2.025(6)	0.487	O12	2.013	0
S2-O6	1.428(7)	1.698	O38	0.509	2
S2-O7	1.449(6)	1.605	O37	0.506	2
S2-O8	1.491(6)	1.433	O36	0.487	2
S2-O5	1.496(6)	1.413	O6	1.698	0
S3-O10	1.439(7)	1.649	O7	1.605	0
S3-O9	1.461(7)	1.554	O10	1.649	0
S3-O12	1.480(6)	1.476	O9	1.554	0
S3-O11	1.494(6)	1.421			

Note: O-H bond valence is 0.73 v.u. for a bond length of 1.0 Å. Bond valance calculation was based on data published in Brown and Altermatt (1985).

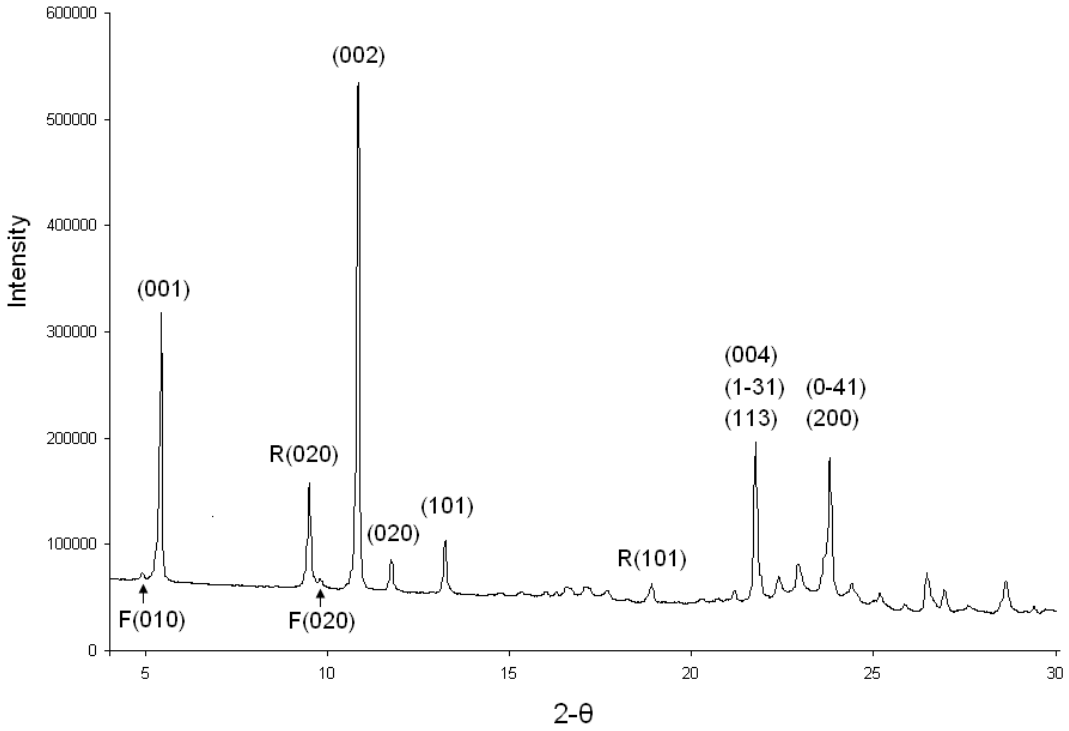

Figure A1. XRD pattern of the new phase with minor rhomboclase and ferricopiapite. Peak indexes are marked. R: rhomboclase; F: ferricopiapite. CuKα radiation was used.

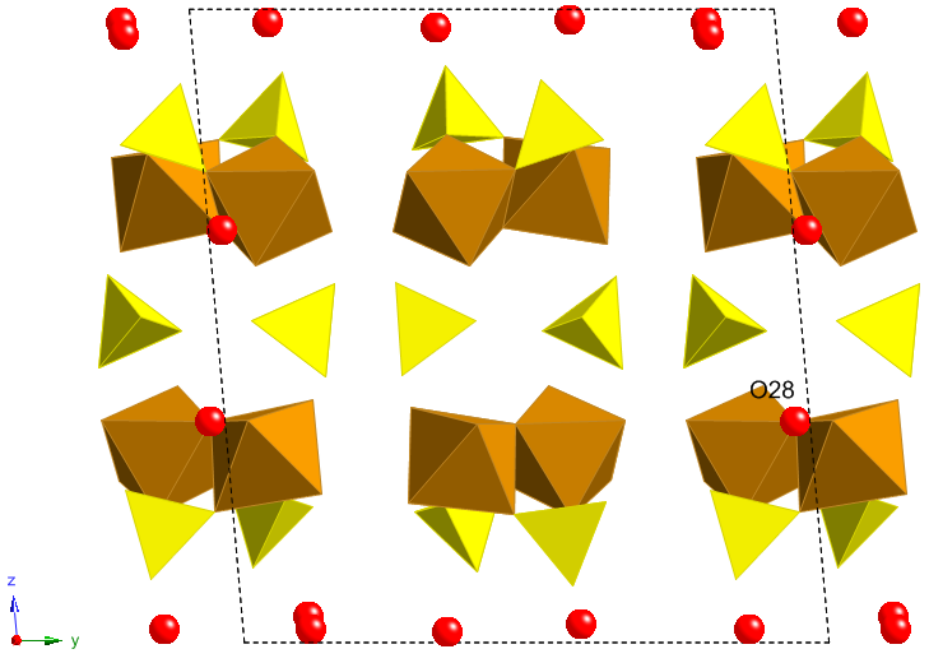

Figure A2. Crystal structure of $(H_3O)Fe_2(OH)(SO_4)_3 \cdot 7H_2O$. Red balls are O atoms of disordered water and hydronium ions, except the one marked with O28, the bridging OH between two FeO_6 octahedra.

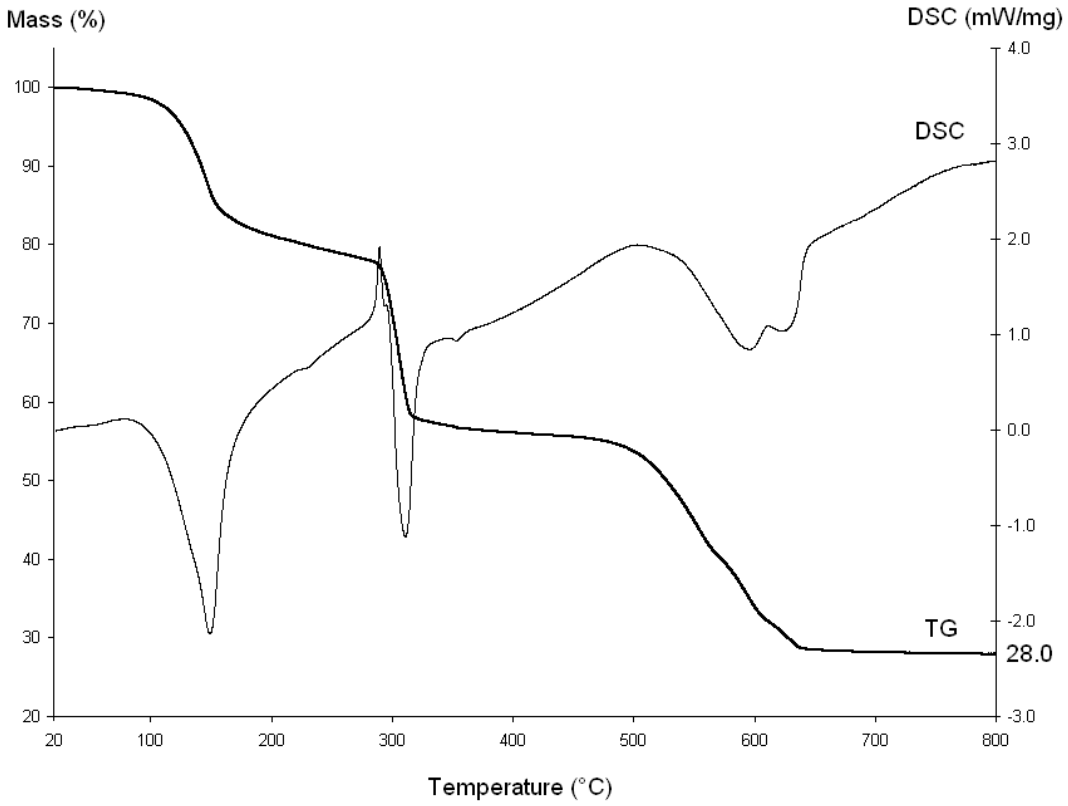

Figure A3. TG and DSC data of $(H_3O)Fe_2(OH)(SO_4)_3 \cdot 7H_2O$ with minor rhomboclase and ferricopiapite.